Predicting earthquake ground shaking due to 1D soil layering and 3D basin structure in SW British Columbia, Canada

by

Sheri Molnar
B.Sc., University of Windsor, 2000
M.Sc., University of Victoria, 2003

A Dissertation Submitted in Partial Fulfillment
of the Requirements for the Degree of

DOCTOR OF PHILOSOPHY

in the School of Earth and Ocean Sciences

© Sheri Molnar, 2011
University of Victoria

All rights reserved. This thesis may not be reproduced in whole or in part, by photocopy
or other means, without the permission of the author.

SUPERVISORY COMMITTEE

Predicting earthquake ground shaking due to 1D soil layering and 3D basin structure in SW British Columbia, Canada

by

Sheri Molnar
B.Sc., University of Windsor, 2000
M.Sc., University of Victoria, 2003

Supervisory Committee

Dr. John Cassidy (University of Victoria, School of Earth and Ocean Sciences and Natural Resources Canada, Geological Survey of Canada)
Co-Supervisor

Dr. Stan Dosso (University of Victoria, School of Earth and Ocean Sciences)
Co-Supervisor

Dr. Garry Rogers (University of Victoria, School of Earth and Ocean Sciences and Natural Resources Canada, Geological Survey of Canada)
Departmental Member

Dr. Carlos Ventura (University of British Columbia, Department of Civil Engineering)
Outside Member

Dr. Patrick Monahan (Penn West Exploration)
Additional Member

ABSTRACT

Supervisory Committee
Dr. John Cassidy (Earth and Ocean Sciences and Geological Survey of Canada)
Co-Supervisor

Dr. Stan Dosso (Earth and Ocean Sciences)
Co-Supervisor

Dr. Garry Rogers (Earth and Ocean Sciences and Geological Survey of Canada)
Departmental Member

Dr. Carlos Ventura (Civil Engineering, University of British Columbia)
Outside Member

Dr. Patrick Monahan (Penn West Exploration)
Additional Member

This thesis develops and explores two methodologies to assess earthquake ground shaking in southwestern British Columbia based on 1D soil layering and 3D basin structure. To assess site response based on soil layering, microtremor array measurements were conducted at two sites of contrasting geology to estimate Rayleigh-wave dispersion curves. A Bayesian inversion algorithm is developed to invert the dispersion data for the shear-wave velocity (V_S) profile together with quantitative uncertainty estimates, accounting rigorously for data error covariance and model parameterization selection. The recovered V_S profiles are assessed for reliability by comparison with invasive V_S measurements at each site with excellent agreement. Probabilistic site response analysis is conducted based on a sample of V_S profiles drawn from the posterior probability density of the microtremor inversion. The quantitative uncertainty analysis shows that the rapid and inexpensive microtremor array method provides sufficient resolution of soil layering for practical characterization of earthquake ground motion.

To assess the effects of 3D Georgia basin structure on long-period (> 2 s) ground motion for large scenario earthquakes, numerical 3D finite difference modelling of viscoelastic wave propagation is applied. Both deep (> 40 km) subducting Juan de Fuca plate and crustal (5 km) North America plate earthquakes are simulated in locations congruent with known seismicity. Simulations are calibrated by comparing synthetic waveforms with 36 selected strong- and weak-motion seismograms of the 2001 M_W 6.8 Nisqually earthquake. The ratio between predicted peak ground motions in models with

and without Georgia basin sediments is applied as a quantitative measure of basin amplification. Steep edges in the upper 1 km of the northwest and southeast extents of the basin are coincident with the appearance of surface waves. Focussing of north-to-northeast propagating surface waves by shallow (< 1 km) basin structure increases ground motion in a localized region of southern Greater Vancouver. This effect occurs for both types of earthquakes located south-southwest of Vancouver at distances greater than ~80 km. The predicted shaking level is increased up to 17 times and the duration of moderate shaking (> 3.4 cm/s) is up to 16 times longer due to the 3D Georgia basin structure.

TABLE OF CONTENTS

Supervisory Committee ii
Abstract iii
Table of Contents v
List of Tables vii
List of Figures viii
Acknowledgements x
1 Introduction 1
1.1 Motivation and objectives 1
1.2 Thesis outline 6
2 Probability analysis of 1D site response from Bayesian inversion of microtremor array data 8
2.1 Introduction 8
2.2 Site selection 12
2.3 Microtremor collection 15
2.4 Empirical amplification spectra 15
2.5 Dispersion curve generation 18
2.6 Bayesian inversion 22
2.6.1 Formulation and algorithms 25
2.6.2 Nonlinear inversion 27
2.6.3 Likelihood and error statistics 29
2.6.4 Model parameterization 31
2.7 Parameter uncertainties and inter-relationships 34
2.7.1 Fraser River delta site 34
2.7.2 Victoria 43
2.8 Assessment of reliability 47
2.9 Site response probability analysis 50
2.9.1 Uncertainty of V_{S30} 50
2.9.2 Uncertainty of amplification spectra 54
2.9.2.1 Uncertainty of amplification due to impedance 55
2.9.2.2 Uncertainty of amplification due to resonance 59
2.10 Discussion and conclusions 61
3 Effects of 3D Georgia basin structure on long-period ground motion 66
3.1 Introduction 66
3.2 Geology and structure of the Georgia basin 68
3.2.1 Physical structure models 71
3.2.1.1 Updated structure models 72
3.3 Finite-difference methodology 78
3.4 Earthquake scenario 1: Deep Juan de Fuca plate earthquakes 79
3.4.1 Seismicity 79
3.4.2 Source model 80
3.4.2.1 Model calibration 82
3.4.3 Results 92

3.4.4 Discussion 104
3.5 Earthquake scenario 2: Shallow North America plate earthquakes 105
3.5.1 Seismicity 105
3.5.2 Source model 107
3.5.3 Results 108
3.5.3.1 San Juan Island event 109
3.5.3.2 Georgia Strait event 115
3.5.4 Discussion 119
3.6 Comparison of deep and shallow earthquake scenarios 120
3.7 Conclusions 125
3.7.1 Future work 129
4 Conclusions 131
4.1 Predicting earthquake ground shaking due to 1D soil layering 131
4.2 Predicting earthquake ground shaking due to 3D basin structure 133
References 136
Appendix A: 3D finite-difference simulations 150

LIST OF TABLES

Table 1. NEHRP site classification based on V_{S30}. 9
Table 2. Weak-motion earthquakes recorded on the Fraser River delta and at the Victoria site. 17
Table 3. Uncertainty estimates of V_{S30} and amplification of PGA and PGV. 53
Table 4. Root-impedance amplification uncertainty estimates. 57
Table 5. SH-wave amplification uncertainty estimates. 61
Table 6. Two sets of the 3D viscoelastic structure model. 75
Table 7. Details of various finite-difference simulations of the Nisqually earthquake. ... 82
Table 8. Ground conditions at 16 selected earthquake recording stations in Georgia basin region. 86
Table 9. Comparison of PGV and intensity as described by level of damage and associated shaking. 93
Table 10. Summary of average peak horizontal motion and peak horizontal basin-amplified motion at 20 selected sites across Greater Vancouver for 11 JdF plate earthquake scenarios. 105
Table 11. Average peak horizontal motion and peak horizontal basin-amplified motion in Georgia basin and Greater Vancouver for two shallow NA plate earthquake scenarios. 120

LIST OF FIGURES

Figure 1. Tectonics of the Cascadia subduction zone 2
Figure 2. Simplified geology map of Georgia basin region 4
Figure 3. Location of the Fraser River delta and Victoria microtremor array sites 14
Figure 4. Spectral ratios for the delta and Victoria sites 17
Figure 5. Example of processing flow to estimate phase velocities from microtremor array measurements 20
Figure 6. Median phase velocity estimates for the delta and Victoria sites 21
Figure 7. Parameterization study for the delta site. 35
Figure 8. Full block-diagonal data error covariance matrix [$(m/s)^2$] estimated for the microtremor dispersion data at the delta site. 36
Figure 9. Histogram and autocorrelation plots of standardized residuals from Bayesian inversion for the delta site 37
Figure 10. Marginal probability distributions of model parameters for the delta site 38
Figure 11. 95% HPD credibility interval widths for V_S profile parameters from various inversions for the delta site 39
Figure 12. Correlation matrix of model parameters for the delta site 41
Figure 13. Selected joint marginal probability distributions for the delta site 41
Figure 14. Marginal probability V_S profile for the delta site 42
Figure 15. Parameterization study for the Victoria site 43
Figure 16. Marginal probability distributions of model parameters for the Victoria site. 45
Figure 17. Correlation matrix of model parameters for the Victoria site 45
Figure 18. Selected joint marginal probability distributions for the Victoria site 46
Figure 19. Marginal probability V_S profile for the Victoria site 46
Figure 20. Comparison of Bayesian inversion results with invasive V_S measurements at the delta site 49
Figure 21. Comparison of Bayesian inversion results with SCPT V_S profile at the Victoria site 49
Figure 22. V_{SZ} for the delta site. Probability distributions of V_{S30}, PGA and PGV amplification factors 52
Figure 23. V_{SZ} for the Victoria site. Probability distributions of V_{S30}, PGA and PGV amplification factors 53
Figure 24. Marginal probability root-impedance and SH-wave amplification spectra for the delta site 57
Figure 25. Marginal probability root-impedance and SH-wave amplification spectra for the Victoria site 59
Figure 26. Regional geology and major tectonic structures of the Georgia basin region. 70
Figure 27. Map of smoothed 250-m basin model V_P surface compared with geological and geophysical datasets. 75
Figure 28. Depth slices of updated basin and non-basin V_P models from surface to 1 km 76
Figure 29. Depth slices of basin and non-basin V_P models from 1 to 7 km depth 77
Figure 30. Map of JdF plate seismicity (1985-1999) in the Georgia basin region 80

Figure 31. Nisqually earthquake source parameters 81
Figure 32. Predicted PGV maps of M_W 6.8 Nisqually earthquake for Georgia basin and Seattle basin regions 83
Figure 33. Comparison of empirical M_W 6.8 Nisqually earthquake recordings and synthetic waveforms for 18 selected strong-motion stations in Seattle basin region 85
Figure 34. Comparison of empirical and synthetic waveforms at 16 selected weak- and strong-motion stations in Georgia basin region 87
Figure 35. Comparison of empirical and predicted PGV for the Nisqually earthquake in this study and those of Frankel et al. (2009) 88
Figure 36. Goodness-of-fit factor for PGV on EW and NS components from simulations in this study and those of Pitarka et al. (2004) 89
Figure 37. Basin amplification maps of the M_W 6.8 Nisqually earthquake simulation 91
Figure 38. Epicentre location map of the 11 M_W 6.8 JdF plate earthquake scenarios 92
Figure 39. EW PGV maps for the 11 simulated M_W 6.8 JdF plate earthquakes 94
Figure 40. NS PGV maps for the 11 simulated M_W 6.8 JdF plate earthquakes 95
Figure 41. Synthetic EW waveforms for the 11 M_W 6.8 JdF plate earthquake scenarios 96
Figure 42. Synthetic NS waveforms for the 11 M_W 6.8 JdF plate earthquake scenarios . 97
Figure 43. Map of EW basin amplification and comparison of synthetic waveforms 99
Figure 44. Map of EW basin amplification and synthetic waveforms across Greater Vancouver 100
Figure 45. Cross-sectional time-snapshots of simulated EW motion 102
Figure 46. Plan view time-snapshots of simulated EW motion 103
Figure 47. Map of NA plate seismicity (1985-1999) in the Georgia basin region 106
Figure 48. Map of shallow recurrent seismicity in SW British Columbia 107
Figure 49. Location map of NA plate earthquake scenarios 109
Figure 50. Maps of predicted PGV and corresponding basin amplification for the SJI scenario earthquake 110
Figure 51. Synthetic waveforms for the SJI scenario earthquake 111
Figure 52. Maps of basin amplification for the SJI scenario compared to the basin model and EW synthetic waveforms at 20 selected sites across Greater Vancouver 113
Figure 53. Time snapshots of simulated EW motion for SJI scenario 114
Figure 54. Maps of predicted PGV and corresponding basin amplification for the GS scenario earthquake 115
Figure 55. Synthetic waveforms for the GS scenario earthquake 117
Figure 56. Time snapshots of simulated EW motion for GS scenario 118
Figure 57. Maps of basin amplification compared to the basin model 119
Figure 58. Comparison of synthetic waveforms in Richmond for deep and shallow earthquakes with epicentre locations in the S and NW part of the basin region. 121
Figure 59. Maps of basin amplification for M_W 6.8 JdF plate earthquake scenario 2 122
Figure 60. Comparison of horizontal waveforms and total horizontal amplitude at two sites in Greater Vancouver for a deep JdF plate and shallow NA plate earthquake 124

ACKNOWLEDGEMENTS

I am profoundly grateful to my MSc and PhD thesis co-supervisors, Drs. John Cassidy and Stan Dosso, for their fantastic support, direction and redirection, tenacity, patience, and humour over our 11 years of collaboration. Thank you to my committee, Drs. Garry Rogers, Patrick Monahan, and Carlos Ventura for their support, helpful discussions, and combined knowledge. I am grateful to my external examiner, Dr. William Stephenson (USGS, Colorado), for his expertise and useful suggestions. Honorary committee member status is bestowed upon Drs. Kim Olsen (SDSU, California) and Andreas Rosenberger (NRCAN, Pacific) for their significant contribution to this work.

I would like to thank Drs. Michael Asten (Monash University, Australia), Cecile Cornou (LGIT, France), Matthais Ohrnberger (Universität Potsdam, Germany), and Marc Wathelet (LGIT, France) for consultation regarding microtremor array methodology. Thank you to NRCAN (Pacific) for field equipment and support, especially technicians Rick Hall and Tim Claydon, and Dr. Issam Al-Khoubbi. Thank you to Tim Côté (NRCAN, Ottawa) for software development. Thank you to my field assistants: Karen Simon and Philippe Benoit.

Dr. Kim Olsen graciously supplied his finite-difference code and the velocity structure model, and provided significant support and guidance. Dr. John He (NRCAN, Pacific) was instrumental in compiling and debugging the MPI finite-difference code and in generating the updated velocity structure model. Special thanks to the Minerva supercomputer personnel at the University of Victoria. I am grateful to Dr. Jim Hunter (NRCAN, Ottawa [retired]), Stephen Glover (BCMEMPR), Dr. David Mosher (NRCAN, Atlantic), and Dr. Ranjan Dash (Chevron) for velocity model data supplication. Maps of the Geological Survey of Canada Open File 2530 were digitized by Scan Conversions, Vancouver. I gratefully acknowledge Drs. Art Frankel (USGS, Washington) and Arben Pitarka (URS Corporation, California) for consultation regarding the finite-difference simulations. Earthquake recordings of the 2001 Nisqually earthquake used in this work were retrieved from the Pacific Northwest Seismic Network and Canadian National Seismic Network on-line catalogues.

This work was primarily conducted at NRCAN (Pacific); thank you to all researchers and staff, especially directors Drs. Ralph Currie and Carmel Lowe. Thank you to Robert Kung for GIS mapping support. Significant computer support was provided by Steve Taylor, Bruce Johnson and Michelle Gorosh. I would also like to thank staff at the School of Earth and Ocean Sciences, University of Victoria.

Thank you to my family, Mary and Joe Molnar and Christa Molnar, for their support, and friends and fellow graduate students for the good times.

This work was financially supported by a National Sciences and Engineering Research Council (NSERC) Canada Graduate Scholarship, an Earth Sciences Sector Post-Graduate Scholarship Supplement, NRCAN (Pacific), and research grants of Drs. Cassidy and Dosso. I gratefully acknowledge the Faculty of Graduate Studies for travel funding.

1 INTRODUCTION

1.1 Motivation and objectives

Earthquakes represent one of the most costly and devastating of natural hazards. Earthquake ground shaking can vary significantly across a region, related to the geological conditions of near-surface sediments and deeper sub-surface structure. As seismic waves pass through material of decreasing impedance, the resistance to motion decreases, and the particle velocity and therefore the amplitude of the seismic waves increase due to conservation of energy. Amplification may also occur at particular frequencies due to resonance of upward-propagating shear waves and laterally-propagating surface waves within near-surface low-velocity layers and sediment-filled basins, respectively. A famous example of earthquake ground motion amplification is the effect of the clay-filled basin of Mexico City during the 1985 M_S 8.1 Michoacán earthquake, more than 300 km distant. Here, peak ground acceleration was generally 14 times greater and the duration of strong shaking was nearly three times longer than on firm ground nearby, which caused 6 billion dollars of damage, primarily to 5-15 storey buildings, and 10,000 casualties (Singh et al. 1998; Reiter 1991; Roullé & Chávez-García 2006). Quantitative prediction of earthquake ground motion at a particular site therefore requires knowledge of the source generated seismic waves and the distributions of the earth's material properties which the waves travel through to reach surface (Sánchez-Sesma et al. 2002). The predictor variable for site response in modern building codes and empirical ground-motion prediction equations (GMPE) is based on the average earth material properties in the upper 30 m, primarily shear-wave velocity, i.e V_{S30}, at a site. The predictor variable proposed for long-period ground motion at sites in sedimentary basins is the depth to a shear-wave velocity (V_S) of 1.5 km/s, i.e. $Z_{1.5}$ (Day et al. 2008). Characterization of earthquake site response therefore relies heavily on an assessment of V_S at a site.

The metropolitan area of Greater Vancouver is the area of highest seismic risk in all of Canada, with a population exceeding 2 million and critical infrastructure situated above the seismically active Cascadia subduction zone (Figure 1a). In this convergent tectonic setting, the oceanic Juan de Fuca (JdF) plate subducts in a NE direction beneath

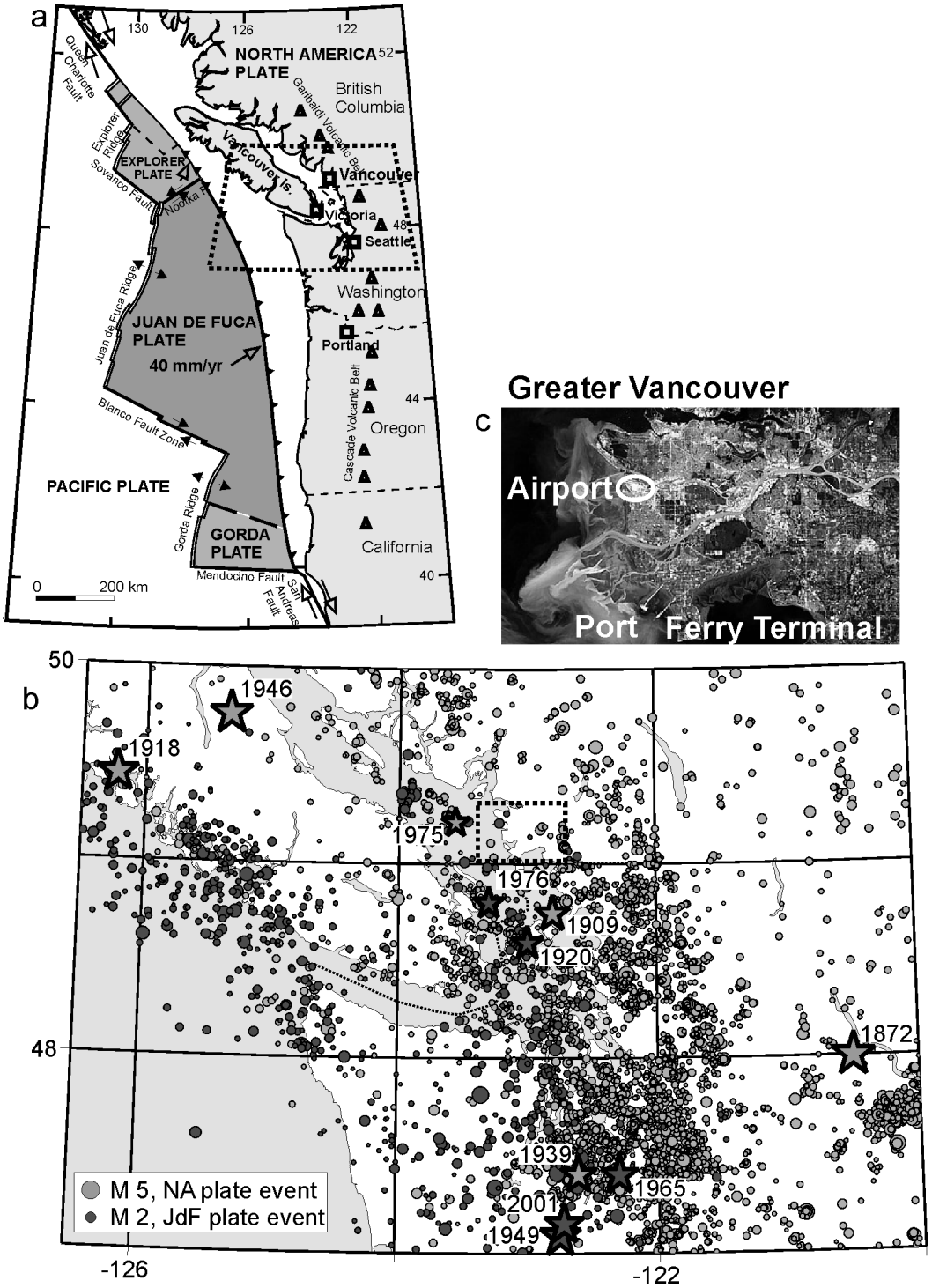

Figure 1. (a) Tectonics of the Cascadia subduction zone (modified from Hyndman et al. 1996). Volcanic centres are shown as triangles. (b) Plan view regional seismicity (1985-1999) map of southwestern British Columbia with epicentres of historical NA plate (M > 7) and JdF plate (M ≥ 6.5) earthquakes denoted by stars. Limits of map are shown as a dotted box in (a). (c) Satellite image of Greater Vancouver. Limits of image are shown as a dotted box in (b).

the continental North America (NA) plate. Earthquakes occur in three zones: (1) at the subduction interface between the two plates, which is currently locked and is accumulating strain to be released in future great earthquakes; (2) within the over-riding NA plate, which is in compression and results in crustal earthquakes and; (3) within the subducting JdF plate, mainly in response to bending of the plate at depth. Three large (M > 7) crustal NA plate earthquakes occurred in Washington (WA) State and on mid-Vancouver Island in 1872, 1918, and 1946, away from moderate and smaller events (Figure 1b). The largest recorded JdF plate earthquakes occurred beneath Puget Sound in 1949 (M_W 7.1), 1965 (M_W 6.5), and 2001 (M_W 6.8), whereas events beneath Georgia Strait have generally been of smaller magnitude ($M_W \leq 5.5$). The M ~9 Cascadia mega-thrust earthquake is beyond the scope of this work and is not considered here.

The critical infrastructure in SW British Columbia, including Canada's second busiest airport, the fourth largest tonnage port in NA, key electrical transmission corridors and a ferry terminal, is primarily located in the southern suburbs of Greater Vancouver (Figure 1c). This area is primarily underlain by Holocene silts and sands of the Fraser River delta and Pleistocene glacial deposits which overlie an irregular Tertiary clastic sedimentary rock surface. This entire sedimentary sequence infills a NW-oriented Late-Cretaceous structural depression (Mustard 1994; England and Bustin 1998), referred to here as the Georgia basin, which extends predominantly eastward across Georgia Strait to mid-Vancouver Island, and southward into mainland WA (Figure 2). The Georgia basin is one in a series of basins spanning from California to southern Alaska along the Pacific margin of North America (England & Bustin 1998) with approximate Tertiary dimensions of 130 by 70 by 5 km. Properties of the Late-Cretaceous and Tertiary Georgia basin sedimentary rocks and its basement (Figure 2) are known from seismic surveys (e.g. White and Clowes 1984), particularly seismic tomography results of the 1998 Seismic Hazards Investigations in Puget Sound (SHIPS) experiment (Zelt et al. 2001; Ramachandran et al. 2004; Dash et al. 2007). Realistic estimates of earthquake ground motion here must account for the combined amplification effect of the impedance ratio between soil layers and surface wave propagation due to the three-dimensional (3D) structure of the Georgia basin.

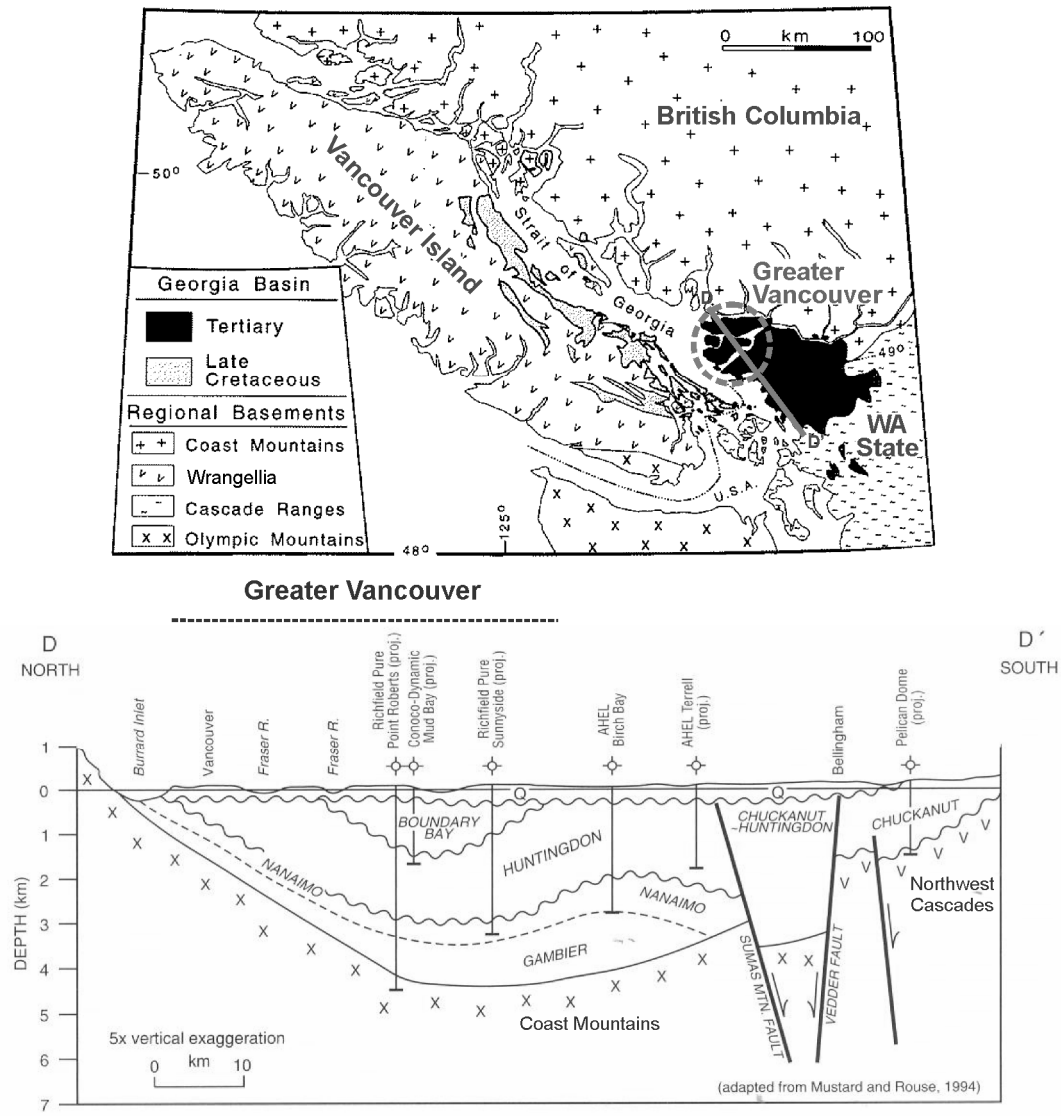

Figure 2. Simplified geology map of Georgia basin region (modified from Mustard et al. 1998). Geological cross-section D-D' corresponds to the solid grey line D-D' in map (modified from Hannigan et al. 2001).

This thesis explores and develops methodologies to improve assessment of earthquake ground shaking in SW British Columbia based on 1D soil layering and 3D basin structure. The microtremor array method involves recording background ambient vibrations with an array of seismic sensors to provide phase velocity estimates of dispersed surface waves which can then be inverted for V_S structure of the subsurface, an important property of the 1D soil layering. One of the objectives in applying the microtremor array method is to examine its effectiveness in retrieving V_S profiles at two

sites of contrasting site amplification behaviour in SW British Columbia and to assess the reliability of the results in comparison with other well-regarded V_S profiling methods. A critical issue identified for future improvement of inversion of microtremor array dispersion data is quantitative and meaningful evaluation of confidence intervals on V_S profiles (Cornou et al. 2006). To address this issue, a nonlinear Bayesian inversion approach is developed to produce unbiased uncertainty estimates which properly quantify the information content of the microtremor array dispersion data. The ultimate goal here is to perform site response probability analyses, examining uncertainty in predicted linear site amplification and corresponding site response characterization due to the uncertainty in V_S structure as quantified by Bayesian dispersion inversion. The potential benefit to the earthquake engineering community is demonstration that a rapid inexpensive V_S profiling method provides sufficient detail of the 1D soil layering for characterization of earthquake ground shaking.

Finite-difference simulations of long-period (> 2 s) ground motions are computed in SW British Columbia for scenario earthquakes in a regional 3D velocity model of the Georgia basin. This research provides the first detailed investigation of 3D earthquake ground motion for a sedimentary basin in Canada. The main objective here is to examine the effect of 3D Georgia basin structure on predicted ground shaking across Greater Vancouver from large (M_W 6.8) scenario earthquakes. The scenario earthquakes considered here include deep (42-55 km) JdF plate events with a seismic radiation pattern of the normal-faulting 2001 M_W 6.8 Nisqually, WA, earthquake (Figure 1b), and shallow (5 km) NA plate earthquakes with a radiation pattern of the blind-thrust 1994 M_W 6.7 Northridge, CA, earthquake. Scenario earthquakes are simulated in different epicentre locations of the Georgia basin region (within 100 km of Vancouver), congruent with known seismicity, to investigate variation in the strength of predicted ground motions and 3D basin effects. In particular to Greater Vancouver, the scenario that generates the strongest and longest shaking (i.e. most hazardous) and the causes of potential basin amplification are investigated. In order to conduct this research, the Georgia basin 3D structure model is revised with recent geological and geophysical information and calibrated by simulating the 2001 M_W 6.8 Nisqually earthquake and comparing the synthetic results with empirical recordings. The results of this research are useful to the

earthquake engineering community to: (1) design structures sensitive to long wavelengths, (2) develop probabilistic seismic hazard maps (e.g. for the Seattle basin region by Frankel et al. 2007), and (3) complement empirical strong-motion datasets for regression of ground-motion prediction (attenuation) relations (e.g. Day et al. 2008).

1.2 Thesis outline

This thesis is organized as follows. Chapter 2 presents probabilistic analysis of 1D site response from Bayesian inversion of microtremor array dispersion data for two sites in SW British Columbia. The structure of this chapter follows the framework for general application of the microtremor array methodology to obtain and validate uncertainty estimates of site amplification. Site selection and data collection are described in Sections 2.2 and 2.3, respectively. Generation of empirical microtremor and/or earthquake amplification spectra and dispersion curves are presented in Sections 2.4 and 2.5, respectively. The Bayesian inversion approach is outlined in Section 2.6, with results presented for the two sites in Section 2.7 and assessed for reliability in comparison to other V_S profiling methods in Section 2.8. The site response probability analysis is carried out in Section 2.9, in which probability distributions of common site response predictors (V_{S30} and amplification spectra) are computed based on the V_S profile probability distribution produced in Section 2.7 and evaluated for site response characterization in comparison with the empirical spectra generated in Section 2.4. Chapter 3 presents application of 3D finite-difference numerical modelling to investigate long-period ground motion in the Georgia basin region of SW British Columbia for scenario earthquakes. Section 3.1 provides an introduction and Section 3.2 discusses the geology and structure of the Georgia basin, as well as development and revision of the 3D structure models. Section 3.3 briefly describes the 3D finite-difference methodology. In each section for the two types of earthquake scenarios considered, deep Juan de Fuca plate events in Section 3.4, and shallow North American plate events in Section 3.5, the observed seismicity, proposed source model, simulation results, and a brief discussion are included. Calibration of the simulations is presented in Section 3.4.2.1, which compares synthetic results with earthquake recordings of a deep Juan de Fuca plate earthquake. Results of deep and shallow earthquake scenarios with similar epicentre locations are compared and

evaluated in terms of shaking duration in Section 3.6. Section 3.7 provides conclusions and recommendations for future work. Chapter 4 provides main conclusions of the research in this thesis.

2 PROBABILITY ANALYSIS OF 1D SITE RESPONSE FROM BAYESIAN INVERSION OF MICROTREMOR ARRAY DATA

2.1 Introduction

Characterization of earthquake ground motion amplification due to near-surface sediments, i.e. site response, is important for seismic hazard assessment. As seismic waves travel from source to surface and pass through material of decreasing impedance, amplification results due to conservation of energy. Amplification may also occur at particular frequencies due to resonance of shear waves within near-surface low-velocity layers. Large variability in earthquake ground motions has been observed, both site-to-site variability for a given earthquake and earthquake-to-earthquake variability at a given site (e.g. Boore 2004). Characterization of site class in modern building codes and site response in recent empirical ground-motion prediction equations (GMPE) are primarily based on the average shear-wave velocity (V_S) in the upper 30 m, V_{S30}, at a site. The U.S. National Earthquake and Hazards Reduction Program (NEHRP) categorizes site response into six site classes (A-F) based primarily on V_{S30} (Table 1). The V_{S30} classification scheme, adopted by the National Building Code of Canada (NBCC 2005), tries to average out earthquake-specific variability in that sites grouped into the same class are expected to experience a similar degree of amplification as determined from many empirical earthquake recordings. Predictions of site amplification in recent GMPEs are calculated directly from the measured V_{S30} value (e.g. Next Generation of ground-motion Attenuation [NGA] relations). For linear or weak motions, site amplification is modelled as a function of $\ln(V_{S30})$. Direct use of the V_{S30} value in the site term of GMPEs was shown to be more effective at determining site-to-site variations than the rock/soil classification scheme (Boore 2004), and nearly as effective (Boore 2004) or slightly more effective (Stewart et al. 2003) than NEHRP site classes, but less effective than using detailed surface geology (Stewart et al. 2003). In Canada, site response determination procedures include: (1) modification of the uniform hazard spectrum (per city) by foundation factors based on V_{S30} (Table 1) or (2) computation of site specific design spectra based on the V_S-depth profile (NBCC 2005). Hence, characterization of earthquake site response relies heavily on an assessment of V_S at a site.

A variety of methodologies have been developed to provide a reliable V_S profile at a site, for which the least expensive and time-consuming method is of great interest to the earthquake engineering community. Invasive methods, which involve placing a seismometer beneath the Earth's surface with a source at the surface or downhole, perform *in situ* measurements of V_S generally in small (e.g. 1-m) depth increments, resulting in resolution of fine structure or layering, until the maximum borehole or penetration depth is reached. Conversely, most surface seismic techniques, based on the inversion of surface-wave dispersion data, lack the ability to resolve fine structure but are less expensive. Surface methods are especially useful in urban areas, but require the assumption of a horizontally stratified earth over the spatial extent of an array of sensors. Active-source seismic techniques, such as spectral analysis (SASW, Stokoe et al. 1994) or multichannel analysis of surface wave methods (Park et al. 1999) generally offer a restricted investigation depth (a few tens of metres) related to the restricted frequency content of the source. The microtremor array method (Aki 1957, Asten & Henstridge 1984, Horike 1985), a passive-source method that uses background (ambient) seismic noise with a wide frequency content from a variety of sources, is generally sensitive to greater depth (e.g. ≥ 100 m, Horike 1985).

Table 1. NEHRP site classification based on V_{S30}.

Site class and description		**V_{S30} range (m/s)**	**Intensity of shaking based on spectral acceleration**	
			Short-period (0.2 s)	**Long-period (1.0 s)**
A	Hard rock	$V_{S30} > 1500$ m/s	0.7 – 0.8	0.5 – 0.6
B	Rock	$760 < V_{S30} \leq 1500$	0.8 – 1.0	0.6 – 0.8
C	Very dense soil and soft rock	$360 < V_{S30} \leq 760$	1.0 (reference ground condition, no amplification)	
D	Stiff soil	$180 \leq V_{S30} \leq 360$	1.0 – 1.3	1.1 – 1.4
E	Soil with soft clay	$V_{S30} < 180$ m/s	0.9 – 2.1	1.7 – 2.1
F		Site-specific analysis required		

The performance of particular V_S measurement methods to provide accurate V_S profiles for site response determination is generally evaluated in terms of: (1) similarity of NEHRP site class and predicted ground motion based on V_{S30} and/or (2) similarity of calculated amplitude spectra due to 1D propagation of horizontally-polarized shear (SH)

waves, seismic impedance ratio, and/or Rayleigh wave ellipticity (e.g. Wald and Mori 2000). Evaluation of invasive and non-invasive methods at six sites in the Santa Clara valley in California yielded similar V_S profiles for which predicted site amplifications agreed within about 10-20% (Boore & Asten 2008, Stephenson et al. 2005). Another comprehensive study of V_S profiling methods at sites in California determined the coefficient of variation (CoV, defined as standard deviation divided by mean) of V_{S30} estimates to be 1-3% for co-located invasive methods, and 5-6% for co-located non-invasive (SASW) methods (Moss 2008). When these V_{S30} uncertainties associated with each V_S measurement method are included in the regression of ground motion data using a Bayesian approach, uncertainty in predicted ground motion is reduced (Moss 2011). Variability of the V_{S30} estimate may not be an issue for NEHRP site classification if the different V_{S30} estimates are all well within the limits of a category, but a shift in the classification may occur if the estimates span the class boundary, resulting in a change in the predicted amplification level. For example, the average maximum difference between V_{S30} estimates derived from three different profiling methods at seven strong-motion instrument sites in Ilan, Taiwan was found to be 43 m/s (Kuo et al. 2009). However, for three of the seven sites, the V_{S30} estimates span the boundary between class D and E resulting in variation of site class, and thus the predicted amplification may depend on the V_S profiling method chosen for site response determination. For large-scale site assessment work (e.g. hazard mapping, urban planning, etc.), transition site classifications (e.g. A-B, B-C, etc.) are sometimes adopted for geologic units with V_{S30} estimates near a classification boundary (e.g. Wills et al. 2000; Monahan et al. 2000).

If only one V_S profiling method is under evaluation then the predicted amplitude spectrum is usually compared with empirical earthquake and/or microtremor spectral ratios. Comparison of predicted site amplification using the V_S profile estimated from dispersion data with empirical earthquake response has led to variable results. In some studies, comparisons have provided good agreement at the fundamental frequency (Di Guilio et al. 2006, Maresca et al. 2006, Ohrnberger et al. 2004) and sometimes at higher-order modes (Thompson et al. 2009, Gitterman et al. 1996). In contrast, in other studies agreement has been observed only with respect to the overall spectral shape (Picozzi et al. 2009), main trend (Parolai et al. 2007), or amplitude (Chavez-Garcia & Tejeda-

Jacome 2010). However, parametric uncertainty analyses have demonstrated that variability in predicted site response is predominantly due to uncertainty in V_S structure, since maximum site amplification is characterized by the near-surface impedance ratio (Seed et al. 1988, Field & Jacob 1993, Li & Assimaki 2010). When uncertainties in the input parameters are accounted for, better agreement is obtained between the predicted and empirical distributions of amplification spectra (Field & Jacob 1993). Assessments of probabilistic seismic hazard therefore need to account for the variability in predicted site amplification due to uncertainty in V_S structure.

Traditionally, theoretical site amplification is calculated using *in situ* V_S measurements with arbitrary estimates of uncertainty (e.g. 10-20%) based on an assumed Gaussian or log-normal distribution to account for the inherent probabilistic nature of site response characterization (e.g. Seed et al. 1988). Similarly, best-fit V_S models from the optimization-based inversion of dispersion data have been used for calculating site amplification, with uncertainties approximated using all or a subset of the models sampled during the inversion process (Di Guilio et al. 2006, Parolai et al. 2007, Fah et al. 2003, Scherbaum et al. 2003, Foti et al. 2009). For example, Scherbaum et al. (2003) examined variability in predicted SH-wave amplification for the 20 best-fitting V_S profiles from joint inversion of dispersion curves and microtremor H/V spectral ratios, and demonstrated no more than 20% difference at the fundamental frequency. In contrast, large uncertainty in fundamental peak amplification (~4-11) was predicted by Fah et al. (2003) based on seven best-fitting V_S profiles from inversion of the microtremor H/V spectral ratio. Foti et al. (2009) applied Monte Carlo sampling to microtremor array dispersion data, then scaled the models to reduce data misfit and retained only those fitting the data to a pre-selected level. A 15% average CoV in overall V_S structure resulted in 8% CoV in predicted peak ground acceleration. However, it should be noted that none of these approaches properly estimate V_S profile uncertainties for use in characterizing site amplification uncertainties. Quantitative and unbiased uncertainty estimation requires not only a nonlinear sampling approach that draws models proportional to their probability, but also rigorous estimation of the data error statistics and an appropriate model parameterization. Bayesian inversion using Markov-chain Monte Carlo methods is applied here to microtremor dispersion data, combining data

error covariance estimation with objective model parameterization based on the Bayesian information criterion, to provide unbiased uncertainty estimation.

The goal here is to examine uncertainty in predicted linear site amplification and corresponding site response characterization due to the uncertainty in V_S structure as quantified by Bayesian inversion of microtremor array dispersion data. Two sites of contrasting site amplification behaviour in British Columbia, Canada, are considered (Section 2.2). The structure of this chapter follows the framework for general application of the microtremor array methodology to obtain and validate uncertainty estimates of site amplification, which includes: collection of microtremor recordings (Section 2.3), generation of empirical microtremor and/or earthquake amplification spectra (Section 2.4), estimation of dispersion curves (Section 2.5), Bayesian inversion for V_S structure (Section 2.6) and uncertainties (Section 2.7) and comparison with other V_S profiling methods (Section 2.8), calculation of V_{S30} and/or amplification spectra probability distributions based on the V_S profile probability distribution (Section 2.9), and evaluation of predicted site response by comparison with empirical spectra (Section 2.9.2). A similar framework was proposed by Gitterman et al. (1996) to evaluate the best-fit V_S model. The work in this chapter has been published in Molnar et al. (2010a) and Molnar et al. (2011, submitted to *Soil Dynamics and Earthquake Engineering*).

2.2 Site selection

Southwestern British Columbia is one of the most seismically active areas in Canada, located at the northern portion of the Cascadia subduction zone. High seismic hazard combined with critical infrastructure and a significant population results in the highest seismic risk in Canada (Onur et al. 2005); hence, seismic hazard assessment is of utmost importance in southwestern British Columbia. The risk is primarily associated with the two largest urban centres, greater Vancouver and Victoria, situated in contrasting geological settings. The local geology in Victoria generally exhibits a strong near-surface impedance contrast with 0-30 m of soft marine silts over glacial deposits and/or very stiff bedrock. Accumulations of these soft silts have been correlated with chimney damage from the M_S 7.3 1946 central Vancouver Island earthquake (> 200 km distant, Wuorinen 1974) and significantly greater earthquake shaking intensity was reported in these areas

in comparison to bedrock sites in the city from felt earthquakes in 1996 (Levson et al. 1998) and 2001 (Molnar et al. 2004). In contrast, the Fraser River delta in southern greater Vancouver, is composed of up to 500 m of Holocene sands and silts, which overlie up to 500 m of over-consolidated Pleistocene glacial and interglacial deposits. The underlying bedrock is dominated by Tertiary sandstone and conglomerate occurring at depths of 350 to 1050 m (Hunter et al. 1998b). From compilation of ~500 surface refraction, downhole, and SCPT measurements conducted across the Fraser River delta (Hunter et al. 1998), the overall shear-wave velocity in the upper 100 m of the Holocene deltaic sediments increases significantly with depth as a result of loading, and is well represented by a power-law gradient (Hunter & Christian 2001). This Holocene-Pleistocene boundary is characterized by an abrupt increase in V_S by a factor of 1.5 to 3.0 (Hunter et al. 1998). Amplification potential varies greatly across the delta as the thickness of the Holocene sediments is extremely variable and the bedrock surface beneath the delta is highly irregular; thick sequences of Fraser River sediments are susceptible to high amplification and liquefaction (Hunter et al. 1998). Figure 3 shows the locations chosen in each city for application of the microtremor array method which are co-located with sites of pre-existing V_S measurements from invasive techniques (seismic cone penetration testing [SCPT; Robertson et al. 1992] and/or surface-to-downhole) for assessment of reliable V_S structure retrieved using the microtremor array method (Section 2.8).

At the Fraser River delta site, V_S measurements are available from a 300-m borehole (Dallimore et al. 1995) and four SCPT sites (Figure 3b). The downhole V_S measurements, shown in Figure 3c and d, generally increase with depth from 125 m/s near the surface to ~500 m/s at the Holocene-Pleistocene boundary at 235-m depth (Hunter et al. 1997), with high (> 600 m/s) velocities within the underlying Pleistocene material. The four SCPT V_S profiles (maximum penetration depths from 31-62 m; Woeller et al. 1994) display the same general trend and range of V_S values within the Holocene material. Significant velocity reversals occur at irregular intervals displaying sensitivity to fine geologic layering.

At Victoria, a single SCPT V_S profile is available (Figure 3f) (Monahan & Levson 2001). The cone penetrated through low velocity material to 17 m depth before meeting

refusal. The average V_S of the upper 17 m based on the SCPT measurements is 108 m/s. Stiff material below 17 m is likely over-consolidated glacial material (V_S of 475 ± 78 m/s, Monahan and Levson 2001) and/or hard bedrock (V_S > 1500 m/s, Monahan and Levson 2000). Thus, the Victoria site likely has a strong near-surface impedance contrast of a factor of ~4 or more.

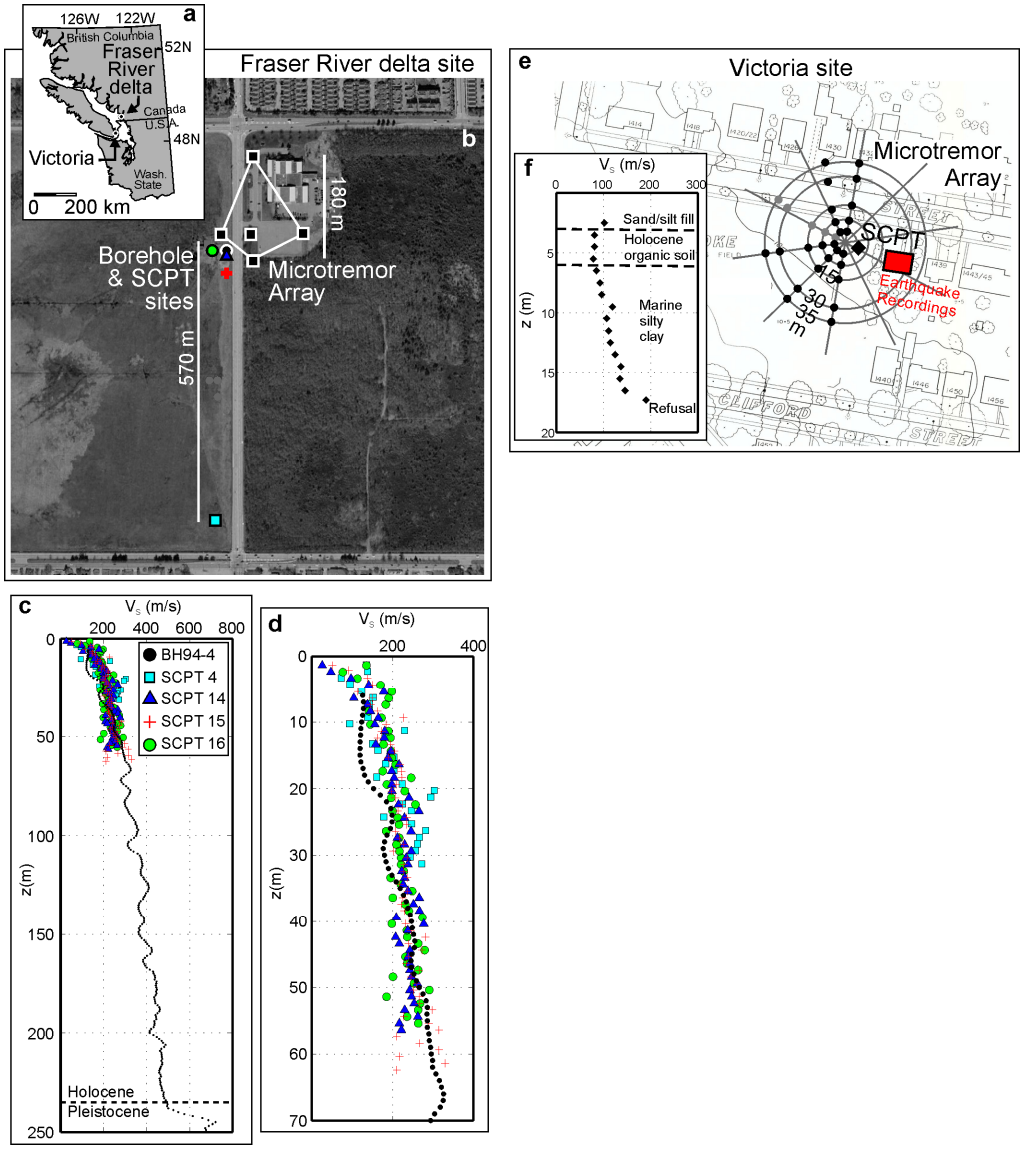

Figure 3. (a) Location of the Fraser River delta and Victoria in southwestern British Columbia. (b) Delta microtremor array site with the largest aperture array indicated by black circles, borehole by the black square, and SCPT sites (locations from Monahan 1999) by coloured symbols. (c) and (d) show the downhole and SCPT measurements at two scales. (e) Victoria microtremor array site showing the five semi-circular arrays (circles, with grey circles denoting non-working sensor), SCPT site, and strong-motion instrument site. (f) SCPT V_S measurements together with the lithologic interpretation from Monahan & Levson (1997).

2.3 Microtremor collection

At the Fraser River delta and Victoria sites, arrays of up to six field units were set into cross-shaped and semi-circular configurations, respectively. Each field unit is composed of a three-component broadband sensor (Guralp CMG-40T with a 0.03-100 Hz passband) connected to a digitizer with 100-Hz sampling, an external GPS antenna for timing, and a small external battery. Overall, the guidelines for collection and processing of microtremor array measurements provided by the European SESAME workgroup were followed (Ohrnberger et al. 2008). To obtain dispersion characteristics over as wide a frequency band as possible, the array aperture is adjusted several times in the field to account for the trade-off between resolution and aliasing of the narrow target wavelength associated with each aperture (Jongmans et al. 2005). The spatial extent of each array is therefore related to the depth of investigation; for the shallow Victoria site, the array radius was varied five times between 5 to 35 m (Figure 3e), whereas at the deep Fraser River delta site the aperture was varied six times between 15 to 180 m (Figure 3b and Figure 6a inset).

Waveform processing of the microtremor recordings included slope and offset removal, and band-pass filtering from 0.1 to 25 Hz. All files were then imported into the GEOPSY database (SESARRAY software package, version 2.6.3; www.geopsy.org) for computing the horizontal-to-vertical spectral ratios presented in the following section. For extraction of dispersion characteristics, the vertical-component microtremor array recordings were grouped according to array aperture, cut to the same duration (43-80 minutes), and processed using frequency-wavenumber techniques as discussed in Section 2.5.

2.4 Empirical amplification spectra

Amplification of earthquake waves due to the soil column at a site is generally investigated using spectral ratio analysis of ground motion recordings. To isolate the soil column response, the amplitude spectra from a recording that includes site effects is divided by the spectrum of a recording that has not been modified by site effects, assuming the same source, path, and instrument effects for the pair of recordings (Borcherdt 1970). The first peak of the amplification spectrum tends to be of largest

amplitude and represents the fundamental frequency of the site (or site period). Traditionally, earthquake response of a soil site is considered relative to amplification with respect to a nearby bedrock site (Steidl 1993; Field and Jacob 1995). In practice, spectral ratios are performed using a variety of ground motion recording pairs: soil-to-rock outcrop, surface-to-downhole, and horizontal-to-vertical (H/V) component. The H/V spectral ratio method has been applied using both earthquake (Lermo and Chavez-Garcia 1993) and microtremor recordings (Nakamura 1989). At strong-motion instrument sites in Victoria, soil-to-rock outcrop and H/V spectral ratios from weak-motion (< 5% g) earthquake recordings generally agree in peak frequency and amplitude (Molnar et al. 2004). Agreement between microtremor and earthquake H/V spectral ratios was also determined at strong-motion instrument sites in Victoria (Molnar & Cassidy 2006) and the Fraser River delta (Molnar et al. 2007). Therefore microtremor and earthquake spectral ratios are regarded as a reliable measure of earthquake site response for the two array sites considered here.

Figure 4 presents the average microtremor H/V ratio (± two standard deviations) and earthquake SH/V ratios from three weak-motion events (Table 2). The horizontal spectrum (H) in the microtremor H/V calculations is the average of smoothed horizontal-component Fourier spectra at all sensors of the array, whereas for the three weak-motion earthquakes, the transverse shear-wave recordings are used to calculate the horizontal spectrum (SH). The vertical spectrum (V) is calculated from the microtremor or earthquake vertical-component recordings. All earthquakes were recorded by GSC accelerometers (DC to 42 Hz passband) that continuously record and communicate via the internet. Earthquake amplitude spectra were computed using data windows that began ~2 s before the S-wave arrival and contained most of the recorded seismic energy. Recordings of three other weak-motion earthquakes at the Fraser River delta sites are too short in duration for use and no other earthquake recordings are available for the Victoria site.

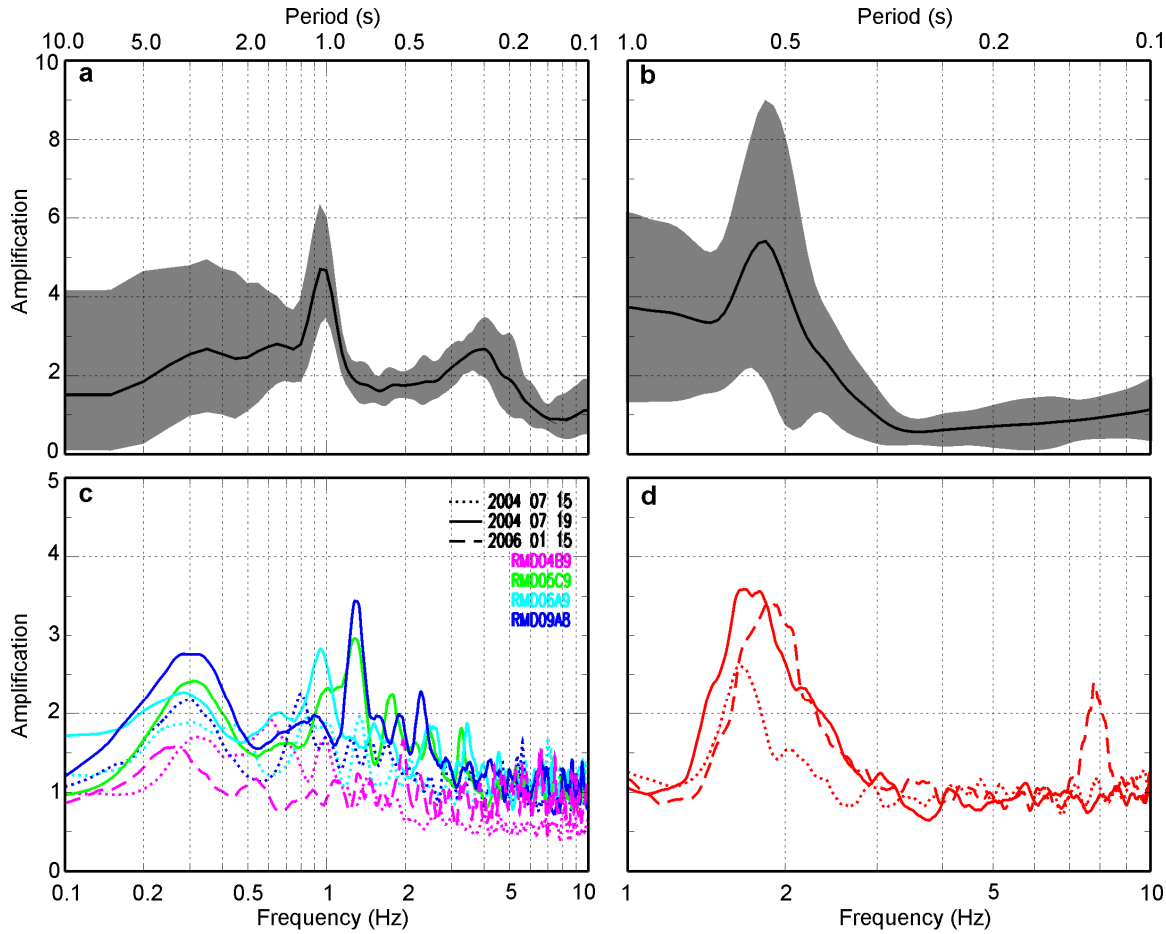

Figure 4. Average microtremor H/V spectral ratio (shaded region indicates ± two standard deviations) for the (a) Fraser River delta and (b) Victoria sites. Earthquake SH/V ratios from three events (Table 2) at (c) four Geological Survey of Canada recording locations on the delta (station names given in legend), and (d) the Victoria strong-motion site. Note amplification axis limit is 10 for microtremor ratios and 5 for earthquake ratios.

Table 2. Weak-motion earthquakes recorded on the Fraser River delta and at the Victoria site.

Date	Magnitude	Depth	Distance	Azimuth	Maximum Acceleration (cm/s^2)
2004-07-15	M_W 5.8	12 km			6.19
	Fraser River delta		~ 300 km	95-110°	2.89
	Victoria		~300 km	95-110°	1.74
2004-07-19	M_W 6.4	12 km			13.78
	Fraser River delta		~ 300 km	95-110°	3.87
	Victoria		~300 km	95-110°	2.45
2006-01-15	M_L 3.6	46 km			14.63
	Fraser River delta		73 km	24°	1.91
	Victoria		22 km	40°	4.11

For the Fraser River delta site, peaks occur in the average microtremor H/V ratio at approximately 0.35, 1.0 and 4.0 Hz, with the largest amplification at 1.0 Hz (Figure 4a). The low fundamental frequency of 0.35 Hz is related to the thick accumulation of Holocene deltaic sediments at the site. SH/V ratios from earthquake recordings at four strong-motion instrument sites on the delta with similar thick sequences of material also show a consistent low fundamental frequency (~0.3 Hz) in Figure 4c. Peaks in some of the earthquake ratios are observed at higher frequencies of approximately 1.0 and 1.4 Hz related to site-dependent first-order modes. The earthquake SH/V ratios show similar low levels of amplification (≤ 3) for the first three modes. Amplitudes of the earthquake SH/V ratios are slightly lower than the microtremor H/V ratio, with the best agreement in amplitude occurring at the ~0.3 Hz fundamental peak.

For the Victoria site, the average microtremor H/V ratio in Figure 4b displays a single peak at nearly 2 Hz, with high amplification of 5.5 relative to vertical motion. The Victoria strong-motion instrument (Figure 3e) recorded the same three earthquakes as on the Fraser River delta (Table 2). SH/V spectral ratios in Figure 4d show a prominent peak near 2 Hz, with amplification of 2.5-4.0, in general agreement with the microtremor H/V ratio distribution. A possible higher-order mode is observed as a peak at 8 Hz from one event.

2.5 Dispersion curve generation

In general, surface seismic techniques exploit the dispersive nature of surfaces waves, in which shorter wavelengths generally arrive later than longer wavelengths since they are confined to lower velocity material at shallower depths. Phase velocity dispersion is measured by an array of sensors to resolve a dispersion curve (velocity as a function of frequency). Wave propagation velocity is primarily influenced by the V_S structure; hence V_S profiles may be estimated by inverting the measured dispersion curve. Frequency-wavenumber (*f-k*) techniques are applied here to determine the phase velocity and direction of the dominant wave travelling across the array. By using vertical-component recordings, Rayleigh waves are assumed to be the dominant wave type. The Fourier transform of the cross-correlation of array recordings provides an *f-k* spectrum, the amplitude of which is associated with the coherency of the signal. For each frequency, the wavenumber

coordinates of the peak of the *f-k* spectrum (k_x, k_y) determines the phase velocity (c) of the dominant wave as well as its propagation direction (ϕ) by

$$c = \frac{2\pi f}{\sqrt{k_x^2 + k_y^2}}, \tag{1}$$

$$\phi = \tan^{-1}\left(\frac{k_x}{k_y}\right). \tag{2}$$

Both the *f-k* method (Lacoss et al. 1969) and the high-resolution *f-k* method (Capon 1969) are applied to the microtremor measurements in this paper, the details of which are provided in Wathelet et al. (2008). The *f-k* method sums spectra phase-shifted by the wavenumber difference between array sensors (or sums time-shifted seismograms) to provide a peak in the *f-k* spectrum. In comparison, the high-resolution *f-k* method provides a peak in the *f-k* spectrum by passing the most coherent signal unsuppressed while suppressing less coherent signals corresponding to other wavenumbers.

Figure 5 depicts an example of the processing flow to estimate phase velocities from microtremor array measurements for the 5-m array at Victoria, carried out using the GEOPSY software. For a particular choice of centre frequency, the microtremor recordings (Figure 5a) are first band-pass filtered in a 0.1-Hz band centred on that frequency. The filtered data are time windowed with window lengths set to 125 times the reciprocal of the centre frequency. The time windows are Fourier transformed and the phase velocity for each window is determined using eq. (1) with a grid search applied to locate the maximum in the wavenumber plane (Figure 5b). This procedure is repeated for 100 logarithmically-spaced centre frequencies from 0.5-20 Hz (corresponding to minimum and maximum time windows of 6.25 and 250 s). A histogram is computed of phase velocity values for all time windows and all frequencies (Figure 5c). Following methodology of Wathelet et al. (2008), theoretical resolution and aliasing frequency limits for each array aperture are based on the minimum (k_{min}) and maximum (k_{max}) wavenumbers of the array response to a vertically incident plane wave, respectively. The grid spacing and search area for the velocity of the wavenumber maxima are set here to $k_{min}/2$ and $1.5k_{max}$ for *f-k* analysis, and $k_{min}/3$ and $2k_{max}$ for high-resolution *f-k* analysis (Ohrnberger et al. 2008). The median phase velocity value is then calculated at each centre

frequency and, if reliable (e.g. within theoretical limits, sufficiently high bin count), is kept (squares in Figure 5c).

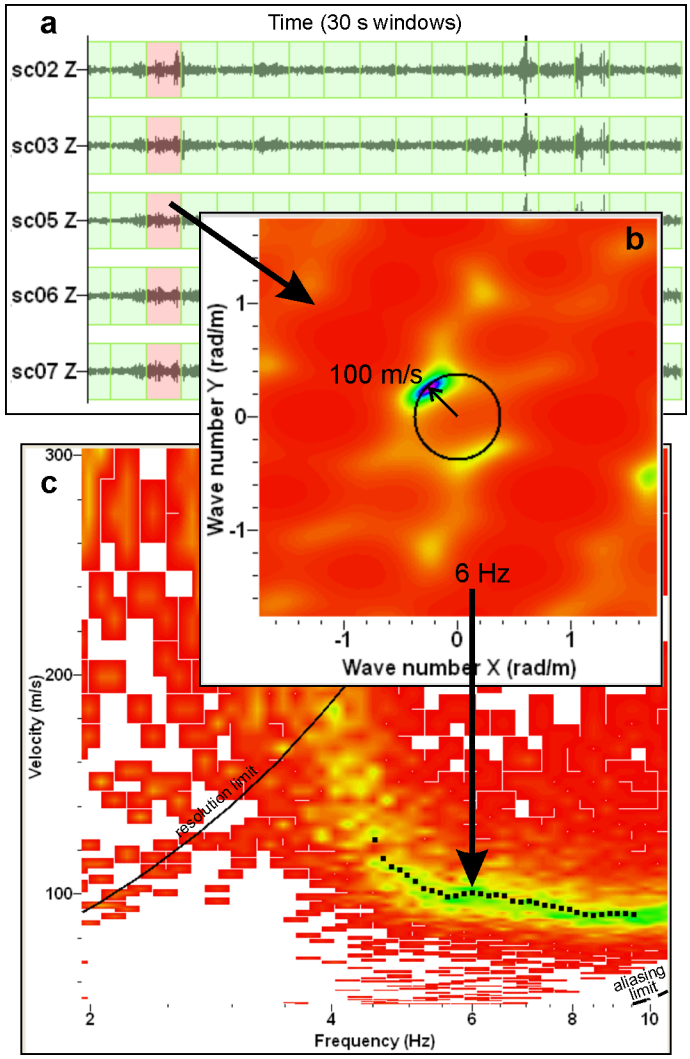

Figure 5. Example of processing flow to estimate phase velocities from microtremor array measurements for the 5-m array at the Victoria site (high-resolution *f-k* results are shown, details in text).

Figure 6 presents the reliable phase velocity estimates determined from both *f-k* and high-resolution *f-k* processing for all array apertures at the two sites. Note that good quality phase velocity estimates are not necessarily produced over the entire theoretical frequency band; hence, the phase velocity range which can be determined for a particular array is difficult to assess *a priori*. The *f-k* and high-resolution *f-k* phase velocity estimates are essentially indistinguishable (similar to Ohrnberger *et al.* 2004; Di Giulio *et al*. 2006; Wathelet *et al.* 2008), and are combined into a single dataset. No reliable phase

velocity values are retrieved at frequencies corresponding to high amplitude peaks in the H/V spectral ratios (Figure 4), below 1 Hz and 2 Hz for the Fraser River delta and Victoria sites, respectively. Fah et al. (2001) determined that fundamental-mode Rayleigh waves dominate in the frequency band above the H/V peak, whereas energy is distributed between higher modes at or below the H/V peak. The phase velocity estimates are averaged to provide a single dispersion curve over the widest possible frequency range. The dispersion curve for the Fraser River delta site (Figure 6c) varies from ~ 400 m/s at 1.2 Hz to 130 m/s at 6.5 Hz with 52 logarithmically-spaced data. The dispersion curve for Victoria (Figure 6d) varies from nearly 300 m/s at 2.4 Hz to ~ 90 m/s at 9.3 Hz with 35 data.

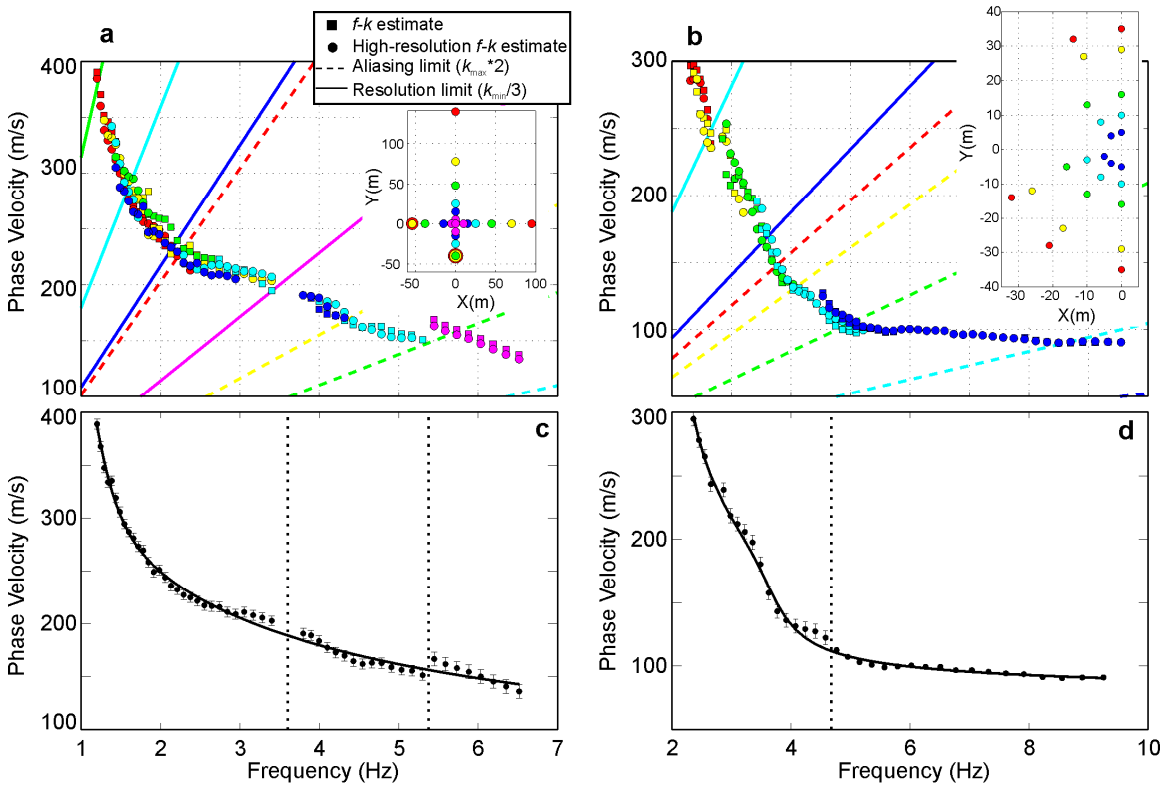

Figure 6. Median phase velocity estimates coloured according to array aperture (insets depict sensor configurations) for the (a) Fraser River delta site and (b) Victoria site. Dispersion curve used in the Bayesian inversion for the delta and Victoria sites are shown in (c) and (d), respectively, with maximum-likelihood standard deviation estimates indicated as error bars. Solid lines show the predicted dispersion curve of the most-probable V_S profile, and dotted lines depict segmentation of data into frequency bands.

2.6 Bayesian inversion

Inversion of surface-wave dispersion data is a non-unique and nonlinear problem such that a range of V_S models can acceptably fit the data. The 3rd International Symposium on the Effects of Surface Geology on Seismic Motion in 2006 conducted a comprehensive noise-blind test of the microtremor array method and its ability to retrieve the subsurface V_S structure, and found that fine-layering and basement depth and velocity were almost never retrieved (Cornou et al. 2006). A critical issue identified for future improvement of microtremor inversion was quantitative and meaningful evaluation of confidence intervals on V_S profiles. Clearly, V_S estimates from inversion of microtremor dispersion data must be shown to be reliable and their uncertainties understood to be used with confidence for seismic design purposes.

A variety of approaches have been applied to invert microtremor array dispersion data based on minimizing the data misfit. However, to date, only relative, qualitative uncertainty analysis has been carried out for microtremor inversion. Recent approaches have included plotting all models considered in the misfit-minimization procedure coloured according to misfit (Di Giulio et al. 2006; Roten & Fäh 2007), plotting a subset of the models based on an arbitrary misfit threshold (Wathelet et al. 2008; Foti et al. 2009), plotting a subset of models which achieve a misfit within an arbitrary level (e.g. 10%) of the best-fit model (Parolai et al. 2007; Picozzi et al. 2009), and plotting the lowest misfit models from multiple inversions of the same data together with their average (Kind et al. 2005). In contrast, quantitative uncertainty estimation requires not only a nonlinear inversion approach that draws models proportional to their probability, but also rigorous estimation of the data error statistics and an appropriate model parameterization. This section applies nonlinear Bayesian inversion with evaluation of data errors and model parameterizations to produce the most-probable model of the subsurface V_S profile together with quantitative uncertainty estimates from microtremor array dispersion data.

A Bayesian inversion approach formulates the inverse problem in terms of the posterior probability density (PPD) of the model parameters (Tarantola 1987; Dosso 2002; Sambridge & Mosegaard 2002), which are considered random variables constrained by data and prior information. The solution is typically quantified in terms of

properties of the PPD that represent optimal parameter estimates (e.g. the maximum *a posteriori*, MAP, model), parameter uncertainties (variances, marginal distributions, and credibility intervals), and parameter inter-relationships (correlations and joint marginal distributions). Computing these properties requires optimizing and integrating the PPD, which must be carried out numerically for nonlinear problems. The MAP model is computed here using an adaptive hybrid optimization algorithm. Parameter uncertainties and inter-relationships are computed using Markov-chain Monte Carlo (MCMC) methods which provide an asymptotically unbiased sample from the PPD (Gilks et al. 1996; MacKay 2003). In particular, an efficient implementation of Metropolis-Hastings sampling is applied which draws parameter perturbations from a proposal distribution based on a linearized approximation to the PPD (Dosso & Wilmut 2008). This proposal distribution incorporates rotation to a principal-component parameter space to efficiently sample correlated parameters and employs Cauchy-distributed perturbations scaled according to the rotated parameter variances to obtain a well-mixed Markov chain.

Bayesian inversion essentially maps data uncertainty distributions into parameter uncertainty distributions (modified by the prior); hence, a meaningful representation of the data uncertainties is required. In particular, the standard assumptions of uncorrelated Gaussian-distributed errors must be examined. Ignoring significant data error correlations (covariance) can lead to under-estimation of uncertainties and sub-optimal parameter estimates. The approach applied here is based on nonparametric estimation of the data error covariance matrix from residual analysis, and on rigorous *a posteriori* statistical tests to examine this estimate and the underlying assumption of Gaussianity (Dosso et al. 2006; Dettmer et al. 2007).

The type of model parameterization to use in shear-wave velocity modelling is often unknown *a priori*. Adopting too few parameters (e.g. layers) can lead to under-fitting the data, biasing parameter estimates and under-estimating parameter uncertainties. In contrast, adopting too many parameters can over-fit the data leading to spurious model structure and under-determined parameters with excessive variance. In some cases, prior geologic information can provide an indication of the V_S structure at a site; however, even in such cases, the dispersion data may not be able to resolve the indicated level of structure, resulting in an over-parameterized (under-determined)

problem. The goal is to determine the simplest parameterization consistent with the resolving power of the data. A common strategy to determine the parameterization is to progressively increase the number of layers (parameters) until the data misfit stops decreasing significantly (e.g. Renalier et al. 2009). However, no rigorous criterion is applied to determine what constitutes a significant misfit decrease, and this approach is prone to over-parameterizing the model. The strategy applied here also examines a variety of possible V_S parameterizations, but differs in that an objective criterion is applied. In particular, the Bayesian information criterion (BIC), which applies a penalty for the number of parameters, is used to determine the most appropriate parameterization (Schwartz 1978; Kass & Raftery 1995; Dettmer et al. 2009). Parameterizations considered vary in the number of layers, and include layers with uniform, linear and power-law gradients. An alternative approach is trans-dimensional inversion, where the number of parameters is treated as an explicit unknown and is sampled in the inversion (Malinverno 2002; Sambridge et al. 2006; Bodin & Sambridge 2009). This has the advantage of including the effect of the uncertainty in parameterization in the parameter uncertainty estimates. Trans-dimensional inversion of the microtremor dispersion data for the two sites investigated here is presented in Dettmer et al. (2011).

Numerical computation of dispersion curves is carried out using the Haskell-Thomson approach (Thomson 1950; Haskell 1953) in which the subsoil is modelled as a stack of homogeneous layers characterized by four parameters: V_S, compressional-wave velocity (V_P), density (ρ), and layer thickness (h), overlying a homogeneous half-space. All four parameters are considered as unknowns in the Bayesian inversions carried out here. Other inversions tend to either neglect ρ (e.g. Foti et al. 2009), or neglect V_P and ρ (Xia et al. 2009), since Rayleigh wave dispersion is less sensitive to these parameters. For example, Xia et al. (1999) demonstrated an average overall error of 8% in V_S when V_P and ρ were fixed at values 25% in error during nonlinear inversion of simulated data. However, by including V_P and ρ in the Bayesian inversions performed here, uncertainties in these parameters are properly accounted for in estimating the V_S uncertainty.

A Bayesian inversion approach was previously applied by Schevenels et al. (2008) to active-source dispersion data. Metropolis-Hastings sampling was used to collect an ensemble of shear-modulus profiles over the upper 6 m of soil, and the

resulting predictions of induced ground vibration spectra were examined. The soil model was represented as a stochastic process characterized by a marginal probability distribution and covariance function (constrained by prior information), and equal likelihood was assigned to all models fitting the data within a pre-selected threshold. Nonlinear inversion of active-source dispersion data was also considered by Calderón-Macías & Luke (2007) who plotted marginal distributions of models sampled in the process of simulated annealing optimization. However, these distributions are expected to be biased since simulated annealing does not sample from the PPD and tends to over-emphasize regions of low misfit. Further, it is not possible to evaluate the degree of bias without carrying out unbiased sampling for comparison. Uniform Monte Carlo (not MCMC) sampling was applied by Socco & Boiero (2008) and Foti et al. (2009) to obtain a large collection of V_S models for inversion of active-source and microtremor dispersion data, employing scaling properties to minimise misfit for efficiency, and plot subsets of the most likely models at a pre-selected confidence level.

A Bayesian inversion approach is applied to microtremor array dispersion data collected at two sites in southwestern British Columbia. For each site, the most appropriate model parameterization is determined and the MAP model (with uncertainties) is taken as the recovered V_S profile in Section 2.7. Previous V_S measurements collected using invasive commercial techniques are used to assess reliability of the Bayesian microtremor inversion results in Section 2.8.

2.6.1 Formulation and algorithms

A Bayesian formulation represents the solution to an inverse problem in terms of the posterior probability density over the parameter space. Let **d** and **m** represent vectors of random variables with N and M elements, respectively, then Bayes' rule states

$$P(\mathbf{m} \mid \mathbf{d})P(\mathbf{d}) = P(\mathbf{d} \mid \mathbf{m})P(\mathbf{m}). \tag{3}$$

When **d** is taken to be the measured data (fixed) and **m** the set of earth model parameters of interest, $P(\mathbf{d})$ is constant, $P(\mathbf{m})$ represents prior information, and the conditional probability $P(\mathbf{d}|\mathbf{m})$ is interpreted as a function of **m** defining the likelihood function, $L(\mathbf{m}) \propto \exp[-E(\mathbf{m})]$, where E is the data misfit function (considered below). Combining data and prior as a generalized misfit

$$\phi(\mathbf{m}) \equiv E(\mathbf{m}) - \log_e P(\mathbf{m}), \tag{4}$$

the PPD can be written

$$P(\mathbf{m} \mid \mathbf{d}) = \frac{\exp[-\phi(\mathbf{m})]}{\int \exp[-\phi(\mathbf{m}')]d\mathbf{m}'}, \tag{5}$$

where the domain of integration spans the M-dimensional parameter space.

In a Bayesian formulation, the multi-dimensional PPD represents the most general solution to an inverse problem. The distribution is typically interpreted by computing properties defining parameter estimates, uncertainties, and inter-relationships, such as the MAP model ($\hat{\mathbf{m}}$), mean model ($\overline{\mathbf{m}}$), model covariance matrix, and one- and two-dimensional marginal probability distributions, defined, respectively, as

$$\hat{\mathbf{m}} = \mathrm{Arg}_{\max}\{P(\mathbf{m} \mid \mathbf{d})\} = \mathrm{Arg}_{\min}\{\phi(\mathbf{m})\}, \tag{6}$$

$$\overline{\mathbf{m}} = \int \mathbf{m}' P(\mathbf{m}' \mid \mathbf{d}) d\mathbf{m}', \tag{7}$$

$$\mathbf{C}_{\mathbf{m}} = \int (\mathbf{m}' - \overline{\mathbf{m}})(\mathbf{m}' - \overline{\mathbf{m}})^T P(\mathbf{m}' \mid \mathbf{d}) d\mathbf{m}', \tag{8}$$

$$P(\mathbf{m}_i \mid \mathbf{d}) = \int \delta(\mathbf{m}_i' - \mathbf{m}_i) P(\mathbf{m}' \mid \mathbf{d}) d\mathbf{m}', \tag{9}$$

$$P(\mathbf{m}_i, \mathbf{m}_j \mid \mathbf{d}) = \int \delta(\mathbf{m}_i' - \mathbf{m}_i)\delta(\mathbf{m}_j' - \mathbf{m}_j) P(\mathbf{m}' \mid \mathbf{d}) d\mathbf{m}', \tag{10}$$

where δ is the Dirac delta function. Parameter uncertainties are also quantified in terms of credibility intervals, such as the β % highest-probability density (HPD) interval, representing the interval of minimum width containing β % of the marginal area. Inter-parameter correlations are quantified by normalizing the covariance matrix to produce the correlation matrix

$$\mathbf{R}_{ij} = \mathbf{C}_{m_{ij}} / \sqrt{\mathbf{C}_{m_{ii}} \mathbf{C}_{m_{jj}}}. \tag{11}$$

Elements R_{ij} are within [-1, 1], with a value of 1 indicating perfect correlation between parameters m_i and m_j, -1 indicating perfect anti-correlation, and zero values indicating uncorrelated parameters.

Prior information considered here consists of uniform distributions for each parameter on bounded intervals $m_i^- \le m_i \le m_i^+$, i.e.

$$P(\mathbf{m}) = \prod_{i=1}^{M} \left(m_i^+ - m_i^-\right)^{-1} \qquad \text{if } m_i^- \le m_i \le m_i^+,\ i=1,M, \tag{12}$$

$$P(\mathbf{m}) = 0 \qquad \text{otherwise.}$$

Lower and upper bounds are chosen here to limit parameters to physically reasonable values, but are wide enough to allow the data (not the prior) to primarily determine the shear-wave velocity profile parameters, thereby quantifying the information content of the data to resolve these parameters. In addition, inter-parameter bounds are applied based on the physical limit for Poisson's ratio, leading to

$$V_S \leq V_P / \sqrt{2}. \tag{13}$$

2.6.2 Nonlinear inversion

Analytic solutions to eqs. (4)–(8) exist for linear inverse problems with Gaussian-distributed errors and infinite uniform or Gaussian prior distributions. For weakly nonlinear problems, local linearization can be applied to provide approximate solutions. However, to properly treat nonlinearity and/or to consider other error or prior distributions, numerical solutions are required. MAP estimates, eq. (6), are determined here by minimizing $\phi(\mathbf{m})$ numerically using adaptive simplex simulated annealing (ASSA, Dosso et al. 2001), a hybrid optimization algorithm that adaptively combines the local downhill simplex method (Nelder & Mead 1965) within a very fast simulated re-annealing global search (Ingber 1989).

The integrals of eqs. (5)–(8), which are of the general form

$$I = \int f(\mathbf{m}')P(\mathbf{m}' \mid \mathbf{d})d\mathbf{m}', \tag{14}$$

are evaluated here using the MCMC method of Metropolis-Hastings sampling. In this method, the model parameters are perturbed repeatedly, with perturbations accepted if a random number ξ drawn from a uniform distribution on [0, 1] satisfies the Metropolis criterion

$$\xi \leq \exp[-\Delta\phi], \tag{15}$$

where $\Delta\phi$ represents the change in ϕ due to the perturbation (this acceptance rule assumes the common case of a symmetric perturbation proposal distribution, which is applied here as described below). Markov-chain theory verifies that this procedure samples asymptotically from the PPD (Gilks et al. 1996; MacKay 2003), and hence integral (12) is evaluated as

$$I = \frac{1}{Q}\sum_{i=1}^{Q} f(\mathbf{m}_i), \tag{16}$$

where the set of models $\{\mathbf{m}_i, i = 1, Q\}$ is collected via Metropolis-Hastings sampling. Practical issues influencing convergence to an unbiased estimate include deleting early samples of the Markov chain, commonly referred to as "burn-in" (a burn-in length of at least 15,000 samples is applied here) and chain-thinning to decrease serial correlation between samples (a thinning factor of 15 is applied). It is worth noting here that models collected in the process of misfit minimization via optimization are generally not sampled proportional to the PPD, and do not provide an unbiased representation of the PPD.

The parameter perturbations in Metropolis-Hasting sampling can be drawn from any proposal distribution: the choice of proposal does not affect the integral estimates at convergence but can strongly affect sampling efficiency. The goal is to achieve a well-mixed Markov-chain that efficiently samples the parameter space, avoiding both small, ineffectual perturbations and high rejection rates. The optimal proposal distribution is given by the PPD itself. Although this is obviously unavailable during sampling, the local linearized approximation to the PPD can be exploited (Dosso & Wilmut 2008). According to standard linearized inverse theory, the PPD is given by an M-dimensional Gaussian distribution about the MAP model with covariance

$$\mathbf{C}_{\mathbf{m}} = \left[\mathbf{J}^T \mathbf{C}_{\mathbf{d}}^{-1} \mathbf{J} + \mathbf{C}_{\hat{\mathbf{m}}}^{-1}\right]^{-1}, \tag{17}$$

where $\mathbf{J}$ is the Jacobian matrix of partial derivatives evaluated at $\hat{\mathbf{m}}$, $\mathbf{J}_{ij} = \partial d_i(\hat{\mathbf{m}}) / \partial m_j$, $\mathbf{C}_{\mathbf{d}}$ is the data covariance matrix, and $\mathbf{C}_{\hat{\mathbf{m}}}$ is the covariance of an assumed Gaussian prior distribution about $\hat{\mathbf{m}}$ (to represent bounded uniform priors, $m_i^- \leq m_i \leq m_i^+$, $\mathbf{C}_{\hat{\mathbf{m}}}$ is taken to be a diagonal matrix with variances equal to those of the uniform distributions, i.e. $\mathbf{C}_{\hat{\mathbf{m}}}$ = diag[$(m_i^+ - m_i^-)^2/12$]). To exploit the linearized approximation in Metropolis-Hastings sampling, perturbations are applied in a principal-component parameter space where the axes align with the dominant correlation directions. The orthogonal transformation (rotation) between physical parameters $\mathbf{m}$ and rotated parameters $\tilde{\mathbf{m}}$ is given by

$$\tilde{\mathbf{m}} = \mathbf{U}^T \mathbf{m}, \qquad \mathbf{m} = \mathbf{U}\tilde{\mathbf{m}}, \tag{18}$$

where $\mathbf{U}$ is the column-eigenvector matrix of the model covariance,

$$\mathbf{C}_{\mathbf{m}} = \mathbf{U}\mathbf{W}\mathbf{U}^T, \tag{19}$$

and $\mathbf{W} = \mathrm{diag}[w_i]$ is the eigenvalue matrix, with w_i representing the parameter variances projected along eigenvector u_i. Rotated parameters are perturbed individually, and the perturbed models rotated back to physical space for misfit evaluation. The covariance decomposition also provides appropriate length scales for perturbations in rotated space. For a linear problem, the optimal proposal distribution for $\tilde{m}_i$ is Gaussian-distributed with variance w_i. However, for nonlinear problems the heavy-tailed Cauchy distribution, with scale parameter set to $(w_i)^{1/2}$ (i.e., the principle-component standard deviation) is more appropriate, providing a greater probability of transiting between potentially disjoint regions of high probability.

The Metropolis-Hastings sampling algorithm developed here is initiated with the MAP model (estimated using ASSA) and linearized model covariance, eq. (17). In the initial burn-in stage, the linearized estimate for $\mathbf{C_m}$ is adaptively replaced with the nonlinear estimate, based on eq. (8) and the burn-in sampling, to better represent the overall covariance of the parameter space and the actual prior distribution (samples collected during burn-in are not used in integral estimates). After burn-in, the sampling convergence is monitored by comparing integral estimates from two independent chains run in parallel: when the maximum difference is suitably small, the procedure is considered to have converged and the final sample is taken as the union of the two samples (Dosso 2002).

For the inversion results presented here, the MCMC samples consisted of about 200,000 to 300,000 models (after chain thinning), which is about a factor of five larger than the number of models evaluated in ASSA optimization runs. As with most other numerical inversions, the number of samples required for integration and optimization and the total computing time increase with the number of model parameters, and numerical inversions are generally restricted to efficient parameterizations, as considered here.

2.6.3 Likelihood and error statistics

Specifying the data uncertainty (error) distribution, which defines the likelihood function, is an important practical aspect of Bayesian inversion. Data uncertainties include both measurement errors (e.g. due to instrument uncertainties and non-Rayleigh wave components) and theory errors (due to the simplified model parameterization and inexact

forward problem), which generally cannot be separated. Since data errors are often not well known *a priori*, physically reasonable assumptions are required about the form of the uncertainty distribution. The numerical inversion described above is general and applicable for any uncertainty distribution. However, lack of specific knowledge of the uncertainty distribution often suggests that a simple distribution, such as a Gaussian, be assumed initially:

$$L(\mathbf{m}) = \frac{1}{(2\pi)^{N/2} \,|\, \mathbf{C_d} \,|^{1/2}} \exp\left[-\left(\mathbf{d} - \mathbf{d}(\mathbf{m})\right)^T \mathbf{C_d}^{-1} \left(\mathbf{d} - \mathbf{d}(\mathbf{m})\right)/2\right] \tag{20}$$

(note that although the data uncertainties are Gaussian-distributed in this equation, the likelihood is a not a Gaussian function of $\mathbf{m}$ if $\mathbf{d}(\mathbf{m})$ is nonlinear). The assumption of Gaussianity should be examined *a posteriori*, and if not justified other possibilities can be considered.

In eq. (20), $\mathbf{C_d}$ represents the data error covariance matrix. Data errors are often assumed to be identical independently-distributed (IID) random variables (i.e. $\mathbf{C_d} = \sigma^2\mathbf{I}$, where σ is the standard deviation and $\mathbf{I}$ the identity matrix). However, significant error correlations can occur (often due to theory errors), and neglecting these correlations can degrade parameter estimates and under-estimate parameter uncertainties. Further, covariance estimation methods based on multiple data-set measurements (e.g., Gouveia & Scales 1998) can fail in such cases, since all data sets may be affected by theory error in a systematic manner.

As an alternative approach, data error statistics can be estimated from data residuals, $\mathbf{r} = \mathbf{d} - \mathbf{d}(\hat{\mathbf{m}})$, where $\hat{\mathbf{m}}$ represents the MAP estimate from a preliminary inversion result assuming IID errors (e.g., Montgomery & Peck 1972; Aster et al. 2005). Essentially, the residuals are considered a realization of the error process from which statistical quantities can be computed. Assuming this represents an ergodic random process, a Toeplitz covariance matrix can be estimated from the residual autocovariance as (Dosso et al. 2008)

$$C_{d_{ij}} = \frac{1}{N-M} \sum_{k=1}^{N-|i-j|} \left(r_k - \bar{r}\right)\left(r_{k+|i-j|} - \bar{r}\right), \qquad i = 1, N; \qquad j \geq i,$$

$$C_{d_{ij}} = C_{d_{ji}}, \qquad i = 1, N; \qquad j < i, \tag{21}$$

where $\bar{r}$ represents the residual mean. This covariance matrix is then applied in subsequent inversions (the procedure can be applied iteratively, and generally converges to a stable result in one or two iterations).

To validate uncertainty assumptions, statistical tests can be applied *a posteriori* to the standardized residuals $\mathbf{C_d}^{-1/2}\mathbf{r}$. For example, the assumption of Gaussianity can be considered qualitatively by comparing a histogram of the residuals to the standard Gaussian distribution. Quantitative statistical tests, such as the Kolmogorov-Smirnov (KS) test (Massey 1951; Freund 1967), can also be applied to provide a *p*-value indicating the level of evidence against the null hypothesis of Gaussian-distributed errors ($p \geq 0.05$ is typically taken to indicate no significant evidence). The assumption of randomness can be considered qualitatively by plotting the residual autocorrelation: uncorrelated errors lead to a narrow peak at zero lag while serial correlations widen the peak. Statistical tests, such as the runs test (Freund 1967), can be applied to quantify the level of evidence against the null hypothesis of uncorrelated errors.

The measured data considered here consist of fundamental-mode Rayleigh wave dispersion curves derived from microtremors recorded by an array of seismographs, with varying aperture to define the dispersion over different frequency bands. This leads to subsets of data (corresponding to different array apertures) with independent and distinct error statistics. Defining K data subsets, $\mathbf{d} = \{\mathbf{d}_k, k = 1, K\}$, and estimating an independent covariance matrix for each subset as above, the likelihood and error functions become

$$L(\mathbf{m}) \propto \prod_{k=1}^{K} \exp\left[-\left(\mathbf{d}_k - \mathbf{d}_k(\mathbf{m})\right)^T \mathbf{C}_{\mathbf{d}_k}^{-1}\left(\mathbf{d}_k - \mathbf{d}_k(\mathbf{m})\right)/2\right], \tag{22}$$

$$E(\mathbf{m}) = \sum_{k=1}^{K} \left(\mathbf{d}_k - \mathbf{d}_k(\mathbf{m})\right)^T \mathbf{C}_{\mathbf{d}_k}^{-1}\left(\mathbf{d}_k - \mathbf{d}_k(\mathbf{m})\right)/2\,. \tag{23}$$

Alternatively, the covariance matrices for the data subsets are combined into a single block-diagonal matrix and the data considered as a single set.

2.6.4 Model parameterization

Determining an appropriate model parameterization is another important aspect of Bayesian inversion. It is important to choose an appropriate parameterization based on an objective criterion to select the simplest parameterization consistent with the resolving power of the data. Several approaches exist to evaluate model parameterizations by

quantifying their likelihood using point estimates (e.g. the MAP estimate). For example, assuming Gaussian-distributed errors, χ^2 probabilities can be used to evaluate the likelihood of a model, and the F test applied to calculate the allowable change in the χ^2 misfit for given significance levels (Montgomery & Peck 1992). However, this method is biased toward unjustifiably complex models (Gelfand & Day 1994), in conflict with the generally accepted concept of Occam's razor that empirically prefers simple models (Parker 1994; MacKay 2003). To avoid this bias, asymptotic methods such as the Akaike information criterion (AIC) have been introduced which penalize complexity in terms number of parameters (the AIC has been considered for microtremor inversion by Savvaidis et al. 2009). However, the AIC is still biased toward complex models for large data sets (Kass & Raftery 1995). The Bayesian information criterion (BIC) is related to Bayes factors and eliminates this bias by accounting for the number of data (Schwartz 1978; Kass & Raftery 1995):

$$-2\log_e P(\mathbf{d} \mid M) \approx \mathrm{BIC} \equiv -2\log_e L(\hat{\mathbf{m}}) + M \log_e N \,. \tag{24}$$

In the formulation used here, this becomes, within an additive constant,

$$\mathrm{BIC} = 2E(\hat{\mathbf{m}}) + M \log_e N \,. \tag{25}$$

Since the BIC is based on the data misfit, the parameterization with the smallest BIC is selected (minimizing the BIC represents an objective form of regularization). However, the BIC provides only a relative ranking of the parameterizations compared; it cannot be directly associated with probability nor yield the significance of the selection.

Model selection based on the BIC is applied here to a variety of different parameterizations of the V_S profile. Parameterizations considered differ in the number of layers and also in the representation of V_S, V_P, and ρ over the layers. Shear-wave velocity models can be composed of combinations of three types of layers in which V_S is either uniform, varies linearly with depth, or varies according to a power-law relationship with depth (the same form of V_S gradient is applied to V_P and ρ in all cases). A uniform velocity layer over a depth interval $[z_0, z_0+h]$ is described by two parameters: V_S and layer thickness, h. A linear velocity dependence can be written

$$V_s(z) = V_s(z_0) + \frac{V_s(h) - V_s(z_0)}{h}(z - z_0) \tag{26}$$

which is described by three parameters $V_S(z_0)$, $V_S(h)$, and h. To represent a linear gradient layer as a series of uniform velocity sub-layers (as required by the forward problem implementation), the layer is partitioned into H sub-layers with boundaries at $\{z_0, z_1, \ldots, z_H = z_0 + h\}$, with the velocity V_{S_i} on the ith sub-layer given by

$$V_{S_i} = \frac{1}{z_{i+1} - z_i} \int_{z_i}^{z_{i+1}} V_S(z) dz = V_S(z_0) + \frac{V(h) - V(z_0)}{2h} (z_{i+1} + z_i - 2z_0). \quad (27)$$

The most general expression for a power-law velocity gradient is

$$V_S(z) = V_S(z_0) + a(z - z_0)^b. \quad (28)$$

However, for the frequency range and depth partitions considered here, a simpler representation with one fewer parameter gives essentially identical inversion results:

$$V_S(z) = a(z - z_0)^b. \quad (29)$$

Assuming a layer thickness $h > 1$ m,

$$a = V_S(z_0 + 1), \text{ and } b = \frac{\log_e V_S(h) - \log_e V_S(z_0 + 1)}{\log_e (h - z_0)}, \quad (30)$$

and the model parameters are taken to be $V_S(z_0 + 1)$, $V_S(h)$, and h. The discretized velocity V_{S_i} on the ith sub-layer of a partitioned power-law layer is given by

$$V_{S_i} = \frac{1}{z_{i+1} - z_i} \int_{z_i}^{z_i+1} V_S(z) dz = \frac{a\left[(z_{i+1} - z_0)^{b+1} - (z_i - z_0)^{b+1}\right]}{(b+1)(z_{i+1} - z_i)}. \quad (31)$$

For both linear and power-law gradients, the exponentially decaying penetration of surface waves into the earth suggests that a logarithmically increasing depth partition of the layer is appropriate. If d is the desired thickness of the first of H sub-layers of the partition, then the thickness of the ith sub-layer is given by dr^{i-1}, where r is the solution to

$$h = \sum_{i=1}^{H} dr^{(i-1)} = \frac{d(1 - r^H)}{1 - r}. \quad (32)$$

Since h increases monotonically with r, this equation is easily solved using line search methods (e.g. bisection).

Finally, the relationship between parameterization selection and data error estimation must be noted, since error statistics are estimated for a particular model (Section 2.6.3) while the choice of parameterization requires error estimates through the likelihood function in eq. (23). The iterative procedure applied here is to carry out a first

stage of model selection in which the data errors are considered IID Gaussian (and hence MAP estimates are independent of the variance). The required error statistics (e.g. covariance matrices) are estimated for the parameterization that minimises the BIC in the first stage, and a second stage of selection is carried out with these statistics applied to all parameterizations. In practice, the error statistics computed for all good models in the first round are found to be similar (where good represents parameterizations with BIC values close to that of the optimal choice), so the procedure is robust, i.e. not sensitive to this choice.

2.7 Parameter uncertainties and inter-relationships

2.7.1 Fraser River delta site

The dispersion curve for the Fraser River delta site (Figure 6c) varies from ~ 400 m/s at 1.2 Hz to 130 m/s at 6.5 Hz with 52 logarithmically-spaced data. The curve is segmented into three frequency bands, delineated by dotted lines. The discontinuity near 5.4 Hz is due to computing the dispersion curve from different array apertures with non-overlapping reliable frequency ranges. The gap in data from 3.4-3.8 Hz is due to spurious phase velocity estimates at these frequencies which correspond to a peak in the observed horizontal-vertical spectral ratio (Figure 4a).

A variety of model parameterizations incorporating the three possible parameter gradients were examined for inverting the Fraser River delta dispersion data. To obtain inversion and model selection results, MAP model estimation was carried out using nonlinear (ASSA) optimization. Prior information was taken to consist of uniform distributions over wide intervals for all parameters: 2-200 m for h, 20-2000 m/s for V_S, 100-3000 m/s for V_P, and 1.2-2.7 g/cm^3 for ρ. The resulting minimum misfit values were used to calculate the BIC and are presented for nine parameterizations in Figure 7. All parameterizations also include a uniform underlying half-space. The preferred parameterization with the lowest BIC value is found for a single power-law gradient layer over a uniform half-space (denoted P in Figure 7). When a uniform layer is added below the power-law layer (PU), the minimum misfit does not decrease significantly and the BIC increases due to the larger number of parameters. Misfit values lower than that of the power-law parameterization can be obtained, but require more complex structure (either

three or four uniform layers, U3 or U4, or a linear gradient layer over two or three uniform layers, LU2 or LU3), such that lower BIC values are not found.

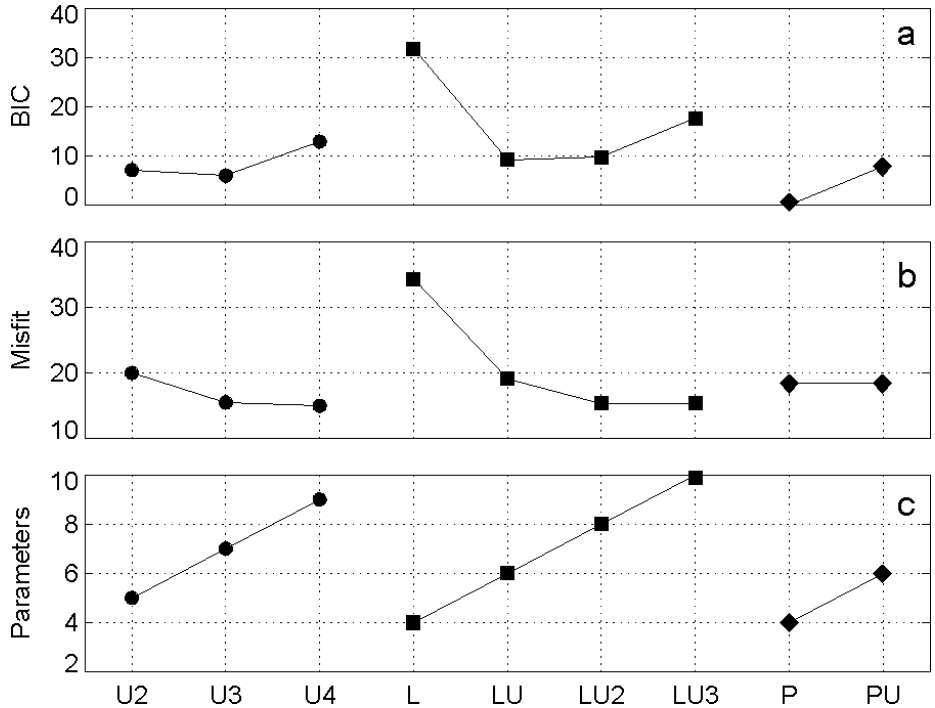

Figure 7. Parameterization study for the Fraser River delta site. Models are separated into three categories based on the initial layer V_S dependence on depth: uniform (U, circles), linear gradient (L, squares), or power-law gradient (P, diamonds). Additional underlying layers have uniform properties denoted by numerals. For display purposes the BIC is shifted so that the minimum value corresponds to zero.

The Bayesian microtremor inversion results in Figure 7 were obtained using the data error covariance matrix shown in Figure 8. This block-diagonal covariance matrix combines three sub-matrices computed from the residual autocovariance segmented over the three frequency bands indicated in Figure 6c, as described in Section 2.5. Lai et al. (2005) also consider the dispersion curve as segmented, derived from averaging of up to 15 independent curves, with errors generally decreasing with frequency. To investigate the necessity of this covariance estimate and the validity of the Gaussian-error distribution, Figure 9 compares standardized residuals from inversions for the power-law model under the assumption of uncorrelated errors (diagonal covariance matrix) and of correlated errors represented by the full block-diagonal covariance matrix of Figure 8. Standardized residuals from the assumption of uncorrelated Gaussian-distributed errors

are plotted in histogram form and compared with the standard Gaussian in Figure 9a, demonstrating reasonably good agreement. The KS test yields a p value of 0.55, indicating no evidence against the null hypothesis of Gaussian errors. The correlation of the residuals is considered in terms of their autocorrelation function in Figure 9b: the central peak exhibits a half-width of 3-4 lag points before decreasing to the noise level indicating the residuals are correlated over this length. The runs test provides extremely strong evidence against the null hypothesis of randomness with $p = 1.8\text{x}10^{-6}$. Alternatively, the histogram of standardized residuals obtained via inversion with the full covariance matrix is shown in Figure 9c and agrees well with the standard Gaussian; the KS test p value is 0.30. The residual autocorrelation function, shown in Figure 9d, has a sharp central peak 1 lag point wide and the runs test yields $p = 0.13$, indicating that the estimated covariance matrix accounts satisfactorily for the data error correlations. The agreement between the dispersion data computed for the MAP model and the measured microtremor dispersion curve is shown in Figure 6c.

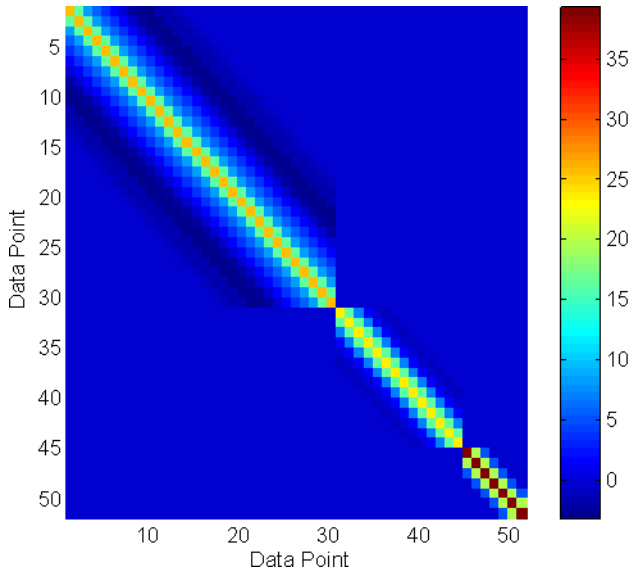

Figure 8. Full block-diagonal data error covariance matrix [$(m/s)^2$] estimated for the microtremor dispersion data at the Fraser River delta site.

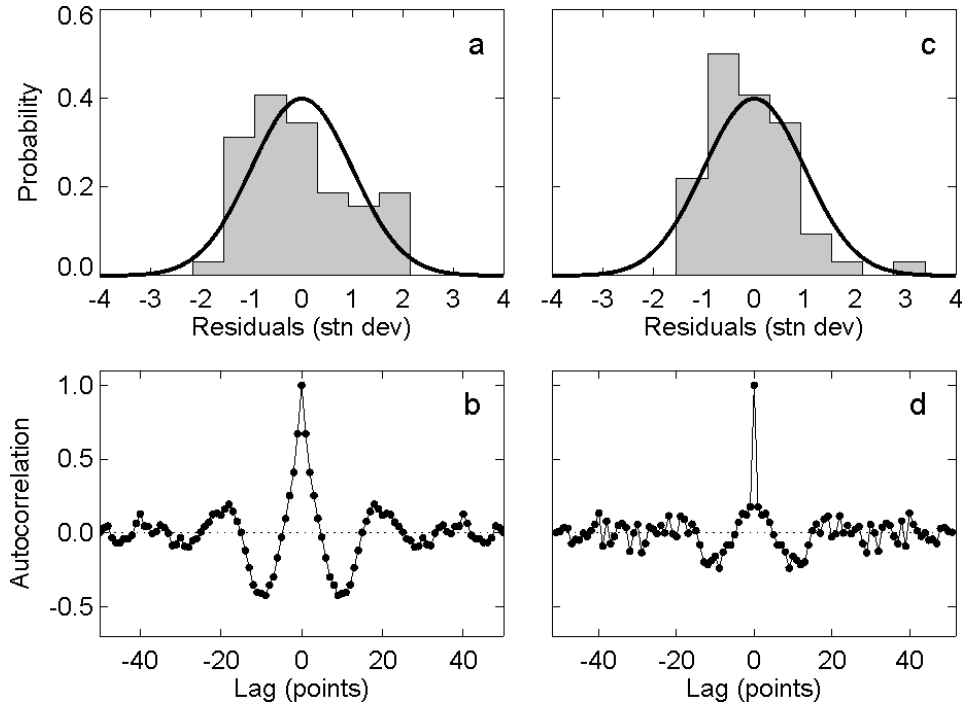

Figure 9. (a) Histogram and (b) autocorrelation of standardized residuals from inversion of Fraser River delta data assuming uncorrelated Gaussian errors; (c) and (d) show same for covariance weighted inversion. Solid curves in (a) and (c) show standard Gaussian distributions.

Bayesian microtremor inversion results for the Fraser River delta site are presented in Figure 10 as marginal probability (uncertainty) distributions of the geophysical model parameters h, V_S, V_P, and ρ. Parameters of the power-law layer of thickness h are defined at 1 m depth (identified by subscript 1) and at the base of the layer (subscript 2); in the underlying uniform half-space parameters are identified by subscript 3. To illustrate the significance of including the full data error covariance matrix in the inversion, Figure 10 compares inversion results for both the full covariance matrix (upper distributions) and for a diagonal covariance matrix (i.e. variance only estimates, lower distributions). The plot bounds equal the prior bounds for V_P and ρ; for h and V_S, the plot bounds are smaller than the prior. Figure 10 demonstrates that neglecting data error covariance produces significantly smaller uncertainties (narrower marginal distributions) than those computed using the full covariance matrix, particularly for h, V_{S2}, and V_{S3}. It is worth emphasizing here that the goal of Bayesian microtremor inversion is not to compute the smallest parameter uncertainties, but rather the correct uncertainties, i.e. uncertainties that properly quantify the data information content. The inversion results

using the full error covariance matrix indicate a 100-160 m thick power-law V_S gradient layer. The shear-wave velocity is resolved better near the surface (V_{S1}, 70-86 m/s) than at the layer base (V_{S2}, 325-425 m/s). The shear-wave velocity of the half-space (V_{S3}) is relatively poorly resolved between approximately 500-1000 m/s (but is higher than at the base of the upper layer), with a positively skewed probability distribution. Distributions for V_P and ρ are not significantly constrained over their prior bounds by either inversion.

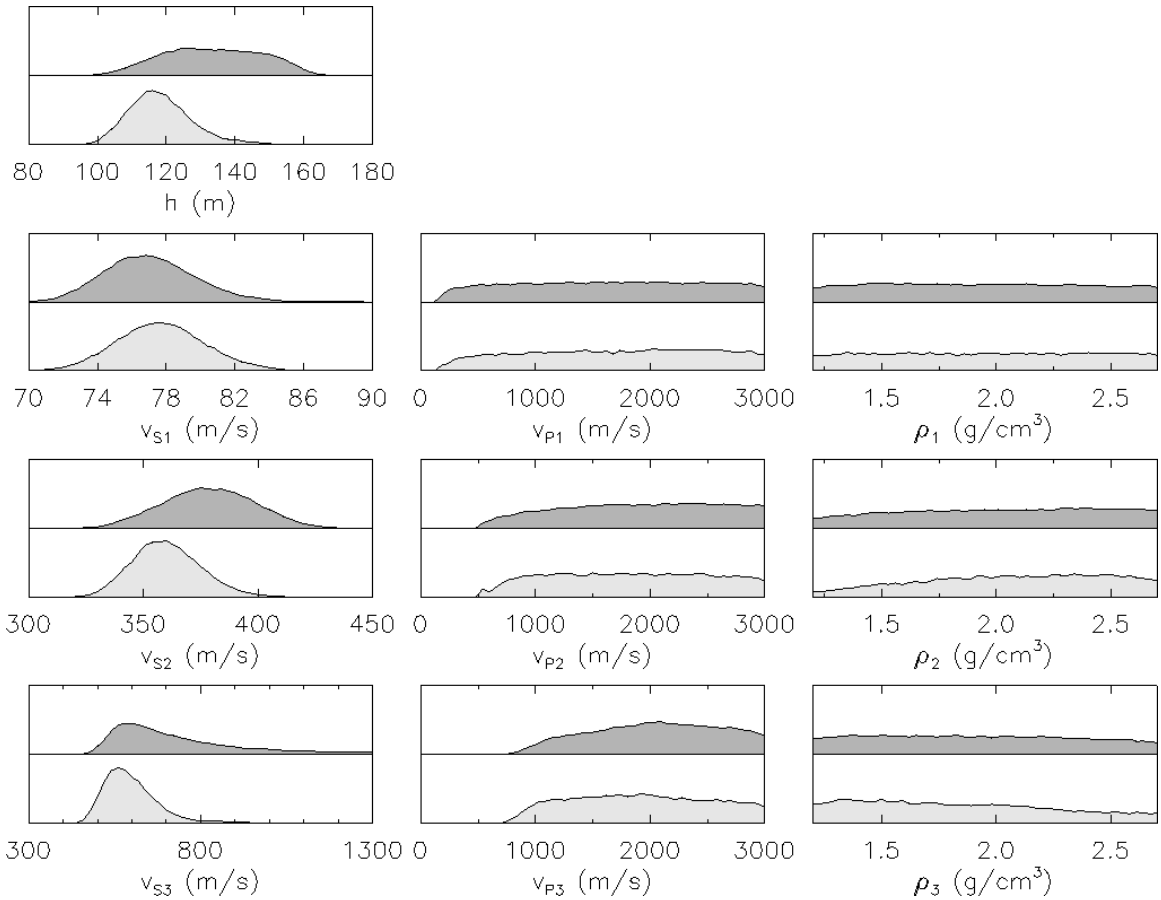

Figure 10. Marginal probability distributions from Bayesian inversion of the Fraser River delta data for the power-law gradient layer parameterization. Upper and lower distributions in each panel represent results obtained using full data covariance matrix and diagonal covariance matrix (variances only), respectively.

One way to quantify the effects of factors such as neglecting data error covariance and fixing ρ and/or V_P in the inversion is to examine credibility interval widths from Bayesian inversion. Figure 11 shows 95% HPD credibility intervals for the parameters defining the shear-wave velocity profile from six inversions that consider various

combinations of including or neglecting error covariance and including or fixing ρ and V_P (fixed at 2.0 g/cm^3 and 1700 m/s, respectively). The results demonstrate that parameter credibility interval widths decrease when data covariance errors are neglected and when ρ and V_P are fixed at reasonable values in the inversion. Hence, to obtain meaningful uncertainty estimates and avoid overly optimistic (potentially misleading) results, both appropriate data error statistics and relevant nuisance parameters should be accounted for in the inversion.

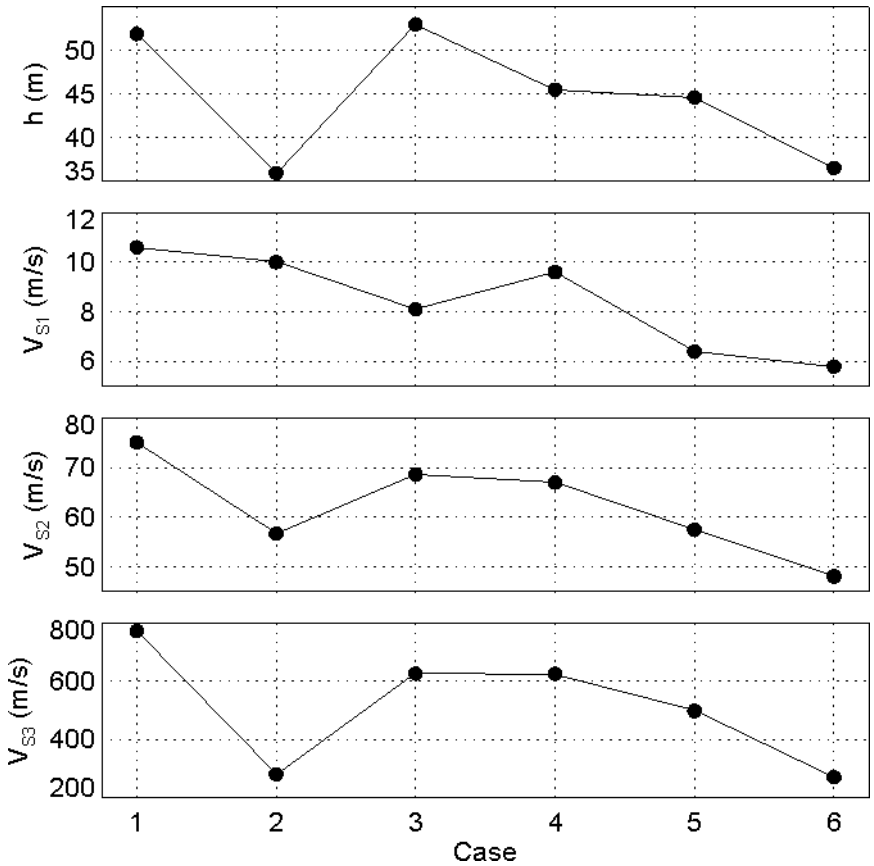

Figure 11. 95% HPD credibility interval widths for shear-wave velocity profile parameters from inversions which include: (1) ρ, V_P, and full error covariance (preferred approach); (2) ρ, V_P but variances only; (3) V_P and full error covariance with ρ fixed at 2.0 g/cm^3; (4) ρ and full error covariance with V_P fixed at 1700 m/s; (5) full error covariance with ρ and V_P fixed; and (6) variances only with ρ and V_P fixed.

Marginal probability distributions for individual parameters are shown in Figure 10 with the effects of all other parameters integrated out. Parameter inter-relationships are examined here in terms of the correlation matrix (Figure 12) and joint marginal

probability distributions (Figure 13). As shown in the top row of the correlation matrix in Figure 12, strong positive correlations exist between h and both V_{S2} and V_{S3}, whereas a weaker negative correlation exists between h and V_{S1}. These inter-parameter relationships indicate the data misfit remains largely unchanged if both h and V_{S2} or both h and V_{S3} are increased in an appropriate manner, or if h is increased and V_{S1} is decreased. These relationships are further illustrated by the joint marginal distributions in the top row of plots in Figure 13, which show elongated regions of high probability, not aligned with the parameter axes, with positive or negative slopes corresponding to positive or negative correlations, respectively. Figure 12 and Figure 13 also show that ρ_1 is positively correlated with both V_{S1} and V_{S2} while ρ_2 is negatively correlated with both of these parameters. Finally, it is worth noting that V_{S1} and V_{S2} are not correlated with each other, and that the compressional-wave velocities exhibit only weak correlations with the shear-wave velocity profile parameters. The sharp edge with positive slope in the joint marginal distribution of V_{P3} and V_{S3} in Figure 13 (bottom right plot) is not a correlation effect, but results from the constraint on Poisson's ratio applied as prior information in the Bayesian inversion.

Figure 13 shows that inter-parameter correlations limit the ability to resolve individual parameters, and have the effect of increasing parameter uncertainties. In particular, the observed correlations between density and shear-wave velocity indicate that holding densities fixed in the inversion (as is commonly done) could significantly affect shear-wave velocity estimates and uncertainties. The effects of inter-parameter correlations are inherent in the physics of the problem, and cannot be addressed by data processing or inversion techniques. To overcome correlations, information must be added to the problem, either in the form of additional data or prior information. For instance, if tighter prior bounds for the range of density values are available, shear-wave velocity uncertainties will be reduced.

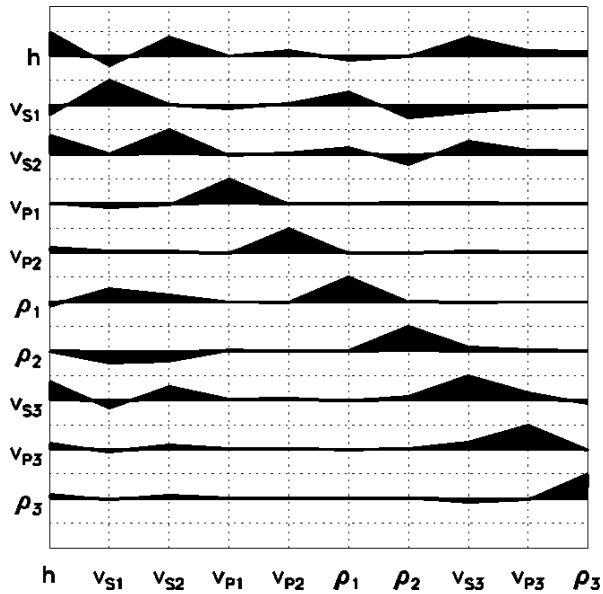

Figure 12. Correlation matrix for the power-law gradient parameterization at the Fraser River delta site.

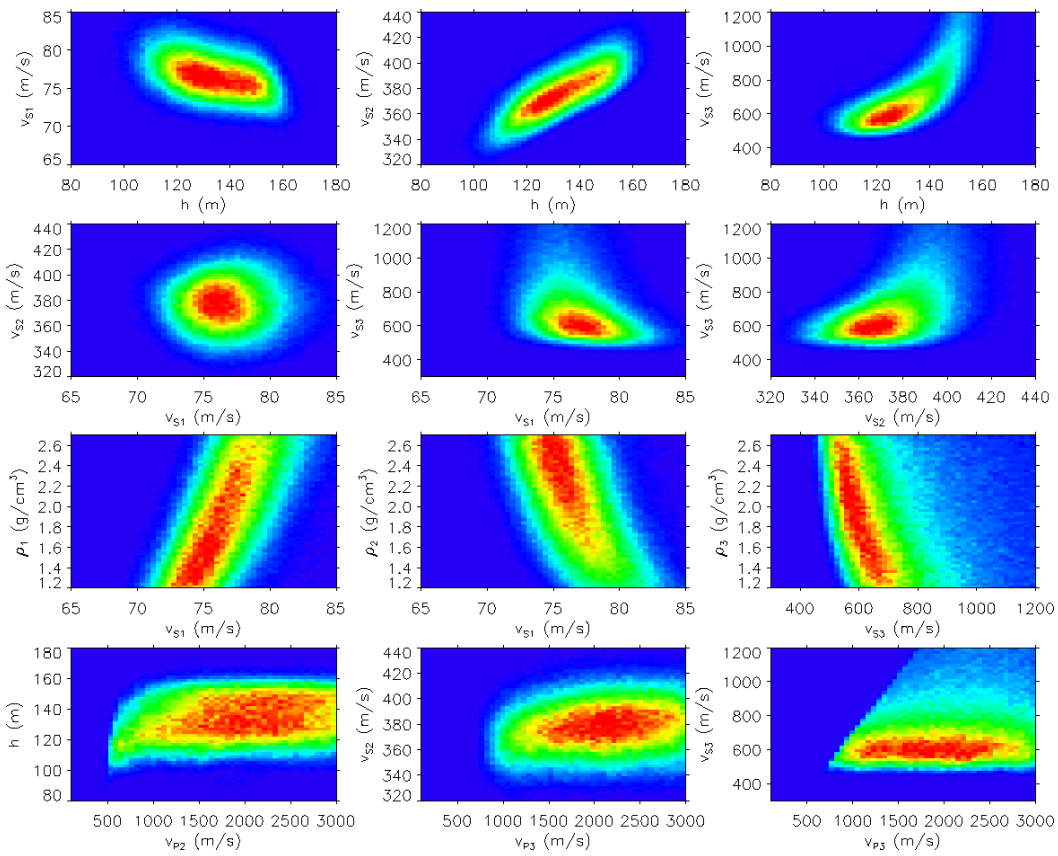

Figure 13. Selected joint marginal probability distributions from inversion of the Fraser River delta data. Each distribution is normalized independently.

To illustrate the Bayesian microtremor inversion result for shear-wave velocity in a more intuitive format, Figure 14 presents a marginal probability V_S profile obtained by converting each model in the PPD sample into a profile, and then integrating the probability of all profiles over a velocity-depth grid. The marginal profile in Figure 14a shows decreasing probability with depth, such that the distribution is scarcely visible on the plot below ~140 m. To more clearly illustrate the relative probability distribution at each depth, the probability is normalized independently at each grid depth in Figure 14b. Figure 14a and b illustrate the loss in resolution with depth over the power-law layer. The transition from the upper layer to the half-space is not clearly defined, occurring between about 110-160 m depth, and the half-space velocity is poorly determined with an uncertainty of several 100 m/s.

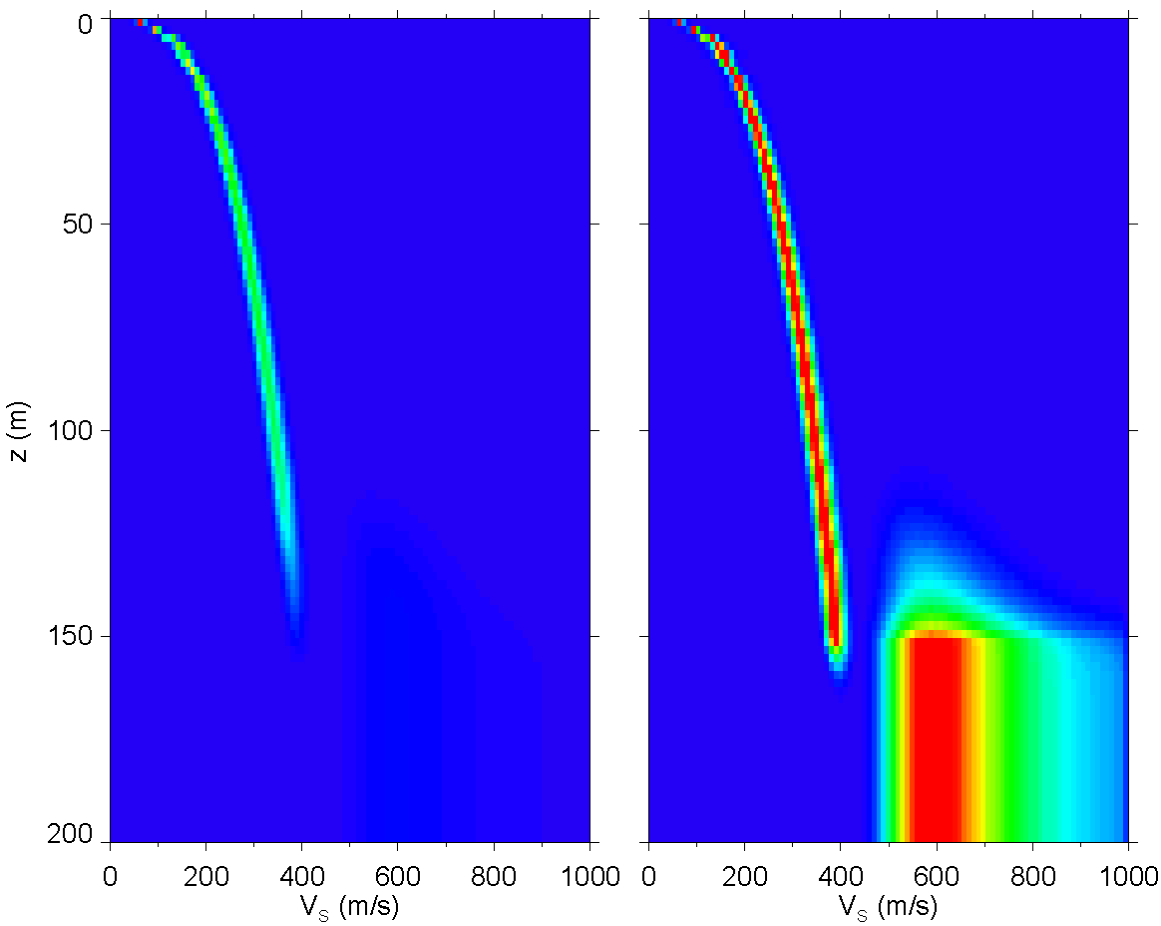

Figure 14. (a) Marginal probability V_S profile from Bayesian inversion for the Fraser River delta data. (b) Marginal profile normalized independently at each depth.

2.7.2 Victoria

The dispersion curve for the Victoria site is shown in Figure 6d and varies from nearly 300 m/s at 2.4 Hz to ~ 90 m/s at 9.3 Hz with 35 logarithmically spaced data.

A variety of possible model parameterizations were examined for the Victoria dispersion data using the same wide prior bounds as for the Fraser River delta site. The preferred parameterization with the lowest BIC value is found for a single linear V_S gradient layer over a uniform half-space (denoted L in Figure 15). Similar misfits are obtained for nearly all of the model parameterizations considered, indicating the data are readily fit with a variety of parameterizations (Figure 14b). Selecting an appropriate model parameterization based on an objective minimum-structure criterion (i.e. the BIC) is particularly effective in this case.

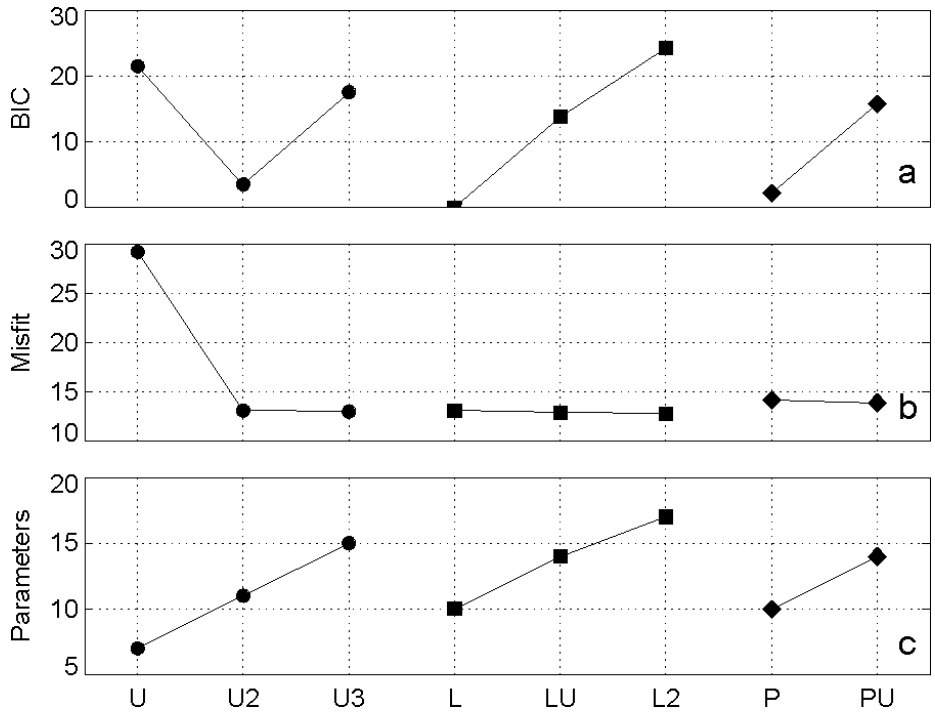

Figure 15. Parameterization study for the Victoria site. Details as in Figure 7.

The data covariance matrix used in the Bayesian microtremor inversions of Figure 14 was computed from residual autocovariance segmented over two frequency bands of the dispersion curve (Figure 6d) based on the reliable frequency ranges of the various array apertures and an apparent change in the error statistics. *A posteriori* KS and runs tests for standardized residuals yielded p values of 0.24 and 0.15, respectively, indicating no significant evidence against the assumption of Gaussian-distributed errors and that the

covariance matrix accounts for error correlations. The agreement between the data computed for the MAP model and the measured microtremor dispersion data is shown in Figure 6d.

Figure 16 presents marginal probability distributions for the parameters of the preferred linear layer model. Parameters of the linear layer of thickness h are defined at 1 m depth (identified by subscript 1) and at the base of the layer (subscript 2); in the underlying uniform half-space parameters are identified by subscript 3. The thickness and shear-wave velocities of the linear layer are well resolved, with V_S increasing from about 78-87 m/s near the surface (V_{S1}) to 110-160 m/s (V_{S2}) at 15-18 m depth (h). The velocity of the half-space (V_{S3}) is poorly resolved but constrained to values > 400 m/s, significantly higher than the base of the upper layer. The compressional-wave velocity and density parameters are largely unresolved, although there is some sensitivity to ρ and particularly V_{P3}.

The correlation matrix and selected joint marginal probability distributions for the linear layer model are shown in Figure 17 and Figure 18, respectively. Strong inter-relationships are indicated for the best determined parameters, with a strong positive correlation between h and $V_{S2,}$ and strong negative correlations between h and V_{S1} and between V_{S1} and V_{S2}. The latter negative correlation differs from that found for the Fraser River delta site, where V_{S1} and V_{S2} were uncorrelated (Figure 12 and Figure 13), and indicates that the average V_S value of the upper layer is an important quantity defining dispersion at the Victoria site. Other differences from the Fraser River delta site include a lack of correlation of V_{S3} with other parameters, and lower correlations of density with V_{S1} and V_{S2}.

Figure 19 presents the marginal probability V_S profile for the Victoria site which shows a well resolved linear gradient of the upper layer and a significant increase in V_S at about 16.5 ± 1.5 m depth, with the half-space V_S value poorly resolved.

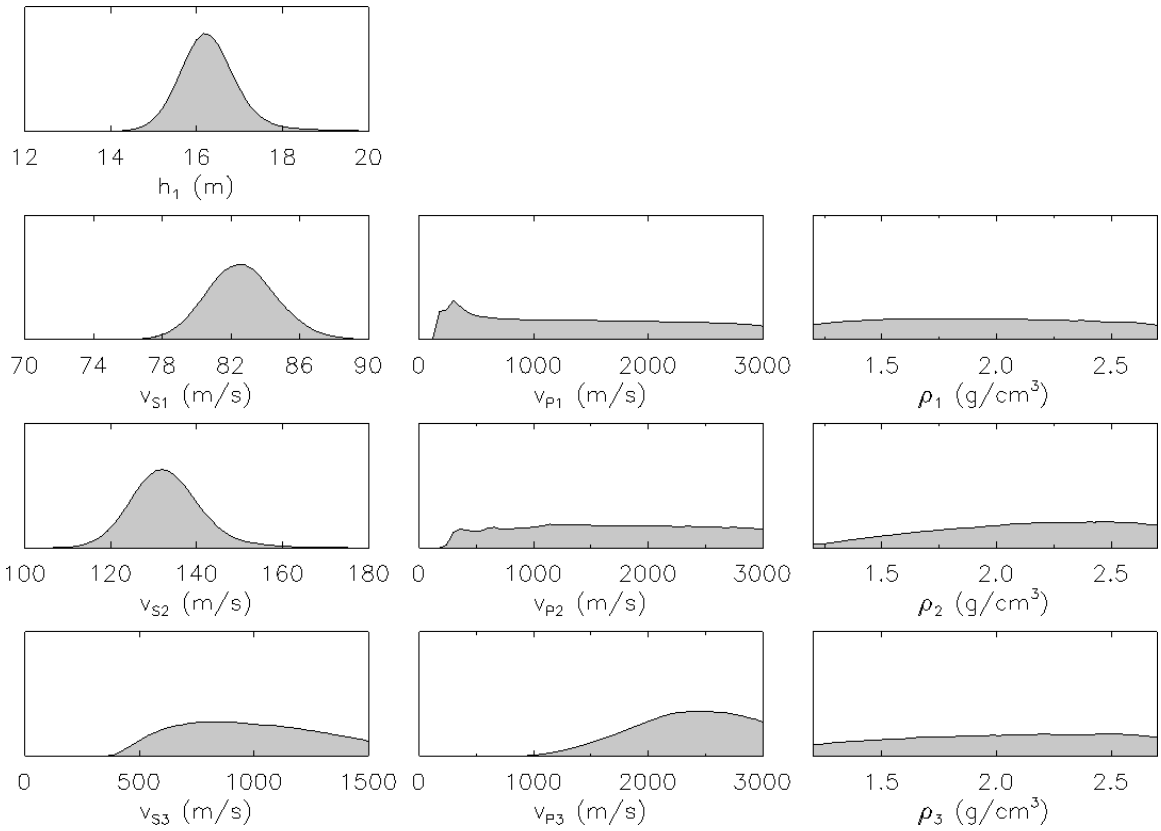

Figure 16. Marginal probability distributions from Bayesian inversion of the Victoria data using full data covariance estimates.

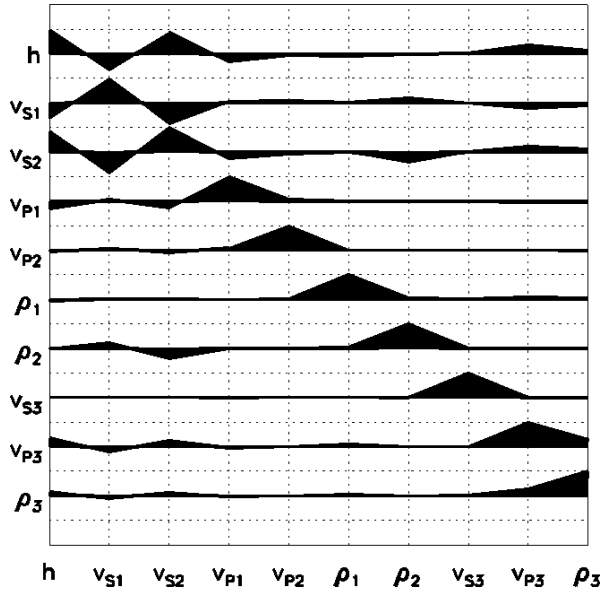

Figure 17. Correlation matrix for the linear gradient parameterization at the Victoria site.

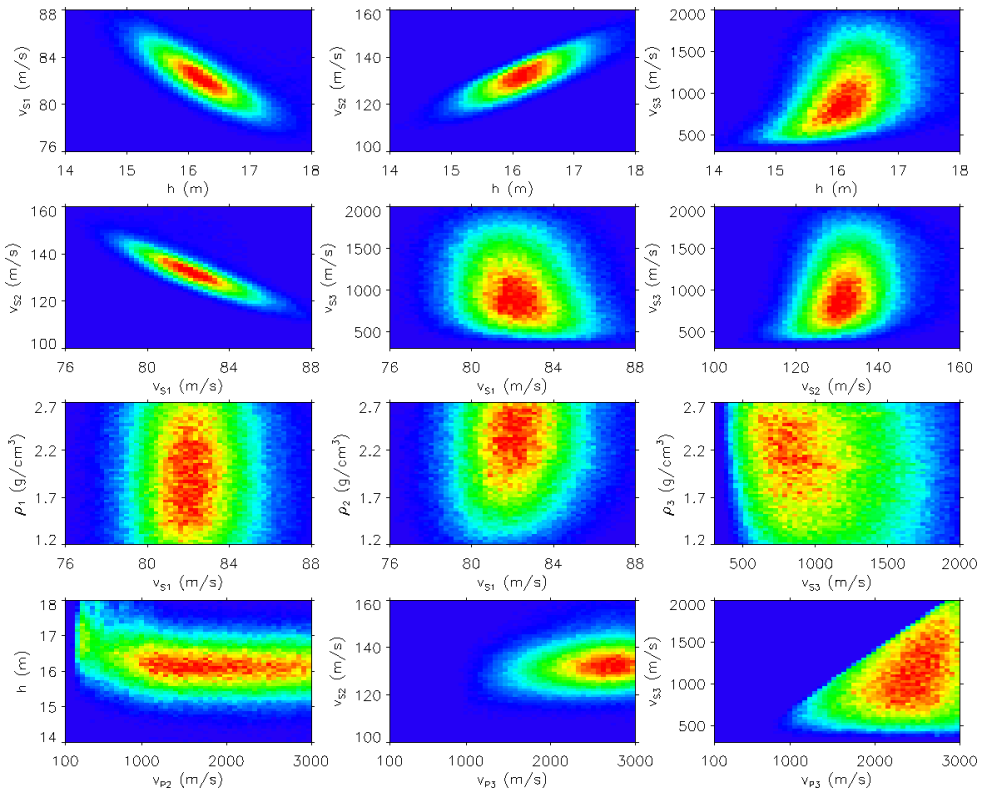

Figure 18. Selected joint marginal probability distributions from inversion of Victoria data. Each distribution is normalized independently.

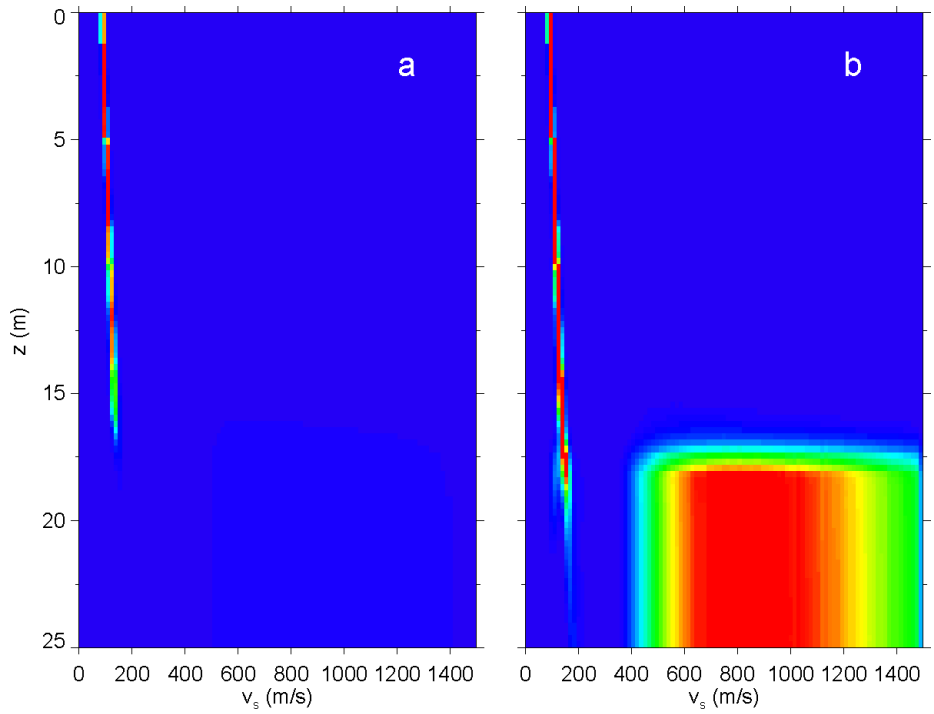

Figure 19. (a) Marginal probability V_S profile from Bayesian inversion for the Victoria data. (b) Marginal profile normalized independently at each depth.

2.8 Assessment of reliability

The V_S profiles determined from Bayesian microtremor inversion are assessed for reliability by comparison with the co-located invasive V_S measurements (SCPT and/or downhole). The V_S profiles of the five invasive method sites at the Fraser River delta site are shown in Figure 3c and d and Figure 20a. The downhole profile shows V_S increasing with depth to 235 m where a significant increase occurs, marking the rapid transition between the base of Holocene deltaic sediments and the Pleistocene glacial till. Velocity reversals occur in both the SCPT and downhole profiles which are larger than their associated measurement errors (Hunter et al. 1991). The reversals indicate the measurements are sensitive to fine layering (i.e. differences between the Holocene deltaic sands and silts). The variation observed in V_S between sites is related to their lateral separation. The downhole measurements at the Fraser River delta site do not show an abrupt velocity increase until 235 m depth (Figure 20a). Hence, the velocity contrast observed in the Bayesian microtremor inversion result between 110-160 m (Figure 20b) is not related to an abrupt geologic change, but results from general sensitivity of the dispersion data to velocities higher than can be represented by the power-law gradient at greater depth, albeit with poor resolution.

Figure 20b compares the invasive V_S measurements with the MAP model and 95% HPD credibility interval from the Bayesian inversion. For direct comparison, the invasive V_S measurements at the five nearby sites are averaged together over the logarithmic depth partitioning of the MAP model. The mean V_S of the invasive methods closely approximates a power-law depth relation as previously noted for the upper 100 m of sediments of the Fraser River delta (Hunter & Christian 2001). Excellent agreement in V_S structure from the surface to over 120 m depth is obtained; the average relative difference between the average of the invasive measurements and the Bayesian inversion result is 5% and shear-wave velocities of the MAP model are within one standard deviation of the average invasive V_S measurements. Below this depth the credibility interval widens yet defines a transition to higher velocities (> 450 m/s by 160 m depth). Forward modelling analysis indicates that dispersion data below 0.9 Hz is sensitive to the downhole-derived increase in V_S at 235 m depth (i.e. the transition from deltaic sediments

to glacial till); hence, resolving this V_S increase is not possible given the 1.2 Hz minimum frequency of the measured dispersion curve.

For comparison, Xia et al. (2000) compared V_S profiles from linearized inversion of Rayleigh wave dispersion data acquired using an active source and a linear array of 60 geophones (referred to as multichannel analysis of surface waves, MASW) with downhole measurements at eight sites across the southern Fraser River delta and obtained average relative differences to 30 m depth of 8-26%, with an overall average of 15%. Woeller et al. (1993) documented V_S profiles from inversion of dispersion data acquired using an active source and multiple deployments of two geophones (spectral analysis of surface waves, SASW) with SCPT measurements at 15 sites on the delta, and obtained generally good agreement. It is also worth noting that differences in shear-wave velocity measurements between the two invasive methods (SCPT and downhole) at sites on the delta reported by Hunter et al. (1991; 2002) appear to be similar in size to the differences between surface-wave inversion results and invasive measurements given above.

For the Victoria site, Figure 21 shows the 16 SCPT V_S values measured at 1-m increments to 17 m depth. As mentioned in Section 2.2, the material below 17 m is likely over-consolidated glacial material (V_S of 475 ± 78 m/s) and/or hard bedrock (V_S > 1500 m/s). In either case, a strong impedance contrast at 17 m depth is expected from refusal of cone penetration. The inversion results for the Victoria site (Figure 21) show a well-determined transition at 15-18 m depth between low velocity (< 150 m/s) and higher velocity (> 500 m/s) material, which likely represents the physical contact between soft clayey silts and stiffer glacial till and/or hard bedrock. Figure 21 presents excellent agreement between the invasive SCPT V_S measurements with the MAP model from Bayesian microtremor inversion; the average relative difference to 17 m depth (basement) is 11%. The depth of the significant velocity increase in the MAP model corresponds closely to the 17 m depth of cone penetration refusal; however, it should be noted that the credibility interval for this transition extends from about 15-18 m. The half-space velocity is poorly resolved, since the minimum frequency of the Victoria dispersion data is 2.4 Hz. Forward modelling analysis indicates that dispersion data at frequencies below 1.8 Hz are sensitive to variation in the half-space velocity.

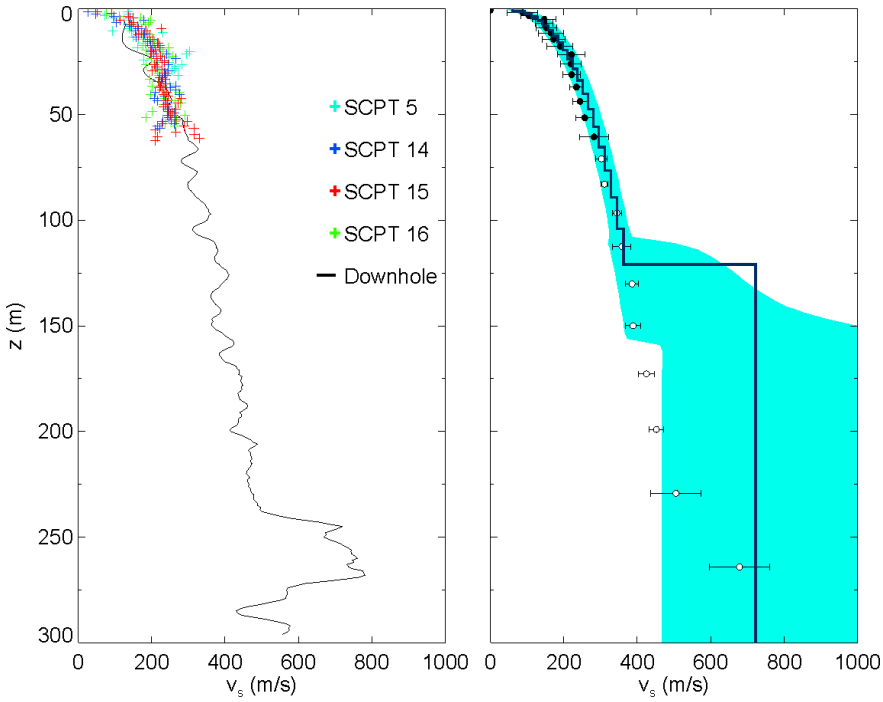

Figure 20. (a) V_S values determined from SCPT and downhole measurements at the Fraser River delta site. (b) MAP model (solid line) and 95% HPD credibility interval (shaded region) from Bayesian inversion. Filled circles indicate averaged SCPT and downhole measurements; open circles indicate downhole-only averages (error bars indicate one standard deviation about the mean).

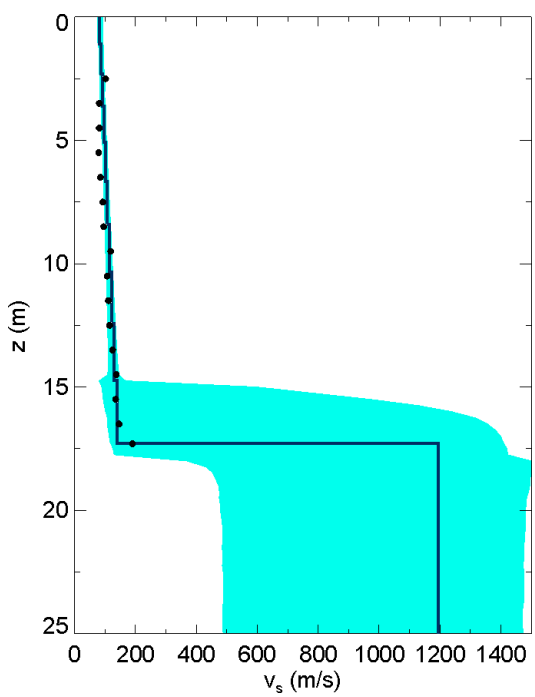

Figure 21. Comparison of V_S profiles at the Victoria site from SCPT measurements (filled circles) with the MAP model (solid line) and 95% HPD credibility interval (shaded region) from Bayesian inversion.

2.9 Site response probability analysis

In theoretical calculations of site amplification, the 1D soil column is represented using an estimate of the V_S profile usually with some measure of its uncertainty. In this section uncertainty in predicted linear site amplification is examined due to uncertainty in V_S structure quantified from Bayesian inversion of microtremor array dispersion data. Based on a sample of V_S profiles drawn from the posterior probability density of the microtremor inversion, probability distributions are computed for common site response predictors including V_{S30} (average shear-wave velocity in the upper 30 m), NEHRP site class, amplification of PGA and PGV, and root-impedance and SH-wave amplification spectra. The SH-wave amplification probability spectra are evaluated by comparison to empirical earthquake and microtremor spectral ratios. The probabilistic site response analysis is applied at two sites in high population centres with strongly contrasting geology and site response located in British Columbia, Canada. The most-probable V_S profiles for the Fraser River delta and Victoria sites shown in Figure 20 and Figure 21, respectively, are also tracked through into predictions of V_{S30} and amplification spectra representative of a single, albeit best-fit, estimate of V_S structure.

2.9.1 Uncertainty of V_{S30}

Categorization of site class in modern building codes primarily uses V_{S30} to predict site amplification based on empirical amplifications derived from analysis of earthquake recordings. V_{S30} is defined as 30 m divided by the shear-wave travel time (in seconds) to 30 m (Borcerdt 1994); hence, the V_{S30} estimate and its uncertainty are most sensitive to the longer travel time within near-surface low velocity material rather than the shorter travel time within higher velocity material at depth.

Recent ground motion prediction equations directly use V_{S30} to calculate site amplification. The term for linear site amplification in Boore and Atkinson's (2008) GMPE is given by:

$$\ln A/A_{ref} = b_{lin} \ln(V_{S30}/V_{ref}), \tag{33}$$

where A is amplification for a particular model with average velocity of V_{S30}, A_{ref} is amplification for a reference model with average velocity of V_{ref}, and b_{lin} is -0.36 and -0.6 for PGA and PGV, respectively. The reference velocity is set here to 620 m/s representative of site class C (Table 1) which is the reference hard-ground condition of

the National Building Code of Canada (2005). In general, surface-wave methods cannot resolve fine structure; hence, uncertainty of an average V_S estimate (i.e. V_{S30}) is a good initial choice for assessing the ability of the microtremor array method to characterize site amplification.

The average V_S from surface to a particular depth z is termed here as V_{SZ} and calculated as

$$V_{SZ} = \frac{z}{\int_0^z \frac{dz}{V_S(z)}}, \tag{34}$$

where $V_S(z)$ is the V_S profile. Statistical measures and probability distributions for V_{SZ} can be computed by applying eq. (34) to a sample of V_S models drawn from the PPD. Figure 22a shows V_{SZ} for the Fraser River delta site. Two standard deviation uncertainties are included to best describe the full distribution. The mean V_{S30} estimate ± two standard deviations for the delta site is 164 ± 43 m/s which spans the boundary between NEHRP site classes D and E. The V_{S30} estimate computed for the most-probable V_S profile is 157 m/s corresponding to class E, but without any indication of uncertainty. As a more meaningful analysis, the V_{S30} probability distribution shown in Figure 22b indicates the probability the delta site corresponds to site class E (95%) rather than class D (5%). Uncertainty in amplification of PGA and PGV with respect to hard ground, shown in Figure 22c and d and listed in Table 3, is calculated using eq. (33) and the V_{S30} probability distribution. A 13% CoV in the V_{S30} estimate results in 5% and 10% CoV in PGA and PGV amplification, respectively. The V_{S30} estimate for the most-probable V_S profile and the mean V_{S30} estimates predict similar PGA and PGV amplification factors (Table 3). Overall, using the V_{S30} probability distribution rather than a single V_{S30} estimate is more informative for NEHRP site classification.

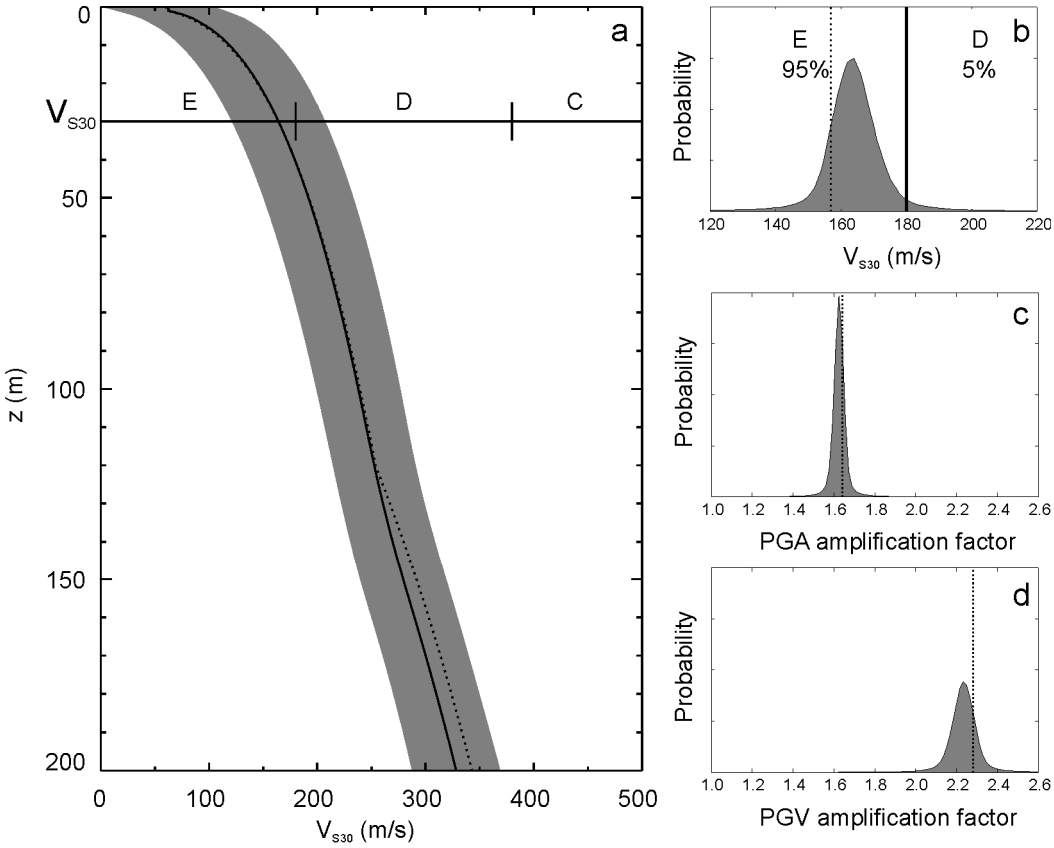

Figure 22. (a) Depth-averaged shear-wave velocity V_{SZ} for the Fraser River delta site. Solid line represents the mean and shaded region corresponds to mean ± two standard deviations. NEHRP site class boundaries, based on V_{S30}, are indicated. Probability distributions of (b) V_{S30}, and (c) PGA and (d) PGV amplification factors with respect to class C. Dotted lines correspond to results for the most-probable V_S model.

At the Victoria site, Figure 23a shows that the mean V_{S30} estimate site ± two standard deviations is 182 ± 31 m/s, at the boundary between NEHRP site classes D and E. Uncertainty of V_{SZ} is ≤ 15 m/s in the upper 16 m, due to the well-determined low V_S of the upper layer in the marginal probability V_S profile, then increases with depth due to the poorly constrained half-space velocity. The V_{S30} probability distribution in Figure 23b indicates 58% probability that the Victoria site corresponds to site class D, slightly more probable than class E (42%). The PGA and PGV probability distributions in Figure 23c and d show amplification could reach 1.8 and 2.3 times that of hard ground, respectively. Overall, the low predicted level of amplification based on V_{S30} at the Victoria site is in disagreement with known high amplification effects from earthquakes (Section 2.4, Figure 4d); the concept of V_{S30} as a site amplification predictor fails in this case. The

well-determined average velocity of the soil layer, i.e. ~100 m/s based on either V_{S5}, V_{S10} or V_{S15}, will cause significant amplification and should be used for site response characterization rather than V_{S30} which averages into the under-lying higher-velocity material.

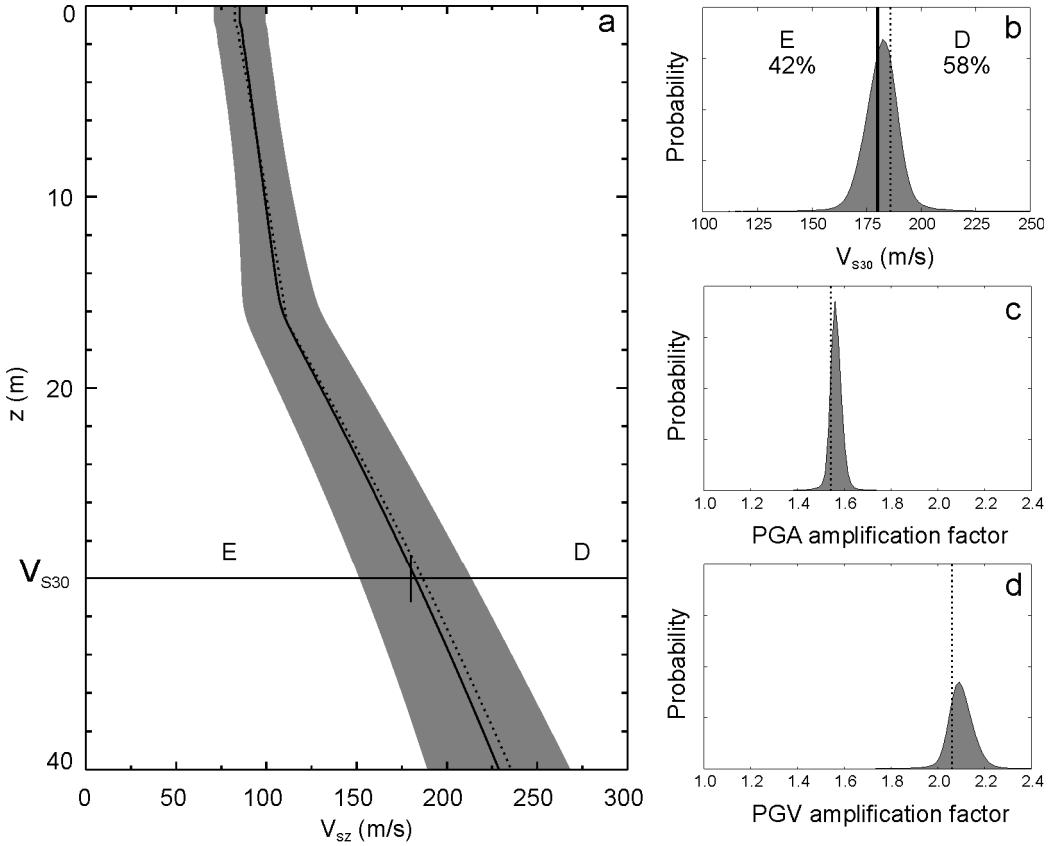

Figure 23. (a) V_{SZ} for the Victoria site. Solid line represents the mean and shaded region corresponds to mean ± two standard deviations. NEHRP site class boundaries, based on V_{S30}, are indicated. Probability distributions of (b) V_{S30}, and (c) PGA and (d) PGV amplification factors with respect to class C. Dotted lines correspond to results for the most-probable V_S model.

Table 3. Uncertainty estimates of V_{S30} and amplification of PGA and PGV.

	Mean ± two std. dev.	**CoV**	**Most-probable V_S model**
Fraser River delta			
V_{S30}	164 ± 43 m/s	13%	157 m/s
PGA factor	1.62 ± 0.16	5%	1.64
PGV factor	2.23 ± 0.44	10%	2.28
Victoria			
V_{S30}	182 ± 31 m/s	9%	186 m/s
PGA factor	1.56 ± 0.18	6%	1.54
PGV factor	2.09 ± 0.17	4%	2.06

2.9.2 Uncertainty of amplification spectra

A better indicator of earthquake site response is the calculation of frequency-dependent amplification based on the entire V_S profile, rather than an average property of the soil column such as V_{S30}. Considering the simplest case of a single soil layer over a half-space bedrock reference, the peak amplification from 1D vertical propagation of SH-waves occurs at resonant frequencies f_n given by (Haskell 1960)

$$f_n = nV_S/4h, \tag{35}$$

where V_S is the shear-wave velocity of the soil, h is the soil thickness, and n = 1, 3, 5, … is the mode number. Resonance results from trapping of SH-waves between the two large seismic impedance boundaries of the surface-soil and the soil-bedrock interfaces (Rial et al. 1992). Amplification factors of both surface motion and resonant peaks are functions of the seismic impedance ratio $\rho_2 V_2/\rho_1 V_1$, where subscripts *1* and *2* refer to the soil and half-space, respectively (Haskell 1960). The maximum amplification due to combined resonance and impedance effects at the surface is twice the impedance ratio (Reiter 1991). If losses due to reflection, scattering, and anelastic attenuation are neglected, the energy is constant, and the amplification at the surface is equivalent to the square root of the impedance ratio, i.e. $[\rho_2 V_2/\rho_1 V_1]^{1/2}$ (Joyner et al. 1981).

Both root-impedance and SH-wave resonance amplification spectra are calculated here using a subsample of up to 30,000 V_S profiles from the PPD using a wide spacing to skip over locally correlated models. The assumption of vertical incidence is used in all calculations; an observable difference in the predicted peak SH-wave amplification does not occur until the incidence angle is ≥ 40° (Field & Jacob 1993; Thompson et al. 2009). The calculations do not include particular earthquake characteristics (faulting type, depth, distance, etc.); the resulting spectra are a measure of amplification based solely on the V_S-depth structure, not absolute measures of ground motion related to a particular earthquake. Fah et al. (2003) showed that at the fundamental frequency, uncertainty in estimated amplification of ~4-11 is increased to ~7-22 by including variability of earthquake characteristics from considering 576 sources at different distances, depths, and with different source mechanisms.

2.9.2.1 Uncertainty of amplification due to impedance

Following Boore (2003) and Boore & Brown (1998), amplification based on the impedance ratio between layers of a particular V_S profile is calculated as

$$A(f(z)) = \sqrt{\frac{\rho_r V_r}{\rho_Z V_{SZ}}}, \tag{36}$$

where density and shear-wave velocity of the reference (i.e. half-space) layer are ρ_r and V_r, respectively, and ρ_Z and V_{SZ} are the equivalent quantities averaged from the surface to a depth, z. From eq. (35), the frequency function $f(z)$ corresponds to a wavelength four times the layer depth. Hence, the lowest frequency calculated corresponds to the quarter wavelength equivalent of the deepest layer in a model (Joyner et al. 1981). Overall, this method provides a smoothed amplification function regarded as an adequate approximation of the site response (Boore & Joyner 1991). Recently, Douglas et al. (2010) proposed replacing the V_{S30} based approach to calculation of site amplification in ground motion prediction equations with root-impedance calculations based on the V_S profile and Poggi et al. (2011) defined a regional reference rock profile from calculated root-impedance spectra for use in seismic hazard assessment in Switzerland.

Uncertainty of root-impedance amplification spectra $A(f)$ is sought due to the uncertainty in V_S structure, such that V_{SZ} in eq. (36) is calculated using the sampled V_S profiles. For both sites, the upper gradient layer is partitioned logarithmically with depth. Densities are set to geologically reasonable values, rather than using the poorly resolved uncertainty distributions derived from the Bayesian inversions in section 2.7. In reality, there is less variation in density than V_S for soils; hence, little variation in amplification is expected from variation in density. Both velocity and density are constrained to increase with depth.

For the Fraser River delta site, the power-law gradient and half-space layers in the sampled V_S profiles are used to calculate V_{SZ} and V_r (representing Holocene deltaic sediments and Pleistocene material, respectively, based on lithologic interpretation of the co-located 300-m borehole shown in Figure 3c). The density of the Holocene sediments ρ_Z is represented by a Gaussian distribution with mean and standard deviation of 2000 and 200 kg/m^3, respectively (Lowe et al. 2003; Dallimore et al. 1995). The density of the Pleistocene reference ρ_r is taken to be a Gaussian with mean and standard deviation 2200

and 200 kg/m^3. Figure 24a presents marginal probability distributions of the resulting root-impedance amplification obtained by integrating the probability of all calculated amplification spectra over an amplification-frequency grid (normalized independently at each frequency). Variation in the low-frequency limit of the spectra results from the variation in the depth of the impedance ratio between 120-160 m. Amplification increases strongly with frequency as quarter-wavelength layers become thinner and the average V_S decreases rapidly according to the power-law gradient. The positively skewed distribution in the half-space velocity causes a positively skewed distribution in amplification. Standard deviation of amplification increases with frequency from 0.5 at 0.5 Hz to 1.1 at 10 Hz (Table 4), suggesting greater sensitivity to variation in near-surface V_S.

Figure 10 and Figure 11 shows that the V_S profile is well determined to only ~120 m depth, while the Pleistocene material representing the reference half-space is known to occur at 235 m depth in the 300-m borehole (Dallimore et al. 1995) (Figure 3c). Hence, the depth and strength of the significant impedance ratio determined in the sampled V_S profiles does not represent known geological structure. To investigate the significance of this inability to resolve deep structure, the sampled V_S profiles are altered by extending the power-law gradient to a depth of 235 m and inserting a half-space velocity representative of Pleistocene material set to a Gaussian distribution with mean and standard deviation of 700 and 100 m/s (Figure 3c). In other words, uncertainty in the depth of the significant impedance ratio is effectively removed, and uncertainty of the reference half-space velocity is slightly decreased in the altered sample of V_S profiles. Figure 24b presents the root-impedance amplification distribution calculated using this geologically-altered V_S probability distribution. Note that the low frequency limit no longer varies because of the fixed 235 m depth of the gradient layer. Again, amplification and its uncertainty increase with frequency, but uncertainty is decreased overall in comparison to the original distribution in Figure 24a (Table 4). Overall, the root-impedance spectra shown in Figure 24a and b agree reasonably well, indicating that the V_S distribution computed by microtremor inversion (without additional geological information at depth) provides adequate prediction of site amplification for this case.

Table 4. Root-impedance amplification uncertainty estimates.

	Mean ± two std. dev.	CoV	Most-probable V_S model
Fraser River delta			
Original sample			
0.5 Hz	1.8 ± 0.5	14%	1.6
10 Hz	3.6 ± 1.1	15%	3.7
Altered sample			
0.3 Hz	1.6 ± 0.3	9%	1.8
10 Hz	3.7 ± 0.7	9%	3.8
Victoria			
2 Hz	5.5 ± 1.3	12%	5.6
10 Hz	5.9 ± 1.4	12%	6.2

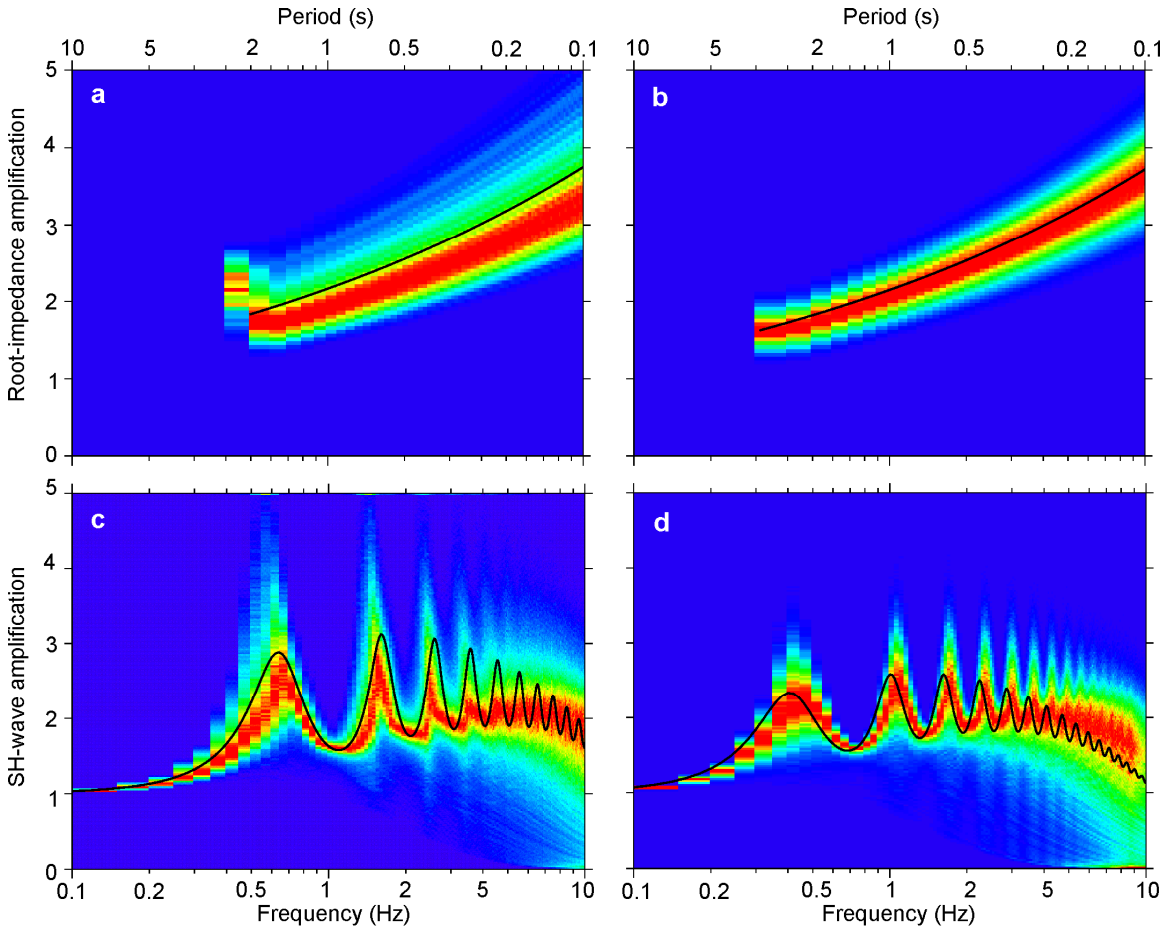

Figure 24. (a) Marginal probability root-impedance amplification spectra for the delta site calculated from the sample of V_S profiles shown in Figure 14. Black line corresponds to root-impedance spectrum predicted for the most-probable V_S profile shown in Figure 20b. (b) Same for the geologically-altered sample of V_S profiles and black line indicating spectrum for the altered most-probable profile (see text for details). Marginal probability SH-wave amplification spectra calculated for (c) the original and (d) altered sample of V_S profiles. Black lines in (c) and (d) correspond to SH-wave spectrum predicted for the original and altered most-probable V_S profile, respectively.

For the Victoria site, the marginal probability V_S profile shown in Figure 19b is taken to represent the geological conditions and the sampled V_S profiles are used in the root-impedance calculations. Even though the half-space velocity determined by Bayesian inversion is not constrained to known velocity limits of either of the two possible materials below 17 m, i.e. either glacial till (~ 500 m/s) or bedrock (> 1500 m/s), it serendipitously encompasses the geological uncertainty. The density of the upper silt layer ρ_Z is represented by a Gaussian distribution with mean and standard deviation of 1850 and 200 kg/m^3, with a minimum cut-off of 1650 kg/m^3. Density of the underlying glacial material and/or bedrock layer ρ_r is taken to be a Gaussian with mean and standard deviation of 2400 and 300 kg/m^3 (Lowe et al. 2003).

The marginal probability root-impedance amplification spectra for the Victoria site, shown in Figure 25a and reported in Table 4, exhibits significant amplification of 4.2-6.8 due to the strong near-surface (15-18 m) impedance contrast between the well-determined low V_S layer and the poorly determined high-velocity half-space. Root-impedance calculations clearly predict high amplification for the Victoria site, in agreement with observed earthquake amplification effects, by accounting for the entire V_S profile. Amplification is relatively frequency-independent in this case since V_S of the upper layer is nearly uniform. The large uncertainty in the half-space velocity (500-1500 m/s) produces a CoV in predicted amplification of 12%.

The root-impedance amplification spectrum calculated for the most-probable (best-fit) V_S profile is shown by a solid line in Figure 24a and b and Figure 25a for the two sites. Inversions based on simply estimating the best-fit model provide only this information, while the Bayesian inversion provides a full uncertainty analysis. The relatively small differences between the spectrum for the most-probable model and the distribution mean (given in Table 4) are due to the nonlinearity of the inversion.

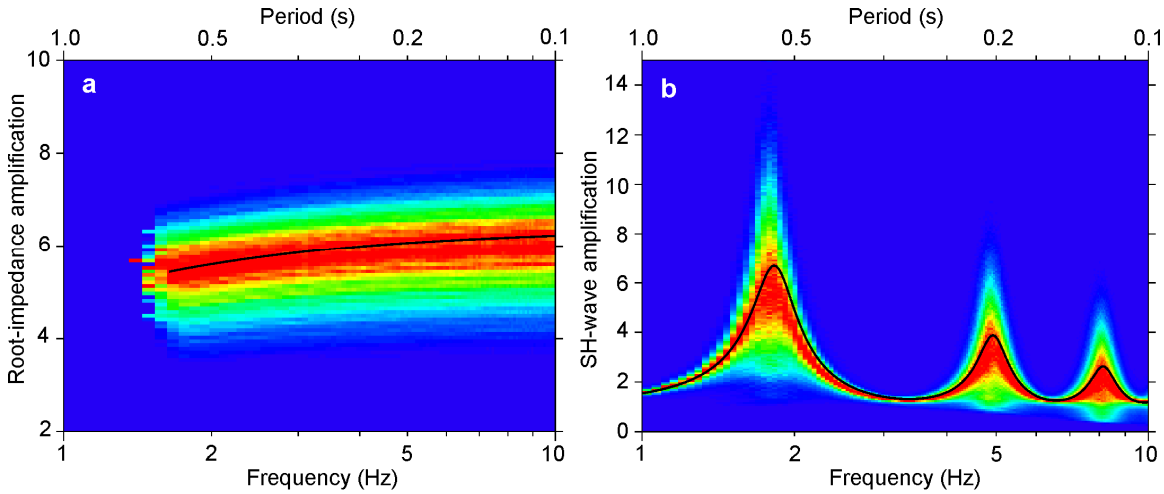

Figure 25. (a) Root-impedance and (b) SH-wave amplification probability distributions for the Victoria site calculated for the V_S probability distribution shown in Figure 19. Black lines correspond to spectrum for the most-probable V_S profile shown in Figure 20.

2.9.2.2 Uncertainty of amplification due to resonance

Linear site amplification that accounts for resonance of vertically-propagating SH-waves is calculated using the NRATTLE routine included in the ground motion simulation package of Boore (2005). The routine calculates the Haskell-Thomson plane SH-wave transfer function for horizontally stratified constant-velocity layers over a uniform velocity half-space at a specified incidence angle (Haskell 1953, Thomson 1950). Peak amplification is proportional to the impedance ratio between the soil layer and half-space and occurs at frequencies of $V_S/4h$, $3V_S/4h$, and $5V_S/4h$ for the first three modes of SH-wave resonance, respectively (Haskell 1960). Frequency-dependent attenuation is implemented in the SH-wave resonance calculations using Q_S, the quality factor of shear-waves. Attenuation increases with frequency; hence, the SH-wave spectral amplitudes calculated here generally decrease with increasing frequency, in contrast to root-impedance amplification results in the previous section where attenuation was not included. Input for the SH-wave calculations are the same V_S profiles sampled from the PPD and Gaussian density distributions used in the root-impedance calculations. The Q_S of the Holocene sediments at the delta site is represented by a Gaussian distribution of mean and standard deviation 20 and 10, respectively; the predominantly marine silt at the Victoria site is represented by a Gaussian of mean and standard deviation of 10 and 10 (Brocher 2008, Frankel et al. 2009), and the Gaussian distributions are cut off at a

minimum of 2 (Olsen 2003). The NRATTLE routine is equivalent to the solution computed by numerical SHAKE analysis Idriss & Sun (1991), except that the latter requires an earthquake ground motion recording as input and uses linear modulus reduction and damping curves to simulate attenuation.

Figure 24c and d shows the marginal SH-wave amplification distributions for the Fraser River delta site calculated using the original and geologically-altered sample of V_S profiles, respectively (as described in Section 2.9.2.1). In both cases, multiple resonant peaks are resolved up to ~ 5 Hz with relatively low amplification (< 5). Peak frequencies of the first-three modes are well determined to within 0.4 Hz (Table 5). Comparing the predicted spectra for the original (Figure 24c) and altered (Figure 24d) samples the peaks shift to lower frequencies and amplification decreases with smaller uncertainties in both quantities. This shift in frequency and amplification of the resonant peaks is most apparent for the fundamental-mode (f_0). The original sample predicts the f_0 at 0.6 ± 0.1 Hz with a large uncertainty in amplification of 2.1, whereas the altered sample predicts f_0 at 0.4 ± 0.1 Hz with a significantly reduced uncertainty in amplification of 0.8. The predicted peak frequencies calculated using the altered V_S profiles are in better agreement with empirical earthquake SH/V ratios shown in Figure 4c, which exhibit low (< 3) amplification at a low f_0 of 0.3 Hz and first higher-order modes (f_1) at < 1.5 Hz. In comparison to the empirical microtremor H/V ratio in Figure 4a, the first two predicted resonant frequencies are also in better agreement with the altered distribution shown in Figure 24d. Nonetheless, the unaltered microtremor inversion results provide useful SH-wave amplification estimates in reasonable agreement with the empirical spectra.

For the Victoria site, the uncertainty distribution in SH-wave amplification displays three resonant modes (Figure 25b). The fundamental frequency f_0 is relatively well determined at 1.8 ± 0.3 Hz as the depth of the strong impedance contrast is well constrained between 15-18 m depth, whereas the peak amplification at f_0 is poorly determined, 6.8 ± 5.0, due to the poorly constrained half-space velocity (500-1500 m/s). The prominent f_0 peak at 1.8 Hz is also clearly observed in both the microtremor H/V and earthquake SH/V ratios in Figure 4b, and d, respectively. The high predicted SH-wave amplification at f_0 is in better agreement with the empirical amplification from the average microtremor response of 5.5 than from earthquake SH-waves of 2.5-3.5. The

higher modes predicted at 5 and 8 Hz (Table 5) are generally not observed in the microtremor H/V and earthquake SH/V ratios. However, the SH/V ratio from a nearby high-frequency content earthquake (Table 2) shows amplification at 8 Hz as predicted. These discrepancies between predicted and empirical amplification for higher-order modes suggest strong attenuation occurs at the Victoria site.

Finally, Figure 24c and d, Figure 25b, and Table 5 show that the SH-wave amplification spectrum for the most-probable V_S profile at each site generally agrees well with the mean of the amplification spectrum probability distribution. However, the spectral uncertainties provided by the Bayesian inversion provide a more robust estimate of SH-wave amplification than simply the best-fit estimate, which is more informative to site response characterization.

Table 5. SH-wave amplification uncertainty estimates.

	Mean ± two std. dev.	**CoV**	**Most-probable V_S model**
Fraser River delta			
Original sample			
A_0	2.9 ± 2.1	36%	2.9
f_0	0.6 ± 0.1 Hz	8%	0.6 Hz
A_1	3.1 ± 2.0	32%	3.1
f_1	1.6 ± 0.3 Hz	9%	1.6 Hz
A_2	3.0 ± 2.0	33%	3.1
f_2	2.5 ± 0.4 Hz	10%	2.6 Hz
Altered sample			
A_0	2.3 ± 0.8	17%	2.3
f_0	0.4 ± 0.1 Hz	13%	0.4 Hz
A_1	2.5 ± 1.0	20%	2.9
f_1	1.1 ± 0.1 Hz	5%	1.0 Hz
A_2	2.5 ± 1.2	24%	2.6
f_2	1.7 ± 0.2 Hz	6%	1.6 Hz
Victoria			
A_0	6.8 ± 5.0	37%	6.7
f_0	1.8 ± 0.3 Hz	8%	1.8 Hz
A_1	4.1 ± 3.5	43%	3.9
f_1	4.9 ± 0.3 Hz	3%	4.9 Hz
A_2	2.9 ± 2.8	48%	2.6
f_2	8.0 ± 0.4 Hz	3%	8.1 Hz

2.10 Discussion and conclusions

A nonlinear Bayesian inversion approach is applied with evaluation of data error statistics and model parameterizations to retrieve the most-probable V_S profile and its uncertainty

from microtremor array dispersion data. The uncertainty in V_S structure as quantified via the Bayesian inversion is then propagated into uncertainty estimates of linear site amplification and assessed for use in site response characterization.

Bayesian inversion of microtremor array dispersion data is applied at two sites in British Columbia to study the ability to recover an accurate V_S profile at both shallow (< 20 m) and deep (> 200 m) sediment sites on the Fraser River delta, and in Victoria, respectively. Microtremors were collected using seismic arrays of five to six sensors with the largest array aperture set according to the depth of interest, i.e. maximum sensor spacing of 70 m at the shallow-sediment Victoria site and 180 m at the thick-sediment Fraser River delta site. Frequency-wavenumber processing techniques are applied to estimate the fundamental-mode Rayleigh wave phase velocity from the microtremor recordings. Reliable phase velocity estimates are obtained between 1.2-6.7 Hz and 2.4-9.0 Hz for the delta and Victoria sites, respectively. Theoretically, dispersion data could have been retrieved over a wider frequency bandwidth; the low frequency limit of the retrieved data is likely a consequence of reduced fundamental-mode Rayleigh wave energy at the fundamental frequency observed in empirical H/V ratios rather than due to resolution limitations of the largest array aperture used in the field.

Bayesian inversion formulates an inverse problem in terms of properties of the posterior probability density of the geophysical model parameters, such as the maximum *a posteriori* model, marginal probability distributions, correlation matrix, and credibility intervals. The MAP model is determined here by numerically minimizing the generalized (data and prior) misfit using adaptive simplex simulated annealing. Other PPD properties are determined using the Markov-chain Monte Carlo method of Metropolis-Hastings sampling, employing a proposal distribution based on a linearized PPD in principal-component parameter space for efficiency.

A key point of this chapter is that reliable parameter uncertainty estimation requires an appropriate data error distribution, with error correlations (if significant) quantified and included in the inversion and results validated by *a posteriori* statistical tests. Data error statistics are found here to vary over the frequency bandwidth of the dispersion curve due, in part, to generating the full curve from segments corresponding to the reliable frequency ranges associated with various array apertures. The approach

applied here for representing data errors uses residual analysis for nonparametric estimation of a block-diagonal covariance matrix, together with rigorous *a posteriori* statistical tests to validate the covariance estimate (runs test) and the assumption of Gaussian-distributed errors (KS test). For the data sets considered here, error correlations are satisfactorily accounted for when the full covariance matrix is used in the Bayesian microtremor inversion. Smaller parameter uncertainty estimates are obtained if data error correlations are neglected; however, these are unjustified and potentially misleading.

It was found that fixing V_P and ρ in the inversion, as is commonly done, resulted in decreased uncertainty bounds for the V_S profile parameters. Further, correlation matrices and joint marginal distributions indicate significant inter-relationships between the V_S profile parameters and ρ and weaker inter-relationships with V_P (some correlations appear to be site specific). Hence, rigorous uncertainty estimates for V_S require accounting for the uncertainties in these nuisance parameters. Wide prior bounds were set on all parameters, encompassing physically realistic values, to allow the data (not the prior) to primarily determine the solution. However, if prior information and/or additional data are available, it is straightforward to include these in Bayesian inversion, which will generally result in smaller V_S uncertainties. For example, if knowledge of an interface depth is available from geophysical or geological information, this can be included (with uncertainties) in the prior. Likewise, joint inversions combining the peak frequency from horizontal-to-vertical spectral ratios with dispersion data may better constrain the basement depth and velocity, and are easily accommodated within a Bayesian formulation; however, this is not done here.

The Bayesian inversion results for the Fraser River delta site show a well resolved V_S profile to at least 110 m depth for a power-law gradient parameterization. At the Victoria site, a layer with low V_S and a weak linear gradient is indicated to 15-18 m depth, above an abrupt increase to higher velocity material. Reliability of the Bayesian inversion results is evaluated by comparison with invasive V_S measurements from seismic cone penetration testing and/or surface-to-downhole methods. The average relative difference between the most-probable V_S model from Bayesian microtremor inversion and SCPT V_S measurements to 17 m depth (basement) is 11% at the Victoria site. Excellent agreement in V_S structure is also obtained for the Fraser River delta site; the

average relative difference between the average of the invasive measurements and the MAP model from the surface to over 120 m depth is 5%. Other evaluations of V_S profiling methods at sites on the Fraser River delta demonstrate similar good agreement between MASW and downhole (Xia et al. 2000), SASW and SCPT (Woeller et al. 1993), and SCPT and downhole (Hunter et al. 1991; 2002) methods.

The most appropriate model parameterization at each site is determined by minimizing the Bayesian information criterion, which provides the simplest model consistent with the resolving power of the data. At both sites, the Bayesian microtremor inversion results do not resolve fine geologic layering and poorly resolves half-space (bedrock) velocity, consistent with known limitations of the microtremor array method (Cornou et al. 2006) and surface-wave methods in general. Good recovery of the overall shear-wave velocity structure is obtained at both sites from microtremor inversion, given appropriately chosen simple parameterizations. Further, rigorous parameter uncertainty estimation quantifies the information content of microtremor array dispersion data for constraining V_S structure in excellent agreement with invasive V_S measurements. Therefore, a probabilistic site response analysis is conducted for each site in which the uncertainty distributions in V_S structure are propagated into uncertainty in predictions of site amplification (V_{S30} and amplification spectra) and examined for application to site response characterization.

At both sites computing the V_{S30} probability distribution is shown to be more informative for site response characterization than a single V_{S30} estimate determined from the most-probable (best-fit) V_S profile. For the Fraser River delta site, the V_{S30} uncertainty distribution spans NEHRP site classes D and E with a 95% probability of class E, which is associated with higher amplification. At Victoria, the V_{S30} distribution occurs at the D/E class boundary with 58% probability of class D, associated with lower amplification. This is in disagreement with known amplification effects of earthquakes and the strong near-surface impedance contrast at ~17 m depth. These results indicate that V_{S30} is not a useful indicator of site response for the Victoria site. However, the V_{SZ} (average V_S to depth z) probability profile computed from the microtremor inversion indicates that V_{S15} would provide a meaningful indicator.

Amplification spectra calculated using the entire V_S profile generally provide a better indicator of earthquake site response than V_{S30}. In this paper, uncertainty distributions for SH-wave amplification spectra based on seismic impedance variations and on resonance are calculated from the sampled V_S profile probability distribution. For the Fraser River delta site, a strong increase with frequency of impedance amplification and associated uncertainty results from the continuous near-surface increase in V_S of the power-law gradient. In terms of SH-wave resonant amplification, relatively low amplification at multiple modes is resolved; peak frequencies are determined within 0.4 Hz and amplification within a factor of 2. When the sampled V_S profiles are altered to represent known geological structure, resonant peaks shift to lower frequency and amplification decreases, in better agreement with empirical spectral ratios. Nonetheless, the unaltered inversion results provide useful SH-wave amplification estimates in reasonable agreement with the empirical spectra, indicating that the limited sensitivity depth of the microtremor data is not a serious constraint.

At the Victoria site, the V_S profile probability distribution indicates a near-surface strong impedance contrast that is well-constrained in depth but relatively unconstrained in velocity. This leads to a root-impedance amplification spectrum that is nearly frequency-independent but with fairly large uncertainty in amplification (factor of 2). The SH-wave amplification spectrum predicts the fundamental resonant frequency at 1.8 ± 0.3 Hz, with large uncertainties in amplification (factor of 5). The predicted fundamental peak frequency agrees well with that from empirical earthquake and microtremor spectral ratios. The amplification level of the fundamental peak agrees with that from microtremor ratios, but is somewhat higher than from earthquake ratios (although they agree within estimated uncertainties).

In summary, the benefits of rigorous uncertainty estimation in site response characterization are illustrated here based on non-invasive seismic methods such as microtremor dispersion inversion. Propagating V_S profile probability distributions, estimated via Bayesian inversion, through to various measures of site amplification quantifies the uncertainties in key predictors such as NEHRP site class, amplification of PGA and PGV, and resonant frequencies and amplifications, indicating the level of confidence that is justified in these predictors.

3 EFFECTS OF 3D GEORGIA BASIN STRUCTURE ON LONG-PERIOD GROUND MOTION

3.1 Introduction

Earthquake waves are altered by three-dimensional (3D) basin structure by the generation of long-period surface waves from the conversion of incident shear waves at the basin edge and/or walls (e.g. Bard & Bouchon 1980), and by the trapping/focussing of shear waves at the basin edge (e.g. Graves et al. 1998). As an example, long-period (~2 s) earthquake ground motion in the soft clay basin of Mexico City during the 1985 M_S 8.1 Michoacán earthquake, more than 300 km distant, was ~14 times higher (Singh et al. 1988) and lasted nearly three times longer than on firm ground nearby (Roullé & Chávez-García 2006). Large amplification in sedimentary basins may also result from constructive interference of upward propagating shear waves and laterally propagating surfaces waves from the basin edges, known as the basin-edge effect. For example, the narrow 30-km long damage pattern in Kobe, Japan, is offset ~1 km from the fault plane of the 1995 M_W 6.9 earthquake and is attributed to the basin-edge effect (Kawase et al. 1996, Pitarka et al. 1997).

Finite-difference 3D modelling of sedimentary basins worldwide has generally shown the largest ground motions are predicted to occur near the source, above the deepest part of the basin, and near its steepest-dipping edges (e.g. Frankel & Vidale 1992; Frankel 1993; Olsen et al. 1995; Olsen & Archuleta 1996). Amplification may also occur immediately behind convex basin edges or bottoms as a focussing effect (Olsen 2000a; Olsen & Schuster 1994). Simulations of 1D and 2D ground motion generally underpredict duration of generated surface waves as out-of-plane wave propagation and 3D mode conversions are not accounted for (Olsen 2000a). Realistic prediction of ground motion in sedimentary basins subject to the threat of future large earthquakes therefore requires 3D modelling (Olsen & Archuleta 1996).

In deep sedimentary basins, the effects of surface waves need to be taken into account in the design of long-period structures and smaller structures undergoing large nonlinear deformations (Joyner 2000; Day et al. 2008). In the Los Angeles (LA) basin, for example, late-arriving surface waves ≥ 3 s dominate strong-motion earthquake

recordings, and their decay rate is less than for shear waves; hence, general ground-motion prediction equations (GMPEs) underestimate amplitude in the basin by as much as a factor of 3 (Joyner 2000). Even at long periods, the chosen site amplification predictor variable of GMPEs is the V_{S30} term (as discussed in Sections 2.1 and 2.9.1). Day et al. (2008) simulated ground motions of 60 scenario earthquakes in the LA basin to complement the empirical strong-motion dataset for development of the Next Generation of ground-motion Attenuation (NGA) relations (Next). The depths to V_S of 1.0, 1.5, and 2.5 km/s ($Z_{1.0}$, $Z_{1.5}$, and $Z_{2.5}$, respectively) are proposed as suitable predictors of long-period motion in basins by Day et al. (2008), with preference for $Z_{1.5}$. In the NGA relations of Chiou & Youngs (2008) and Campbell & Bozorgnia (2008), $Z_{1.0}$ and $Z_{2.5} > 3$ km terms have been added to the V_{S30}-based site predictor term to better approximate long-period motion. Generation of the 2008 US national seismic hazard maps use these attenuation relations for crustal earthquakes in the Pacific Northwest (Petersen et al. 2008). In Canada, future seismic hazard maps will be generated using these NGA relations for shallow crustal earthquakes in British Columbia (Atkinson & Goda 2011). Ultimately, 3D basin effect simulations should be directly incorporated in the generation of probabilistic seismic hazard maps, as was carried out for Seattle, Washington by Frankel et al. (2007).

The area of highest seismic risk in Canada is metropolitan Greater Vancouver, where over 2 million people and critical infrastructure are exposed to seismicity related to the Cascadia subduction zone (Onur et al. 2005). Greater Vancouver is underlain by the Georgia basin, a Late-Cretaceous sedimentary basin; surficial Holocene sediments of the Fraser River delta in southern Greater Vancouver (as discussed in Section 2.2) compose the upper-most sediments of the basin. Amplification of earthquake ground motion here from inevitable future large earthquakes is not only dependent on the 1D soil column (as examined in Chapter 2) and non-linear response of the sediments, but is also dependent on the 3D structure of the Georgia basin. Realistic estimates of earthquake ground motion must account for all of these components. Previous numerical modelling of earthquake response on the Fraser delta has concentrated on the effect of the 1D soil layering, confirming amplification due to the thick accumulations of Holocene deltaic and/or Pleistocene glacial sequences (Onur et al. 2004; Finn et al. 2003; Harris et al. 1998).

The goal of this chapter is to use 3D finite-difference numerical modelling to compute long-period (> 2 s) ground motions in the Georgia basin region of British Columbia for scenario earthquakes to quantify effects due to 3D basin structure. The Pacific Northwest 3D velocity model of Stephenson (2007) is the base elastic structure model. It is modified here by updating velocities in the upper 1 km for the Georgia basin region (Section 3.2.1.1), and is used to generate a 3D non-basin velocity model. Two sets of viscoelastic 3D basin models are produced by assigning different degrees of anelastic attenuation to the lowest velocity sediments. Simulated long-period ground motions are then calibrated by comparison with empirical earthquake recordings of the 2001 M_W 6.8 Nisqually, WA, earthquake (Section 3.4.2.1). Realistic scenarios of large (M_W 6.8) Cascadia-specific earthquakes are considered here, including JdF plate earthquakes at 40-55 km depth (Section 3.4) and NA plate earthquakes at 5 km depth (Section 3.5) that rupture according to the Nisqually earthquake and 1994 M_W 6.7 Northridge earthquake, respectively, in locations congruent with known seismicity. Amplification due to 3D basin structure is then evaluated as the ratio of peak horizontal motion from simulations of the same scenario earthquake in 3D basin and non-basin structure models, as performed for the LA basin by Olsen (2000b). Limitations of this work include uncertainty in accuracy of physical-structure and source-rupture models, omission of low velocity material (e.g. water and up to 300 m of Holocene sediments) and surface topography in the 3D structure models, inability to resolve frequencies > 0.5 Hz, and the low number of scenarios. Hence, the work presented in this chapter represents an important first step towards quantifying the effect of the 3D sedimentary Georgia basin structure on earthquake ground motion in SW British Columbia.

3.2 Geology and structure of the Georgia basin

The Georgia basin is underlain by west-vergent thrust sheets (Monger 1990) of three basement rocks; Devonian to Jurassic volcanic arc assemblage rocks of Wrangellia to the W, Middle Jurassic and Early Cretaceous plutonic granitic rocks of the Coast Mountains to the NE, and Devonian to Cretaceous volcanic and meta-sedimentary rocks of the Cascades Mountains to the SE, as shown in Figure 2 and Figure 26 (Gordy 1988, Monger 1990, Monger & Journey 1994). The Georgia basin is either a foreland basin, formed by

Late-Cretaceous W-SW thrusting of eastern basement rocks (Mustard 1994) in response to underplating of an oceanic plate beneath the NA plate (Mustard & Rouse 1994), or a subduction-related forearc basin situated atop of a continental fragment (Wrangellia) between the arc-trench gap (England and Bustin 1998). Initial westward basin-wide deposition of eroded eastern basement rocks occurred in an alluvial and coastal marine setting (Mustard 1994) producing Late-Cretaceous Nanaimo group rocks (Figure 26), exposed in the NE Comox and Nanaimo sub-basins. Deposition continued during the Paleocene-Eocene in a terrestrial lower alluvial fan to fluvial environment, predominantly in the SE of the basin in response to dextral strike-slip faults (Mustard & Rouse 1994; England & Bustin 1998), producing Tertiary Huntingdon (Mustard & Rouse 1994) and Chuckanut (Johnson 1984) formation rocks in the Whatcom and Chuckanut sub-basins, respectively (Figure 26). During the Late Eocene, westward accretion of Pacific Rim and Crescent Terranes caused 20-30% shortening and deformation of the basin into a NW-trending fold and thrust belt (England and Calon 1991, CFTB in Figure 26). In the Neogene, significant erosion of Nanaimo group rocks along the eastern margin occurred due to rapid uplift and along the western margin due to eastward tilting and uplift of Vancouver Island (Mustard 1994; England & Bustin 1998). The resulting depression between Vancouver Island and the Coast Mountains preserved the basin (Monger 1990) and caused localized deposition of fluvial sediments beneath Greater Vancouver, i.e. the Miocene-Pliocene Boundary Bay formation in Figure 26 (Mustard & Rouse 1994). Pleistocene glacial and inter-glacial sediments and Holocene fluvial-deltaic deposits of the Fraser River comprise the upper-most sedimentary sequence of the present Georgia basin, as discussed previously in Section 2.2. Beneath Greater Vancouver (Figure 2), the Whatcom sub-basin is comprised of ~2.5 km of Tertiary Huntindon formation rocks, overlain by ~1.2 km of Neogene Boundary Bay formation rocks (Mustard & Rouse 1994) and up to ~1 km of Quaternary deposits of the Fraser River (Clague et al. 1998; Hunter et al. 1998). Tertiary Chuckanut formation rocks are ~6 km thick in the SE Georgia basin (Mustard & Rouse 1994; Johnson 1984).

The present extent of the Tertiary Georgia basin (Figure 26) is predominantly bounded by the Gabriola Island fault to the N, the Outer Island fault to the W (Dash et al. 2007; Ramachandran et al. 2004), and the San Juan Island thrust fault complex to the S

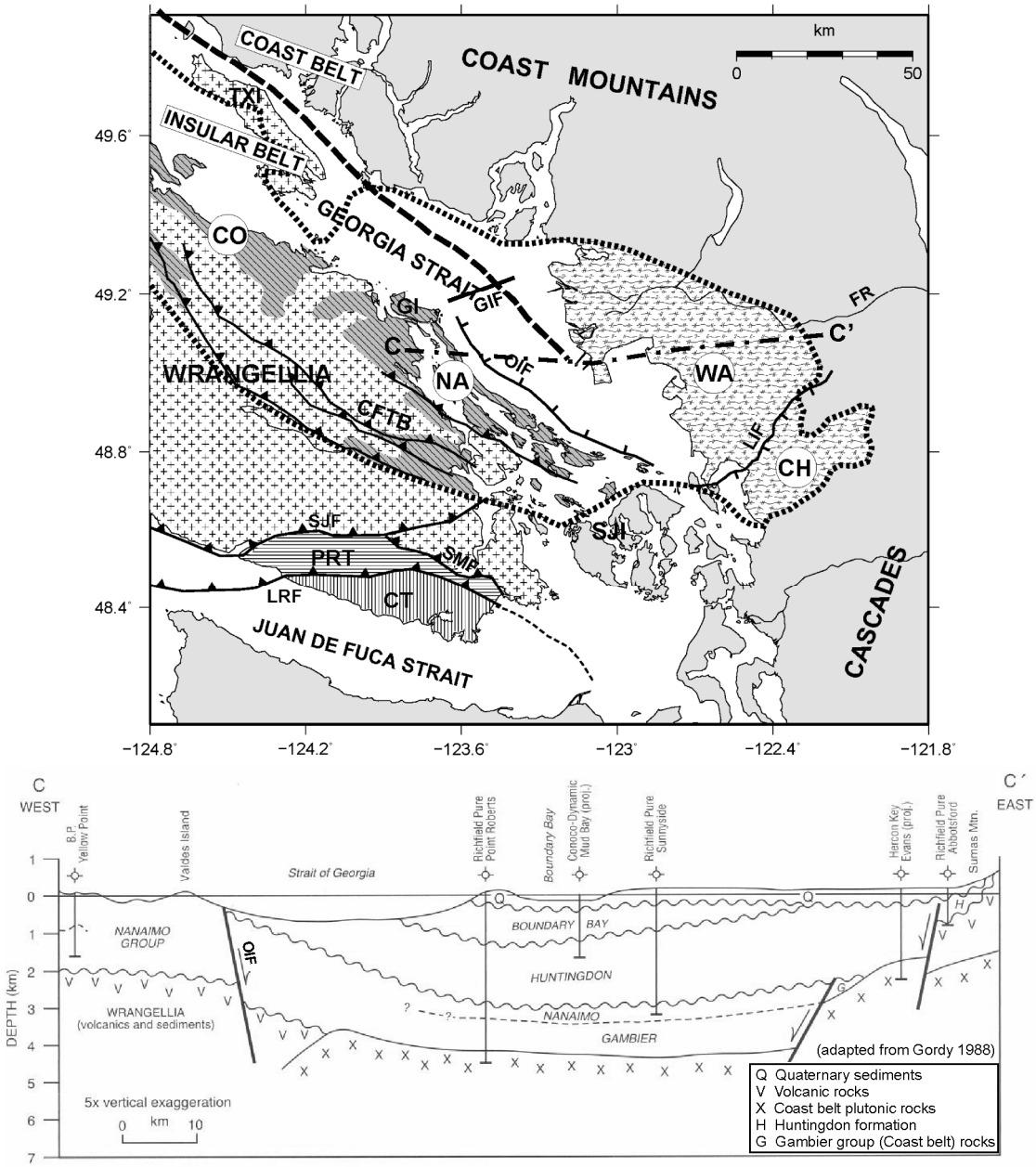

Figure 26. Regional geology and major tectonic structures of the Georgia basin region. The basin is outlined by a heavy dotted line. Late-Cretaceous Nanaimo group rocks are exposed on eastern Vancouver Island. Tertiary and Quaternary sediments are exposed in the SE part of the basin. Abbreviated names of sub-basins are: Comox, CO; Nanaimo, NA; Whatcom, WA; and Chuckanut, CH. Abbreviated names of faults are: Outer Island, OIF; Gabriola Island, GIF; and Cowichan fold and thrust belt, CFTB (modified from Dash et al. 2007). Geological cross-section based on labelled oil wells corresponds to the dot-dash line C-C' in the map above (modified from Hannigan et al. 2001).

(Monger 1990; Mustard 1994). The basin overlaps the Coast and Cascade basement rocks to the E (Monger 1990). The Gabriola Island fault is coincident with a zone of shallow recurrent seismicity (Cassidy et al. 2000) and is the basis for the shallow NA plate earthquakes simulated in Section 3.5. In regional tomographic V_P models, Wrangellia rocks at < 2 km depth correspond to ~5.5-6.0 km/s (Ramachandran et al. 2004), thus the basement top (or basin depth) is represented by the 6 km/s contour in regional velocity models (White and Clowes 1984, Zelt et al. 2001; Ramachandran et al. 2004) or conservatively by the 5.5 km/s contour (Dash et al. 2007). Higher velocities are consistently determined in the NW portion of the basin than the SE, i.e. Late-Cretaceous Nanaimo group rocks are associated with V_P of 4.5-6.0 km/s and Tertiary formation rocks are constrained to V_P of 3.0-4.5 km/s (White and Clowes 1984; Zelt et al. 2001; Ramachandran et al. 2004; Dash et al. 2007). Overall, the basin is observed to deepen from 2-4 km in the NE to 8-9 km in the SW based on a 6 km/s V_P base (Ramachandran et al. 2004). The approximate dimensions of the Tertiary Georgia basin are considered here to be 130 by 70 by 5 km.

3.2.1 Physical structure models

The base elastic 3D model is a clipping of the Stephenson (2007) Pacific Northwest 3D velocity model, spanning from northwest WA to southern British Columbia, with dimensions of 337.5 km NS by 200 km EW by 60 km Up-Down and a spatial uniform-grid resolution of 250 m. The model was graciously provided by Dr. Kim Olsen (San Diego State University). The 3D elastic model is described fully in Stephenson (2007) and only a brief description is given here. The physical model is represented by six geologic units (continental basin sediments, crust and mantle, and oceanic sediments, crust, and mantle) characterized by V_P, V_S, and density. The most important parameters are V_S and Q_S, which govern shear and surface wave arrivals associated with the strongest ground motions (Brocher 2007). The thickness of the oceanic crust was set to 5 km. The 3D sedimentary basin structure in the Georgia basin region is primarily constrained by the tomographic V_P model (1 km grid) of Ramachandran et al. (2004; 2006). The V_P/V_S ratio for Quaternary basin sediments varies from 2.5 at the surface to 2.2 at 1 km depth. Tertiary sediments are set to a V_P/V_S ratio of 2, and their base is taken as the 4.5 km/s isovelocity contour (Ramachandran et al. 2006). Densities are derived from the V_P model

using the Nafe-Drake relation (Ludwig et al. 1970). Surface topography is not included. The minimum V_S is set to 625 m/s for computational feasibility. In southern Greater Vancouver, up to 300 m of Holocene deltaic sediments of the Fraser River (Section 2.2) are not included. The surface of the 3D basin model therefore represents over-consolidated Pleistocene glacial sediments or stiff soil sites (considered as the base of the 1D soil column in Section 2.9.2). This is a significant limitation to modelling of the potential earthquake ground motion here and the overall amplitude and duration of simulated ground motions in the Georgia basin are likely underestimated.

3.2.1.1 Updated structure models

In the Georgia basin region, V_P in the upper 1 km of the 3D basin model (Stephenson 2007) is lower in the NW portion of the basin than towards the SE for the same depth, resulting in a NE-SW trending velocity contrast that runs beneath Greater Vancouver. This velocity contrast is not supported in the upper 1 km structure by geological and structural information (Section 3.2), and likely results from extrapolation of the 1-km gridded V_P model of Ramchandran et al. (2006) to the surface. Simulations using the original 3D basin model show long-period ground motions mimic the 500-m isovelocity structure (Molnar et al. 2009). Good agreement between simulated and empirical M_W 6.8 Nisqually waveforms were obtained for the Seattle basin region (Molnar et al. 2010b) since significant effort had gone into validating the 3D model there (Frankel & Stephenson 2000; Hartzell et al. 2002; Pitarka et al. 2004; Frankel et al. 2007; 2009), whereas synthetic waveforms significantly over-predicted empirical waveform amplitudes in Georgia basin by a factor of 3.3 (Molnar et al. 2010b). Development of a 3D density model (Lowe et al. 2003) of the region based on the V_P model of Zelt et al. (2001) identified four regions with thick accumulations of unconsolidated Pleistocene and younger sediments not resolved in the velocity model but known from high-resolution shallow seismic data (Hamilton 1991; Mosher & Hamilton 1998). Low-density sediments not resolved in the velocity model important to the thesis work here occur in central Georgia Strait to the W of Bowen Island (Figure 27) where the thickest section of pre Late Wisconsinan sediments occur in the area overlain by up to 100 m of younger sediments, and between Galiano Island and Point Roberts Peninsula (Figure 27) where ~500 m of unconsolidated sediments are imaged at the extreme south of the seismic

survey area (Lowe et al. 2003). This latter discrepancy persists S of the seismic survey area suggesting that a trough of unconsolidated Pleistocene and Holocene sediments may extend southwards into southernmost Georgia Strait (Lowe et al. 2003). Therefore, velocity structure information was collected and assembled to update the upper 1 km of the 3D model in the Georgia Basin region for the modelling work in this thesis.

Resources for geologic and geophysical (V_P) information included: the surficial geology map of the Geological Survey of Canada (GSC); the 800-m depth surface of the 600-m gridded tomographic V_P model of Dash et al. (2007); GSC marine seismic survey data (Hamilton 1991; Hamilton & Mosher 1998; D. Mosher, personal supplication); oil well logs and reports (Hannigan et al. 2001; Hurst 1991; MEMPR reports); provincial government non-confidential geological and geophysical reports (MEMPR reports); interpreted geological cross-sections of Gordy (1988); and interpreted V_S profiles at borehole, seismic cone penetration test, and surface refraction and seismic reflection sites on the Fraser River delta (J. Hunter, personal supplication [raw datasets published in Hunter et al. 1998]). Using ArcMap software, a layer of V_P estimates from all datasets was generated for each of the four depth layers between the surface and 1 km depth (e.g. velocity estimates for the 250-500 m layer are shown in Figure 27). The V_P data of each layer were interpolated to 250-m raster datasets, merged with the base elastic 3D model, and minimally smoothed over the updated region. Assembly of the updated 0-250 m, 250-500 m (Figure 27), 500-750 m, and 750-1000 m depth layers of the V_P model was accomplished using Paraview software by Dr. John He at Natural Resources Canada (Pacific). Overall, the predominant NE-SW velocity contrast in the upper 1-km beneath Greater Vancouver is removed.

The base of the Tertiary basin sediments for the Seattle basin was taken as the 4.5 km/s isovelocity contour for which V_P/V_S was set to 2 (Section 3.2.1). In contrast, the base of the Georgia basin is composed of Late-Cretaceous Nanaimo Group rocks, inferred as the 5.5-6.0 km/s isovelocity surface in regional tomographic V_P models (Zelt et al. 2001; Ramachandran et al. 2004; 2006; Dash et al. 2007). Hence, the V_P/V_S ratio is set to 2 for $V_P \leq 5.5$ km/s in the updated 3D basin model, which effectively causes low V_S values to extend to greater depths in the updated model. Otherwise, relationships of V_P with V_S remain unchanged. Densities are derived from the V_P model using the Nafe-

Drake relation (Ludwig et al. 1970) and are in agreement with the 3D Georgia basin density model of Lowe et al. (2003).

A non-basin model is generated from the updated basin model by setting the minimum V_P to 5.5 km/s, effectively removing basin sediments. Figure 28 and Figure 29 compare the updated basin and non-basin models in the upper 7 km. The maximum depth in the SE extent of the Georgia basin is 6.5 km; hence, the basin and non-basin models are identical at 7 km depth (Figure 29). Simulations using the non-basin model represent shaking due to source characteristics and background regional structure. For the same earthquake scenario, comparison and ratio calculation of peak motions predicted using the basin and non-basin models provide a quantitative measure of 3D Georgia basin effects. Thus, synthetic waveforms predicted from simulations using the basin and non-basin models are referred to throughout the thesis as basin and non-basin waveforms. The advantage of calculating basin/non-basin ratios of peak motion noted by Olsen (2000b) is the removal of geometrical spreading effects included in the basin response and the non-basin reference value for a given site, with the disadvantage that artifacts occur in maps of basin/non-basin peak motion due to singularities in the rupture pattern.

The duration of shaking is strongly dependent on anelastic attenuation of the model (Olsen et al. 1995). Two contrasting sets of frequency-independent Q_S-V_S relations are assigned to the updated 3D elastic basin model and listed in Table 6. Ground motions simulated using both high and low viscoelastic models are compared with empirical M_W 6.8 Nisqually earthquake recordings for calibration (Section 3.4.2.1). The high viscoelastic model uses Q_S relations of Olsen (2003) for sediments of the LA basin (V_P generally $\leq$ 4 km/s), and the low viscoelastic model uses Q_S relations of Frankel et al. (2009) for sediments of the Seattle basin ($V_P \leq 4.5$ km/s). The empirical Q_S relations of Brocher (2008) are encompassed by the two end-member viscoelastic models used here. The Georgia basin is composed of relatively stiff sediments with $V_P \leq 5.5$ km/s (Section 3.2), most similar to sediments in the Seattle basin. Frankel et al. (2009) found that varying Q_S had relatively little effect to the simulated ground motion amplitude: ~5% difference in 1-Hz amplitudes when Q_S is nearly halved (85 to 48 for V_S of 600 m/s). The minimum V_S of 625 m/s used here results in Q_S of 88 and 12.5 for the low and high viscoelastic models, respectively. Little amplitude difference is observed in the simulated

long-period ground motions for the M_W 6.8 Nisqually earthquake between the two sets of viscoelastic 3D models (see Figure 33 and Figure 34). The low viscoelastic 3D model (Q_S relations of Frankel et al. 2009) is used for simulation of Georgia basin JdF plate events (Section 3.4.3) and the NA plate event (Section 3.5), which generates slightly higher long-period ground motions than the high viscoelastic 3D model, but is considered to be more geologically reasonable.

Table 6. Two sets of the 3D viscoelastic structure model.

Low Q_S model (high attenuation)	**High Q_S model (low attenuation)**
Q_S=0.02V_S, V_S < 1 km/s Q_S =0.15V_S, V_S > 1 km/s Q_P=2Q_S	Q_S =0.1643V_S -14, V_S < 1 km/s Q_S =0.15V_S, V_S > 1 km/s Q_P=2Q_S

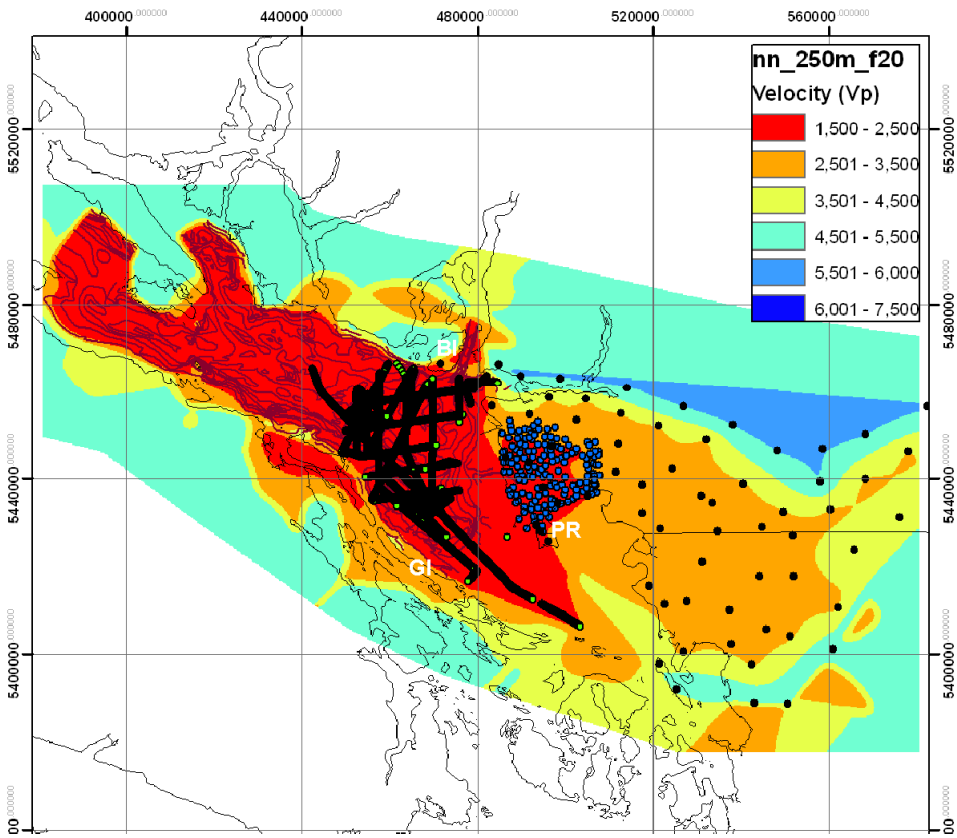

Figure 27. Smoothed V_P surface based on V_P estimates from marine seismic survey data in Georgia strait (blue lines and green circles), geotechnical V_S profiling methods on the Fraser River delta (blue circles), and interpreted geological data (purple circles). Coastline is shown by thin black line, and Bowen Island (BI), Galiano Island (GI) and Point Roberts (PR) Peninsula are labelled.

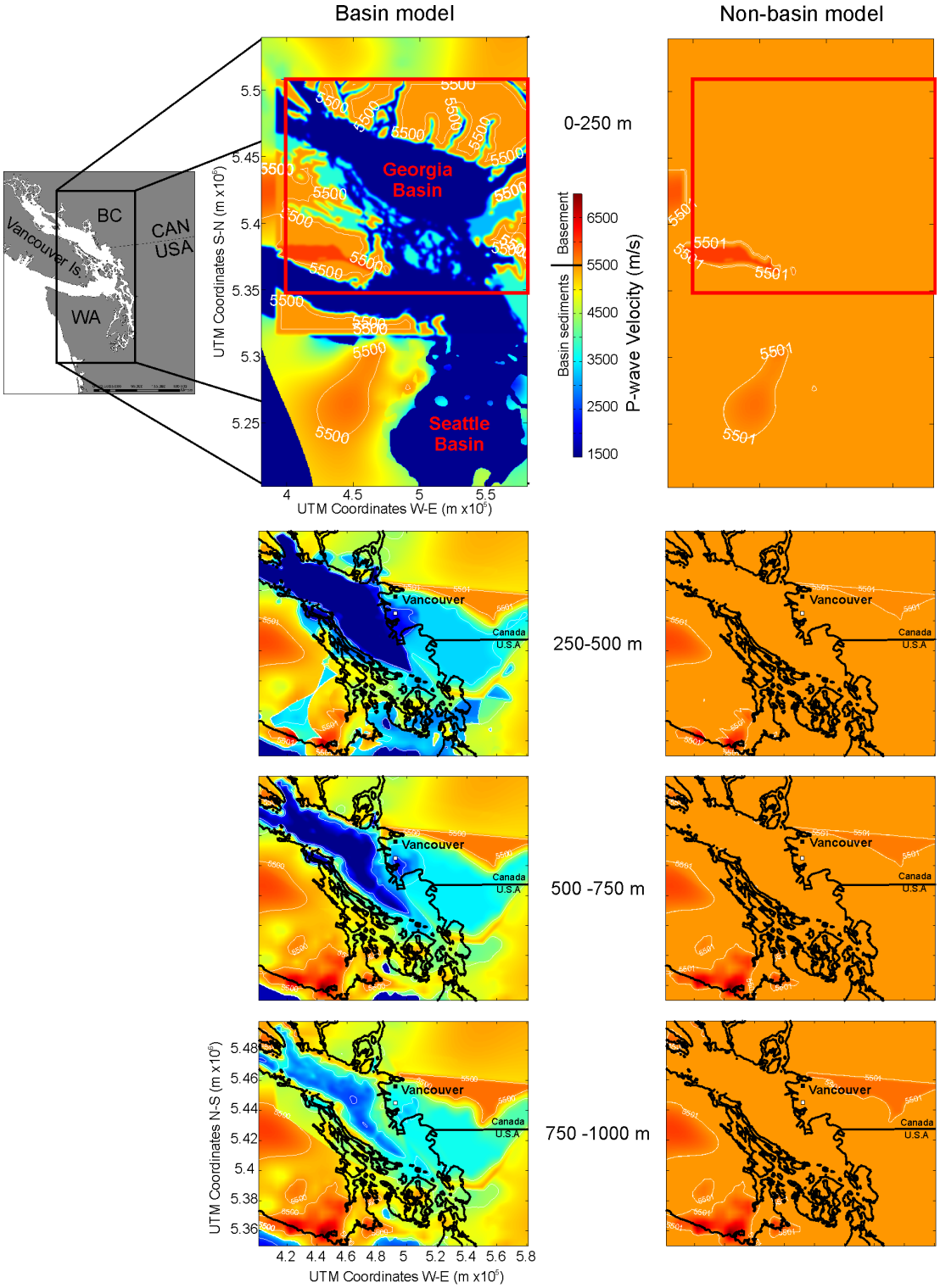

Figure 28. Depth slices of updated basin and non-basin V_P models from surface to 1 km (white lines are contours ≤ 5.5 km/s in 1 km/s intervals). For Georgia basin region models, black line is coastline, and squares correspond to locations of Vancouver (black) and Richmond (white).

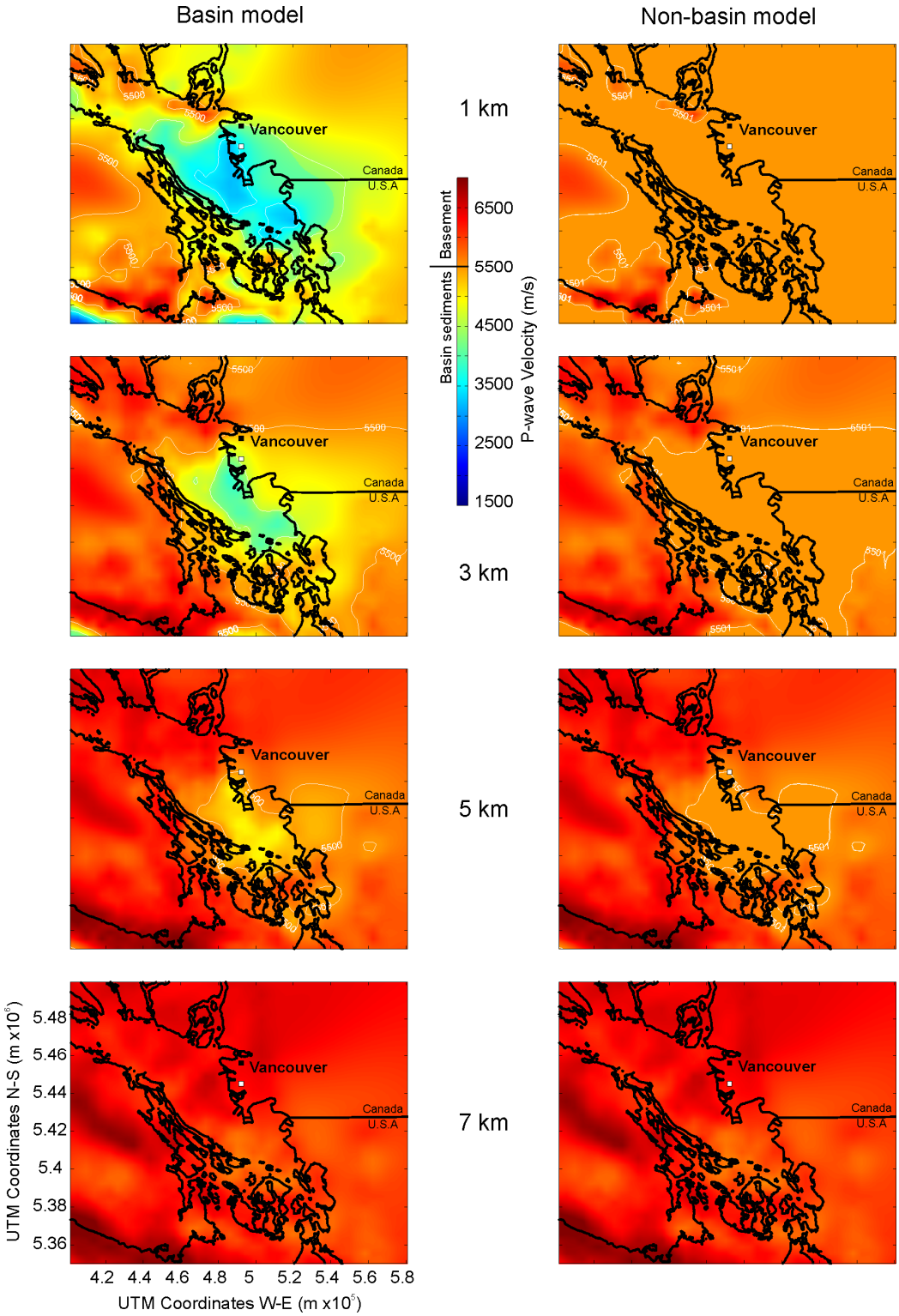

Figure 29. Depth slices of basin and non-basin V_P models for the Georgia basin region (white lines are contours ≤ 5.5 km/s in 1 km/s intervals). Black line is coastline and squares correspond to locations of Vancouver (black) and Richmond (white).

3.3 Finite-difference methodology

Finite-difference schemes are commonly applied to model 3D seismic wave propagation to investigate basin effects. The 3D elastic equations of motion are solved here using the scheme of Kim Olsen (1994) with fourth-order accuracy in space and second-order accuracy in time. The physical model is represented by a uniform cubic mesh discretized with a spacing equivalent to 5 nodes per minimum shear wavelength (e.g. Levander 1988; Moczo et al. 2000), which limits the maximum resolvable frequency. In this work, the uniform grid size of the physical model is 250 m with a minimum shear-wave velocity of 625 m/s (Section 3.2), such that the maximum resolvable frequency is 0.5 Hz (2 s period). Day et al. (2008) note that synthetic time histories become spectrally deficient above the resolvable-frequency limit, which has the effect of biasing ground motion estimates near this cut-off frequency.

Following Graves (1996), the properties of each unit cell consist of wavefield variables (three velocity components and six stress components) and media (Lamé) parameters defined at specific nodes of the cell, with cell lengths defined as half the distance between the centres of two adjacent cells. Velocity components are used as a substitute for time-differentiated displacements in order to formulate the solution in terms of first-order differential equations. The system is staggered in space and time so that the velocities are updated independently from the stresses (requiring less computational memory and increasing efficiency). Viscoelasticity is incorporated using a coarse-grained stress relaxation memory variable at each stress node point to approximate anelastic losses independently for both P- and S-waves specified as Q_P and Q_S (Day 1998; Day & Bradley 2001). Reflections from the sides and bottom of the model are minimized using either: (1) absorbing boundary conditions (Clayton & Engquist 1977), and a zone of highly attenuative material (Cerjan et al. 1985), or (2) a perfectly-matched absorbing layer (PML) with strong damping applied to orthogonal-component reflections (Collino & Tsogka 2001). Shallow earthquake scenarios are conducted here using the first set of boundary conditions, which are more stable but less efficient, whereas deep earthquake scenarios are conducted using PML conditions for efficiency. All simulations are conducted using a 5-km (20 cell) boundary zone applied to the model sides and bottom.

The seismic source is a composition of the moment tensor contribution (body force couples characterized by strike, dip, rake, and moment), and a kinematic slip-rate (velocity) function of specified duration (rise time) initiated within the 3D model space. The seismic source is implemented in the finite-difference grid by adding $-M_{ij}(t)/V$ to $S_{ij}(t)$ where $M_{ij}(t)$ is the ijth component of the moment tensor for the earthquake, $V = dx^3$ is the cell volume, and $S_{ij}(t)$ is the ijth component of the stress tensor on the fault at time t (Olsen 2000b).

The finite-difference scheme was graciously provided by Dr. Kim Olsen (San Diego State University). Dr. John He at Natural Resources Canada (Pacific) compiled the code on the Minerva IBM Nighthawk-2 SP supercomputer at the University of Victoria, which runs up to 64 375-MHz RS-2000 processors communicating via parallel input-output message-passing interface. The wall clock time for each simulation is dependent on the size of the physical model; 120 s simulations of the deep and distant M_W 6.8 Nisqually earthquake took ~72 hours (Section 3.4.2.1), while 70-90 s simulations of each deep JdF plate event (Section 3.4.3) and shallow NA plate events (Section 3.5) took approximately 7 and 3 hours, respectively.

3.4 Earthquake scenario 1: Deep Juan de Fuca plate earthquakes

To investigate deep JdF plate earthquake scenarios, large (M_W 6.8) normal-faulting earthquakes are simulated at 42-55 km depth at 11 locations in the Georgia basin region. Simulation of the 2001 M_W 6.8 Nisqually earthquake (55 km depth) is performed to calibrate synthetic results with empirical earthquake recordings.

3.4.1 Seismicity

The most frequent earthquakes in Greater Vancouver are JdF plate events (Halchuk & Adams 2004). Figure 30 shows subducting JdF plate earthquakes are concentrated in Puget Sound or along the Strait of Georgia coincident with the bend in the coastline (Bolton 2003; Rogers 1998). Events that occur beneath the W coast of Vancouver Island are not of concern to this study. The JdF plate is dipping at a maximum of 30º beneath Georgia Strait/Puget Sound such that the majority of events occur at 45-65 km depth and few extend to 80 km (Bolton 2003). The larger magnitude JdF plate events tend to exhibit normal faulting (Ristau et al. 2007), consistent with down-dip tension from first-motion

analyses (Bolton 2003). The largest JdF plate earthquakes occurred in 1949 (M_W 7.1), 1965 (M_W 6.5) and 2001 (M_W 6.8) beneath southern Puget Sound. Moderate sized events occurred beneath Georgia strait in 1909 (M ~6), 1920 (M ~5.5), and 1976 (M_W 5.3). The activity rate of M 5 JdF plate events/year is 0.0932 (1 every ~10 years) and the best-estimate maximum magnitude is 7.1 (Adams & Halchuk 2003).

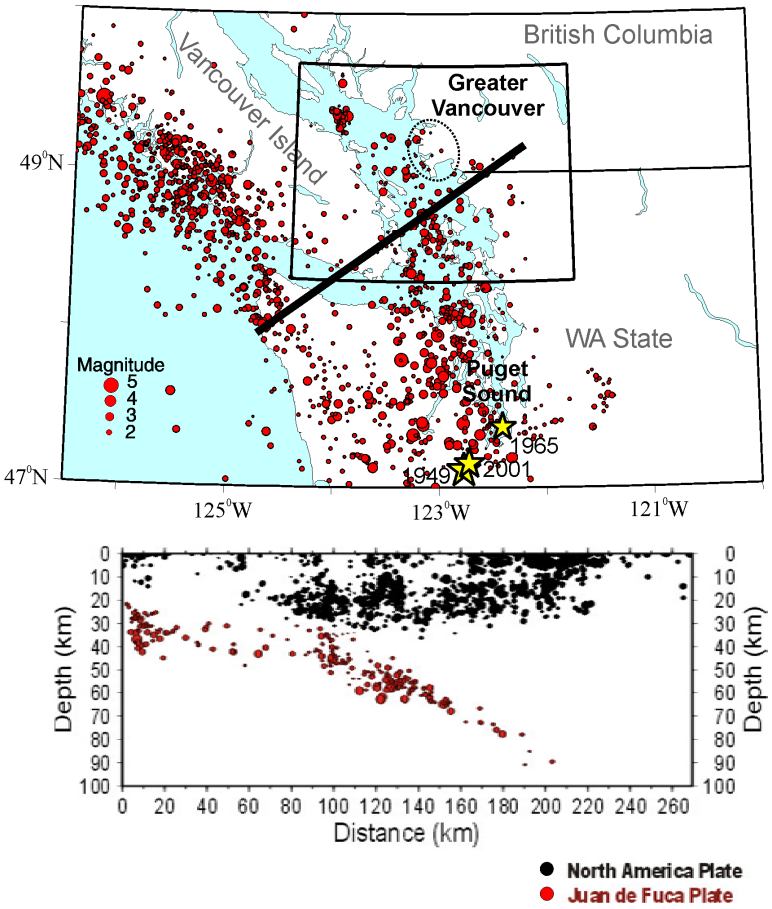

Figure 30. Map of JdF plate seismicity (1985-1999) in the Georgia basin region (black box corresponds to model limits). Significant earthquakes (M > 6) represented by yellow stars and labelled by year. Thick black line denotes seismic cross-section shown in bottom panel.

3.4.2 Source model

Each JdF plate earthquake is represented by a moment-tensor-rate function initiated at a single point within the 3D model space. The most recent large magnitude JdF plate event is the 2001 M_W 6.8 Nisqually earthquake. A comprehensive study of seven moment tensor solutions of this event by Bustin et al. (2004) showed that the range in depth solutions was 49-55 km, total moment solutions was 1.4-2.0 x10^{19} Nm, and in fault plane

solutions was a strike and dip of 347-1° and 69-75° (alternate fault plane solutions had a range in strike and dip of 172-214° and 17-21°). Kao et al. (2008) applied a source-scanning algorithm to local seismic waveforms and showed unambiguously that rupture occurred along the N-striking steeply E-dipping fault plane. The imaged source process occurs in two pulses, with a slightly stronger second pulse and a total duration of ~6-7 s. Rupture characteristics of the large JdF plate events in 1949 and 1965 are also best represented by a double-pulse release of seismic moment, with duration of 12-22 s for the larger (M_W 7.1) 1949 event (Wiest et al. 2007).

Simulations of the Nisqually earthquake source have been validated with empirical waveforms for the Seattle basin region by Pitarka et al. (2004) and Frankel et al. (2007; 2009). The Nisqually earthquake source models of these two studies are based primarily on the source model of Ichinose et al. (2004). As shown in Figure 31, the Nisqually earthquake source model of Pitarka et al. (2004) is defined by two point sources separated in time by 1.5 s. The first source has a strike, dip and rake of 356°, 68° and -90° with a 4.0 s duration (rise time) and total moment of 7 x 10^{18} Nm, whereas the second source has a rake of -100°, a 4.5 s rise time, and moment of 1.1 x 10^{19} Nm. The total seismic moment is 1.8 x 10^{19} Nm, equivalent to a M_W 6.8 event. In the source model of Frankel et al. (2007), the two point sources both have durations of 4 s and are separated by 1.7 s. The frequency content of the Pitarka et al. (2004) moment-tensor-rate function is < 0.5 Hz (Figure 31c). Pitarka et al. (2004) and Frankel et al. (2007) have shown good agreement between their synthetic waveforms and empirical Nisqually recordings at Seattle basin sites, such that either source model appears valid for use. The Pitarka et al. (2004) model is used here to simulate the 2001 M_W 6.8 Nisqually earthquake as it is also used for this purpose by Frankel et al. (2009).

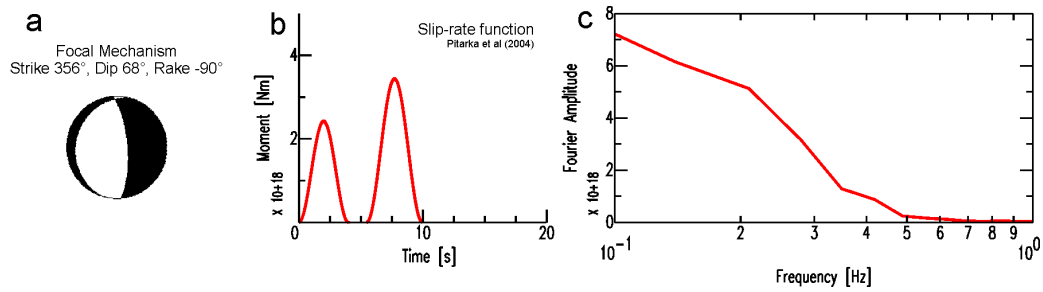

Figure 31. (a) Beach ball representation of double-couple focal mechanism of first point source (second source has 10° difference in rake). (b) Moment-tensor rate function of Pitarka et al. (2004) for *Mxx* component. (c) Amplitude spectra of moment-tensor rate function in (b).

3.4.2.1 Model calibration

The goal here is to calibrate the updated 3D basin model so that long-period ground motions can be predicted accurately in the Georgia basin region for future large earthquakes. Finite-difference simulations of the 2001 M_W 6.8 Nisqually earthquake have been conducted for the Seattle basin region by Pitarka et al. (2004) and Frankel et al. (2007; 2009). These studies compared synthetic waveforms with empirical Nisqually earthquake waveforms at selected strong-motion sites of the Pacific Northwest Seismograph Network (PNSN) and Seattle Urban Hazard Seismic Array (SUHSA) situated on stiff Pleistocene sediment and/or Tertiary rock. The results of the Nisqually earthquake simulation presented in this section are most similar to those of Frankel et al. (2009), using the same source model of Pitarka et al. (2004) and the same 3D viscoelastic basin model (Table 7). A similar set of 18 PNSN and SUHSA strong-motion stations were chosen here for comparison of synthetic and empirical waveforms.

Table 7. Details of various finite-difference simulations of the Nisqually earthquake.

	Pitarka et al. (2004)	**Frankel et al. (2007; 2009)**	**This study**
FD scheme	Pitarka (1999)	Liu & Archuleta (2002)	Olsen (1994)
Grid spacing	Regular mesh with variable spacing in vertical direction (200 m minimum)	70 m upper horizontal 210 m lower horizontal 70-500 m vertical	250 m uniform
Max. Frequency	0.5 Hz	0.5 Hz (2007; 2009) 1.0 Hz (2009)	0.5 Hz
Min. V_S	600 m/s	600 m/s	625 m/s
Model	• Elastic V_P model of Parsons (2001) • Q_S of 50 for unconsolidated sediments	• Elastic V_P model of Stephenson (2007) • high Q_S relations (i.e. Q_S of 89-141 in upper 1 km)	• Elastic V_P model of Stephenson (2007) • high Q_S (same as Frankel et al. 2009) and low Q_S relations (i.e. 13-19 in upper 1 km)
Model dimensions	61 x 82 x 62 km	~100 x ~150 x 60 km	200 x 337.5 x 60 km
Source depth	59 km	52 km (2007) 55 km (2009)	55 km

The Nisqually earthquake simulation is conducted here three times, once each for the updated basin model with low and high Q_S relations, and once for the non-basin model. The simulations encompass the Georgia basin region, N of the Seattle basin, such that the model dimensions are significantly larger than those of Pitarka et al. (2004) and

Frankel et al. (2007; 2009) (Table 7). Each 120 s simulation of the Nisqually earthquake took ~ 72 wall clock hours.

Figure 32 shows simulated PGV maps for the Georgia and Seattle basin regions for the two horizontal directions of motion (NS and EW directions correspond to radial and transverse motion, respectively). For the Seattle basin region, high EW ground motions occur near the epicentre due to the source radiation pattern, whereas high NS motions occur in the basin, in agreement with Pitarka et al. (2004) and Frankel et al. (2009). The opposite is observed for the Georgia basin region, higher EW than NS motion occurs in this basin. Predicted ground motions in the Seattle basin region, within 75 km of the epicentre, are ≤ 5 cm/s, whereas in the Georgia basin region, over 150 km distant, peak ground motions are < 1 cm/s.

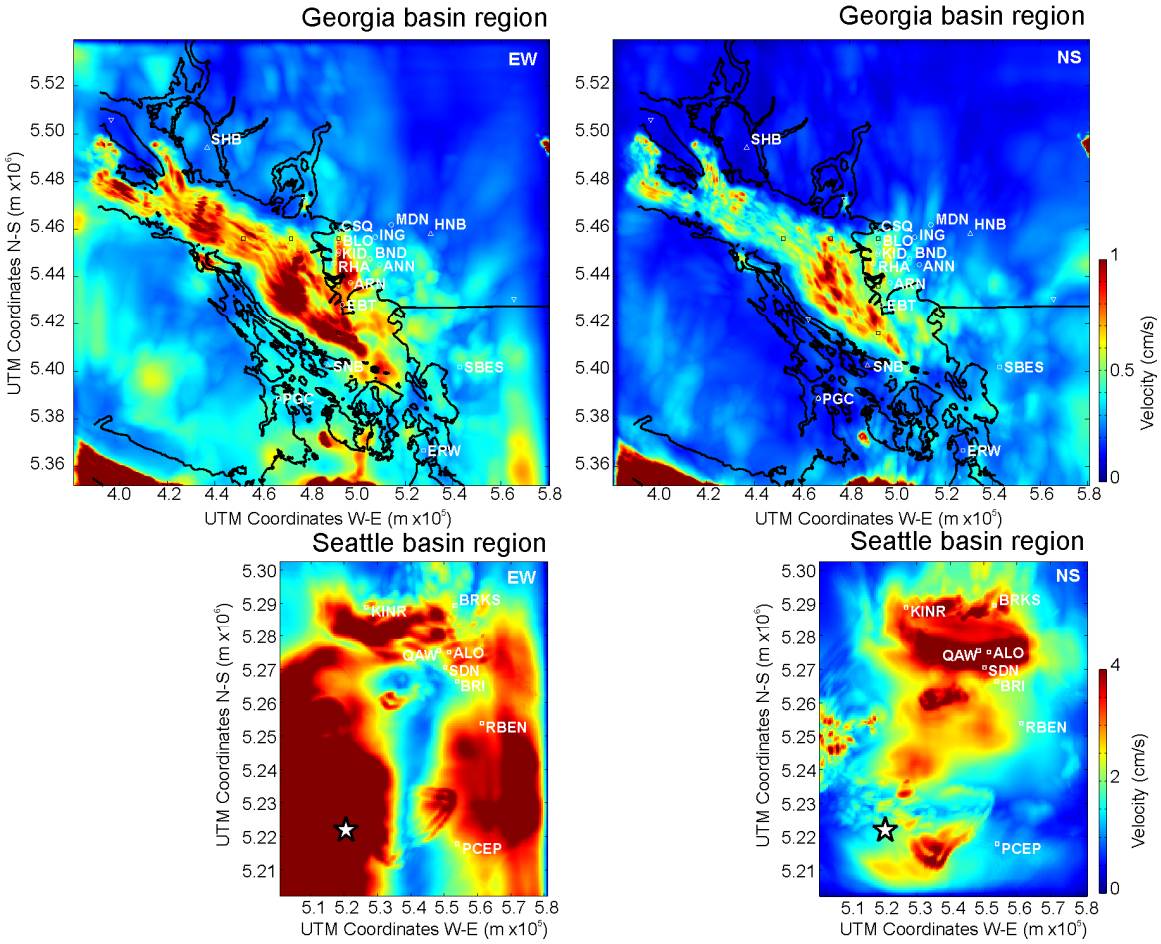

Figure 32. Predicted PGV maps of M_W 6.8 Nisqually earthquake for Georgia basin (upper panels) and Seattle basin (bottom panels) regions (note different y-axis limits for each region). Earthquake epicentre is shown by star in Seattle basin region maps. White squares denote locations of selected earthquake recording sites labelled with code names.

Figure 33 compares empirical and synthetic waveforms at the 18 selected PNSN and SUHSA strong-motion sites in the Seattle basin region (locations labelled on Figure 32). All empirical waveforms are synchronized to 10:54:26 PST (time zero), the origin time of the Nisqually earthquake is 6.78 s later at 10:54:32.78 PST and the synthetics have been shifted to 10:54:33.75 PST (i.e. synthetic S-waves arrive ~1 s later than empirical). The qualitative agreement observed between waveforms here is similar to that shown in Pitarka et al. (2004) and Frankel et al. (2007; 2009), such that their conclusions are still valid here. Frankel et al. (2007) note that "synthetics capture the basic observations that seismograms on rock and near the basin edge have relatively simple, short duration S-waves, whereas stations in the Seattle basin have more complex, longer duration waveforms, with phases following the S-waves"; hence, the deep basin structure affects long period motion. Significant long period ground motions are generated at the southern edge of the Seattle basin (large velocity contrast), in agreement with observed higher amplification for earthquakes from the south-southwest (Frankel et al. 2009), and coincident with the zone of chimney damage from the Nisqually earthquake (Stephenson et al. 2006).

For each station, two sets of synthetic waveforms are shown in Figure 33, from simulations based on low Q_S and high Q_S relations (Section 3.2.1.1). There is little amplitude difference between the two sets of synthetic waveforms. The low viscoelastic model generates slightly higher ground motions, but is considered to be more geologically reasonable. Reported PGV is based on these low viscoelastic synthetic waveforms.

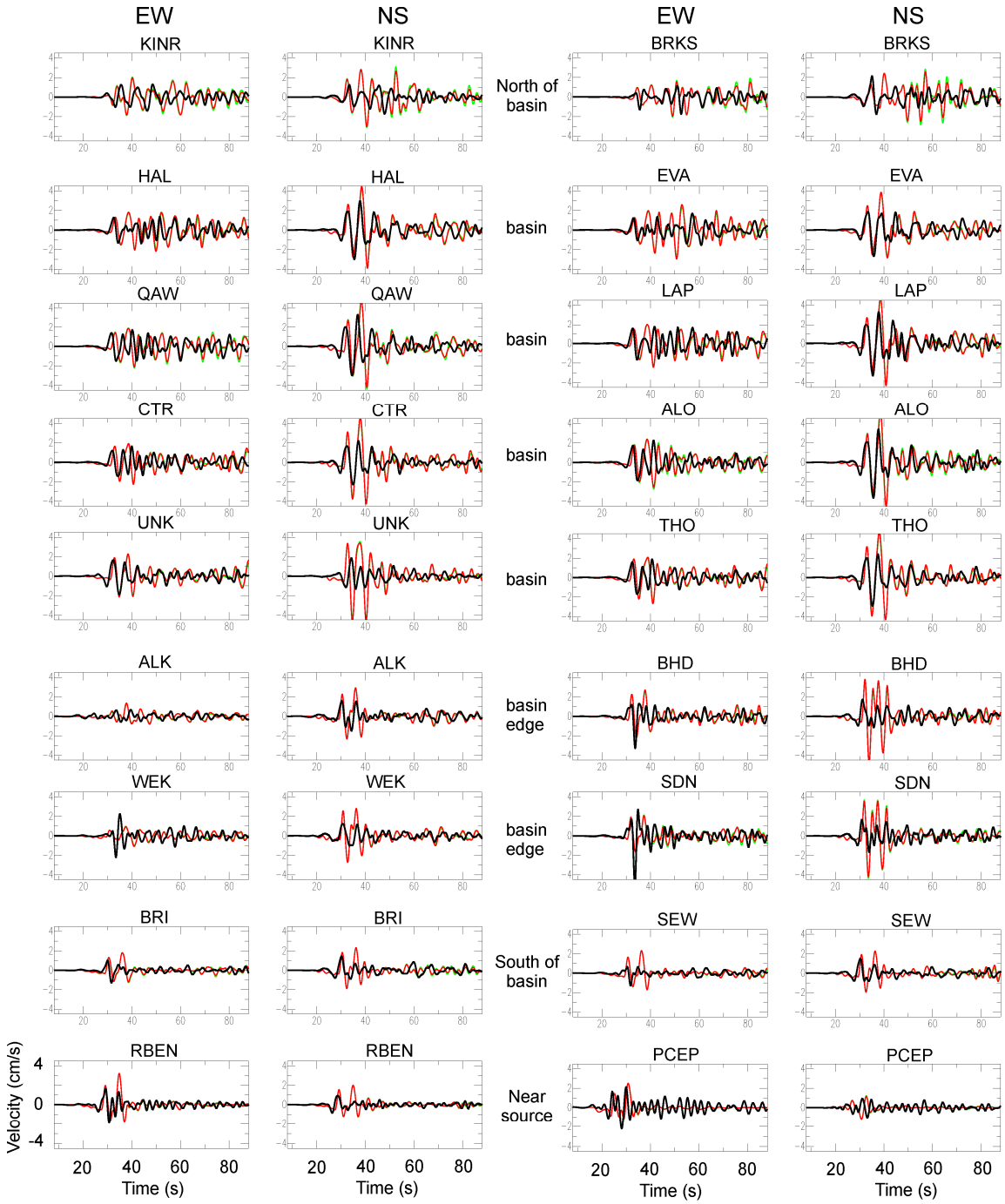

Figure 33. Comparison of empirical M_W 6.8 Nisqually earthquake recordings (black lines) and synthetic (green lines correspond to high Q_S model and red lines to low Q_S model) waveforms for 18 selected strong-motion stations in Seattle basin region.

Figure 34 presents waveform comparisons for 16 selected weak- and strong-motion sites in the Georgia basin region. Of the 16 sites, two are PNSN strong-motion stations in NE WA, four are weak-motion seismograph stations of the Canadian National

Seismograph Network (CNSN) located on rock sites surrounding the Georgia basin, and the remaining ten stations are strong-motions stations of the Geological Survey of Canada and British Columbia Hydro located in Greater Vancouver, four of which are located on the low-velocity Holocene sediments of the Fraser River delta (as labelled in Figure 32). The strong-motion stations in British Columbia (Table 8) are predominantly Kinemetrics SSA-2 instruments with trigger thresholds of 0.2% and 0.4% g for rock and soil sites, respectively. The duration of earthquake recordings at rock sites is generally < 35 s; longer duration records are obtained at the soil sites (50-97 s). These strong-motion instruments operate on batteries with internal clocks which drift over time, such that accurate timing is not obtained. Each empirical waveform is shifted based on best visual fit with the corresponding synthetic waveform, the average offset is ~55 s, similar to the time of the S-wave arrival at SNB and HNB of ~50 s and ~60 s, respectively (Figure 34).

Table 8. Ground conditions at 16 selected earthquake recording stations in Georgia basin region.

Station Code	Ground conditions
ANN	350 m to Tertiary rock (100 m Holocene, 250 m Pleistocene sediments)
ARN	750 m to Tertiary rock (250 m Holocene, 500 m Pleistocene sediments)
BLO	Tertiary rock
BND	Pleistocene sediments over Tertiary rock
CSQ	Tertiary rock
EBT	500 m of Pleistocene sediments over Tertiary rock
ERW	Cretaceous rock
HNB	Tertiary rock
ING	400 m Pleistocene sediments over Tertiary rock
KID	200 m to Tertiary rock (40 m Holocene, 160 m Pleistocene sediments)
MDN	7 m Pleistocene sediments over Tertiary rock
PGC	Bedrock (Quartz diorite)
RHA	800 m to Tertiary rock (300 m Holocene, 500 m Pleistocene sediments)
SBES	Tertiary rock
SHB	Bedrock (Coast Mountains)
SNB	Cretaceous rock

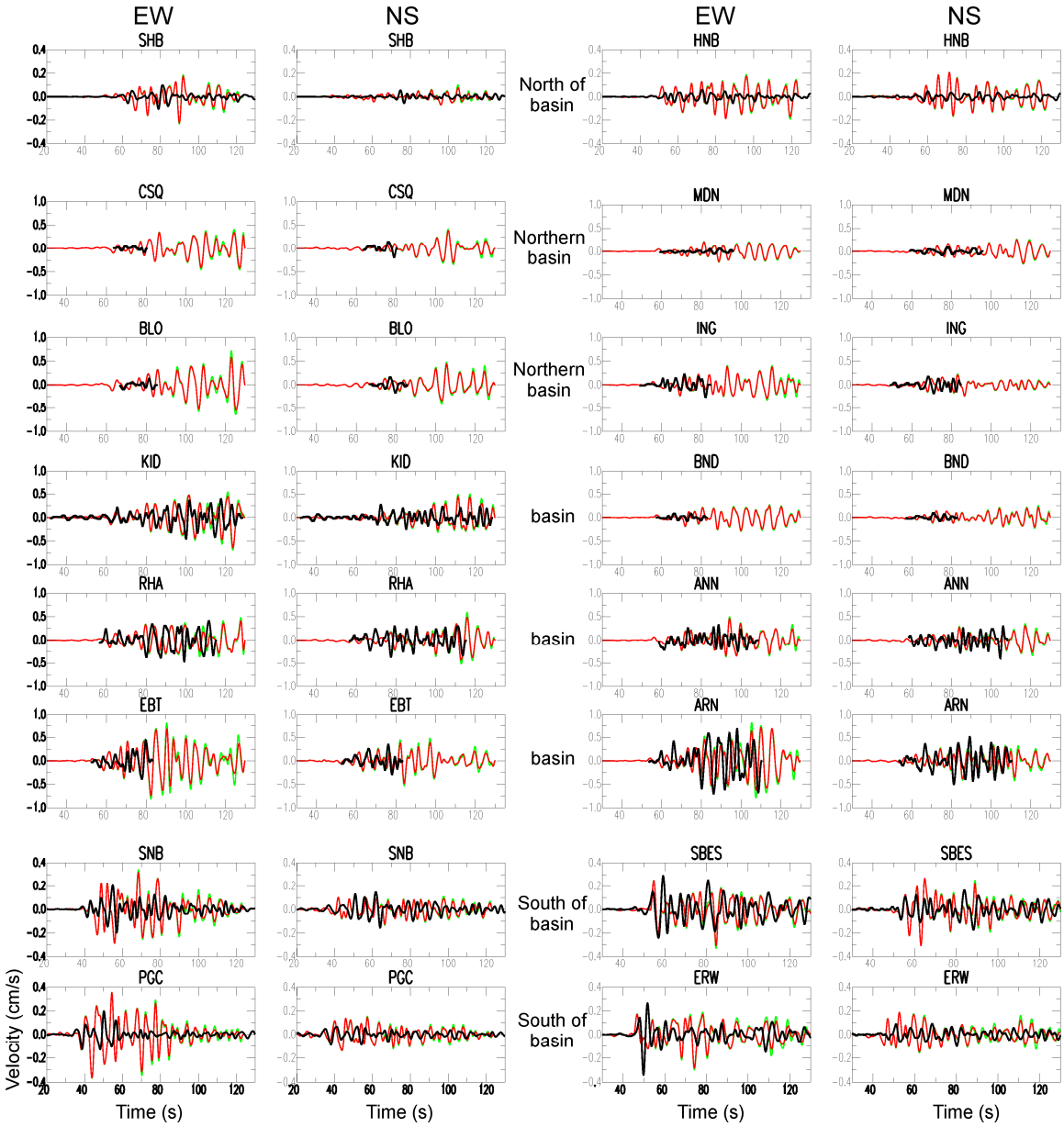

Figure 34. Comparison of empirical (black) and synthetic (green corresponds to high Q_S model and red to low Q_S model) waveforms at 16 selected weak- and strong-motion stations in Georgia basin region (note different y-axis limits). Panels are presented according to spatial distribution, i.e. bottom-left corresponds to south-west.

Following Frankel et al. (2009), Figure 35 compares empirical and predicted PGVs for the Seattle basin sites. The seismograms are band-pass filtered between 0.01-0.5 Hz in this study, those of Frankel et al. (2009) are filtered at 0.2-0.4 Hz. Frankel notes that their predicted PGVs are consistent with those of the data, especially for the geometrical mean of the two horizontal components. The PGVs from the largest

horizontal component are somewhat larger than observed, which reflects the over-prediction of NS motion at several stations. Frankel et al. (2009) report the bias and standard deviation between empirical and predicted PGV values is a factor of 1.1 and 1.3, respectively. The simulations conducted in this study generally over-predict empirical PGV in the Seattle basin region (PGV > 1 cm/s), but capture the trend of the data. For the Georgia basin region (PGV < 1 cm/s), larger variation is obtained between empirical and predicted PGVs. The average factor of PGV over-prediction is 1.6 and 2.0 for the 18 strong-motion stations in the Seattle basin region and the 16 selected stations in the Georgia basin region, respectively (overall average of 1.8).

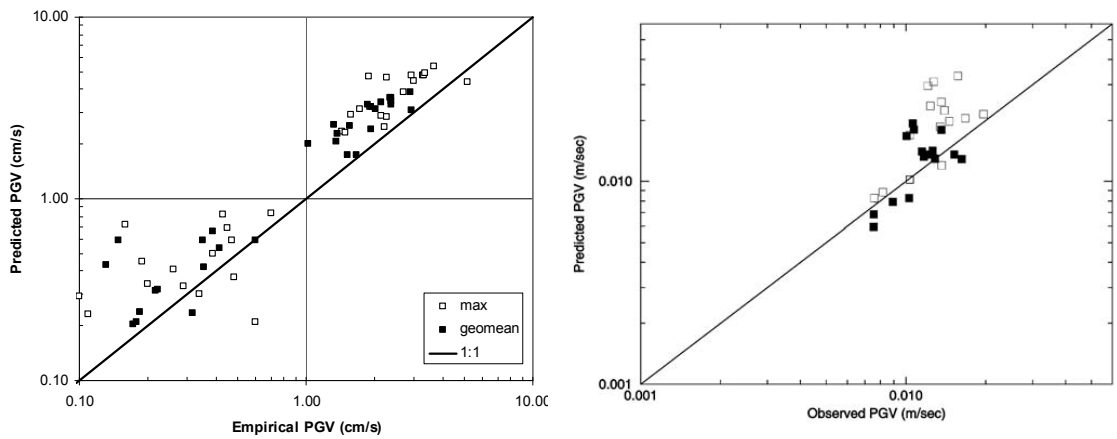

Figure 35. Comparison of empirical (observed) and predicted PGV for the Nisqually earthquake simulated in this study (left panel). Open squares are based on largest peak velocity from the two horizontal components for a given station; filled squares are based on geometrical average of two horizontal components at a given station. Results of Frankel et al. (2009) shown in right panel.

The goodness-of-fit factor used by Pitarka et al. (2004) is given by

$$f_1 = \exp\left[-\left(\frac{Syn - Obs}{\min(Syn, Obs)}\right)^2\right], \tag{37}$$

where *Obs* and *Syn* are measures of a ground-motion parameter using empirical and synthetic waveforms, respectively, and min(*Syn,Obs*) is the smaller of the two; f_1 varies from 0 to 1, with 1 corresponding to identical empirical and predicted ground-motion measures. In this study, f_1 is calculated using the PGV of waveforms band-pass filtered at 0.01-0.5 Hz, those of Pitarka et al. (2004) are filtered at 0.02-0.5 Hz. Pitarka et al. (2004)

obtain the best waveform and amplitude agreement in the NS waveforms, especially at sites in the central part of the basin (Figure 36).

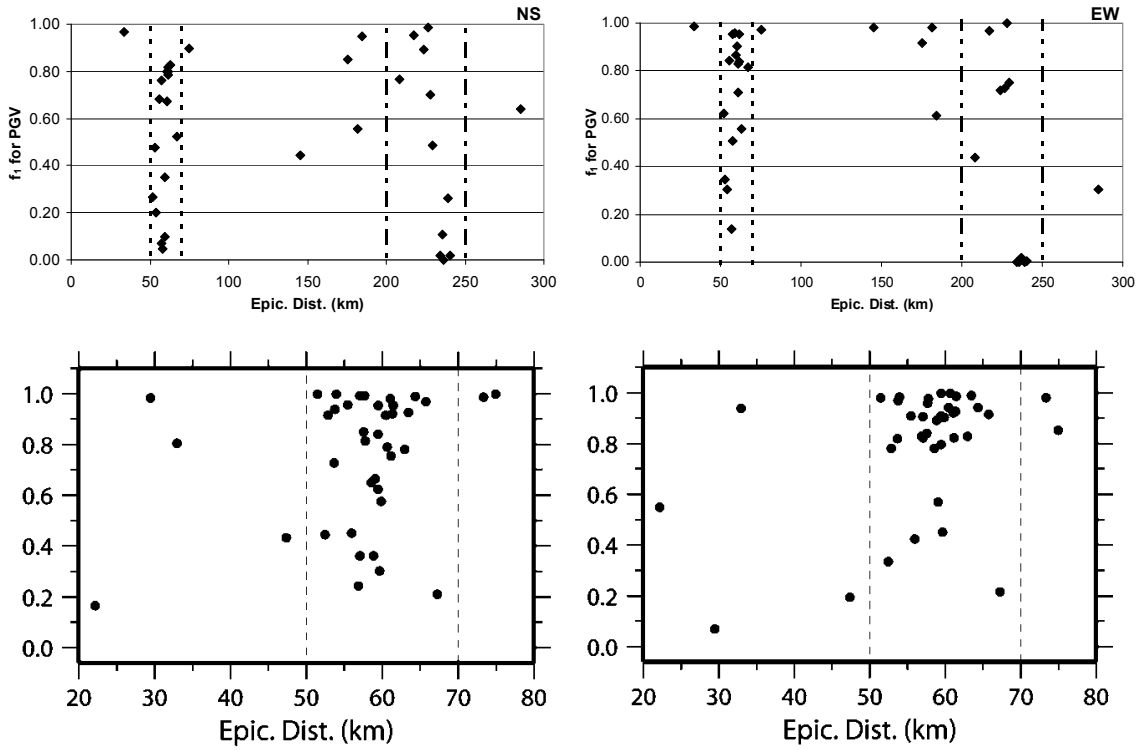

Figure 36. Goodness-of-fit factor, f_1, for peak ground velocity on EW (left panels) and NS (right panels) components from simulations in this study (top panels) and those of Pitarka et al. (2004) (bottom panels). Vertical dashed lines indicate the epicentral distance of the southern and northern edges of the Seattle basin, and dot-dashed lines indicate the southern and northern edges of the Georgia basin.

Ground motions in the Georgia basin region from the M_W 6.8 Nisqually earthquake are significantly lower than the Seattle basin region, as the 55-km deep earthquake is > 150 km distant (Figure 35). Ground motion in the EW direction is predicted to be larger than the NS direction for a given location (Figure 32). Empirical recordings at stations S of the Georgia basin (ERW, PGC, SBES, SNB) generally show larger EW than NS arrivals (Figure 34), in agreement with predictions, but overall the synthetic amplitudes are larger (Figure 35 shows PGV estimates are slightly over-predicted in Seattle basin region before waves propagate N). For stations in the Georgia basin (ANN, ARN, EBT, ING, KID, RHA), peak amplitudes are in good agreement with empirical recordings (Figure 36). Good agreement occurs because empirical PGV at soil

sites (ANN, ARN, KID, RHA) is similar to the PGV of later-arriving surface waves in the synthetic waveforms (Figure 34). For rock or stiff soil sites in the northern part of the Georgia basin (BLO, BND, CSQ, MDN), empirical records are generally < 20 s in duration and PGV is related to first arrival S-waves, whereas PGV of the longer duration synthetic waveforms is associated with later-arriving surface waves (Figure 34); hence, PGV is over-predicted (Figure 35) or agrees poorly with empirical recordings (Figure 36) for the northern basin sites. The 3D Georgia basin structure results in peak ground motion associated with later-arriving surface waves, EW motion greater than NS motion, from simulation of the M_W 6.8 Nisqually earthquake.

Simulation of the M_W 6.8 Nisqually earthquake and comparison with empirical recordings demonstrates good agreement in amplitude and phase of first arrival S-waves at stations within 100 km of the source (Seattle basin region, Figure 33), providing confidence in the Nisqually source model. Overall, general agreement of the waveforms in the Seattle basin region is achieved and estimates of PGV are over-predicted by a factor of ~1.6. For the Georgia basin region, validation of the simulated ground motions with generally low amplitude and short duration empirical recordings of the Nisqually earthquake is a challenge, especially without accurate timing for a majority of the recordings and knowledge that the waves propagating N out of the Seattle basin region are already slightly over-predicted before they enter the Georgia basin from the S. However, the Nisqually source model is shown to provide reasonable agreement in the near-source region, so simulations of large JdF plate scenario earthquakes in the Georgia basin region are conducted using this source model (Section 3.4.2).

The effects of the 3D Georgia basin structure is assessed in Figure 37, which shows peak basin amplification maps (basin/non-basin PGV) of the Georgia basin region and comparison of synthetic (basin and non-basin model) waveforms at five select locations. Amplification within the 5-km border of highly absorbing and attenuative material is shown, but is not considered further. The basin model includes both the Seattle and Georgia basins, whereas the non-basin model does not include either basin (Section 3.2.1.1). Figure 37 demonstrates the peak basin amplification factor is > 10 in the Georgia basin. In other words, when basin sediments are included in the physical structure model, predicted peak ground motion is 10 times greater than the predicted

background peak motion. Comparison of basin and non-basin waveforms in Figure 37 demonstrates that the increase in predicted peak motion amplitude is due to later-arriving surface waves present in the basin waveforms but not the non-basin waveforms. For the two onshore sites in Greater Vancouver, the average PGV predicted for the basin model is 0.6 cm/s generated by surface waves arriving at > 80 s in the 130 s simulation. The average increase in peak motion due to basin structure (basin/non-basin PGV factor) is 7.8 at these two sites. Overall, the presence of 3D Georgia basin structure has significantly increased the levels and duration of predicted ground shaking, even though the level of ground motion is not significant at this distance.

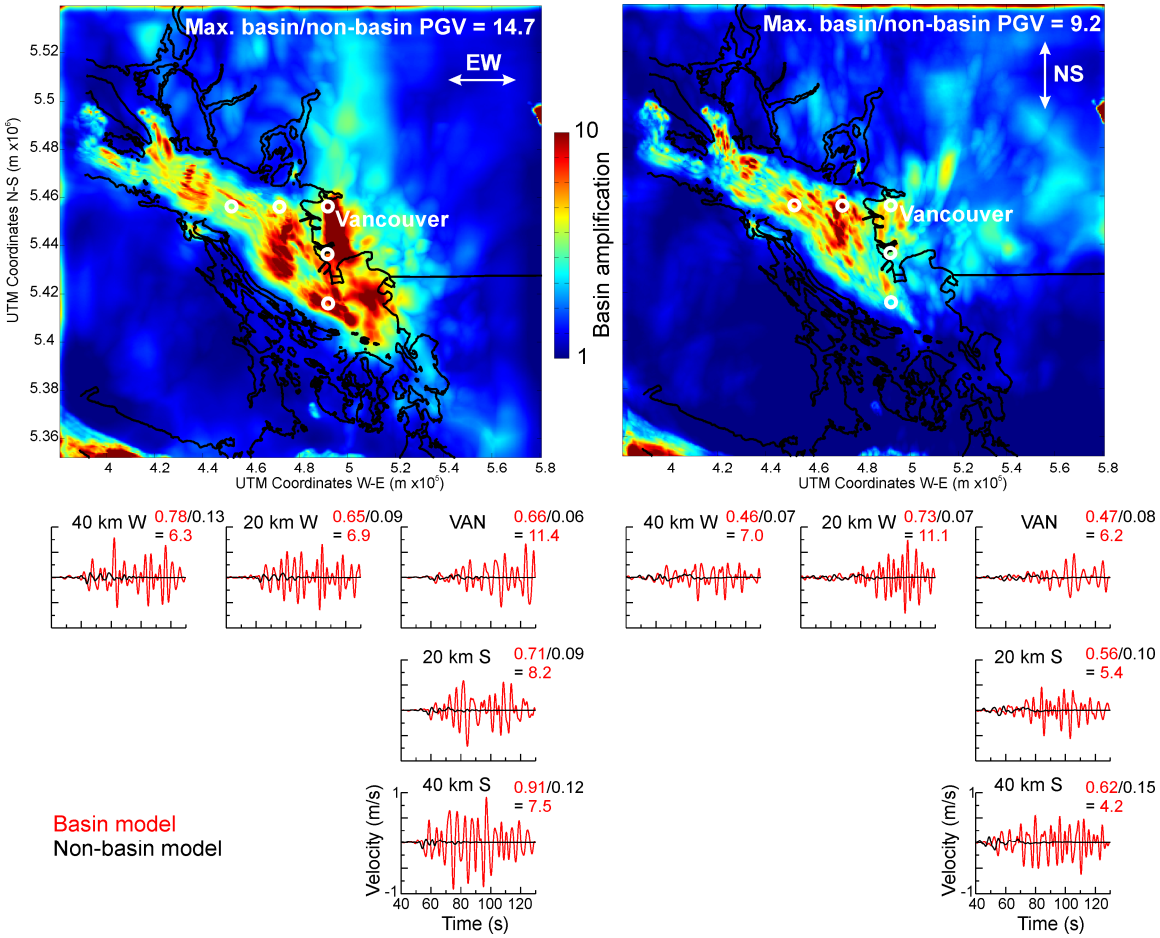

Figure 37. Basin amplification maps of the M_W 6.8 Nisqually earthquake simulation (black line is coastline). Synthetic waveforms are shown for Vancouver (VAN) and four other locations (white circles in maps). Numbers given in top right of each panel corresponds to simulated basin model PGV (cm/s) / non-basin model PGV (cm/s) = basin amplification factor.

3.4.3 Results

The goal of this section is to quantify the 3D Georgia basin effect on long-period ground shaking in Greater Vancouver for scenarios of M_W 6.8 JdF plate earthquakes. The Nisqually earthquake source model (Section 3.4.2) is initiated at 11 different locations (Figure 38) spanning Georgia Strait, based primarily on recorded seismicity (Figure 30). Earthquakes are simulated at the top of the subducting JdF plate, which dips NE beneath Greater Vancouver; hence, the shallowest earthquakes occur towards the SW. The maximum source depth is constrained to 55 km by the maximum depth of the velocity structure models at 60 km. The most realistic scenarios are those along the extent of Georgia Strait for the chosen magnitude and depth limitations of the model (scenarios 1, 2, 6, 10 and 11); ground motions are likely overpredicted for scenarios furthest NE (scenarios 3, 4, and 8).

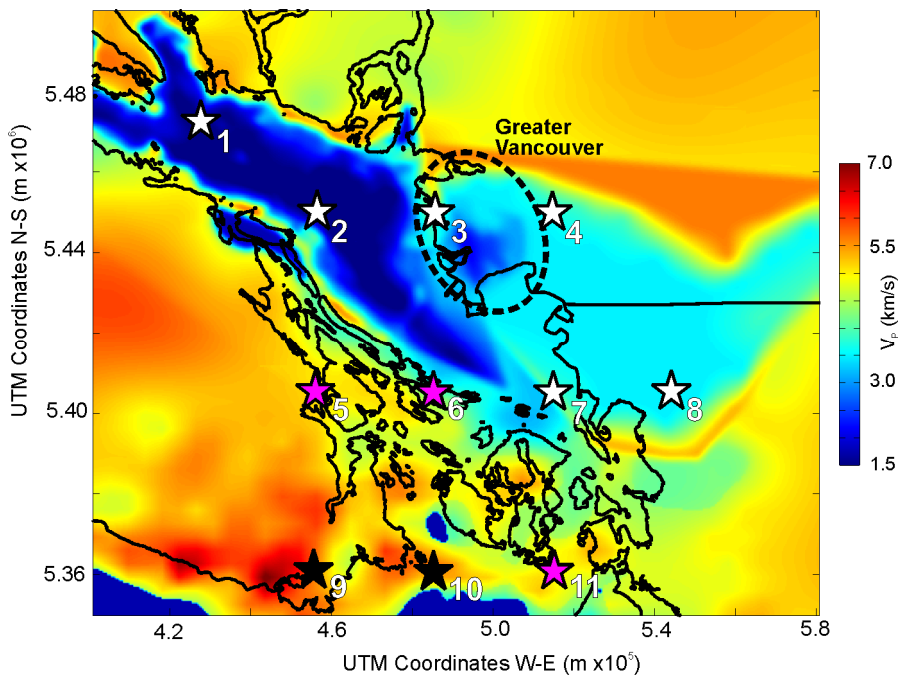

Figure 38. Georgia basin V_P model (500-m surface) with epicentre locations of 11 simulated M_W 6.8 JdF plate earthquakes shown as stars (colour corresponds to hypocentre depth: black is 42 km, pink is 48-53 km, and white is 55 km). Black line corresponds to coastline and area of Greater Vancouver is outlined by thick dashed line.

Figure 39 and Figure 40 show the distribution of predicted PGV in the Georgia basin region for EW and NS horizontal motions, respectively, of all 11 scenarios simulated in the 3D basin model. Layout of maps corresponds to spatial distribution of

scenario epicentres. For EW motion, higher amplitudes always occur W of the source. For NS motion, higher amplitudes occur SE of the source for the N-most locations (scenarios 1 to 8), and NE of the source for the S-most locations (scenarios 5 to 11). The consistent behaviour of simulated ground motions for different source locations is due to the source radiation pattern, readily apparent in the non-basin model simulations (an example for scenario 5 is shown in Figure 39 and Figure 40). The strongest ground motion (PGV) predicted within the Georgia basin is reported in the upper right of each panel. Amplitudes shown outside of the chosen spatial limits of the Georgia basin and within the 5-km boundary zone are not considered. The range in predicted maximum horizontal PGV in the Georgia basin is 3.6 to 15.5 cm/s, corresponding to shaking intensities of V-VI (Table 9). For context, the 2001 M_W 6.8 Nisqually earthquake produced PGVs of ≤ 5 cm/s in the Seattle basin (Figure 33) and resulted in $2 billion US dollars worth of damage in Washington.

Table 9. Comparison of PGV and intensity as described by level of damage and associated shaking (modified from Wald et al. 1999 and Wood & Neumann 1931).

Intensity	**IV**	**V**	**VI**	**VII**	**VIII**	**IX**
PGV (cm/s)	1.1 – 3.4	3.4 – 8.1	8.1 – 16	16 – 31	31 – 60	60 – 116
Damage	None. Windows rattle.	Very light. Pictures move.	Light. Plaster cracks.	Moderate. Fall of cornices.	Moderate-Heavy. Failure of masonry walls.	Heavy. Collapse of masonry buildings.
Shaking	Light. Vibration of passing heavy truck.	Moderate. Felt outdoors, sleepers awakened.	Strong. Felt by all, people walk unsteadily.	Very strong. Difficult to stand or walk.	Severe.	Violent. General panic.

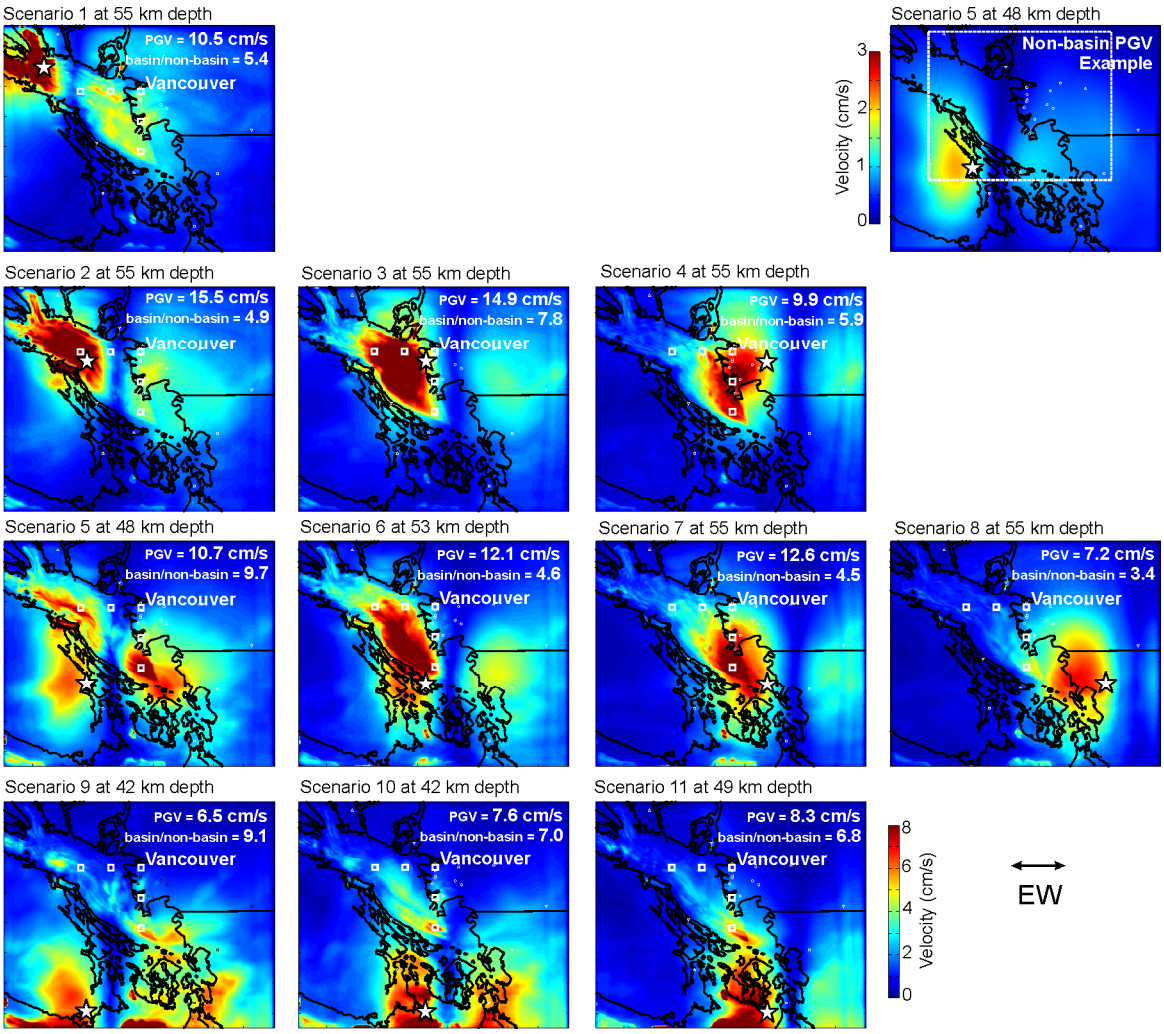

Figure 39. EW PGV maps for 11 M_W 6.8 JdF plate scenario earthquakes simulated in the Georgia basin model (black line is coastline). Maps are presented according to spatial distribution of earthquake epicentres (stars). White squares correspond to waveform locations shown in Figure 41. Top right panel shows an example PGV map from simulation of scenario 5 in the non-basin model (white dashed box corresponds to limits of Georgia basin used to report maximum values).

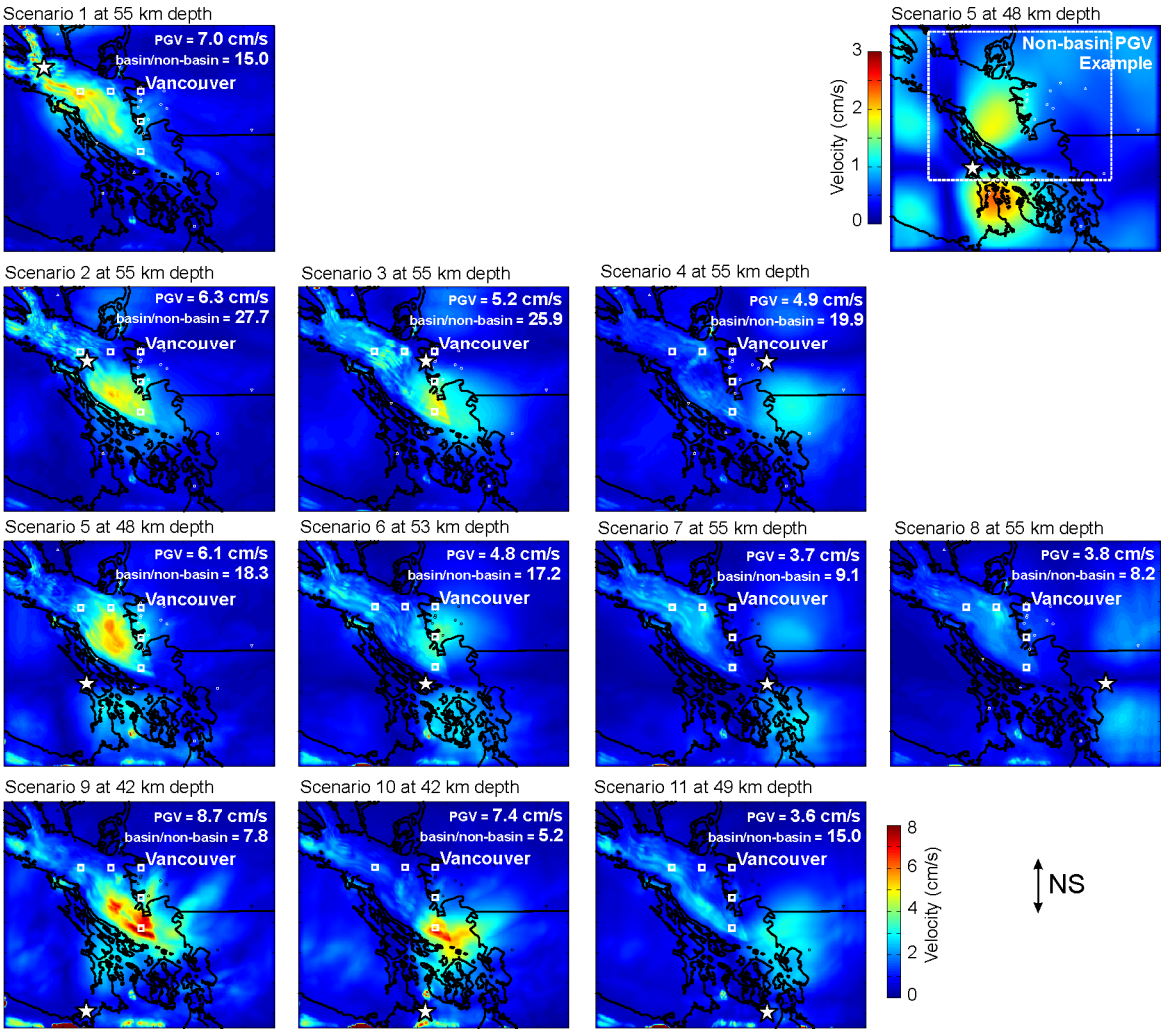

Figure 40. NS PGV maps for 11 M_W 6.8 JdF plate scenario earthquakes simulated in the Georgia basin model. Details as provided in Figure 39.

Figure 41 and Figure 42 present EW and NS synthetic waveforms, respectively, for Vancouver and four other sites, 20 and 40 km both W and S of the city, of all 11 simulations. Synthetic basin and non-basin waveforms are shown at all five sites for each of the 11 scenario earthquakes, presented according to spatial location (white squares in Figure 39 and Figure 40). Examination of basin waveforms in comparison to non-basin waveforms across the Georgia basin demonstrates whether PGV is related to amplification of early-arrival source-generated S-waves (shown by both sets of synthetic waveforms) or later-arrival basin-generated surface waves (shown only by basin waveforms). In general, the presence of 3D Georgia basin structure increases the level and duration of predicted ground motion relative to the non-basin background response.

The largest differences between basin and non-basin waveform content, i.e. the largest effects due to 3D Georgia basin structure, occur in Georgia strait. The strongest predicted ground motion in Vancouver is 6.2 cm/s for scenario 4 with an epicentre located ~25 km E of the city (Figure 41). For this scenario, PGV is associated with early-arrival S-waves and the basin waveform is slightly amplified in comparison to the non-basin waveform in Figure 41 due to decreased impedance of the basin sediments. The largest increase in peak motion due to basin structure (basin/non-basin PGV factor) in Vancouver is 5.8 for scenario 9, associated with later-arriving surface waves of relatively low amplitude. Scenario 9 also generates significant surface waves at the site 20 km south of Vancouver, in the city of Ladner, for both EW and NS motion (Figure 41 and Figure 42).

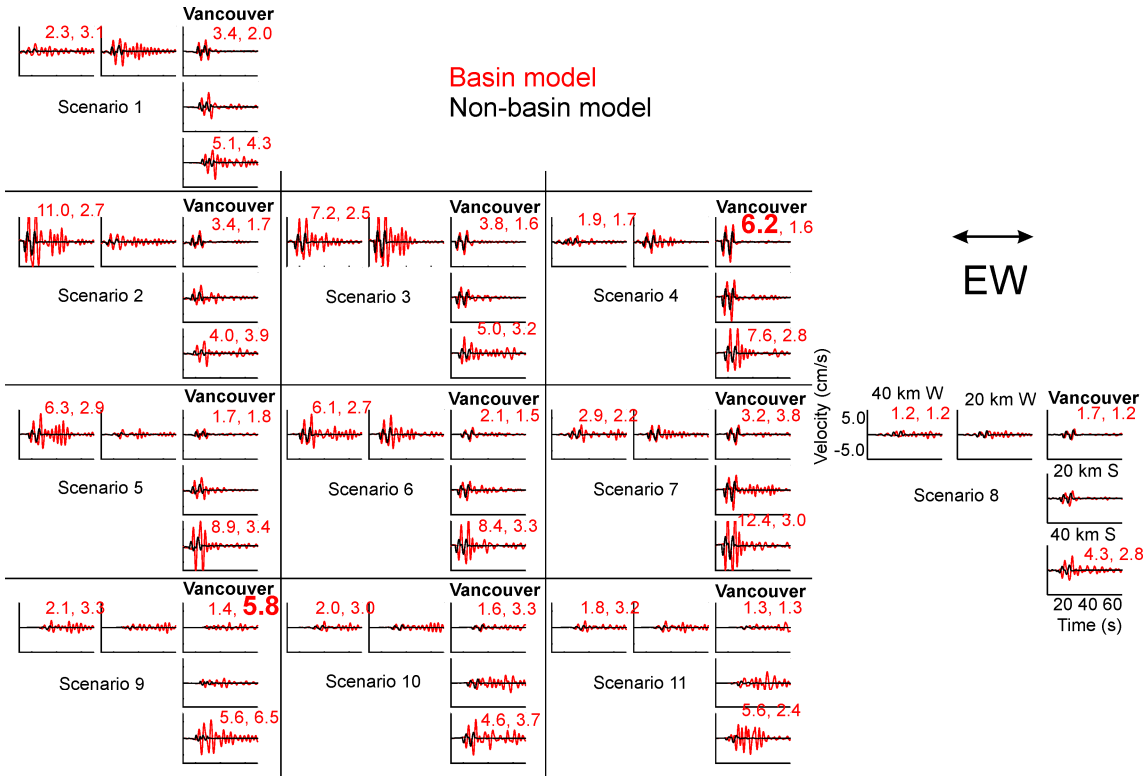

Figure 41. Synthetic EW waveforms at five select locations (panel layout corresponds to spatial location as shown by white squares in Figure 39) for each of the 11 M_W 6.8 JdF plate earthquake scenarios. Numbers given in top right of select panels corresponds to PGV (cm/s) and basin amplification factor. For Vancouver, the highest PGV is 6.2 cm/s (scenario 4) and highest basin amplification is 5.8 (scenario 9), denoted by larger font numbers.

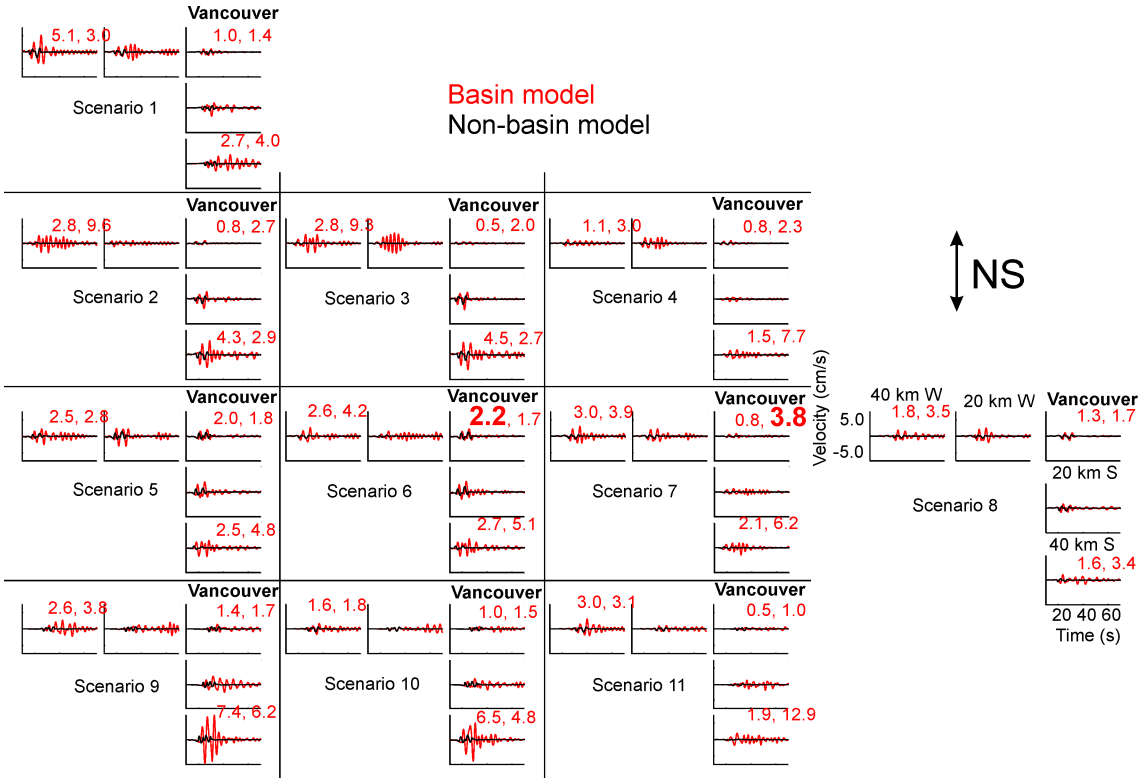

Figure 42. Synthetic NS waveforms at five select locations for each of the 11 M_W 6.8 JdF plate earthquake scenarios. Details as provided in Figure 41. For Vancouver, the largest PGV is 2.2 cm/s (scenario 6) and highest basin amplification factor is 3.8 (scenario 7), denoted by larger font numbers.

To further investigate Georgia basin effects from a deep JdF plate earthquake located SW of Greater Vancouver, an additional 26 simulations are conducted (13 simulations each for the basin and non-basin models), for which the epicentre of the SW-corner scenario 9 earthquake is moved incrementally 5-km E and N towards scenario epicentres 10 and 5, respectively. Figure 43 shows the distribution of peak basin-amplified EW motion (basin/non-basin PGV) in the Georgia basin region for the scenario 10 km E of epicentre location 9. The highest onshore basin amplification occurs ~10 km S of Vancouver, in the city of Richmond. Synthetic waveforms are examined at a particular location in this circular high basin amplification area in Richmond (white square in Figure 43), for all 16 SW-located earthquake scenarios. When the JdF plate earthquake is simulated in the SW corner (scenario 9) of the basin model, predicted PGV is 3.6 cm/s due to a large negative arrival at 40-50 s, which is 8.7 times greater than the predicted non-basin peak motion. This peak continues to dominate predicted long-period

ground motions if the scenario earthquake is moved up to 20 km N (towards scenario 5) and 20 km E (towards scenario 10). The highest basin-amplified peak motion in Richmond is ~11 for an epicentre located 10 km E of scenario 9 in the simulation (corresponding basin amplification map is shown in Figure 43). For scenarios 5 and 10, Figure 43 shows PGV of the basin waveform is slightly lower and corresponds to early-arriving S-waves and later-arriving surface waves, respectively. The arrival at 40-50 s is still present in these waveforms but is no longer associated with the strongest motion. The basin amplification factor is significantly reduced in Richmond for these scenarios because PGV of the basin and non-basin waveforms has decreased slightly and increased, respectively. The strength of basin-amplified peak motion is dependent on the variation in PGV of both basin and non-basin waveforms.

The cause of the highest basin amplification in southern Greater Vancouver, for a JdF plate earthquake simulated 10 km E of scenario 9, is investigated further. Figure 44 shows the circular area of high basin amplification in Richmond primarily corresponds to the edge of lowest-velocity sediments in the upper 1 km of the basin model. Synthetic EW waveforms are examined at 20 locations across Greater Vancouver in a 5-km grid as shown in Figure 44. Peak motion in basin waveforms across the metropolitan area is associated with later-arrival (> 40 s) surface waves. For the location of highest basin amplification and five other sites, PGV corresponds to a large negative arrival between 40-50 s (locations denoted by black squares in Figure 44). This phase is apparent slightly earlier or later in other basin waveforms located towards the SW and NE, respectively, but no longer corresponds to the maximum amplitude (dotted circles in Figure 44).

Time-snapshots of peak velocities for 30 s of the basin model simulation are presented in Figure 45 and Figure 46 to investigate the generation of peak waveform arrivals at the location of highest basin amplification in southern Greater Vancouver (Richmond). Peaks in the first 35 s are associated with the two direct S-wave arrivals (labelled as 1 and 2) of the double point source model (Section 3.4.2) and their reflections (labelled as r1 and r2), easily recognized by their circular wave fronts, which are distorted as they radiate into and propagate NE across the basin. This is in agreement with similarity between basin and non-basin waveforms for the first ~40 s of the simulations (Figure 43 and Figure 44), for which arrivals in the basin waveforms are delayed and of

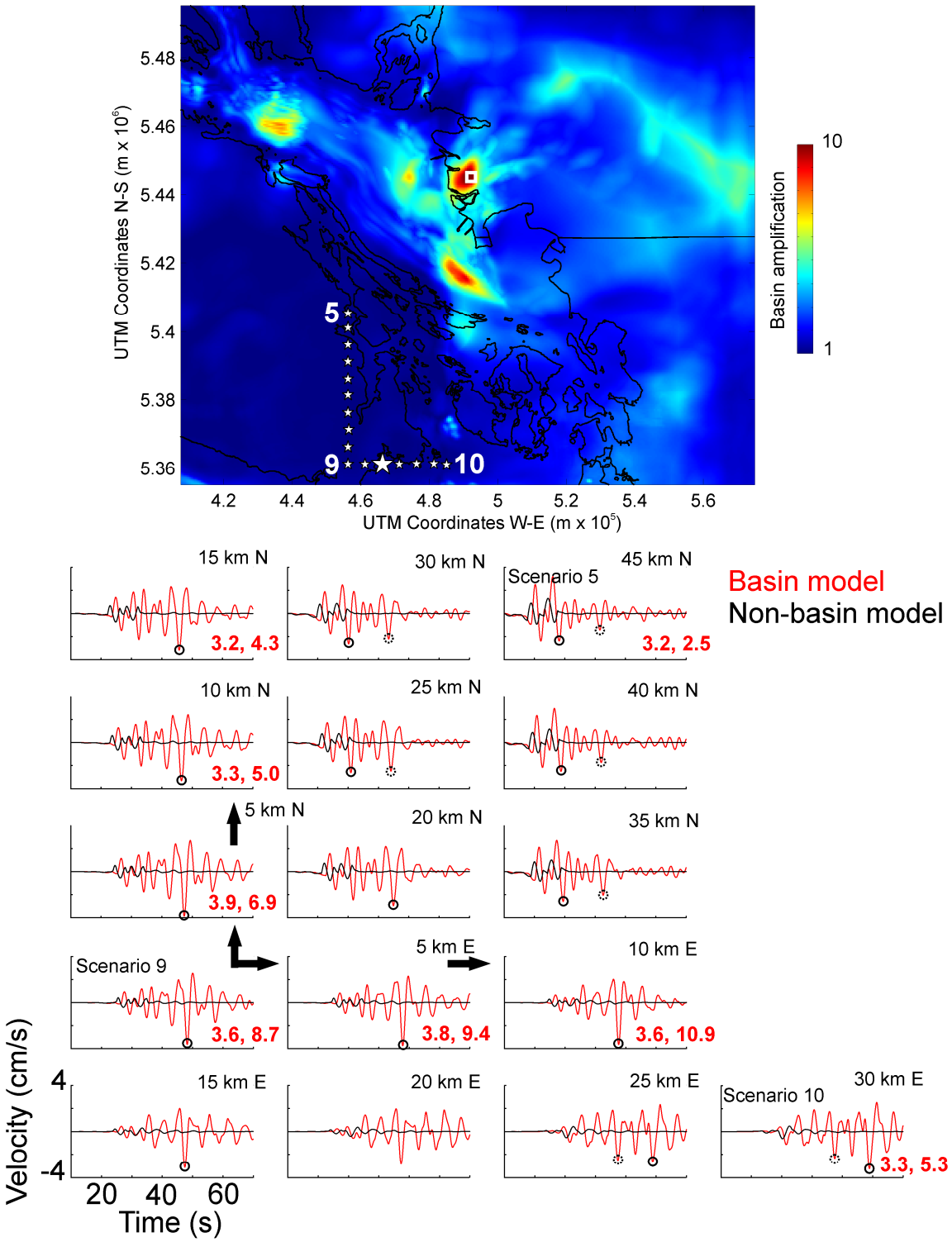

Figure 43. Map of EW basin amplification for a M_W 6.8 JdF plate scenario earthquake (epicentre denoted by the large white star and black line is coastline). Comparison of synthetic waveforms at the location of highest basin amplification in Greater Vancouver (white square on map) for earthquakes simulated in 5-km increments E and N of scenario 9 (epicentres marked by small stars on map). Solid circles denote PGV and dotted circles track PGV arrival for scenario 9. Red numbers correspond to PGV (cm/s) and basin amplification factor.

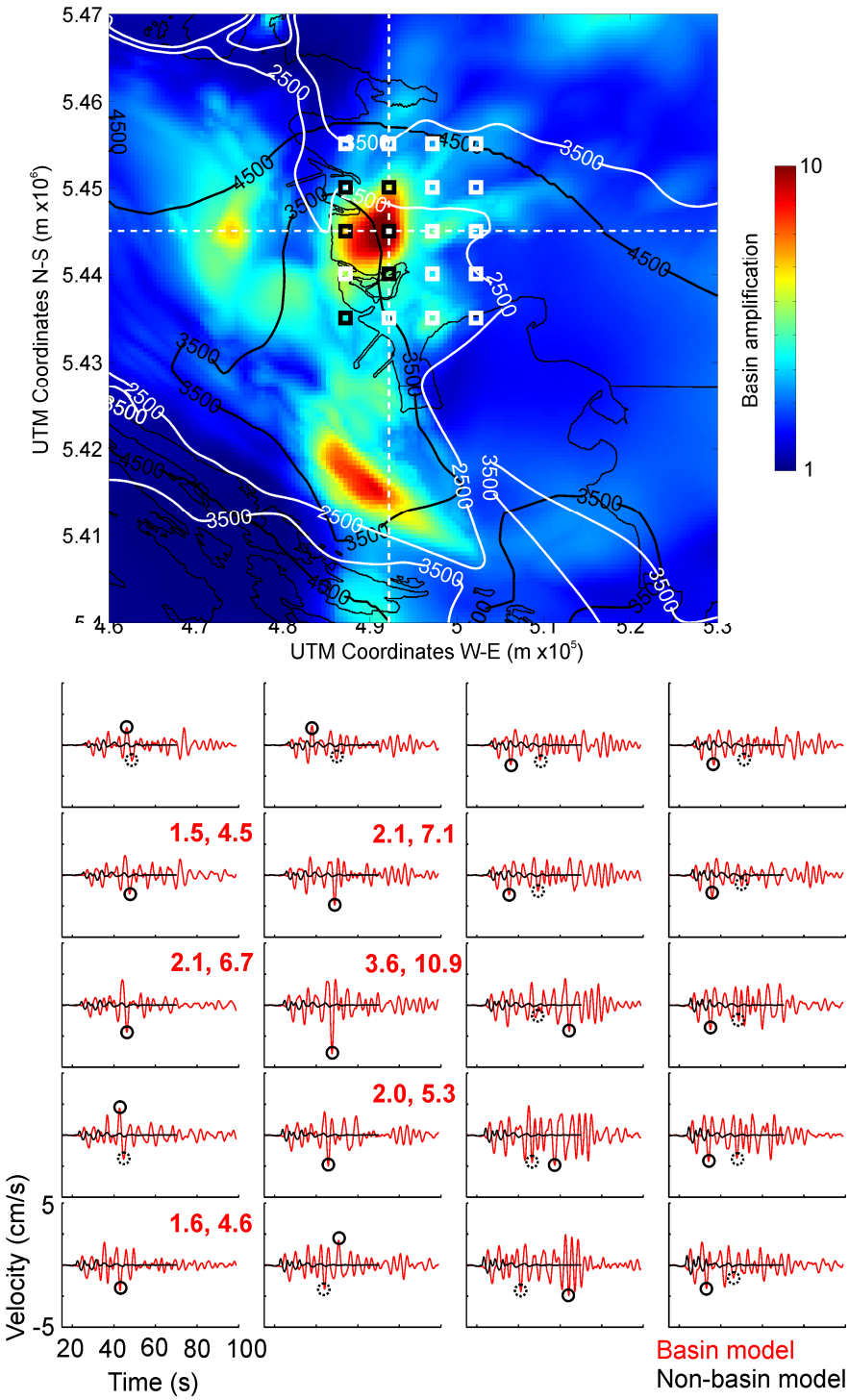

Figure 44. Map of EW basin amplification across Greater Vancouver (coastline is thin black line) for scenario 10 km E of epicentre location 9 with contours of the basin V_P model at 250 m (thick white lines) and 1 km (thick black lines) depth. Dashed white lines correspond to cross-sections shown in Figure 45. Synthetic EW waveforms correspond to grid of 20 locations (5-km spacing) shown by squares on map. Solid circles denote PGV and dotted circles track PGV arrival for scenario 9. Red numbers correspond to PGV (cm/s) and basin amplification factor. Locations for which PGV is due to the same PGV arrival for scenario 9 are shown by black squares on map.

larger amplitude due to inclusion of basin sediments (V_P < 5.5 km/s). The delay of particular peak arrivals at the surface in comparison to at depth is readily apparent in the cross-section time-snapshots in Figure 45. By 35 s in the simulation, the 3D Georgia basin structure generates and sustains surface waves, denoted by black dashed lines in Figure 45 and Figure 46, strongest in the deep narrow SE extent of the basin such that the waves are primarily aligned in a NW-SE sense along the basin axis (Figure 46). The positive peak at 41 s is the first surface wave arrival for Richmond. As surface waves approach Richmond from the SW, they travel slightly faster immediately W due to higher velocity material, and slightly slower immediately E due to lower velocity material, i.e. a basin edge, resulting in slight rotation to an ENE propagation direction (Figure 46). The large negative peak at 47.5 s occurs from constructive interference of EW motion surface waves with the basin-edge as shown by the relatively high amplitudes in this location (Figure 46) and the large amplitude of this arrival in comparison to its amplitude at other nearby locations (Figure 44). Destructive interference of this arrival occurs at the location 5 km E (Figure 44). Other phases predominantly decay in amplitude as they propagate NE. The strength of the constructive interference is related to the propagation direction of surface waves generated in the upper 1 km of the 3D basin structure, reaching a maximum when the source epicentre is located 10 km E of scenario 9 (Figure 43). The amplitude of later-arriving surface waves in Richmond is relatively high and concentrated at the edge of the lowest-velocity material (Figure 46). Zones of high basin amplification in Georgia Strait, W and S of the onshore circular high amplification area (Figure 44), are also coincident with basin edges in the upper 500-1000 m (Figure 46).

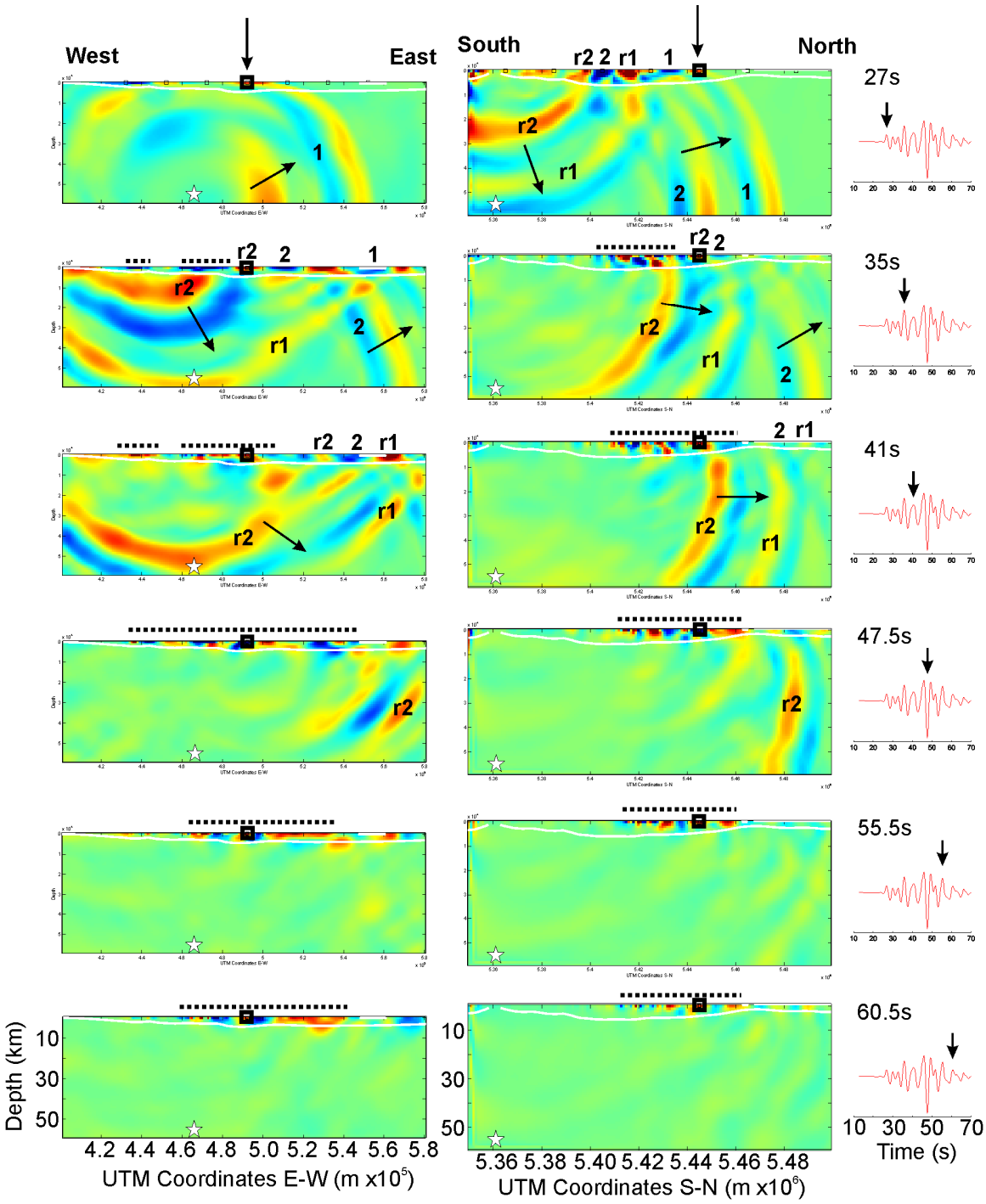

Figure 45. Cross-sectional time-snapshots of simulated EW motion for a scenario 10 km E of location 9 in the basin model (saturation of the blue (red) hue corresponds to PGV of -1.0 (1.0) cm/s). Star denotes scenario hypocentre, white line is 5.5 km/s V_P contour (representing base of basin), and black square denotes location of highest basin amplification. The synthetic waveform for this location is shown on right and corresponding timing of simulation snapshot is indicated by black arrows. Details in text.

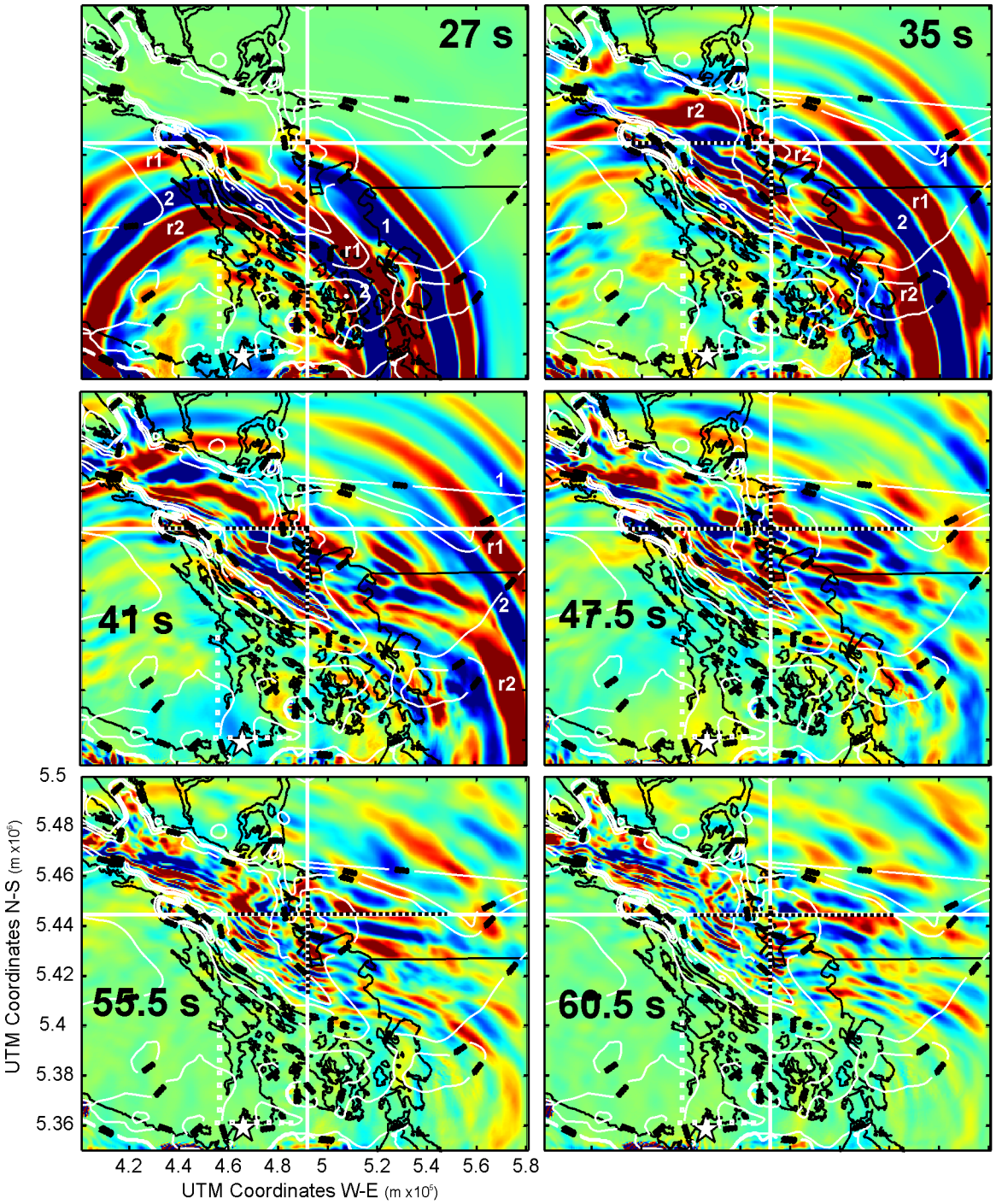

Figure 46. Plan view time-snapshots of simulated EW motion for same scenario shown in Figure 45 (saturation of the blue (red) hue corresponds to PGV of -1.0 (1.0) cm/s). Thick white lines correspond to cross-sections and intersection point corresponds to waveform shown in previous figure. Star denotes scenario epicentre, and thin white lines are contours of basin V_P model structure at 500 m depth. Details in text.

3.4.4 Discussion

Scenario M_W 6.8 JdF plate earthquakes are simulated in Georgia basin and non-basin structure models to predict long-period ground motions in Greater Vancouver. The presence of the Georgia basin significantly increases the level of predicted long-period ground motions. For all 11 simulations (Figure 39 and Figure 40), the average maximum horizontal peak ground motion in the Georgia basin is 8.1 ± 3.5 cm/s (one standard deviation) and the average maximum basin amplification (basin/non-basin PGV) is 10.8 ± 7.0, i.e. average increase in peak motion is an order of magnitude larger than the background non-basin peak motion. More importantly, in the onshore Greater Vancouver region, the average horizontal peak motion is 2.6 ± 1.6 cm/s at all 20 selected sites (as in Figure 44), for which the average maximum PGV always corresponds to EW horizontal motion (Table 10). Therefore, on average, the predicted intensity of shaking at stiff soil sites in Greater Vancouver for a M_W 6.8 JdF plate earthquake corresponds to intensity IV (Table 9). The basin structure model does not include topography or sediments with V_S < 625 m/s which will also amplify ground shaking. For reference, PGV at stiff soil sites in the Seattle basin region also correspond to intensity IV from the 2001 M_W 6.8 Nisqually earthquake, which caused $2 billion US dollars worth of damage in Washington.

The average increase in peak motion due to basin structure (basin/non-basin PGV) in Greater Vancouver is 2.3 ± 1.1 (Table 10). For comparison, Olsen (2000b) determined the maximum average basin amplification of the LA basin for nine scenario events to be 4.2. The highest amplification in peak motion due to the presence of the Georgia basin is associated with scenarios 9 and 10 (Table 10). Detailed investigation of the localized high basin response ~10 km S of Vancouver (city of Richmond) showed that basin-amplified peak motion reaches a maximum of 11 for an event 10 km E of scenario 9 due to constructive interference of surface waves generated by shallow 3D basin structure (< 1 km depth). The proposed predictor variable for basin amplification is the depth to V_S of 1.0 ($Z_{1.0}$), 1.5 ($Z_{1.5}$) or 2.5 ($Z_{2.5}$) km/s (Day et al. 2008). Amplification due to 3D basin structure is shown here to primarily correspond to the lowest-velocity sediments at the 500 and 750 m depth slices of the basin model, corresponding to V_S of 1.5-2.0 km/s. Hence, the use of $Z_{1.5}$ or $Z_{2.0}$ may be an appropriate predictor of amplification for the Georgia basin.

Table 10. Summary of average peak horizontal motion and peak horizontal basin-amplified motion at 20 selected sites across Greater Vancouver for 11 JdF plate earthquake scenarios.

Scenario	Basin model PGV (cm/s) EW	Basin model PGV (cm/s) NS	Basin/Non-basin PGV factor EW	Basin/Non-basin PGV factor NS
1	3.70	1.99	2.33	2.71
2	3.84	1.81	2.05	2.08
3	3.27	1.88	1.76	1.95
4	7.24	0.93	1.88	3.50
5	2.98	2.58	2.07	2.41
6	2.42	2.90	1.66	1.89
7	4.94	0.93	1.72	2.95
8	2.43	1.38	1.52	1.68
9	1.71	2.78	4.11	2.69
10	2.23	1.44	4.32	1.78
11	1.94	1.11	1.57	2.95
All	3.3 ± 1.8	1.8 ± 0.9	2.3 ± 1.2	2.4 ± 1.0
Total Average	2.6 ± 1.6		2.3 ± 1.1	
10 km E of 9	*1.73*	*2.58*	*4.67*	*2.76*

3.5 Earthquake scenario 2: Shallow North America plate earthquakes

To investigate crustal North American plate earthquake scenarios, large (M_W 6.8) blind-thrust earthquakes are simulated at 5 km depth in two different locations of recurring shallow seismicity in the Georgia basin region.

3.5.1 Seismicity

Crustal NA plate earthquakes show no obvious correlation with mapped surface faults of the region (Rogers 1998), and large (M > 7) historical events (1872, 1918, 1946) have occurred in Washington state and on Vancouver Island away from moderate and smaller events that occur predominantly beneath the Strait of Georgia (Figure 47). These latter crustal NA events occur in a bimodal depth distribution (see bottom panel of Figure 30); moderate events in 1939, 1975, 1990, 1996 and 1997 have occurred at shallow depths (< 5 km) followed by numerous aftershocks, and the smallest events are concentrated at depths of 15-25 km. Examination of fault-plane solutions (i.e. focal mechanisms) of over 1000 NA plate earthquakes shows no dominant style of faulting; ~30% of faulting is strike-slip, thrust, or some combination thereof (Balfour et al. 2011a). The maximum compressive stress direction from inversion of focal mechanisms is parallel to the subduction margin, oriented NS beneath Georgia Strait (Balfour et al. 2011a). The

activity rate of M 5 NA plate events/year spanning southern Puget Sound to Vancouver is 0.0592 (1 every ~20 years) (Adams & Halchuk 2003). The best-estimate maximum magnitude of NA plate earthquakes for this region is 7.3 (Adams & Halchuk 2003).

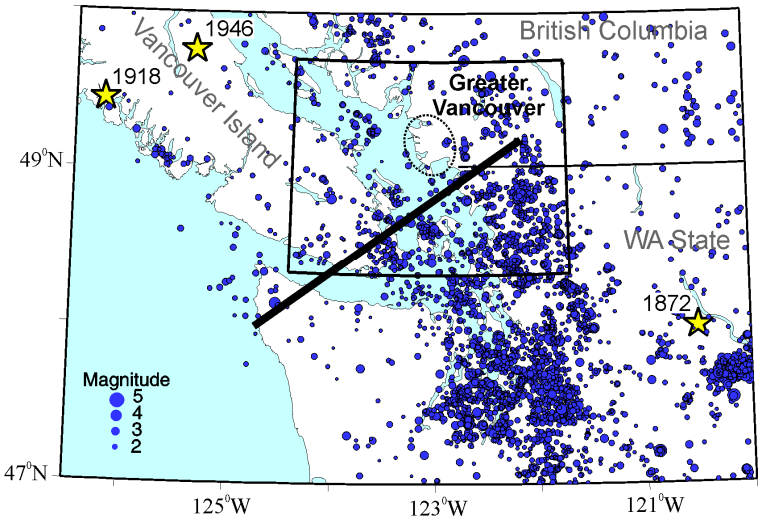

Figure 47. Map of NA plate seismicity (1985-1999) in the Georgia basin region (black box corresponds to model limits). Significant earthquakes (M ≥ 7) are represented by yellow stars and labelled by year. Thick black line corresponds to seismic cross-section shown in Figure 30.

Two zones of persistent shallow seismicity delineate possible active faults in Georgia Strait. One zone of shallow (< 6 km) earthquakes occurs 30 km W of Greater Vancouver (Figure 48). In 1975, a shallow M 4.9 thrust earthquake (Rogers 1979) with a long aftershock sequence occurred here. In 1997, a M_L 4.6 thrust earthquake at 3-4 km depth also occurred here, accompanied by a M_L 3.4 foreshock and ~53 small magnitude (M_L < 2) aftershocks (Cassidy et al. 2000). Focal mechanism solutions of both the fore- and main-shocks show thrust faulting (strike 262°, dip 47° [N], slip 98° or strike 71°, dip 44° [S], slip 82°). Relocation of the largest magnitude (M ≥ 1.5) aftershocks delineate a 53° N-dipping trend (Figure 48), with a temporal sequence that migrates northward (i.e. downdip). An EW-striking and ~50° N-dipping fault plane agrees with interpreted seismic reflection profiles and the magnetic anomaly trend (Mosher et al. 2000). The fault appears to have Holocene movement of up to 40 m which pinches out at the seafloor where a chain of pockmarks occur W of the epicentre location (Riedel et al. 2002). Recently, Balfour et al. (2011b) determined a 60° N-dipping alignment of shallow (10-15 km) earthquakes beneath San Juan Island, ~ 50 km S of Greater Vancouver.

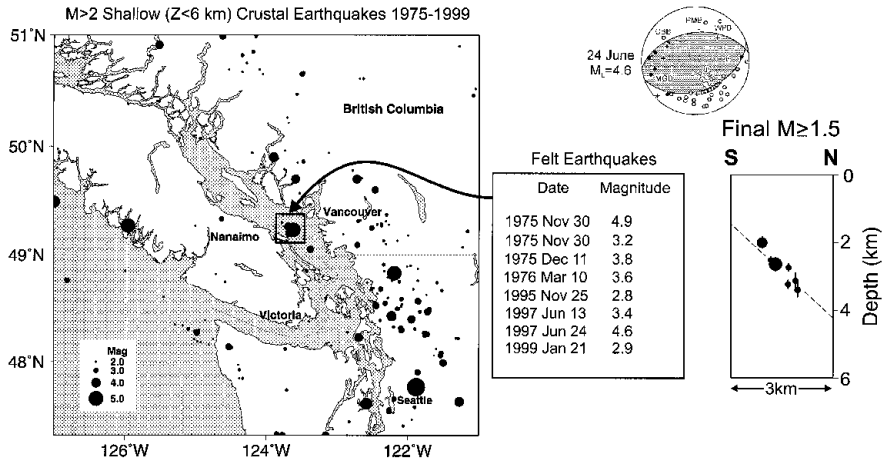

Figure 48. Map of shallow recurrent seismicity in SW British Columbia, focal mechanism of 1997 M_L 4.6 event and cross-section of its aftershock sequence (modified from Cassidy et al. 2000).

3.5.2 Source model

Rupture of large blind-thrust NA plate earthquakes is characterized here based on the slip distribution of the 1994 M_W 6.7 Northridge earthquake as determined by Wald et al. (1996). The plane is sub-divided into a number of sub-faults (Hartzell & Heaton 1983) for which the slip-rate function and duration of slip are constant; however, these parameters vary between sub-faults to characterize variation in the source rupture process. The area under the slip-rate function equals the seismic moment released by the sub-fault; hence the total seismic moment of the entire fault equals the summation of all sub-fault moments. The height of the function is normalized to give the desired final slip and the duration is the rise time. To simulate the propagation of the rupture front across the entire fault, each sub-fault is lagged appropriately in time to include the travel-time difference due to the varying source-to-station positions based on a chosen rupture velocity (Wald et al. 1996).

For simulation of NA plate crustal earthquakes in the Georgia basin region, an EW-striking, 45° N-dipping fault geometry is chosen for simplicity, in reasonable agreement with observed recurrent seismicity. The total seismic moment is set to 1.8×10^{19} Nm, equivalent to a M_W 6.8 event, same as the deep JdF plate earthquake scenarios. Fault parameterization and sub-fault moment distribution are based primarily on distribution of slip for the 1994 M_W 6.7 Northridge blind-thrust earthquake as

determined by Wald et al. (1996). The fault is set to a width of 17.5 km and down-dip length of 24.5 km, respectively (Figure 49), and subdivided into 14 sub-faults in each direction for a total of 196 sub-faults. Moment release of each sub-fault is characterized by a half-cosine function with a constant rise time of 2 s and proportional to a rotated version of the Northridge slip distribution. Generally, rise time is short compared to overall duration (~10%, Heaton 1990) and a relatively short rise time is characteristic of both the 2005 M_W 7.6 Kashmir, Pakistan, and the 1999 M_W 7.6 Chi-chi, Taiwan, thrust-mechanism earthquakes and seems typical of intra-continental events (Avouac et al. 2006). The relation of Sommerville (1999) gives a rise time ~1.3 s for the Northridge event. A constant 2-s rise time is used here, as a variable rise time is considered to add unsupported source complexity. It is worth noting, however, that Benites & Olsen (2005) examined the use of variable rise times in simulation of the Wellington, New Zealand, fault rupture, which reduced amplitudes by 25%, but produced a similar radiation pattern.

Modification of the Northridge slip distribution included rotation by 180° such that large slip produced near the source occurs in the near-surface rather than at depth, i.e. relocation of the 20-km Northridge hypocentre to 5 km depth (Figure 49). The preferred direction of rupture here is down-dip (towards north) based on temporal occurrence of the 1997 aftershock sequence (Cassidy et al. 2000). Minimal slip occurs up dip (Figure 49), but is constrained to 1250 m depth, i.e. a blind-thrust event. A constant 3.0 km/s rupture velocity (V_r) is used, as determined for the Northridge event (Wald et al. 1996), which is approximately 80% of the local shear-wave velocity in the 3D model (Graves & Pitarka 2004). Initiation times of each sub-fault are based on the distance of each sub-fault centre to the hypocentre divided by the constant 3.0 km/s rupture velocity. Based on the furthest distance, the total duration of the source process is 10.3 s.

3.5.3 Results

Two crustal NA plate earthquake scenarios representing a large (M_W 6.8) blind-thrust earthquake at 5 km depth are considered for the Georgia basin region (Figure 49). Two zones of recurrent shallow seismicity delineate similar N-dipping active fault plane structures, such that the source model described above is applicable for both scenarios. The epicentre of each scenario is 40 km W and 80 km S of Vancouver, beneath NW Georgia Strait (scenario GS) and San Juan Island, WA, (scenario SJI), respectively.

Rupture is propagated N (down-dip) in both cases, such that motion is directed beneath Greater Vancouver for the SJI scenario. The maximum depth of the 3D physical structure models is set here to 25 km depth, since the maximum depth of the fault plane is ~19 km, which significantly reduces the wall-clock simulation time to ~3 hours. The simulation results of the SJI event are presented first as the source location is similar to the detailed discussion of the JdF plate scenarios (Section 3.4.3).

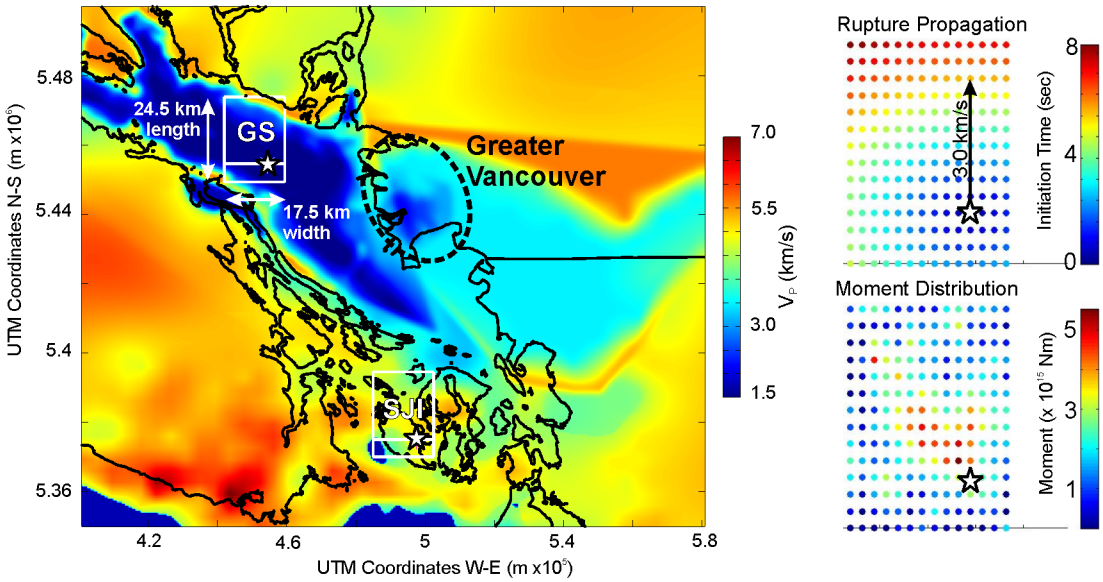

Figure 49. Map of basin V_P model at 500 m depth and locations of two NA plate earthquake scenarios. White star and box denotes projected 5-km hypocentre and 45° N-dipping fault plane, respectively. Fault plane is characterized by 196 sub-faults and their corresponding initiation time and seismic moment are shown in panels on the right.

3.5.3.1 San Juan Island event

A shallow M_W 6.8 NA plate earthquake scenario is simulated at 5 km depth beneath San Juan Island, WA, 80 km S of Vancouver, for each of the 3D physical structure (basin and non-basin) models. Predicted basin-model peak ground motions and the pattern of basin-amplified peak motion are similar for both horizontal directions of motion as shown in Figure 50. The average maximum horizontal PGV in the region ranges from 34 cm/s to 109 cm/s for non-basin and basin model simulations, respectively. The strongest predicted shaking occurs near the epicentre in both cases, but > 25 cm/s shaking occurs in Georgia Strait and in SW Greater Vancouver when basin sediments are included. Maximum basin-amplified peak motion in Georgia basin is ~10 for NS motion and

significantly higher for EW motion, which is due to a slight offset in the radiation minima along the W coastline of Greater Vancouver for the basin and non-basin model simulations. Zones of high basin amplification occur W and S of Greater Vancouver in Georgia Strait and in SW Greater Vancouver. The basin amplification pattern is discussed in detail later in this section.

Comparison of basin and non-basin waveforms at nine locations across Georgia basin (Figure 51) demonstrates basin model PGV is primarily due to a high amplitude surface wave arrival. For sites in the SE part of the basin, similar high NS amplitudes are exhibited by the initial S-wave arrival and by a surface wave arrival shortly thereafter, i.e. basin-edge generated surface wave. The SE basin-edge surface wave propagates predominantly N. For NW basin sites, lower amplitude basin-edge surface waves are generated (furthest selected sites from the source) and multiple surface wave cycles are present.

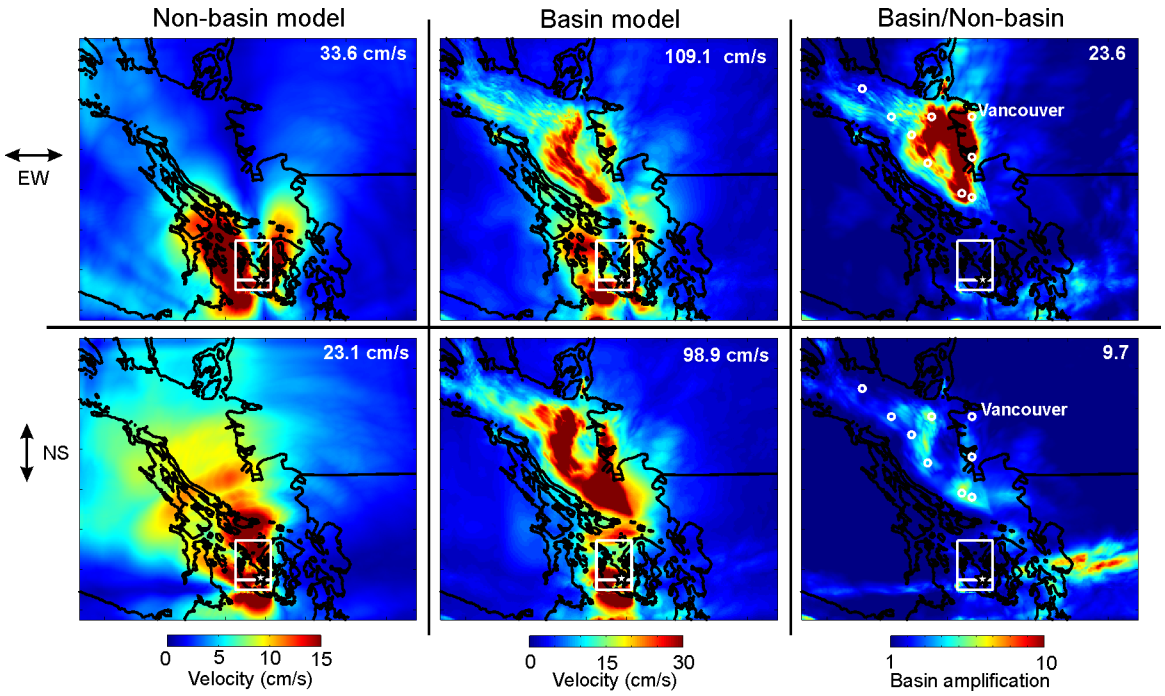

Figure 50. Maps of predicted PGV and corresponding basin amplification (basin/non-basin PGV) for the SJI scenario earthquake (white star denotes epicentre, white box corresponds to a projection of the 45° N-dipping fault plane, and black line is coastline). Number in top right of each map corresponds to maximum value. White circles correspond to waveform locations shown in Figure 51.

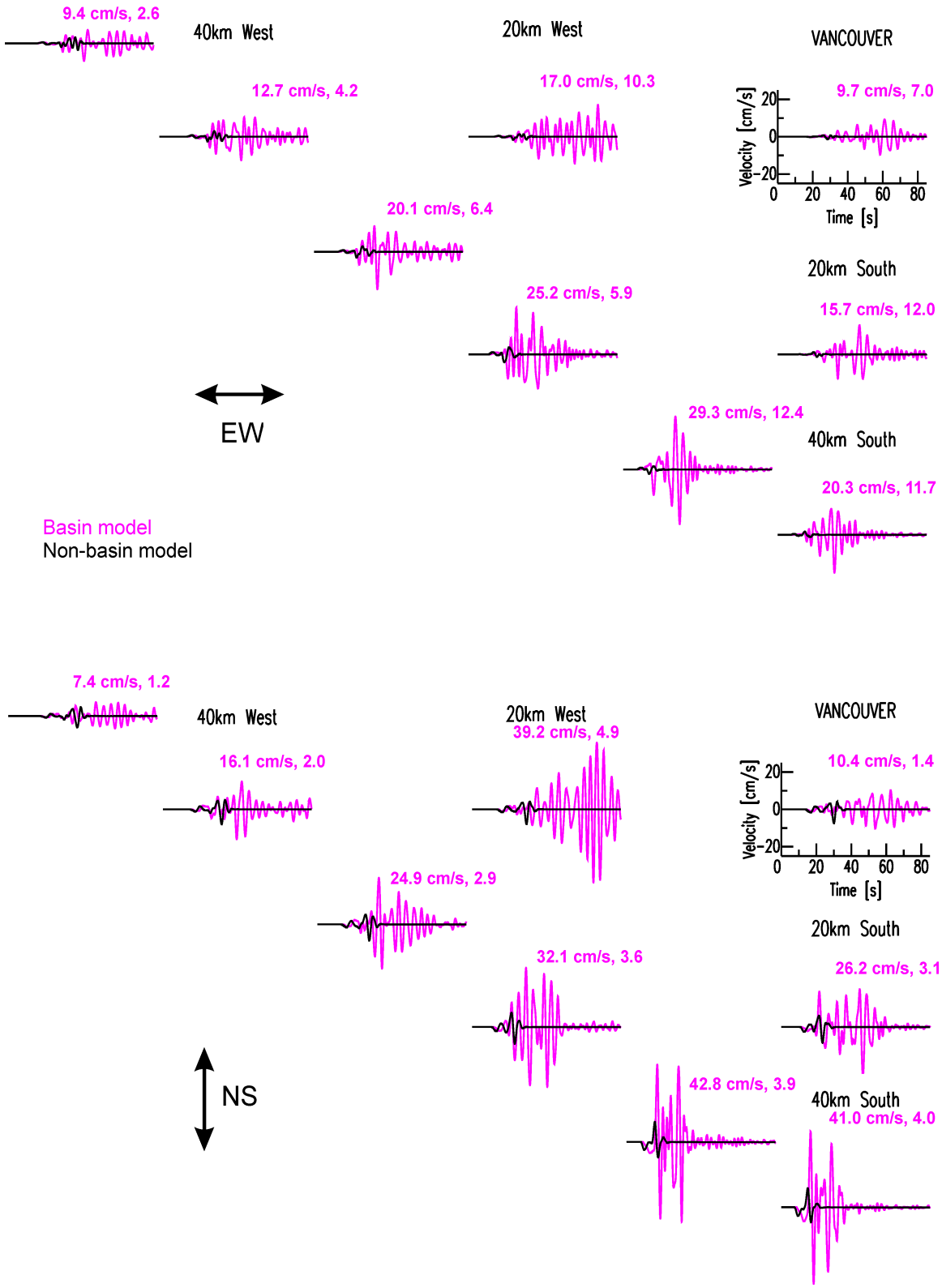

Figure 51. Synthetic waveforms for the SJI scenario earthquake at locations shown by white circles in Figure 50.

The pattern of basin-amplified peak motion and associated comparison of basin and non-basin waveforms at 20 sites selected across Greater Vancouver are shown in Figure 52. At the 20 sites across Greater Vancouver, the average horizontal basin model PGV is 13.9 ± 6.8 cm/s, corresponding to intensity VI (Table 9), and the average increase in peak motion due to presence of the Georgia basin is 6.0 ± 6.8. Overall, both horizontal directions of motion demonstrate similar zones of basin amplification, an onshore circular region in SW Greater Vancouver, and offshore regions W and S of Vancouver. These zones of high amplification were also observed from simulations of deep JdF plate earthquakes (Figure 43 and Figure 44). The circular zone of high amplification in SW Greater Vancouver is due to a large arrival at 50-60 s in the basin waveforms (Figure 52), similar to the deep JdF plate scenarios. For the SJI scenario here, as the SE basin-edge generated surface waves propagate N across Greater Vancouver, constructive interference amplifies the 50-60 s arrivals predominantly at W-most locations in southern Greater Vancouver (Richmond and Ladner).

Plan and cross-section time-snapshots of the simulation are presented in Figure 53 for EW motion. Northward propagation of surface waves is apparent early in the simulation and interference between scattered waves in the basin sediments is apparent later in the simulation. In plan view, there is a warping of the surface wave fronts as they propagate N towards the location of high basin amplification in SW Greater Vancouver (white filled square) primarily coincident with basin structure in the upper 1 km. The constructive interference of surface waves at the basin-edge here causes higher amplitude waves to propagate N out of the basin (observed at 75 s in the simulation). Comparison of the EW and NS waveforms is discussed further in Section 3.6 with respect to those of the deep JdF plate scenario simulations.

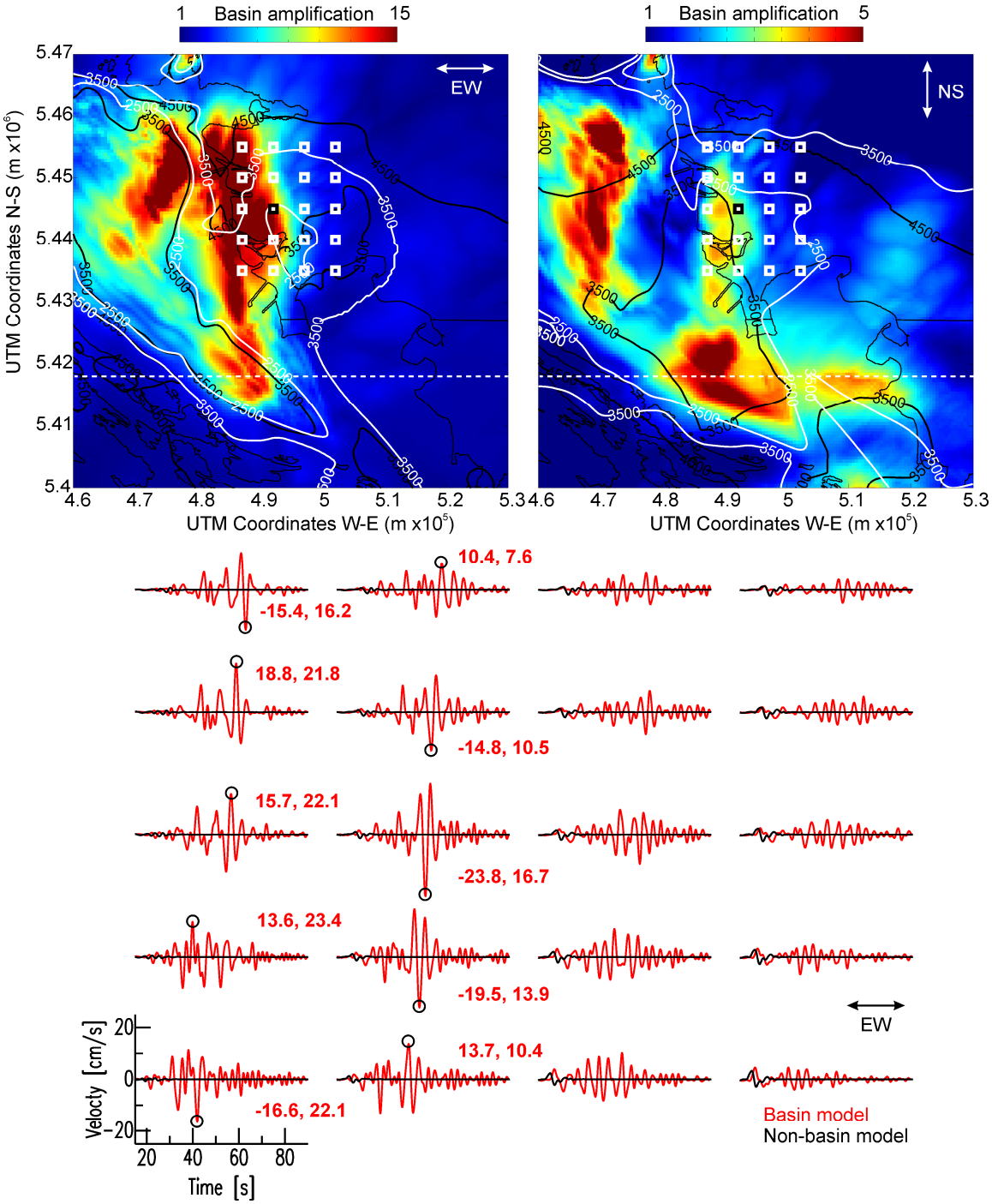

Figure 52. Maps of basin amplification for the SJI scenario (thin black line is coastline and dashed white line corresponds to W-E cross-sections shown in Figure 53). On EW map, contours of basin V_P model at 500 m (thick white lines) and 750 m (thick black lines) depth are shown. On NS map, contours of basin V_P model at 250 m (thick white lines) and 1 km (thick black lines) depth are shown. Comparison of EW synthetic waveforms at 20 selected sites across Greater Vancouver (shown by squares in maps). Solid circles denote PGV and red numbers correspond to PGV (cm/s) and basin amplification factor.

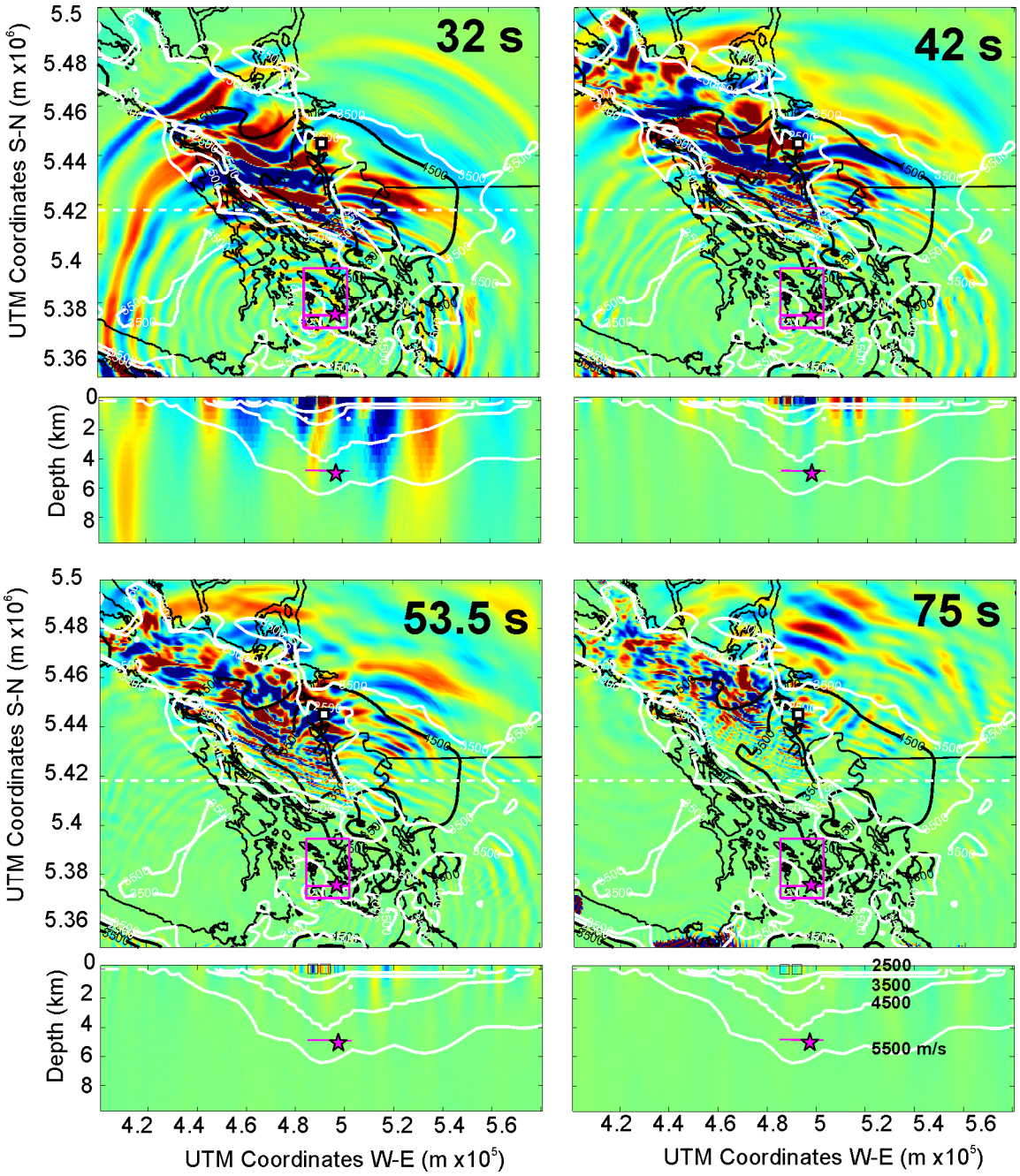

Figure 53. Time snapshots of simulated EW motion for SJI scenario (saturation of the blue (red) hue corresponds to PGV of -5.0 (5.0) cm/s**)**. Plan view snapshots show coastline (thin black line), contours of basin V_P model at 250 m depth (white lines) and 1 km (thick black lines) depth, location of W-E cross-section (dashed white line), location of investigated basin amplification (white square), earthquake epicentre (star), and projected 45° N-dipping fault plane (magenta box). Cross-section snapshots show contours of basin V_P model (white lines) and projected fault trace (magenta line) and hypocentre (star) of SJI event.

3.5.3.2 Georgia Strait event

A shallow M_W 6.8 NA plate earthquake scenario is simulated at 5 km depth beneath NW Georgia Strait, 40 km W of Vancouver, for each of the basin and non-basin structure models. Distribution of predicted non-basin and basin model PGV for both horizontal directions and resulting basin amplification (basin/non-basin PGV) in the Georgia basin region are shown in Figure 54 for this scenario. The average maximum horizontal PGV in the region ranges from 33 cm/s to 183 cm/s for non-basin and basin model simulations, respectively. The strongest predicted shaking occurs near the epicentre in both cases, but > 30 cm/s shaking occurs towards the SE when basin sediments are included. Maximum amplification in peak horizontal motion due to 3D basin structure is ~20. Zones of high basin amplification occur W and S of Greater Vancouver in Georgia Strait as observed for other scenarios. However, for this scenario, basin amplification extends further SE than previously observed into Bellingham, WA.

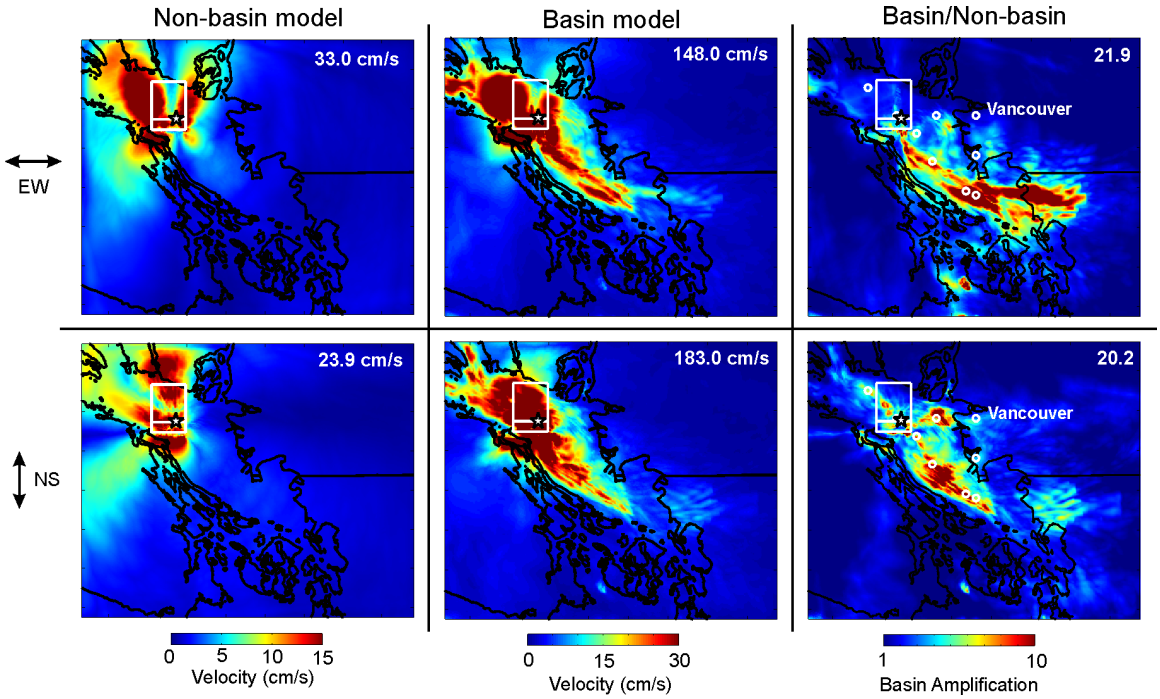

Figure 54. Maps of predicted PGV and corresponding basin amplification for the GS scenario earthquake. Details as provided in Figure 50.

Figure 55 presents comparison of basin and non-basin synthetic waveforms extracted at nine sites across the basin. Basin-edge generated surface waves arrive shortly after the initial S-wave arrival at NW sites close to the hypocentre. Surface waves

generated in the epicentral area propagate E and SE across the basin (Figure 56) and are associated with the first 40 s of simulation at SE-located sites (Figure 55). For the SE-located sites, a large negative arrival occurs at ~50 s in the basin model waveforms (Figure 55). Cross-section time-snapshots of the basin model simulation show that this phase penetrates as much as 4 km into the basin, and occurs from constructive interference of E- and SE-propagating surface waves as they are focussed in the deep SE portion of the basin (Figure 56 and Figure 57). Surface waves persist here and even increase in amplitude near the end of the 90 s simulation. For Bellingham, WA, the high basin response observed in Figure 54 is related to focussing of late-arriving SE propagating surface waves (Figure 56) due to shallowing of basin sediments offshore W WA (Figure 57). The SE-propagating surface waves leak E across Greater Vancouver with relatively low amplitude due to a lack of constraining basin structure here (Figure 57). Average horizontal peak motion predicted at 20 sites across Greater Vancouver for the Georgia basin model is 4.0 ± 1.6 cm/s, corresponding to intensity V. The average increase in peak horizontal motion due to 3D basin structure is 3.0 ± 0.9 times the non-basin model level.

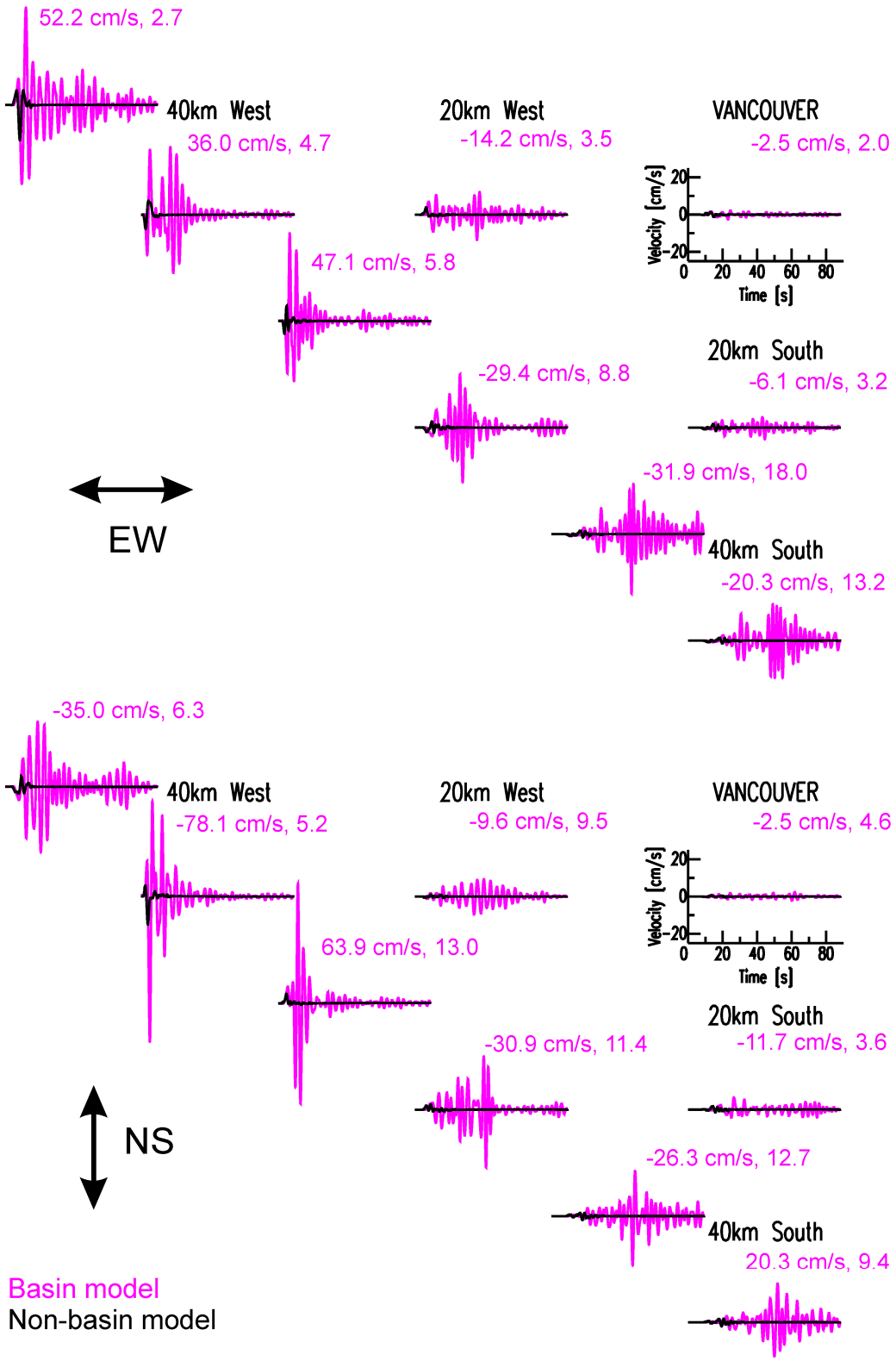

Figure 55. Synthetic waveforms for the GS scenario earthquake at locations shown by white circles in Figure 54.

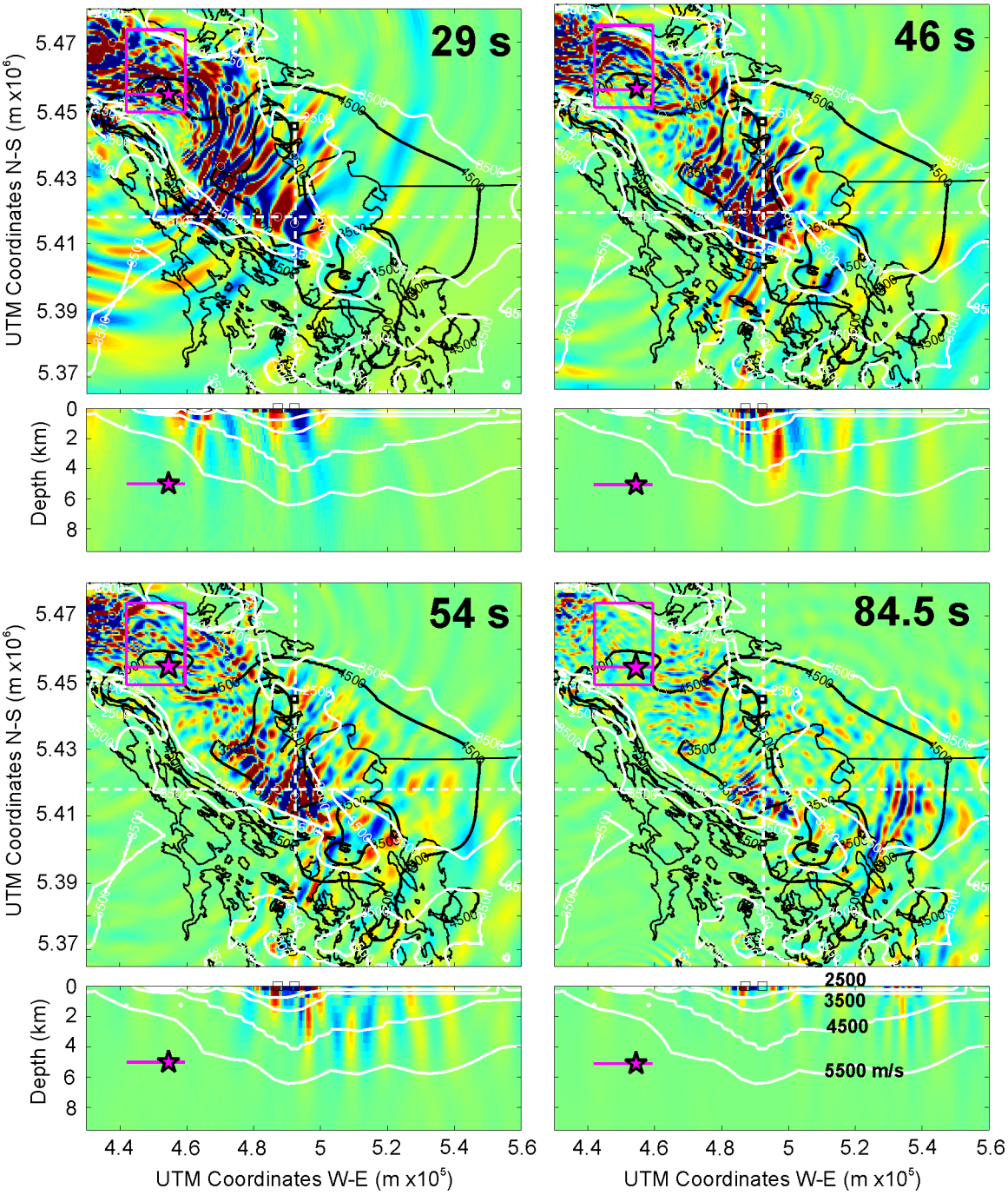

Figure 56. Time snapshots of simulated EW motion for GS scenario. Details as provided in Figure 53.

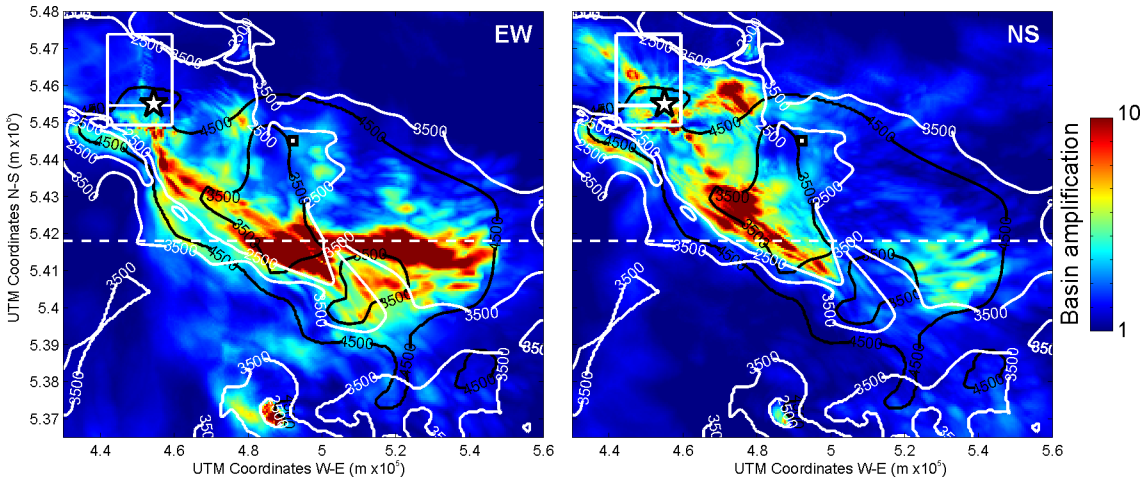

Figure 57. Maps of basin amplification with contours of the basin V_P model at 250 m (thick white lines) and 1 km (thick black lines) depth. Dashed white line corresponds to W-E cross-section shown in Figure 56.

3.5.4 Discussion

For both shallow M_W 6.8 NA plate scenarios, very strong ground motions (> 20 cm/s) occur in Georgia basin and the largest basin-edge surface waves are generated closest to the epicentre. On average, higher ground motions occur in the basin for the GS scenario located 40 km W of Vancouver than the SJI scenario located 80 km S of the city (Table 11). For the SJI scenario, large basin-edge surface waves are generated in the deeper SE part of the basin, then propagate predominantly N beneath Greater Vancouver where they are focussed (amplified) by shallowing of the basin, and then exit the basin NW of Vancouver with increased amplitude. For the GS scenario, larger basin-edge surface waves are generated in the shallower and steeper NW part of the basin and propagate both E and along the long axis of the basin (NW-SE sense), past Greater Vancouver, and into the deeper SE basin where they are focussed and persist for the duration of the 90 s simulation. Hence, for the same given large blind-thrust earthquake, greater shaking and basin amplification occurs when the fault ruptures beneath the NW part of the basin (Table 11). The impact to Greater Vancouver is the opposite; greater shaking and basin amplification are predicted for the SJI scenario located 80 km S (Table 11) due to focussing of surface waves generated in the deeper SE part of the basin as they propagate N beneath the city. Conclusions drawn here are based on simulation of only two shallow NA plate earthquakes with the same source radiation pattern, which is not an extensive

examination of potential basin effects for these types of earthquakes. Further discussion and recommendations for future work are outlined in Section 3.7.

Table 11. Average peak horizontal motion and peak horizontal basin-amplified motion in Georgia basin and Greater Vancouver for two shallow NA plate earthquake scenarios.

Scenario (distance from Vancouver)	Average of 6 sites in Georgia basin		Average of 20 sites across Greater Vancouver	
	Basin-model PGV (cm/s)	Basin/Non-basin PGV factor	Basin-model PGV (cm/s)	Basin/Non-basin PGV factor
SJI (80 km S)	23.4 ± 11.5	5.1 ± 3.6	13.9 ± 6.8	6.0 ± 6.8
GS (40 km W)	39.3 ± 17.8	9.3 ± 4.5	4.0 ± 1.6	3.0 ± 0.9

3.6 Comparison of deep and shallow earthquake scenarios

Simulations of both deep JdF plate and shallow NA plate M_W 6.8 earthquake scenarios have been conducted in the NW and S-SW regions of the 3D structure models. In this section, the 3D basin response is examined for both deep and shallow events with a similar epicentre location and implications to seismic hazard in Greater Vancouver is discussed.

For discussion of S-SW located sources, the shallow SJI scenario of Section 3.5.3.1 is compared with deep JdF plate scenarios 9 and 10. Comparison of Georgia basin model PGV maps (Figure 50 for the shallow source and Figure 39 and Figure 40 for the deep sources) indicates significantly higher ground motions are predicted for a shallow source than a deep source in the same location, as expected, but also demonstrates a similar distribution: high amplitudes occur at the epicentre location and in the deep SE part of the basin (S of Greater Vancouver). The pattern of basin-amplified peak motion (Figure 44 and Figure 52) is similar; highest basin amplification occurs in a localized circular zone in S-SW Greater Vancouver and offshore to the S and W. Figure 58 shows that the predicted ground shaking (basin model waveform) at the location of high basin amplification in Richmond (white squares in Figure 43, Figure 53 and Figure 56) is remarkably similar between the two types of earthquakes, displaying the largest amplitude arrival between 40-60 s. Basin-edge surface waves are generated as first arrival source-generated S-waves traverse the S edge of the deeper SE part of the basin, then propagate predominantly N-NE across the basin. Surface wave amplitudes generally decay during N propagation; however, constructive interference in a localized circular

region in Richmond causes the arrival at 40-60 s to increase due to focussing of surface waves as the basin shallows here. This occurs in the same location for both horizontal directions of motion when the waves propagate N (shallow SJI scenario, Figure 53), but when the waves propagate NE (deep JdF plate scenario, Figure 46) constructive interference occurs in the same location for EW motion and at sites 10 km E for NS motion (not shown).

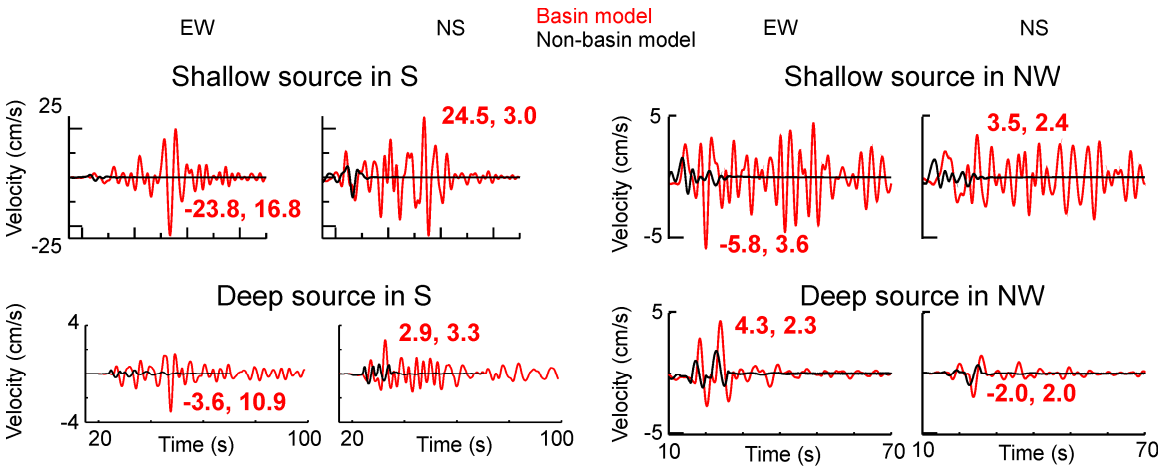

Figure 58. Comparison of synthetic waveforms in Richmond for deep and shallow earthquakes with epicentre locations in the S and NW part of the basin region.

For NW located sources, the shallow GS scenario of Section 3.5.3.2 is compared with deep JdF plate scenario 2. Similar to the comparison of S-SW located sources, higher ground motions result from the shallow source than the deep source as expected, particularly in the epicentral area and in the deep SE part of the basin (Figure 54 for the shallow source and Figure 39 and Figure 40 for the deep source). However, the overall distribution of peak ground motions is slightly different between the two types of sources, primarily due to different source radiation patterns. Amplification due to 3D basin structure (Figure 54 and Figure 59) is similar between source types for EW motion, in which the highest basin amplification occurs SE of the NW-located epicentres, whereas for NS motion, the highest amplification occurs SE and NW of the shallow and deep epicentre locations, respectively. These observations are also demonstrated by comparison of the basin waveforms in Greater Vancouver for the two types of sources (Figure 58), in which the level of shaking is similar but the waveforms are different. For the deep source, PGV is associated with first arrival source-generated S-waves which

does not generate significant surface waves, whereas for the shallow source, PGV is associated with an early basin-edge generated surface wave but the entire 90 s waveform is composed of similar amplitude arrivals.

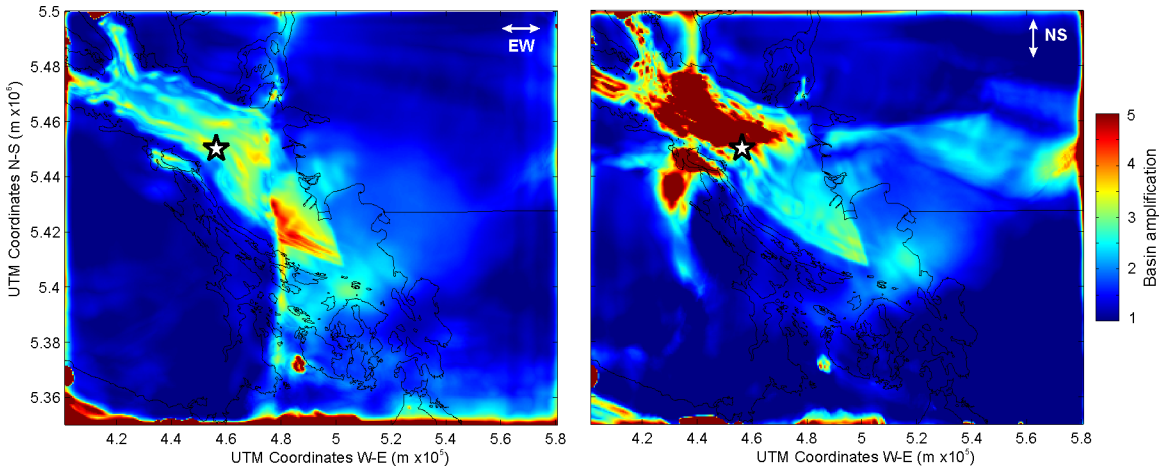

Figure 59. Maps of basin amplification for M_W 6.8 JdF plate earthquake scenario 2 located 40 km W of Greater Vancouver (epicentre shown by star and black line is coastline).

The duration of strong shaking is investigated in Greater Vancouver for deep and shallow earthquakes. Bommer & Martinez-Pereira (1999) review 30 different definitions of strong motion duration and define three generic groups: (1) bracketed or envelope duration is the time interval between the first and last amplitude of a specified threshold level, (2) effective or uniform duration is the sum of the time periods during which the amplitude is greater than the specified threshold, and (3) significant duration is based on the accumulation of energy in a waveform represented by the integral of the squared time-series record bounded by specified threshold levels. All definitions rely on an arbitrarily-chosen threshold level; hence, there is no universally accepted definition (Bommer & Martinez-Pereira 1999). The threshold level chosen here is 3.4 cm/s, the division between shaking intensity IV and V given in Table 9. Examination of $\geq$ 3.4 cm/s shaking in Greater Vancouver is investigated for two earthquake scenarios: deep JdF plate earthquake scenario 2 and shallow NA plate earthquake scenario SJI.

The total amplitude of horizontal motion (Tumarkin & Archuleta 1997) is calculated here as

$$A(t) = \sqrt{a_{EW}(t)^2 + a_{NS}(t)^2}\ , \tag{38}$$

where $a_{EW}(t)$ and $a_{NS}(t)$ are the EW and NS velocity waveforms, respectively. Both bracketed and effective durations are calculated at a threshold of 3.4 cm/s for horizontal waveforms of the two scenario earthquakes at two locations in Greater Vancouver (Figure 60). Significant durations are not presented here since the cumulative integral of total horizontal waveform amplitude is different between the two scenarios and a common threshold is not applicable. Figure 60 shows the duration of > 3.4 cm/s shaking is longer for a shallow event due to sustained basin-generated surface waves, whereas for a deep earthquake the duration of high amplitude shaking is short, related to early S-wave arrivals that do not persist. For the shallow NA plate scenario earthquake, the effective duration of > 3.4 cm/s shaking in Vancouver and Ladner is up to 16 times longer due to the presence of the 3D Georgia basin.

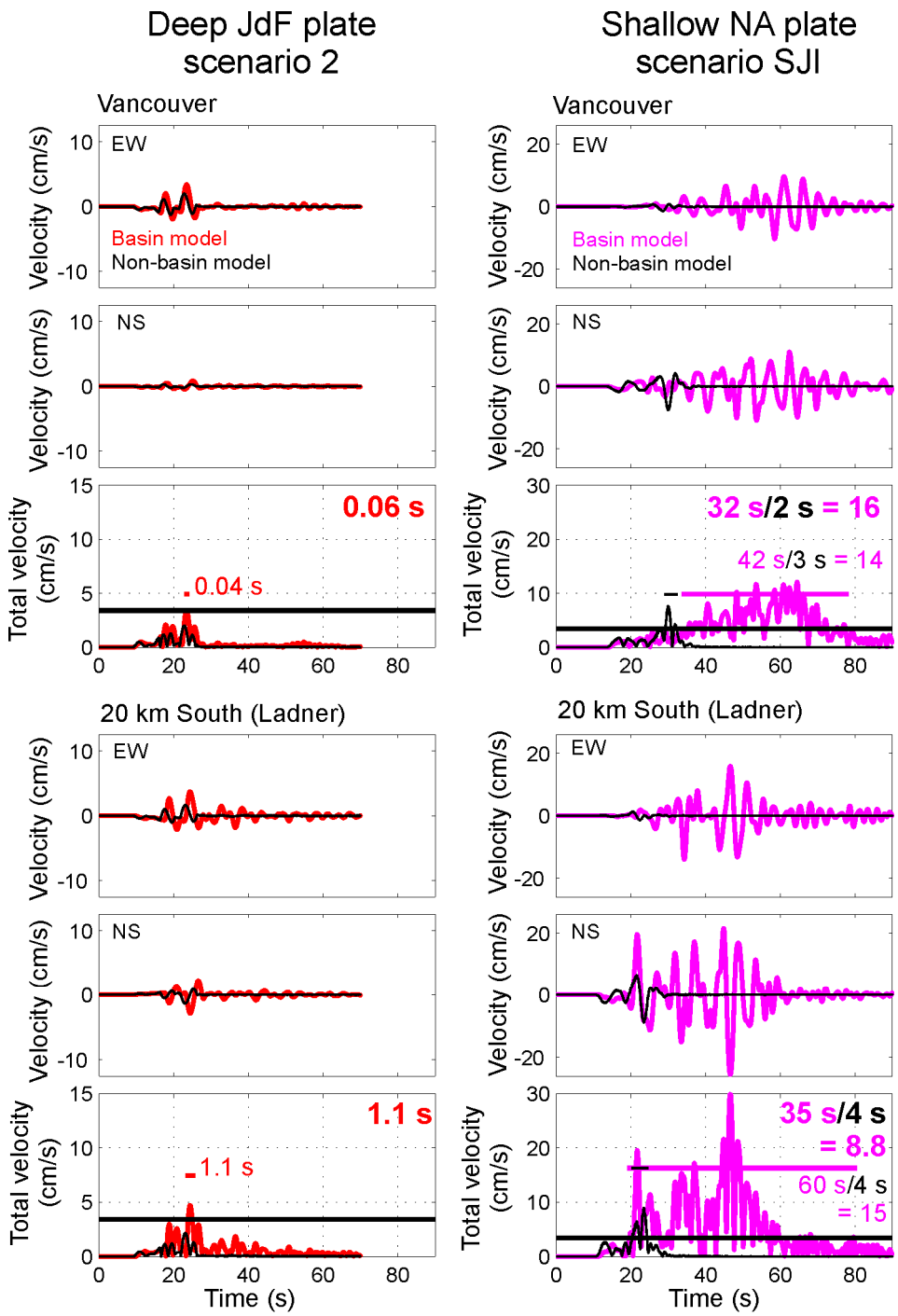

Figure 60. Comparison of horizontal waveforms and total horizontal amplitude at two sites in Greater Vancouver for a deep JdF plate and shallow NA plate earthquake. Large numbers given in top right of panels correspond to effective duration of > 3.4 cm/s shaking. The colour bar and number denotes the bracketed duration of 3.4 cm/s shaking.

3.7 Conclusions

Finite-difference modelling of 3D long-period (> 2 s) ground motions is conducted here for large (M_W 6.8) scenario earthquakes to investigate effects of the Georgia basin structure in SW British Columbia. Shorter period ground motions are not resolved, limited by the grid spacing and minimum V_S chosen for the 3D basin model according to a 5 node per minimum shear wavelength rule-of-thumb commonly used for fourth-order finite-difference schemes. The Pacific Northwest 3D velocity model of Stephenson (2007) is used as the base elastic structure model. The minimum V_S is set to 625 m/s, representative of a Pleistocene glacial (stiff) sediment surface. The Georgia basin is elongate in a NW-SE orientation, with depths of < 3 km NW and < 7 km SE of Greater Vancouver. The upper 1 km of the 3D structure model is revised in the Georgia basin region using recent geologic and geophysical information from a variety of sources. A non-basin model is generated from the updated 3D basin model by setting the minimum V_P to 5.5 km/s, effectively removing the lowest velocity (basin) sediments. The quantitative measure of 3D Georgia basin effects used here is calculation of the increase in peak motion for basin and non-basin model simulations (basin/non-basin PGV factor). Two sets of viscoelastic 3D basin models are generated with either high or low anelastic attenuation assigned to the lowest-velocity basin sediments. However, this does not significantly affect predicted long-period ground motions.

Earthquakes in both the upper crust of the NA plate and within the subducting JdF plate are simulated within the Georgia basin region with hypocentres in realistic locations based on known seismicity. Shallow NA plate events are characterized here by EW-striking blind-thrust faults which initially rupture at 5 km depth then propagate predominantly N (down-dip). The fault plane is discretized into 196 sub-faults which each release different portions of the total seismic moment in 2 s bursts, based on the slip distribution of the M_W 6.7 Northridge earthquake. Deep JdF plate earthquakes are characterized by the source process of the 2001 M_W 6.8 Nisqually earthquake: a N-striking steeply E-dipping normal fault event that ruptures at a single point in two 4.0-4.5 s pulses separated by 1.5 s. The magnitude chosen to simulate scenario earthquakes in the Georgia basin region is M_W 6.8, equivalent to 1.8×10^{19} Nm of total seismic moment. The ground motions predicted here may be adjusted to other magnitudes based on variation in

total seismic moment. For example, adjustment of predicted amplitudes to M_W 7.0 or 7.3 earthquakes is a factor of 2 or 5.

Comparing predicted waveforms from finite-difference modelling to seismograms of the 2001 M_W 6.8 Nisqually earthquake demonstrates that general agreement in amplitude and phase of first arrival S-waves is obtained at stations in the Seattle basin within 100 km of the source. In this near-source region, estimates of PGV display high goodness-of-fit factors (this study and Pitarka et al. 2004) and are over-predicted by a factor of ~1.6 (this study) and 1.1 (Frankel et al. 2009). Overall, general agreement of waveforms in the near-source region is achieved and provides confidence in the use of the Nisqually earthquake source model to simulate large JdF plate scenario earthquakes in the Georgia basin region. Predicted long-period ground motions in Vancouver and 20 km S in Ladner are < 1 cm/s but are significantly amplified due to the presence of 3D Georgia basin structure by an average of 8 times relative to peak non-basin motion.

For all simulations, some general effects are observed consistently when Georgia basin sediments (1.5 km/s < V_P < 5.5 km/s) are included in the 3D structure model. The symmetry of the seismic radiation pattern is distorted and the area of strong ground motion is increased. Surface waves are generated in the SE and NW parts of the basin coincident with steep basin edges in the upper 1 km of the model. The distribution of basin-amplified motion primarily corresponds to the lowest-velocity sediments at the 500 and 750 m depth surfaces, related to V_S of 1.5-2.0 km/s. Hence, the use of $Z_{1.5}$ or $Z_{2.0}$ as a predictor of basin amplification is likely an appropriate measure for the Georgia basin. Overall, stronger and longer ground shaking occurs across Greater Vancouver for earthquakes located S-SW of the city at distances greater than ~80 km, regardless of source depth and rupture style.

A total of 11 deep (42-55 km) JdF plate earthquakes are simulated beneath Georgia Strait based on known seismicity, with ~30-40 km gridded spacing between epicentre locations. The seismic radiation pattern of all deep JdF plate earthquake simulations generates the largest ground motions immediately W of the epicentre in the EW direction of horizontal motion. The average maximum horizontal peak ground motion for a M_W 6.8 JdF plate earthquake in the Georgia basin model is 8.1 ± 3.5 cm/s (one standard deviation uncertainty) and the average maximum basin amplification

(basin/non-basin PGV) is 10.8 ± 7.0, i.e. average increase in peak motion is an order of magnitude larger than the background peak motion. The average basin amplification at 20 sites across Greater Vancouver is 2.3 ± 1.1. The highest basin amplification in the city is associated with earthquakes located SW of the city. A total of 13 other M_W 6.8 JdF plate scenario earthquakes are simulated in the SW corner of the model to fully investigate the cause of high basin response in Greater Vancouver. Basin amplification reaches a maximum of 11 in a localized region 10 km S of Vancouver (in Richmond) for these events due to constructive interference of NE-propagating surface waves focussed by shallow (< 1 km) basin structure beneath the city. The high basin amplification is associated with an arrival at 40-50 s which dominates the basin model waveform when the epicentre is within 20 km of the SW corner location.

Two NA plate earthquake simulations are conducted in locations of shallow recurrent seismicity: a source located 40 km W of Vancouver beneath Georgia Strait and a source located 80 km S of the city beneath San Juan Island, WA. The radiation pattern of the shallow NA plate earthquake simulations generates high ground motions immediately E and N of the epicentre in both horizontal directions of motion. High ground motions occur elsewhere in the region depending on the propagation direction of basin-edge generated surface waves; amplification due to 3D basin structure occurs SE and N of epicentres located NW and S of Greater Vancouver, respectively. Across Greater Vancouver, the average maximum horizontal peak ground motions (and basin amplification factor) are 4.0 cm/s (3 times background level) and 14 cm/s (6 times) for the two NA plate events located to the NW and S, respectively.

Of the M_W 6.8 earthquake scenarios considered, the earthquake that generates the strongest and longest ground motions in Greater Vancouver is a shallow blind-thrust NA plate earthquake 80 km S of the city with peak ground motions of ~10 cm/s due to multiple-cycles of later-arriving basin-edge-generated surface waves (duration of shaking > 3.4 cm/s is up to 16 times longer than if Georgia basin sediments are not included). Similar shaking levels of ~7 cm/s occur across Greater Vancouver for a deep JdF plate earthquake located ~25 km E of the city, but are associated with short durations due to early-arriving source-generated S-waves which do not persist. Interestingly, for a shallow or deep earthquake directly S of the city, the same waveform (i.e. 3D basin response) is

generated for both horizontal directions; if the epicentre is moved W the similarity between both horizontal waveforms is reduced, but higher amplitudes occur for the shallow case, as expected. However, if a shallow or deep earthquake occurs NW of Greater Vancouver, shaking is generally ≤ 5 cm/s but the duration of shaking is longer for a shallow event due to sustained basin-generated surface waves and shorter for a deep event due to source-generated S-waves.

It is worth noting that mid-crustal NA plate earthquakes which predominantly occur at 15-25 km depth have not been addressed here, but are assumed to produce lower ground motions for the corresponding shallow NA plate scenario. Rupture of the entire locked thrust fault of the Cascadia subduction zone is beyond the scope and computational feasibility of this work. Olsen et al. (2008a) simulated a N-rupturing M_W 9.0 Cascadia mega-thrust scenario, based on source characteristics of the 2004 M_W 9.1-9.3 Sumatra-Andaman mega-thrust earthquake, and predict long-period (> 2 s) ground motions in Vancouver with maximum peak ground velocity of 10 cm/s and effective durations of moderate shaking (> 5 cm/s) of ~4 minutes. In comparison, similar peak ground motion amplitudes are predicted across Greater Vancouver here for a large shallow NA plate earthquake 80 km S of the city, but the effective duration of ≥ 5 cm/s shaking is 22-27 s, much shorter than the duration of the M_W 9 mega-thrust event, as expected.

The work presented in this chapter is a first attempt to address the effect of 3D Georgia basin structure on earthquake ground shaking in Greater Vancouver and the first such study for a sedimentary basin in Canada. The results provide significant insight to the expected amplification in ground shaking due to 3D basin structure. Limitations of this work include: uncertainty in accuracy of physical-structure and source-rupture models; omission of low-velocity (V_S < 625 m/s) materials in the 3D structure models, such as water and up to 300 m of Holocene Fraser River delta sediments; omission of surface topography; inability to resolve frequencies > 0.5 Hz; and the low number of scenarios overall. Conclusions as to the overall most hazardous scenario earthquake are limited to the simulations conducted here and are specific to the chosen epicentre locations and earthquake rupture styles. The realistic scenario earthquakes considered here show that 3D Georgia basin structure can amplify shaking up to ~17 times in

Greater Vancouver. In addition, the duration of moderate shaking (> 3.4 cm/s) is up to 16 times longer due to sustained basin-generated surface waves. Overall, this study has shown that the presence of 3D Georgia basin structure increases the level and duration of predicted long-period ground shaking, effects typically related to earthquake damage.

3.7.1 Future work

Recent advances in finite-difference methods, source models, and computer speed would allow more complete and realistic ground motion prediction in the future. For instance, finite-difference codes that employ non-uniform gridding (e.g. Pitarka 1999, Liu & Archuleta 2002) would improve computational efficiency, especially with respect to simulations of deep JdF plate events. Inclusion of surface topography in finite-difference schemes is becoming more common (e.g. Aagaard et al. 2008), whereas the effect of anelastic attenuation may still be excluded (e.g. Nilsson et al. 2007). Advances in characterization of the source rupture process include dynamic (e.g. Olsen et al. 2008b) or stochastic-dynamic (Guatteri et al. 2004; Mai et al. 2001) rupture models rather than the kinematic slip models used here. Dynamic rupture models include spontaneous rupture fluctuations or are characterized by less coherent wavefields as they include variability in speed, shape, and direction of the slip (Mai et al. 2001; Olsen et al. 2008b), which have the effect of lowering predicted ground motions (Olsen et al. 2008b).

The updated 3D physical structure model can be further improved by: (1) incorporation of the 600-m gridded SHIPS tomography V_P model of Dash et al. (2007) (only the 800-m surface was used here), (2) validation by comparison with empirical earthquake recordings, either existing weak-motion recordings of lower magnitude earthquakes with focal mechanism solutions or future recordings of large earthquakes, (3) reduction in spatial resolution (greater smoothing) of the updated upper 1-km structure in accordance with the low frequency simulations, and (4) increasing the maximum depth to ~80 km for simulation of JdF plate earthquakes (constrained to maximum depth of 55 km here).

Conclusions as to the most hazardous deep JdF plate earthquake for Greater Vancouver are relatively robust since the most-likely locations and rupture style of such an event have been included in the simulations presented here. However, conclusions as to the most hazardous shallow NA plate earthquake require additional future work. In this

thesis, scenario NA plate earthquakes are simulated in the location of potential (small) active faults with the radiation pattern of a real earthquake as a first step. The next steps could include simulating NA plate events in locations of known fault and lineament structures or in a gridded manner similar to that of the JdF plate scenarios. Further, the radiation pattern could be systematically altered (up- or down-dip ruptures, greater slip up- or down-dip, strike-slip radiation patterns, variable rise times per sub-fault, variable rupture velocity, etc.). Due to the limited knowledge of large shallow NA plate earthquakes in the region, the simulation possibilities are fairly open-ended. However, it is only knowledge of the location and rupture character of future large NA plate earthquakes in southwestern British Columbia that is unknown, not the potential of such events. A recent comparable example is the 4 September 2010 M_W 7.1 shallow (11 km) earthquake that ruptured 40 km westward of Christchurch, New Zealand, along a previously unknown fault buried below the Cantebury alluvial valley. On 22 February 2011, a M_W 6.3 aftershock occurred along another buried fault structure 10 km south of the city at 5 km depth causing severe damage and casualties. Predicting earthquake ground shaking due to 3D basin structure in southwestern British Columbia is considered an important step towards understanding the potential impact of future large earthquakes here.

4 CONCLUSIONS

This thesis explores and develops two current methodologies to examine potential earthquake ground shaking amplification in SW British Columbia based on 1D soil layering and 3D basin structure.

4.1 Predicting earthquake ground shaking due to 1D soil layering

A methodology to obtain and validate uncertainty estimates of 1D site amplification from microtremor array data is developed. The microtremor array method determines phase velocity dispersion of Rayleigh surface waves from multi-instrument recordings of urban noise. Inversion of dispersion curves for V_S structure is a non-unique and nonlinear problem such that meaningful evaluation of confidence intervals is required. Quantitative uncertainty estimation requires not only a nonlinear inversion approach that samples models proportional to their probability, but also rigorous estimation of the data error statistics and an appropriate model parameterization. To achieve this, a Bayesian formulation is developed which represents the solution of the inverse problem in terms of the posterior probability density (PPD) of the geophysical model parameters. Markov-chain Monte Carlo methods are used with an efficient implementation of Metropolis-Hastings sampling to provide an unbiased sample from the PPD to compute parameter uncertainties and inter-relationships. Nonparametric estimation of the data error covariance matrix from residual analysis is applied with rigorous *a posteriori* statistical tests to validate the covariance estimate and the assumption of a Gaussian error distribution. The most appropriate model parameterization is determined using the Bayesian information criterion, which provides the simplest model consistent with the resolving power of the data. Parameterizations considered vary in the number of layers, and include layers with constant velocity as well as linear and power-law gradients. Parameter uncertainties are found to be under-estimated when data error correlations are neglected and when compressional-wave velocity and/or density (nuisance) parameters are fixed in the inversion.

The microtremor array method is applied at two sites of contrasting site amplification behaviour in SW British Columbia to examine its effectiveness in

retrieving V_S profiles of the 1D soil column in relatively deep (> 200 m) and shallow (< 20 m) geological settings on the Fraser River delta in Greater Vancouver and in Victoria, respectively. The V_S profiles obtained by Bayesian inversion are compared with invasive V_S measurements to assess their reliability for calculations of potential earthquake ground motion amplification. A well resolved V_S profile to at least 110 m depth is determined at the Fraser River delta site for a power-law gradient parameterization. At the Victoria site, a layer with low V_S and a weak linear gradient is indicated to 15-18 m depth, above much higher velocity material. At both sites, excellent agreement is obtained between the Bayesian microtremor inversion results and invasive V_S measurements from seismic cone penetration testing and/or surface-to-downhole methods.

Site response probability analyses are performed in which uncertainty in predicted linear site amplification and corresponding site response characterization are quantified due to the uncertainty in V_S structure from Bayesian microtremor inversion. Using a sample of V_S profiles drawn from the PPD, probability distributions are computed for common predictors of site amplification including V_{S30} (average shear-wave velocity in the upper 30 m), NEHRP site class, amplification of PGA (peak ground acceleration) and PGV (peak ground velocity), and root-impedance and SH-wave amplification spectra. The site amplification probability distributions for the two sites are shown to be much more informative than amplification estimated for a single best-fit V_S profile by characterizing the uncertainty and therefore level of confidence in the predictions. For the Fraser River delta site, the V_{S30} uncertainty distribution spans NEHRP site classes D and E with a 95% probability of class E, which is associated with higher amplification. At Victoria, the V_{S30} distribution occurs at the D/E class boundary with 58% probability of class D, associated with lower amplification, in disagreement with known earthquake response. These results indicate that V_{S30} is not a useful indicator of site response for the Victoria site. However, the V_{SZ} (average V_S to depth z) probability profile computed from the microtremor inversion indicates that V_{S15} would provide a meaningful indicator. The SH-wave amplification probability spectra are evaluated by comparison to empirical earthquake and microtremor spectral ratios, with generally good agreement in resonant peak frequencies and amplification levels, providing confidence that the primary influence of site-specific structure is appropriately accounted for. For the Fraser River

delta site, relatively low amplification at multiple modes is resolved; peak frequencies are determined within 0.4 Hz and amplification within a factor of 2. The inversion results provide useful SH-wave amplification estimates in reasonable agreement with the empirical spectra even though the basement layer is poorly resolved in this deep setting. For Victoria, the SH-wave amplification spectrum predicts the fundamental resonant frequency at 1.8 ± 0.3 Hz, with large uncertainties in amplification (factor of 5). The predicted fundamental peak frequency agrees well with that from empirical earthquake and microtremor spectral ratios.

4.2 Predicting earthquake ground shaking due to 3D basin structure

Finite-difference modelling of 3D wave propagation is used to address the effects of 3D Georgia basin structure on potential earthquake ground shaking in Greater Vancouver. The surface of the 3D basin model represents over-consolidated Pleistocene glacial sediments of the Fraser River delta; hence, long-period (> 2 s) ground motions predicted by finite-difference modelling are considered as the base input motions to the 1D soil layering (shown to increase ground shaking by a factor of ~2) and therefore considered to underestimate overall potential earthquake ground shaking in southern Greater Vancouver. The quantitative measure of amplification due to 3D basin structure used here is the ratio between predicted peak ground motions of scenario earthquakes in 3D models with and without Georgia basin sediments (i.e. a minimum V_P of 5.5 km/s for the background regional model).

The scenario earthquakes considered here include deep (42-55 km) JdF plate events with rupture characteristics of the normal-faulting 2001 M_W 6.8 Nisqually, WA, earthquake, and shallow (5 km) NA plate earthquakes characterized by rupture of the blind-thrust 1994 M_W 6.7 Northridge, CA, earthquake. Earthquake scenarios are simulated within the Georgia basin region in realistic locations based on known seismicity. Thus, predicted ground motions and 3D basin effects presented here are specific to the source models used, i.e. how the total seismic moment is distributed in time and space. The magnitude chosen to simulate scenario earthquakes in the Georgia basin region is M_W 6.8, which allows calibration of the synthetic waveforms with recordings of the 2001 M_W 6.8 Nisqually earthquake. General agreement in phase and

amplitude of predicted and empirical waveforms in the near-source region is achieved. Confidence in the use of the Nisqually source model to simulate large JdF plate earthquakes in the Georgia basin region is obtained.

The presence of Georgia basin sediments in the 3D structure model distorts the symmetrical seismic radiation pattern and increases the area of strong ground motion. Comparison of synthetic waveforms from simulation of a realistic scenario earthquake in each of the basin and non-basin 3D structure models clearly demonstrates that the level and duration of predicted shaking is significantly increased due to the 3D Georgia basin structure, effects which relate directly to earthquake damage. In the upper 1 km of the basin model, steep edges and the lowest-velocity sediments (V_S of 1.5-2.0 km/s) are coincident with the appearance of surface waves and high basin amplification areas, respectively. An appropriate predictor of basin amplification for the Georgia basin is likely the depth to V_S of 1.5 or 2.0 km/s, i.e. $Z_{1.5}$ or $Z_{2.0}$.

Of greatest interest is the potential increase in ground shaking across Greater Vancouver due to the 3D Georgia basin structure. The average increase in predicted peak horizontal motion due to the presence of the 3D Georgia basin (basin/non-basin PGV factor) determined at 20 sites across Greater Vancouver is 2.3 ± 1.1 for 11 deep JdF plate scenarios, 6.0 ± 6.8 and 3.0 ± 0.9 for the two NA plate scenarios, and is 7.5 ± 3.2 for the Nisqually earthquake. A possible explanation for variation in the basin-amplified peak motion was given by Olsen (2000) who examined peak basin-amplified motion for nine scenario earthquakes in the LA basin region and concluded: “amplification tends to increase with distance from the causative fault to the basin structure. It is possible that this pattern is due to higher amplification of the more complex wavefield impinging onto the basin structure from the distant earthquakes compared to that of the predominant body waves from nearby earthquakes.” This effect is clearly demonstrated from examination of the synthetic waveforms in southern Vancouver (Richmond) for JdF plate scenario earthquakes simulated in 5-km increments N and E of the SW corner of the model (e.g. Figure 43 of Section 3.4.3).

The cause of the highest basin amplification localized in southern Greater Vancouver is constructive interference of surface waves focussed by shallow (< 1 km) basin structure beneath the city. This focussing in southern Greater Vancouver only

occurs when surface waves propagate N-NE, i.e. for earthquakes located S-SW of the city which generate basin-edge surface waves in the upper 1 km of the SE basin. High amplification due to 3D basin structure always occurs for all types of earthquakes located S-SW of Greater Vancouver at distances greater than ~80 km, but high amplitude shaking only occurs if the input level of shaking is high, i.e. a shallow or near-by earthquake.

Of the M_W 6.8 earthquake scenarios considered, the earthquake that generates the strongest and longest ground motions in Greater Vancouver is a shallow blind-thrust earthquake 80 km S of the city, which generates peak ground motions of ~10 cm/s due to multiple-cycles of later-arriving basin-edge-generated surface waves. The duration of moderate (> 3.4 cm/s) shaking is up to 16 times longer than if Georgia basin sediments are not included. Similar shaking levels of ~7 cm/s occur across Greater Vancouver for a deep JdF plate earthquake located ~25 km E of the city, but are associated with short durations due to early-arriving source-generated S-waves.

Overall conclusions drawn by Olsen & Archuleta (1996) with respect to simulations of scenario earthquakes in the Los Angeles basin are valid here: “the 3D structure coupled with different source depths, mechanism, and rupture propagation highlight the large variability of the ground motion for earthquakes of similar seismic moment”. Finite-difference simulations of realistic large earthquakes in the Georgia basin region demonstrate stronger and longer ground shaking occurs across Greater Vancouver for earthquakes located S-SW of the city at distances greater than ~80 km, regardless of source depth and rupture style. Overall, a broad-scale understanding of the effect of 3D Georgia basin structure on ground shaking in southwestern British Columbia has been achieved. This study has shown that the presence of 3D Georgia basin structure increases the level and duration of predicted long-period ground shaking, effects typically related to the spatial distribution of earthquake damage.

REFERENCES

Aagaard BT, RW Graves, A Rodgers, TM Brocher, RW Simpson, D Dreger, NA Petersson, SC Larsen, S Ma & RC Jachens, 2010. Ground-motion modeling of Hayward fault scenario earthquakes, Part II: Simulations of long-period and broadband ground motions, *Bull. Seis. Soc. Am.*, **100**, 2945-2977.

Adams JA & S Halchuk, 2003. Fourth generation seismic hazard maps of Canada: Values for over 650 Canadian localities intended for the 2005 National Building Code of Canada, Geological Survey of Canada Open File 4459, 155 p.

Aki K, 1957. Space and time spectra of stationary stochastic waves, with special reference to microtremors, *Bull. Earthq. Res. Inst.*, **35**, 415-456.

Asten MW & JD Henstridge, 1984. Array estimators and use of microseisms for reconnaissance of sedimentary basins, *Geophys.*, **49**, 1828-1837.

Aster RC, B Borcher & CH Thurber, 2005. *Parameter Estimation and Inverse Problems*, Elsevier, Amsterdam.

Atkinson GM & K Goda, 2011. Effects of seismicity models and new ground-motion prediction equations on seismic hazard assessment for four Canadian cities, *Bull. Seis. Soc. Am.*, **101**, 176-189.

Avouac J, F Ayoub, S Leprince, O Konca & DV Helmberger, 2006. The 2005, M_w 7.6 Kashmir earthquake: Sub-pixel correlation of ASTER images and seismic waveforms analysis, *Earth Planet. Sci. Lett.,* **249**, 514-528

Bakır B, H Suoğlu & T Yılmaz, 1999. An overview of local site effects and the associated building damage in Adapazarı during the 17 August 1999 İzmit earthquake, *Bull. Seis. Soc. Am.,* **92**, 509-526.

Balfour NJ, JF Cassidy, SE Dosso & S Mazzotti, 2011a. Mapping crustal stress and strain in southwest British Columbia, *J. Geo. Res.*, **116**, B03314, doi:10.1029/2010JB008003.

Balfour NJ, JF Cassidy & SE Dosso, 2011b. Identifying active structures using double-difference earthquake relocations in southwest British Columbia and the San Juan Islands, WA, *Bull. Seis. Soc. Am.*, submitted.

Bard P-Y & M Bouchon, 1980. The two-dimensional resonance of sediment-filled valleys, *Bull. Seis. Soc. Am.*, **75**, 519-541.

Benites R & KB Olsen, 2005. Modelling Strong Ground Motion in the Wellington Metropolitan Area, New Zealand, *Bull. Seis. Soc. Am.*, **95**, 2180–2196.

Bodin T, & M Sambridge, 2009. Seismic tomography with the reversible jump algorithm, *Geophys. J. Int.*, **178**, 1411-1436.

Bolton MK, 2003. Juan de Fuca plate seismicity at the northern end of the Cascadia subduction zone, *M.Sc. thesis*, School of Earth and Ocean Sciences, University of Victoria, Victoria, B.C.

Bommer JJ & A Martinez-Pereira, 1999. The effective duration of earthquake strong motion, *J. Eq. Eng.*, **3**, 127-172.

Boore DM, 2003. Simulation of ground motion using the stochastic method, *Pure Appl. Geophys.,* **160**, 635-676.

Boore DM, 2004. Can site response be predicted?, *J. Earth. Eng.*, **8**, 1-41.

Boore DM, 2005. SMSIM – Fortan programs for simulating ground motions from earthquakes: Version 2.3 – a revision of USGS Open File Report 96-80-A, Online Manual, http://www.daveboore.com/software_online.htm.

Boore DM & WB Joyner, 1991. Estimation of ground motion at deep-soil sites in eastern North America, *Bull. Seis. Soc. Am.*, **81**, 2167-2185.

Boore DM & LT Brown, 1998. Comparing shear-wave velocity profiles from inversion of surface-wave phase velocities with downhole measurements: Systematic differences between the CXW method and downhole measurements at six USC strong-motion sites, *Seis. Res. Letters*, **89**, 222-229.

Boore DM & GM Atkinson, 2008. Ground-motion prediction equations for the average horizontal component of PGA, PGV, and 5%-damped PSA at spectral periods between 0.01 s and 10.0 s, *Eq. Spec.,* **24**, 99-138.

Boore DM & MW Asten, 2008. Comparison of shear-wave slowness in the Santa Clara valley, California, Using blind interpretations of data from invasive and noninvasive methods, *Bull. Seis. Soc. Am.*, **98**, 1983-2003.

Booth DB, RE Wells & RW Givler, 2004. Chimney damage in the Greater Seattle area from the Nisqually earthquake of 28 February 2001, *Bull. Seis. Soc. Am.*, **94**, 1143-1158.

Borcherdt RD, 1970. Effects of local geology on ground motion near San Francisco Bay, *Bull. Seis. Soc. Am.*, **60**, 29-61.

Borcherdt RD, 1994. Estimates of site-dependent response spectra for design (methodology and justification), *Earth. Spec*., **10,** 617-653.

Brocher TM, 2007. Key elements of regional seismic velocity models for long period ground motion simulations, *J. Seis.*, doi:10.1007/s10950-007-9061-3.

Brocher TM, 2008. Compressional and shear-wave velocity versus depth relations for common rock types in northern California, *Bull. Seis. Soc. Am.*, **98**, 950-968, doi:10.1785/0120060403.

Bustin A, RD Hyndman, A Lambert, J Ristau, J He, H Dragert & M Van der Kooij, 2004. Fault parameters of the Nisqually earthquake determined from moment tensor solutions and the surface deformation from GPS and InSAR, *Bull. Seis. Soc. Am.*, **94**, 363-376.

Calderón-Macías C & B Luke, 2007. Improved parameterization to invert Rayleigh-wave data for shallow profiles containing stiff inclusions, *Geophys.*, **72**, U1-U10.

Campbell KW & Y. Bozorgnia, 2008. NGA ground motion model for the geometric mean horizontal component of PGA, PGV, PGD, and 5% damped linear elastic response spectra for periods ranging from 0.01 to 10 s, *Eq. Spec.,* **24**, 139-171.

Capon J, 1969. High-resolution frequency-wavenumber spectrum analysis, *Proceedings IEEE,* **57**, 1408– 1418.

Cassidy JF, GC Rogers & FA Waldhauser, 2000. Characterization of active faulting beneath the Strait of Georgia, British Columbia, *Bull. Seis. Soc. Am.*, **90**, 1188-1199.

Cerjan C, D Kosloff, R Kosloff, M Reshef, 1985. Absorbing boundary conditions for acoustic and elastic wave equations, *Bull. Seis. Soc. Am.,* **67**, 1529-1540.

Chavez-Garcia FJ & J Tejeda-Jacome, 2010. Site response in Tecoman, Colima, Mexico-II. Determination of subsoil structure and comparison with observations, *Soil Dyn. Eq. Eng.*, **30**, 717-723.

Chiou B-S & RR Youngs, 2008. An NGA model for the average horizontal component of peak ground motion and response spectra, *Eq. Spec.,* **24**, 173-215.

Clague JJ, 1998. Geological setting of the Fraser River delta, *in* Geology and Natural Hazards of the Fraser River Delta, British Columbia, JJ Clague, JL Luternauer & DC Mosher (eds.), Geological Survey of Canada Bulletin 525, 7-16.

Clayton R & B Engquist, 1977. Absorbing boundary conditions for acoustic and elastic wave equations, *Bull. Seis. Soc. Am.,* **67**, 1529–1540.

Collino F & C Tsogka, 2001. Application of the PML absorbing layer model to the linear elastodynamic problem in anisotropic heterogeneous media, *Geophys.,* **66**, 294-307.

Cornou C, M Ohrnberger, DM Boore, K Kudo & P-Y Bard, 2006. Derivation of structural models from ambient vibration array recordings: Results from an International blind test, *in* Proceedings 3rd International Symposium on the Effects of Surface Geology on Seismic Motion, Grenoble, France, August 30th-September 1st, 2006.

Dalguer LA, K Irikura, JD Riera & HC Chiu, 2001. The importance of the dynamic source effects on strong ground motion during the 1999 Chi-Chi, Taiwan, earthquake: Brief interpretation of the damage distribution on buildings, *Bull. Seis. Soc. Am.*., **91**, 1112-1127.

Dallimore SR, KA Edwardson, JA Hunter, JJ Clague, JL Meldrum & JL Luternauer, 1995. Composite geotechnical logs for two deep boreholes in the Fraser River delta, British Columbia; Geological Survey of Canada, Open file 3018.

Dash RK, GD Spence, M Riedel, RD Hyndman & TM Brocher, 2007. Upper-crustal structure beneath the Strait of Georgia, Southwest British Columbia, *Geophys. J. Int.,* doi:10.1111/j.1365-246X.2007.03455.x

Day SM, 1998. Efficient simulation of constant Q using coarse-grained memory variables, *Bull. Seis. Soc. Am.,* **88**, 1051–1062.

Day SM, R Graves, J Bielak, D Dreger, S Larsen, KB Olsen, A Pitarka & L Ramirez-Guzman, 2008. Model for basin effects on long-period response spectra in southern California, *Eq. Spec.*, **24**, 257-277.

Day SM & CR Bradley, 2001. Memory-efficient simulation of anelastic wave propagation, *Bull. Seis. Soc. Am.,* **91**, 520-531.

Dettmer J, SE Dosso & CW Holland, 2007. Uncertainty estimation in seismo-acoustic reflection travel-time inversion, *J. Acoust. Soc. Am.*, **122**, 161-176.

Dettmer J, SE Dosso & CW Holland, 2009. Model selection and Bayesian inference for high-resolution seabed reflection inversion, *J. Acoust. Soc. Am.,* **125**, 706-716.

Dettmer J, S Molnar, G Steininger, SE Dosso & JF Cassidy, 2011. Trans-dimensional inversion of microtremor array dispersion data with hierarchial autoregressive error models, *Geoph. J. Int.*, submitted.

Di Giulio G, C Cornou, M Ohrnberger, M Wathelet & A Rovelli, 2006. Deriving wavefield characteristics and shear-velocity profiles from two-dimensional small-aperture arrays analysis of ambient vibrations in a small-size alluvial basin, Colfiorito, Italy, *Bull. Seis. Soc. Am.*, **96**, 1915-1933.

Dosso SE, 2002. Quantifying uncertainties in geoacoustic inversion I: A fast Gibbs sampler approach, *J. Acoust. Soc. Am.*, **111**, 2166-2177.

Dosso SE & MJ Wilmut, 2008. Uncertainty estimation in simultaneous Bayesian tracking and environmental inversion, *J. Acoust. Soc. Am.*, **124**, 82-97.

Dosso SE, MJ Wilmut & A-L S Lapinski, 2001. An adaptive-hybrid algorithm for geoacoustic inversion, *IEEE J. Ocean. Eng.*, **26**, 324-336.

Dosso SE, PL Nielsen & MJ Wilmut, 2006. Data error covariance in matched-field geoacoustic inversion, *J. Acoust. Soc. Am.,* **119**, 208-219.

Douglas J, P Gehl, LF Bonilla, O Scotti, J Regnier, A-M Duval & E Bertrand, 2010. Making the most of available site information for empirical ground-motion prediction, *Bull. Seis. Soc. Am.*, **99**, 1502-1520.

England TDJ & RM Bustin, 1998. Architecture of the Georgia basin, southwestern British Columbia. *Bull. Can. Pet. Geo.*, **46**, 288-320.

Fah D, F Kind & D Giardini, 2001. A theoretical investigation of average H/V ratios, *Geophys. J. Int.*, **145**, 535-549.

Fah D, F Kind & D Giardini, 2003. Inversion of local S-wave velocity structures from average H/V ratios, and their use for the estimation of site-effects, *J. Seis.*, **7**, 449-467.

FEMA P-750, 2009. NEHRP (National Earthquake Hazards Reduction Program) Recommended Seismic Provisions for New Buildings and Other Structures, Building Seismic Safety Council, Washington, DC, 406 p.

Field EH & KH Jacob, 1993. Monte-Carlo simulation of the theoretical site response variability at Turkey flat, California, given the uncertainty in the geotechnically derived input parameters, *Eq. Spec.,* **9**, 669-701.

Field EH & KH Jacob, 1995. A comparison and test of various site-response estimation techniques, including three that are not reference-site dependent, *Bull. Seis. Soc. Am.*, **85**, 1127-1143.

Finn WDL, E Zhai, T Thavaraj, X-S Hao, & CE Ventura, 2003. 1-D and 2-D analyses of weak motion data in Fraser Delta from 1996 Duvall earthquake, *Soil Dyn. and Earth. Eng.*, **23**, 323-329.

Foti S, C Comina, D Boiero & LV Socco, 2009. Non-uniqueness in surface-wave inversion and consequences on seismic site analyses, *Soil Dyn. Eq. Eng.*, **29**, 982-993.

Frankel A, 1993. Three-dimensional simulations of ground motions in the San Bernardino valley, California, for hypothetical earthquakes on the San Andreas fault, *Bull. Seis. Soc. Am.*, **83**, 1020-1041.

Frankel A & J Vidale 1992. A three-dimensional simulation of seismic waves in the Santa Clara valley, California, from a Loma Prieta aftershock, *Bull. Seis. Soc. Am.*, **82**, 2045-2074.

Frankel A & W Stephenson, 2000. Three-dimensional simulations of ground motions in the Seattle region for earthquakes in the Seattle fault zone, *Bull. Seis. Soc. Am.,* **90**, 1251–1267.

Frankel AD, WJ Stephenson, DL Carver, RA Williams, JK Odom & S Rhea, 2007. Seismic hazard maps for Seattle incorporating 3D sedimentary basin effects, nonlinear site response, and rupture directivity, USGS Open File Report 2007-1175, 77 p.

Frankel AD, WJ Stephenson & D Carver, 2009. Sedimentary basin effects in Seattle, Washington: Ground-motion observations and 3D simulations, *Bull. Seis. Soc. Am.*, **99**, 1579-1611.

Freund JE, 1967. *Modern Elementary Statistics*, Prentice-Hall, Englewood Cliffs, NJ.

Gelfand AE & DK Dey, 1994. Bayesian model choice: Asymptotics and exact calculations, *J. R. Stat. Soc.* **56**, 501-514.

Gilks WR, S Richardson & DJ Spiegelhalter (eds.), 1996. *Markov Chain Monte Carlo in Practice,* Chapman & Hall, Boca Raton, FL.

Gitterman Y, Y Zaslavsky, A Shapira & V Shtivelman, 1996. Empirical site response evaluations: case studies in Israel, *Soil Dyn. Earth. Eng.,* **15**, 447-463.

Gordy PL, 1988. Evaluation of the hydrocarbon potential of the Georgia depression, BC Ministry of Energy, Mines & Petroleum Resources, 80 p.

Gouveia WP & JA Scales, 1998. Bayesian seismic waveform inversion: parameter estimation and uncertainty analysis, *J. Geophys. Res*., **103**, 2759-2779.

Graves R, 1996. Simulating seismic wave propagation in 3D media using staggered-grid finite differences, *Bull. Seis. Soc. Am.,* **86**, 1091–1106.

Graves R & A Pitarka, 2004. Broadband time history simulation using a hybrid approach, *in* Proceedings 13th World Conference on Earthquake Engineering, Vancouver, BC, Canada, August 1-6 2004, Paper 1098.

Graves RW, A Pitarka & P Sommerville, 1998. Ground-motion amplification in the Santa Monica area: Effects of shallow basin-edge structure, *Bull. Seis. Soc. Am.*, **88**, 1224-1242.

Guatteri M, PM Mai & GC Beroza, 2004. A pseudo-dynamic approximation to dynamic rupture models for strong ground motion prediction, *Bull. Seis. Soc. Am.*, **94**, 2051-2063.

Halchuk S & JA Adams, 2004. Deaggregation of seismic hazard for selected Canadian cities, *in* Proceedings 13th World Conference on Earthquake Engineering, Vancouver, BC, Canada, August 1-6 2004, Paper 2470.

Hamilton TS, 1991. Seismic stratigraphy of unconsolidated sediments in the central Strait of Georgia: Hornby Island to Roberts Bank. Geological Survey of Canada, Open File 2530 (9 sheets).

Hannigan PK, JR Dietrich, PJ Lee & KG Osadetz, 2001. Petroleum resource potential of sedimentary basins on the Pacific margin of Canada, Geological Survey of Canada, Bulletin 564, 72 p.

Harris JB, JA Hunter, JL Luternauer, WDL Finn, 1995. Site amplification modelling of the Fraser Delta, British Columbia, *in* Proceedings of the 48th Canadian Geotechnical Conference, **2**, 947–54.

Hartzell SH & TH Heaton, 1983. Inversion of strong ground motion and teleseismic waveform data for the fault rupture history of the 1979 Imperial Valley, California, earthquake, *Bull. Seis. Soc. Am.*, **73**, 1553-1583.

Hartzell S, A Leeds, A Frankel, R Williams, J Odum, W Stephenson & W Silva, 2002. Simulations of broadband ground motions including nonlinear soil effects for a magnitude 6.5 earthquake on the Seattle fault, Seattle, Washington, *Bull. Seis. Soc. Am.*, **92**, 831–853.

Haskell NA, 1953. The dispersion of surface waves on multilayered media, *Bull. Seis. Soc. Am.,* **43**, 17-34.

Haskell NA, 1960. Crustal reflection of plane SH waves, *J. Geophys. Res*., **65**, 4147-4150.

Heaton TH, 1990. Evidence for and implications of self-healing pulses of slip in earthquake rupture, *Phys. Earth Planet. Int.,* **64**, 1-20.

Horike M, 1985. Inversion of phase velocity of long-period microtremors to the S-wave-velocity structure down to the basement in urbanized areas, *J. Phys. Earth*, **33**, 59-96.

Hunter JA & HA Christian, 2001. Use of shear-wave velocities to estimate thick soil amplification effects in the Fraser River delta, British Columbia, *in* Symposium Proceedings on the Application of Geophysics to Engineering and Environmental Problems, Denver, Colorado, Environmental and Engineering Geophysical Society.

Hunter JA, DJ Woeller & JL Luternauer, 1991. Comparison of surface, borehole, and seismic cone penetrometer methods for determining the shallow shear wave velocity structure in the Fraser River delta, British Columbia, *in* Current Research, Part A, Geological Survey of Canada, Paper 91-1A, 23-26.

Hunter JA, SR Dallimore & HA Christian, 1997. Borehole measurements of shear wave discontinuities in Quaternary sediments, Fraser River delta, British Columbia; *in* Current Research 1997-A, Geological Survey of Canada, 159-165.

Hunter JA, RA Burns, RL Good & CF Pelletier, 1998. A compilation of shear-wave velocities and borehole geophysical logs in unconsolidated sediments of the Fraser River delta, British Columbia, Geological Survey of Canada, Open File 3622.

Hunter JA, B Benjumea, JB Harris, RD Miller, SE Pullan, RA Burns & RL Good, 2002. Surface and downhole shear-wave seismic methods for thick soil site investigations, *Soil Dyn. Eq. Eng.*, **22**, 931-941.

Hurst PD, 1991. Petroleum geology of the Bellingham basin, Washington and evaluation of the AHEL and partners Birch Bay No. 1 well, *Wash. Geol.*, **19**, 16-18.

Hyndman RD, GC Rogers, H Dragert, K Wang, JJ Clague, J Adams & PT Bobrowsky, 1996. Giant earthquakes beneath Canada's west coast, *Geoscience Canada*, **23**, 63-72.

Idriss IM & JI Sun, 1992. User's Manual for SHAKE91: A computer program for conducting equivalent linear seismic response analyses of horizontally layered soil deposits, Center for Geotechnical Modeling, Department of Civil and Environmental Engineering, University of California, Davis, California, November, 12 p.

Ingber L, 1989.Very fast simulated re-annealing, *Mathl. Comput. Modelling*, **12**, 967-973.

Johnson S, 1984. Stratigraphy, age, and paleogeography of the Eocene Chuckanut Formation, northwest WA, *Can. J. Earth. Sci.*, **21**, 92-106.

Jongmans D, M Ohrnberger & M Wathelet, 2005. Final report WP13: Recommendations for quality array measurements and processing, European Commission – Research General Directorate, Site Effects Assessment Using Ambient Excitiations (SESAME), Deliverable 24.13, March 2005.

Joyner WB, 2000. Strong motion from surface waves in deep sedimentary basins, *Bull. Seis. Soc. Am.*, **90**, 6B, S95-S112.

Joyner WB, RE Warrick & TE Fumal, 1981. The effect of Quaternary alluvium on strong ground motion in the Coyote Lake, California, earthquake of 1979, *Bull. Seis. Soc. Am.*, **71**, 1333-1349.

Kao H, K Wang, R-Y Chen, I Wada, J He & SD Malone, 2008. Identifying the rupture place of the 2001 Nisqually, Washington, earthquake, *Bull. Seis. Soc. Am.*, **98**, 1546-1558.

Kass RE & AE Raftery, 1995. Bayes factors, *J. Am. Stat. Assoc.*, **90**, 773-795.

Kawase H, 1996. The cause of the damage belt in Kobe: 'the basin-edge effect', constructive interference of the direct S wave with the basin-induced diffracted/Rayleigh waves, *Seis. Res. Lett.*, **67**, 25-35.

Kind F, D Fäh & D Giardini, 2005. Array measurements of S-wave velocities from ambient vibrations, *Geophys. J. Int.*, **160**, 114-126.

Kuo C-H, D-S Cheng, H-H Hsieh, T-M Chang, H-J Chiang, C-M Lin & K-L Wen, 2009. Comparison of three different methods in investigating shallow shear-wave velocity structures in Ilan, Taiwan, *Soil Dyn. Earth. Eng.,* **29**, 133-143.

Lacoss RT, EJ Kelly & MN Toksoz, 1969. Estimation of seismic noise structure using arrays, *Geophys.,* **34**, 21-38.

Lai C, S Foti & G Rix, 2005. Propagation of data uncertainty in surface wave inversion, *J. Environ. Eng. Geophys.,* **10**, 219–228.

Lermo J & FJ Chavez-Garcia, 1993. Site effect evaluation using spectral ratios with only one station, *Bull. Seis. Soc. Am.*, **83**, 1574-1594.

Levander AR, 1988. Fourth-order finite-difference P-SV seismograms, *Geophys.,* **53**, 1425–1436.

Levson VM, PA Monahan & DJ Mate, 1998. Observed relationships between geology and liquefaction/amplification hazards, *in* Proceedings of the 8th International Congress, International Association for Engineering Geology and the Environment, September 21-25 1998, D Moore & O Hungr (eds.), Vancouver, Canada, 849-855.

Li W & D Assimaki, 2010. Site- and motion-dependent parametric uncertainty of site-response analyses in earthquake simulations, *Bull. Seis. Soc. Am.,* **100**, 954-968.

Liu P-C & RJ Archuleta, 2002. The effect of a low-velocity surface layer on simulated ground motion, *Seis. Res. Lett.*, **73**, 267.

Lowe C, SA Dehler & BC Zelt, 2003. Basin architecture and density structure beneath the Strait of Georgia, British Columbia, *Can. J. Earth Sci.,* **40**, 965–981.

Ludwig WJ, JE Nafe, CL Drake, 1970. Seismic refraction. *in* The sea, AE Maxwell (ed.), vol 4. Wiley-Interscience, New York, 53–84.

MacKay DJC, 2003. *Information Theory, Inference, and Learning Algorithms,* Cambridge University Press, Cambridge, U.K.

Mai PM, M Guatteri & GC Beroza, 2001. A stochastic-dynamic earthquake source model for strong motion prediction, *in* Proceedings 7th US National Conference Eathquake Engineering, July 21-25 2002, Boston, MA.

Malinverno A, 2002. Parsimonious Bayesian Markov chain Monte Carlo inversion in a nonlinear geophysical problem, *Geophys. J. Int.*, **151**, 675–688.

Maresca R, D Galluzzo & E Del Pezzo, 2006. H/V Spectral ratios and array techniques applied to ambient noise recorded in the Colfiorito basin, central Italy, *Bull. Seis. Soc. Am.*, **96**, 490-505.

Massey FJ, 1951. The Kolmogorov-Smirnov test for goodness of fit, *J. Am. Stat. Assoc.,* **46**, 68-78.

MEMPR reports – Non-confidential geological and geophysical reports released to June 2009, Province of British Columbia, Ministry of Energy, Mines & Petroleum Resources, Titles Division, Victoria, BC.

Report 29, Oil and Gas Possibilities in Sections 16, 17, Twp 2, WCM Fraser Valley, Crickmay C.H., 1941.

Report 33. Report, Newton Area, Fraser Valley, Johnson R.V., 1946.

Report 59. Fraser River Delta, Slipper S.E., 1950.

Report 899. Seismic Survey, Fraser Valley Area, Grinsfelder D., 1960.

Report 1034. Geology of Gulf Islands Area, Henderson G.G.L. & Vigrass L.W., 1962.

Report 1052. Interim Geology Report, Georgia Strait, Bell G.L., 1962.

Report 1275. Geophysical Investigation, Strait of Georgia, McKee A.H., 1966.

Report 1474. Marine Seismic Report, Georgia Strait, Machacek V., 1970.

Report 1530. "Vibroseis" Project, Strait of Georgia Area, Shepeard W.W., 1970.

Report 1779. Reservoir Exploration Project, Fraser Valley, Ramsay E.A., 1973.

Report 2009. Underground Gas Storage Prospects - Lower Fraser Valley, Sproule & Associates, 1976.

Report 2594. Geological Rpt & Gas Storage Potential – Pitt Meadows Area, P. 3134, Curr R., 1989.

Report 2604. Geological Rpt. & Gas Storage Potential – Pitt Meadows Area, P. 3133, Curr R., 1989.

British Columbia Resources Canada Ltd., 1987a. Well history report, BP Yellow Point d-84-C, BC Dept. Mines & Petroleum Resources, Open File WA06451.

British Columbia Resources Canada Ltd., 1987b. Well history report, BP Laurel Harmac c-36-F, BC Dept. Mines & Petroleum Resources, Open File WA06452.

Richfield Oil Corporation, 1962. Well history report, Richfield Pure Sunnyside 16-13, BC Dept. Mines & Petroleum Resources, Open File WA00913.

Richfield Oil Corporation, 1963. Well history report, Richfield Pure Point Roberts 6-3-5, BC Dept. Mines & Petroleum Resources, Open File WA01075.

Moczo P, J Kristek & L Halada, 2000. 3D Fourth-Order Staggered-Grid Finite-Difference Schemes: Stability and Grid Dispersion, *Bull. Seis. Soc. Am.*, **90**, 587–603.

Molnar S & JF Cassidy, 2006. A comparison of site response techniques using weak-motion earthquakes and microtremors, *Eq. Spec.*, **22**, 169-188.

Molnar S, JF Cassidy & SE Dosso, 2004. Comparing intensity variation of the 2001 Nisqually earthquake to geology in Victoria, British Columbia, *Bull. Seis. Soc. Am.*, **94**, 2229-2238.

Molnar S, JF Cassidy, PA Monahan, T Onur, C Ventura & A Rosenberger, 2007. Earthquake site response studies using microtremor measurements in southwestern British Columbia, *in* Proceedings 9th Canadian Conference on Earthquake Engineering, Ottawa, Ontario, June 26-29, 2007, Paper 1182.

Molnar S, JF Cassidy, SE Dosso & KB Olsen, 2009. 3D Ground Motion in the Georgia Basin Region of SW British Columbia for Intra-slab Earthquake Scenarios, AGU/CGU Joint Assembly, Abstract S31A-05.

Molnar S, SE Dosso & JF Cassidy, 2010a. Bayesian inversion of microtremor array dispersion data in southwestern British Columbia, *Geophys. J. Int.*, **183**, 923-940.

Molnar S, JF Cassidy, SE Dosso & KB Olsen, 2010b. 3D Ground motion in the Georgia basin region of SW British Columbia for Pacific Northwest scenario earthquakes, *in* Proceedings 9th US National and 10th Canadian Conference on Earthquake Engineering, Toronto, Ontario, July 25-29, 2010, Paper 754.

Molnar S, SE Dosso & JF Cassidy, 2011. Site response probability analysis from Bayesian inversion of microtremor array dispersion data, *Soil. Dyn. Earth. Eng.*, submitted.

Monahan PA, 1999. The application of cone penetration test data to facies analysis of the Fraser River delta, British Columbia, *Ph.D. Thesis*, University of Victoria, Victoria, British Columbia.

Monahan PA & VM Levson, 1997. Earthquake hazard assessment in greater Victoria, British Columbia: Development of a shear-wave velocity model for the Quaternary deposits, *in* Geological Fieldwork 1996, British Columbia Geological Survey, Paper 1997-1, 467-479.

Monahan PA & VM Levson, 2000. Quaternary geological map of Greater Victoria, British Columbia Geological Survey, Ministry of Energy and Mines, Victoria, B.C., Geoscience Map 2000-2.

Monahan PA, VM Levson, P Henderson & A Sy, 2000. Relative amplification of ground motion hazard map of greater Victoria, British Columbia Geological Survey, Ministry of Energy and Mines, Victoria, British Columbia, Geoscience Map 2000-3.

Monahan PA & VM Levson, 2001. Development of a shear-wave velocity model of the near-surface deposits of southwestern British Columbia, Canada, *in* Proceedings 4th International Conference on Recent Advances in Geotechnical Earthquake Engineering and Soil Dynamics, San Diego, California, March 26-31, 2001, Paper 11.16.

Monger JWH, 1990. Georgia Basin: Regional setting and adjacent Coast Mountains geology, British Columbia, *in* Current Research, Part F, Geological Survey of Canada, Paper 90-1F, 95-107.

Monger JWH & JM Journey, 1994. Basement geology and tectonic evolution of the Vancouver region, *in* Geology and Geological Hazards of the Vancouver Region, Southwestern British Columbia, JWH Monger (ed.), Geological Survey of Canada, Bulletin 481, 3-25.

Montgomery DC & EA Peck, 1992. *Introduction to Linear Regression Analysis,* Wiley, New York.

Mosher DC & TS Hamilton, 1998. Morphology, structure and stratigraphy of the offshore Fraser Delta and adjacent Strait of Georgia, *in* Geology and natural hazards of the Fraser River Delta, British Columbia. J.J. Clague, J.L. Lautenauer & D.C. Mosher (eds.), Geological Survey of Canada, Bulletin 525, 147–160.

Mosher DC, JF Cassidy, C Lowe, Y Mi, RD Hyndman, GC Rogers & MA Fisher, 2000. Neotectonics in the Strait of Georgia: Tentative correlation of seismicity with shallow geologic structure in southwestern British Columbia, Geological Survey of Canada, Current Research 2000-A22, 1-9.

Moss RES, 2008. Quantifying measurement uncertainty of thirty-metre shear-wave velocity, *Bull. Seis. Soc. Am.*, **98**, 1399-1411.

Moss RES, 2011. Reduced sigma of ground-motion prediction equations through uncertainty propagation, *Bull. Seis. Soc. Am.,* **101**, 250-257.

Mustard PS, 1994. The Upper Cretaceous Nanaimo Group, Georgia basin. *in* Geology and Geological Hazards of the Vancouver Region, Southwestern British Columbia, JWH Monger (ed.), Geological Survey of Canada, Bulletin 481, 27-95.

Mustard PS & GE Rouse, 1994. Stratigraphy and evolution of Tertiary Georgia basin and sub-adjacent Upper Cretaceous sedimentary rocks, southwestern British Columbia and northwestern Washington State. *in* Geology and Geological Hazards of the Vancouver Region, Southwestern British Columbia, JWH Monger (ed.), Geological Survey of Canada, Bulletin 481, 97-179.

Mustard PS, JJ Clague, GJ Woodsworth, CJ Hickson, LE Jr. Jackson, JL Luternauer, JWH Monger, BD Ricketts, RJW Turner, JA Hunter & PA Monahan, 1998. Geology and geological hazards of the Greater Vancouver area. *in* Urban Geology of Canadian Cities. PF Karrow & OL White (eds.), Geological Association of Canada, Special Paper 50, 39-70.

Nakamura Y, 1989. A method for dynamic characteristics estimation of subsurface using microtremor on the ground surface, *Quarterly Reports of the Railway Technical Research Institute*, **30**, 25-33.

National Building Code of Canada, 2005. National Research Council Canada, 1167p.

Nelder JA & R Mead, 1965. A simplex method for function minimization, *Computer Journal*, **7**, 308–313.

Next generation of ground-motion attenuation models, *Eq. Spec.* **24**, **1** (2008).

Nilsson S, NA Petersson, B Sjögreen & HO Kreiss, 2007. Stable difference approximations for the elastic wave equation in second order formulation, *SIAM J. Numer. Anal.,* **45**, 1902–1936.

Ohrnberger M, E Schissele, C Cornou, M Wathelet, A Savvaidis, F Scherbaum, D Jongmans & F Kind, 2004. Microtremor array measurements for site effect investigations: Comparison of analysis methods for field data crosschecked by simulated wavefields, *in* Proceedings 13th World Conference on Earthquake Engineering, Vancouver, Canada, August 1-6, 2004, Paper 940.

Ohrnberger M, M Wathelet, C Cornou, A Savvaidis & N Theodoulis, 2008. Using ambient vibration array techniques for site characterization and seismic microzonation, SESARRAY course, December 6-12, 2008, Thessaloniki, Greece.

Olsen KB, 1994. Simulation of three-dimensional wave propagation in the Salt Lake Basin, *Ph.D. Thesis*, University of Utah, Salt Lake City, Utah, 157 p.

Olsen KB & GT Schuster, 1994. Three-dimensional modeling of site amplification in East Great Salt Lake Basin, U.S. Geological Survey Technical Report, 1434-93-G-2345, 102 p.

Olsen KB, JC Pechmann & GT Schuster, 1995. Simulation of 3D elastic wave propagation in the Salt Lake basin, *Bull. Seis. Soc. Am.*, **85**, 1688-1710.

Olsen KB & RJ Archuleta, 1996. Three-dimensional simulation of earthquakes on the Los Angeles fault system, *Bull. Seis. Soc. Am.*, **86**, 575-596.

Olsen KB, 2000a. 3D Viscoelastic wave propagation in the Upper Borrego valley, California, constrained by borehole and surface data, *Bull. Seis. Soc. Am.*, **90**, 134-150.

Olsen KB, 2000b. Site amplification in the Los Angeles basin from three dimensional modelling of ground motion, *Bull. Seis. Soc. Am.,* **90**, S77–S94.

Olsen KB, 2003. Estimation of Q for long-period (> 2 sec) waves in the Los Angeles basin, *Bull. Seis. Soc. Am.*, **93**, 627-638.

Olsen KB, SM Day, JB Minster, Y Cui, A Chourasia, M Faerman, R Moore, P Maechling & T Jordan, 2006. Strong shaking in Los Angeles expected from southern San Andreas earthquake, *Geophys. Res. Lett.,* **33**, L07305, doi:10.1029/2005GL025472.

Olsen KB, WJ Stephenson & A Geisselmeyer, 2008a. 3D Crustal structure and long-period ground motions from a M9.0 megathrust earthquake in the Pacific Northwest region, *J. Seis.*, **12**, 145-159.

Olsen KB, SM Day, JB Minster, Y Cui, A Chourasia, D Okaya, P Maechling & T Jordan, 2008b. TeraShake2: Spontaneous rupture simulations of M_W 7.7 earthquakes on the southern San Andreas fault, *Bull. Seis. Soc. Am.*, **98**, 1162-1185.

Onur T, CE Ventura & WDL Finn, 2005. Regional seismic risk in British Columbia – Damage and loss distribution in Victoria and Vancouver, *Can. J. Civ. Eng.*, **32**, 361-371.

Onur T, S Molnar, J Cassidy, CE Ventura & K X-S Hao, 2004. Estimating site periods in Vancouver and Victoria, British Columbia using microtremor measurements and SHAKE analyses, Canadian Geotechnical Conference, Quebec City, Quebec, October 24-27, 2004, 8 p.

Park CB, RD Miller & J Xia, 1999. Multichannel analysis of surface waves, *Geophys*. **64**, 800-808.

Parker RL, 1994. *Geophysical Inverse Theory,* Princeton University Press, Princeton, NJ.

Parolai S, M Mucciarelli, MR Gallipoli, SM Richwalski & A Strollo, 2007. Comparison of empirical and numerical site responses at the Tito test site, southern Italy, *Bull. Seis. Soc. Am.*, **97**, 1413-1431.

Petersen MD, AD Frankel, SC Harmsen, CS Mueller, KM Haller, RL Wheeler, RL Wesson, Y Zeng, OS Boyd, DM Perkins, N Luco, EH Field, CJ Wills & KS Rukstales, 2008. Documentation for the 2008 Update of the United States National Seismic Hazard Maps: U.S. Geological Survey Open-File Report 2008–1128, 61 p.

Picozzi M, A Strollo, S Parolai, E Durukal, O Ozel, S Karabulut, J Zschau & M Erdik, 2009. Site characterization by seismic noise in Istanbul, Turkey, *Soil Dyn. Eq. Eng.*, **29**, 469-482.

Pitarka A, 1999. 3D elastic finite-difference modelling of seismic motion using staggered grids with nonuniform spacing, *Bull. Seis. Soc. Am.,* **89**, 54–68.

Pitarka A, K Irikura & T Iwata, 1997. Modelling of ground mtion in the Higashinada (Kobe) area for an aftershock of the 1995 January 17 Hyogo-ken Nanbu, Japan, earthquake, *Geophys. J. Int.*, 231-239.

Pitarka A, R Graves & P Somerville, 2004. Validation of a 3D velocity model of the Puget Sound region based on modeling ground motion from the 28 February 2001 Nisqually earthquake, *Bull. Seis. Soc. Am.*, **94**, 1670–1689.

Poggi V, B Edwards & D Fah, 2011. Derivation of a reference shear-wave velocity model from empirical site amplification, *Bull. Seis. Soc. Am.,* **101**, 258-274.

Ramachandran K, SE Dosso, CA Zelt, GD Spence, RD Hyndman & TM Brocher, 2004. Upper crustal structure of southwestern British Columbia from the 1998 Seismic Hazards Investigation in Puget Sound, *J. Geophys. Res.,* **109**, B09303, doi:10.1029/2003JB002826.

Ramachandran K, RD Hyndman & TM Brocher, 2006. Regional P wave velocity structure of the northern Cascadia subduction zone, *J. Geo. Res*., **111**, B12301, doi:10.1029/2005JB004108.

Reiter L, 1991. Earthquake ground motion: Site effects, *in* Earthquake hazard analysis: Issues and insights, Columbia Univ. Press, NY, p.147-163.

Renalier F, D Jongmans, M Wathelet, C Cornou, B Endrun, M Ohrnberger & A Savvaidis, 2009. Influence of parameterization on inversion of surface wave dispersion curves and definition of a strategy of inversion, EGU General Assembly, Geophysical Research Abstracts, **11**, EGU2009-7799.

Rial JA, NG Saltzman & H Ling, 1992. Earthquake-induced resonance in sedimentary basins, *Amer. Sci.,* **80**, 566-578.

Riedel M, V Barrie, P Hill, TM Brocher, TL Pratt & RD Hyndman, 2002. Mapping of near surface active faults in Georgia Strait, *Eos Trans*. AGU, **83**, Fall Meet. Suppl., Abstract S22B-1031.

Robertson PK, RG Campanella, ASCE Members, D Gillespie & A Rice, 1992. Seismic CPT to measure in situ shear wave velocity, *ASCE Journal of Geotechnical Engineering*, **112**, 791-803.

Ristau J, GC Rogers & JF Cassidy, 2007. Stress in western Canada from regional moment tensor analysis, *Can. J. Earth Sci.*, **44**, 127-148.

Rogers GC, 1998. Earthquakes and earthquake hazard in the Vancouver area, *in* Geology and Natural Hazards of the Fraser River Delta, British Columbia, JJ Clague, JL Luternauer & DC Mosher (eds.), Geological Survey of Canada, Bulletin 525, 17-25.

Roten D & D Fäh, 2007. A combined inversion of Rayleigh wave dispersion and 2-D resonance frequencies, *Geophys. J. Int.*, **168**, 1261-1275.

Roullé A & FJ Chávez-García, 2006. The strong ground motion in Mexico City : Analysis of data recorded by a 3D array, *Soil. Dyn. Eq. Eng.*, **26**, 71-89.

Sambridge M & K Mosegaard, 2002. Monte Carlo methods in geophysical inverse problems, *Rev. Geophys.*, **40**, 1-29.

Sambridge M, K Gallagher, A Jackson & P Rickwood, 2006. Trans-dimensional inverse problems, nodel comparision and the evidence. *Geophy. J. Int.,* **167**, 528-542.

Sánchez-Sesma FJ, VJ Palencia & F Luzón, 2002. Estimation of local site effects during earthquakes: An overview, *ISET Journal of Earthquake Technology*, Paper 423, **39**, 167-193.

Savvaidis A, M Ohrnberger, M Wathelet, C Cornou, P-Y Bard & N Theodulidis, 2009. Variability analysis of shallow shear wave velocity profiles obtained from dispersion curve inversion considering multiple model parameterizations, SSA Meeting, Monterey, CA, *Seis. Res. Lett.*, **80**, 354.

Scherbaum F, K-G Hinzen & M Ohrnberger, 2003. Determination of shallow shear wave velocity profiles in the Cologne, Germany area using ambient vibrations, *Geophys. J. Int.*, **152**, 597-612.

Schevenels M, G Lombaert, G Degrande & S François, 2008. A probabilistic assessment of resolution in the SASW test and its impact on the prediction of ground vibrations, *Geophys. J. Int.*, **172**, 262-275.

Schwartz G, 1978. Estimating the dimension of a model, *Ann. Stat.,* **6**, 461-464.

Seed HB, MP Romo, JI Sun, A Jaime & J Lysmer, 1988. The Mexico earthquake of Spetmber 19, 1985 – Relationships between soil conditions and earthquake ground motions, *Eq. Spec*., **4**, 687-729.

Singh SK, E Mena & R Castro, 1988. Some aspects of the source characteristics and ground motion amplifications in and near Mexico city from acceleration data of the September 1985, Michoacan, Mexico earthquakes, *Bull. Seis. Soc. Am.*, **78**, 451-477.

Socco LV & D Boiero, 2008. Improved Monte Carlo inversion of surface wave data, *Geophys. Prospect.*, **56**, 357-371.

Sommerville P, K Irikura, R Graves, S Sawada, D Wald, N Abrahamson, Y Iwasaki, T Kagawa, N Smith & A Kowada, 1999. Characterizing crustal earthquake slip models for the prediction of strong ground motion, *Seis. Res. Lett.*, **70**, 59-80.

Steidl JH, AG Tumarkin & RJ Archuleta 1996. What is a reference site?, *Bull. Seis. Soc. Am.*, **86**, 1733-1748.

Stephenson WJ, 2007. Velocity and density models incorporating the Cascadia subduction zone for 3D earthquake ground motion simulations, Version 1.3: USGS, Earthquake Hazards Ground Motion Investigations, Open-File Report 2007–1348, 24 p.

Stephenson WJ, JN Louie, S Pullammanappallil, RA Williams & JK Odum, 2005. Blind shear-wave velocity comparison of ReMi and MASW results with boreholes to 200 m in Santa Clara valley: Implications for earthquake ground-motion assessment, *Bull. Seis. Soc. Am.*, **95**, 2506-2516.

Stephenson WJ, AD Frankel, JK Odum, RAWilliams & TL Pratt, 2006. Towards resolving an earthquake ground motion mystery in west Seattle, Washington state: Shallow seismic focusing may cause anomalous chimney damage, *Geophys. Res. Lett*., doi:10.1029/2005GL025037.

Stewart JP, AH Liu & Y Choi, 2003. Amplification factors for spectral acceleration in tectonically active regions, *Bull. Seis. Soc. Am.,* **93**, 332–352.

Stokoe KH, SG Wright , JA Bay & JM Roesset, 1994. Characterization of geotechnical sites by SASW method, *in* Geophysical characterization of sites, RD Woods (ed.), Proceedings of the 13th ICSMFE, International Science Publisher, New York, 15-25.

Tarantola A, 1987. *Inverse Problem Theory: Methods for Data Fitting and Model Parameter Estimation,* Elsevier, Amsterdam.

Thomson WT, 1950. Transmission of elastic waves through a stratified solid medium, *J. Appl. Phys.*, **21**, 89-93.

Thompson EM, LG Baise, RE Kayan & BB Guzina, 2009. Impediments to predicting site response: Seismic property estimation and modeling simplifications, *Bull. Seis. Soc. Am.*, **99**, 2927-2949.

Tumarkin AG & RJ Archuleta, 1997. Recent advances in prediction and processing of strong ground motions, *Natural Hazards* **15,** 199–215.

Wald L & J Mori, 2000. Evaluation of methods for estimating linear site-response amplifications in the Los Angeles region, *Bull. Seis. Soc. Am.*, **90**, S32-S42.

Wald DJ, TH Heaton & KW Hudnut, 1996. The slip history of the 1994 Northridge, California, earthquake determined from strong-motion, teleseismic, GPS, and leveling data, *Bull. Seis. Soc. Am.*, **86**, S49-S70.

Wald DJ, V Quitoriano, TH Heaton & H Kanamori, 1999. Relationship between Peak Ground Acceleration, Peak Ground Velocity, and Modified Mercalli Intensity in California, *Eq. Spec.*, **15**, 557-564.

Wathelet M, D Jongmans, M Ohrnberger & S Bonnefoy-Claudet, 2008. Array performances for ambient vibrations on a shallow structure and consequences over V_S inversion, *J. Seis.*, **12**, 1-19.

White DJ & RM Clowes, 1984. Seismic investigation of the Coast plutonic complex – Insular belt boundary beneath the Strait of Georgia. *Can. J. Earth Sci.*, **21**, 1033-1049.

Wiest KR, DI Doser, AA Velasco & J Zollweg, Source inversion and comparison of the 1939, 1946, 1949 and 1965 earthquakes, Cascadia subduction zone, western Washington, *Pure Appl. Geophys.*, **164**, 1905-1919.

Wills CJ, M Peterson, WA Bryant, M Reichle, GJ Saucedo, S Tan, G Taylor & J Treiman, 2000. A site-conditions map for California based on geology and shear-wave velocity, *Bull. Seis. Soc. Am.,* **90**, S187-S208.

Woeller DJ, JL Luternauer & JA Hunter, 1993. Presentation and interpretation of seismic cone penetration test data, Fraser River delta, British Columbia, Geological Survey of Canada, Open File 2715.

Wood HO & F Neumann, 1931. Modified Mercalli intensity scale of 1931, *Bull. Seis. Soc. Am.,* **21,** 277-283.

Wuorinen V, 1974. A Preliminary seismic microzonation of Victoria, British Columbia, *M.A. Thesis*, University of Victoria, Victoria, British Columbia.

Xia J, RD Miller & CB Park, 1999. Estimation of near-surface shear-wave velocity by inversion of Rayleigh wave. *Geophys.,* **64**, 691-700.

Xia J, RD Miller, CB Park, JA Hunter & JB Harris, 2000. Comparing shear-wave velocity profiles from MASW with borehole measurements in unconsolidated sediments, Fraser River delta, BC, Canada, *J. Env. Eng. Geophys.*, **5**, 1-13.

Xia J, RD Miller, X Yixian, L Yinhe, C Chao, L Jiangping, J Ivanov & C Zheng, 2009. High-frequency Rayleigh-wave method, *J. Earth. Sci.*, **20**, 563-579.

Zelt BC, RM Ellis, CA Zelt, RD Hyndman, C Lowe, GD Spence & MA Fisher, 2001. Three-dimensional crustal velocity structure beneath the Strait of Georgia, British Columbia, *Geophy. J. Int.,* **144**, 695–712.

APPENDIX A: 3D FINITE-DIFFERENCE SIMULATIONS

This appendix provides movies of selected 3D finite-difference simulations presented and discussed in Chapter 3. Each movie consists of six panels: EW (top), NS (middle), and UD (bottom) directions of ground motion for the non-basin model (left) and the basin model (right) simulations, for the same M_W 6.8 scenario earthquake. The coastline (black line) and location of highest basin amplification in Greater Vancouver (magenta square) are plotted for reference. 70-s simulations for the following deep JdF plate earthquake scenarios are provided: scenarios 1, 2, 6, and 10 (see Figure 38). 88-s simulations for the two shallow NA plate scenarios are provided: San Juan Island (Section 3.5.3.1) and Georgia Strait (Section 3.5.3.2) events.